# THE EFFECT OF BORON SUBSTITUTION ON THE STRUCTURE OF CALCIUM-ALUMINOSILICATE CALCIUM-FLUORO-ALUMINOSILICATE GLASSES AND GLASS-CERAMICS


**By**

**Siqi Zhang**

A thesis submitted to the University of Birmingham for the degree of DOCTOR OF PHILOSOPHY

School of Metallurgy and Materials

The University of Birmingham

**January 2016**

# ABSTRACT

This work focuses on the effect of boron substitution for aluminium on the structure of a series of fluorine-free ($4.5SiO_2$-$3Al_2O_3$-$1.5P_2O_5$-5CaO) and fluorine-containing ($4.5SiO_2$-$3Al_2O_3$-$1.5P_2O_5$- 3CaO-$2CaF_2$) glasses. The resultant glass ceramics have been studied by using a combination of analytical tools like helium pycnometer, FTIR, Raman, XRD, multinuclear MAS-NMR spectroscopy and thermal analysis by DSC and TGA. The morphology of the crystal phases was observed by ESEM, and the identification of the composition observed was achieved by EDX. Substituted aluminium glass contains high amount of boron (75 and 100 molar%) couldn't be processed due to phase separation and glass crystallisation. Boron couldn't substitute for a larger amount of aluminium in the glass structure. It is very hard to make aluminium-free glass, but we can reduce the content of aluminium in the glass composition. The density of both boron-substituted aluminium glasses and glass ceramics decreased with increasing boron content. The glass transition temperature decreased generally with an increase of boron substitution in fluorine-free glasses, and the glass transition temperature ($T_g$) remained almost stable in fluorine-containing glasses. With a high amount of boron substitution for aluminium, the $T_g$ and glass crystallization temperature ($T_p$) decreased obviously, which promoted the Ca-P main phase crystallising at a lower temperature. With an increase of the boron substitution for aluminium, the peaks related to Si-O-NBOs (non-bridging oxygens) decreased in intensity, suggesting that there was a decrease in the number of NBOs. With different

sintering temperatures of 700°C, 900°C, and 1100°C, it was indicated in the fluorine-free glass ceramics that calcium phosphate ($Ca_4P_2O_9$) was the first phase to be formed below the sintering temperature at 900°C. When the sintering temperature was raised to 1100°C, the calcium phosphate ($Ca_4P_2O_9$) phase transferred to the tricalcium phosphate [$Ca_3(PO_4)_2$] phase, and anorthite and aluminium phosphorus phases were crystallised subsequently as second and third phases. The fluorapatite phase was the first phase to be formed in the fluorine-containing glass ceramics, and with the sintering temperature raised to 1100°C, the mullite and aluminium phosphorus phases were crystallised in the glass structure and were decreased with the increase of boron substitution. All the NMR results investigate lots of information of the structure of boron-substituted glasses and glass-ceramics which are agree with XRD results. ESEM and EDX analysis showed changes in the composition of glass ceramics with boron substitution.

# ACKNOWLEDGEMENTS

I am a split-location Phd student, and during these years I am so grateful to my academic supervisor, Artemis Stamboulis (University of Birmingham) and Wen Ni (University of Science and Technology Beijing), for their presence, encouragement, support and guidance in UK and China.

I would like to thank James Bowen from our university chemical engineering helping me to do the Raman analysis, Mitra A. M. P. Kashani, Zuzanna Trzcinska and Zeinab Salary from our biomaterial group for being always present and willing to provide assistance during my research and they overall support. I would also like to express my gratitude to Frank, Jess, and Paul for teaching me how to use the DSC, TGA, FTIR, XRD, ESEM and EDX machines and the many kindnesses they show me.

I would like to thank Ningning Wu from institute of chemistry chinese academy of science helping me to investigate all NMR results, and Zhongjie Wang, Shujie Gao and all the fellows in Pro. Ni's group for providing assistance on the glass making, sintering, part of XRD analysis and them all support.

Finally, I would like to thank my friends and my family, for always believing in me and supporting me and being next to me in every step I choose to take.

# FIGURE CAPTIONS

composition for boron-substituted fluorine-containing glasses.

**Figure 4.2.8:** The variation in second glass crystallisation temperature ($T_{p2}$) with composition for boron-substituted fluorine-containing glasses.

**Figure 4.2.9:** B0, B5, B10, B15, B25, and B50 boron-substituted fluorine-free glasses with different heating rates of 10, 20, and 40$^{o}$C/min.

**Figure 4.2.10:** FB0, FB5, FB10, FB15, FB25, and FB50 boron-substituted fluorine-containing glasses with different heating rates of 10, 20, and 40$^{o}$C/min.

**Figure 4.2.11:** TGA and DSC analysis of B7.5 and FB7.5 glasses.

**Figure 4.2.12:** XRD results of B25, B50, FB25, and FB50 boron-substituted glasses.

**Figure 4.2.13:** XRD results of 25, B50 and FB0, FB2.5, FB25, FB50 boron substituted glasses hold temperature at 700$^{o}$C.

**Figure 4.2.14:** XRD results of boron substituted fluorine-free glasses hold temperature at 900$^{o}$C.

**Figure 4.2.15:** XRD results of boron substituted fluorine containing glasses hold temperature at 900$^{o}$C.

**Figure 4.2.16:** X-ray powder diffraction spectra of heat-treated (1100$^{o}$C), boron-substituted fluorine-free glass ceramics. The heat-treated B0 glass spectrum is presented as reference material. ○ = calcium phosphate, ● = anorthite, □ = aluminium phosphate.

**Figure 4.2.17:** XRD results of boron substituted fluorine-free glasses hold temperature at 1100$^{o}$C.

**Figure 4.2.16:** X-ray powder diffraction spectra of heat-treated (1100$^{o}$C), boron-substituted fluorine-containing glass ceramics. The heat-treated FB0 glass spectrum is presented as reference material. □ = aluminium phosphate, ▼= fluorapatite, ▽ = mullite.

**Figure 4.2.18:** XRD results of boron substituted fluorine containing glasses hold temperature at 1100$^{o}$C.

**Figure 4.3.1:** Density of boron-substituted fluorine-free glass ceramics (heat treated temperature at 1100$^{o}$C).

**Figure 4.3.2:** Density of boron-substituted fluorine-containing glass ceramics (heat

treated temperature at 1100°C).

**Figure 4.3.3:** FTIR spectra of all boron-substituted fluorine-free glass ceramics (hold at 900°C).

**Figure 4.3.4:** FTIR spectra of all boron-substituted fluorine-containing glass ceramics (hold at 900°C).

**Figure 4.3.5:** FTIR spectra of all boron-substituted fluorine-free glass ceramics (hold at 1100°C).

**Figure 4.3.6:** FTIR spectra of all boron-substituted fluorine-containing glass ceramics (hold at 1100°C).

**Figure 4.3.7:** Raman spectra of boron-substituted fluorine-free glass ceramics (hold at 1100°C).

**Figure 4.3.8:** Raman spectra of boron-substituted fluorine-containing glass ceramics (hold at 1100°C).

**Figure 4.3.3.1:** $^{29}$Si MAS-NMR spectra of boron-substituted fluorine-free glass ceramics heat treated at 1100°C. The spinning bands are marked with ●.

**Figure 4.3.3.2:** $^{29}$Si MAS-NMR spectra of boron-substituted fluorine-containing glass ceramics heat treated at 1100°C. The spinning bands are marked with ●.

**Figure 4.3.3.3:** $^{27}$Al MAS-NMR spectroscopy of boron-substituted fluorine-free glass ceramics heat treated at 1100°C. The spinning bands are marked with ●.

**Figure4.3.3.4:**$^{27}$Al MAS-NMR spectroscopy of boron-substituted fluorine-containing glass ceramics heat treated at 1100°C. The spinning bands are marked with ●.

**Figure 4.3.3.5:** $^{31}$P MAS-NMR spectroscopy of boron-substituted fluorine-free glass ceramics heat treated at 1100°C. The spinning bands are marked with ●.

**Figure 4.3.3.6:** $^{31}$P MAS-NMR spectroscopy of boron-substituted fluorine-containing glass ceramics heat treated at 1100°C. The spinning bands are marked with ●.

**Figure 4.3.3.7:** $^{11}$B MAS-NMR spectroscopy of boron-substituted fluorine-free glass ceramics heat treated at 1100°C. The spinning bands are marked with ●.

**Figure 4.3.3.8:** $^{11}$B MAS-NMR spectroscopy of boron-substituted fluorine-containing glass ceramics heat treated at 1100°C. The spinning bands are marked with ●.

# TABLE CAPTIONS

**Table 4.3.3.8:** $^{11}B$ MAS-NMR spectroscopy of boron-substituted fluorine-containing glass ceramics heat treated at 1100$^{o}$C.

**Table 4.3.3.9:** $^{19}F$ MAS-NMR spectroscopy of boron-substituted fluorine-containing glass ceramics heat treated at 1100$^{o}$C.

# ABBREVIATIONS

| | |
|---|---|
| **A-W** | **Apatite-wollastonite-containing** |
| **APS** | **Amorphous phase separation** |
| **BO** | **Bridging oxygen** |
| **DSC** | **Differential scanning calorimetry** |
| **EDX** | **Energy dispersive x-ray analysis** |
| **ESEM** | **Environmental scanning electron microscope** |
| **FAP** | **Fluorapatite** |
| **FTIR** | **Fourier transform infra-red spectroscopy** |
| **GICs** | **Glass ionomer cements** |
| **GPCs** | **Glass polyalkenoate cements** |
| **HCA** | **Hydroxycarbonate** |
| **HAP** | **Hydroxyapatite** |
| **KBr** | **Potassium bromide** |
| **MAS-NMR** | **Magic-angle spinning nuclear magnetic resonance** |
| **NBO** | **Non-bridging oxygen** |
| **OD** | **Optical density** |
| **PAA** | **Polyacrylic acid** |
| **RM-GIC** | **Resin-modified glass ionomer cement** |
| **SANS** | **Small angle neutron scattering** |
| **SEM** | **Scanning electron microscope** |
| **TA** | **Tartaric acid** |
| **TCP** | **Tricalcium phosphate** |
| **$T_g$** | **Glass transition temperature** |
| **$T_p$** | **Glass crystallisation temperature** |
| **TGA** | **Thermogravimetric analysis** |
| **XRD** | **X-ray powder diffraction** |

# CONTENTS

# CHAPTER 1 INTRODUCTION

Calcium-aluminosilicate and calcium fluoro-aluminosilicate glasses are commonly used for the formation of polyalkenoate cements，which have significant applications in the medical and dental fields. Previous studies have indicated that such glasses can crystallize to form β-tricalcium phosphate and fluorapatite [1-2], which are the main mineral phase in tooth and bone. Kokubo et al. [3] have developed an apatite wollastonite glass ceramic that showed bone bonding following implantation and having adequate mechanical strength. Hatton et al. [4] suggested that apatite-mullite glass-ceramics improved bone response and none of them affected bone mineralization. Stamboulis et al. [5] reported that apatite–mullite ceramics do not release aluminium to the surrounding tissue and therefore are not cytotoxic. However, due to previous negative results in the literature, aluminium is not a desirable element in glass ceramics; therefore, it is important to explore other options—for example, aluminium-free glasses and glass ceramics. Boron trioxide ($B_2O_3$) is a glass former like silica, increases the chemical resistance of the glass and is also a possible substitute for aluminium to reduce the aluminium content of calcium-aluminosilicate glass. Boron can reportedly replace Al atoms to form the network with Si in many boro-aluminosilicate glasses [6]. But the influence of additional boron on the network of boron-substituted apatite has been rarely reported. This study focuses on the effect of boron substitution over aluminium producing boron-substituted aluminosilicate and fluoro-aluminosilicate glasses and glass ceramics. The cation substitution took place in 0, 2.5, 5, 7.5, 10, 12.5, 15, 25, 50, 75 and 100% molar content of boron. The samples were all characterised by Helium Pycnometer, DSC, TGA, FTIR, RAMAN,

XRD, SEM, EDX, and multinuclear MAS-NMR in order to observe the effects of boron substitution on the structure of glasses and glass-ceramics.

## Thesis layout:

This thesis is divided into seven main chapters. Chapter 1 is the introduction of the thesis and layout. Chapter 2, the literature review, begins with a review the background knowledge of the biomaterials and bone repair. The middle part of the review focuses on the history of bioglass, research on glass ionomer cements, and the development of dental materials. The last part of the review concentrates on the structure and crystallization of glass, especially the development and advantages of borosilicate glass and finally includes research aims. Chapters 3 to 6 encompass all the experimental work. In those chapters, the properties of new substituted glasses and glass-ceramics are reported using characterisation techniques of Helium Pycnometer, DSC, TGA, FTIR, RAMAN, XRD, SEM, EDX, and MAS-NMR methods. Chapter 3 introduces the conditions and details of each analysis. A series of glasses and glass-ceramics of various boron concentrations were made and their glass transition temperatures, crystallization temperatures, crystallized phases, microstructures, chemical shifts, and sintering properties were reported in Chapter 4. After that, the comparison and reasons for different amounts of boron substitution will be discussed in Chapter 5. Chapters 6 and 7 draw the conclusions and propose future work for the further development of boron-substituted glasses and glass-ceramics.

# CHAPTER 2 LITERATURE REVIEW

## 2.1 The background of biomaterials

Biomaterials are commonly used as prostheses in dental, ophthalmological, cardiovascular, orthopaedic, and reconstructive surgery, as well as in other applications such as surgical sutures, bioadhesives, and controlled drug-release devices [7]. Biomaterials science includes diagnostics and therapeutics. It encompasses basic sciences (biology, chemistry, and physics), engineering, and medicine. The progress of biomaterials science to clinically important medical devices is dependent on: (1) sound engineering design; (2) invitro testing, in both animals and humans; (3) clinical realities; and (4) the involvement of industry, permitting product development and commercialization [7].

**Bone and biomaterials repair**

Biomaterials also play a very important role in bone repair and regeneration, which to deal with musculoskeletal problems, including bone and joint pathologies which lead to tissue degeneration and inflammation are among the main causes of chronic pain, physical disability, and work absenteeism in both developed and developing countries, and they affect millions of people diseases. Freeman and Hatton [4] suggested bone defects and augment bone volume could be repaired by new materials such as oesteoconductive material, which has good mechanical properties and can be economically produced with variety of shapes. The materials such as calcium phosphate ceramics, cements, glasses and glass-ceramics are normally used as a solution to the cases where bone substitutes were required to fill bone defects and

craniomaxillofacial defects. Besides, the development of calcium phosphate cements to load with specific drugs and antibiotics will further avoid the undesirable infection problems. The bioactive potential of some calcium phosphate ceramics and bioglasses were exploited to enhance the integration and binding between the implants and the surrounding tissues. The use of bioactive ceramics and glasses for coatings has come up as an answer to the implant loosening problems. Therefore, the design, research, and improvement of bioglass, glass-ceramics, and glass ionomer cement in laboratory scale are the first steps of the research on biomaterials.

## 2.2 The history of bioglass

Bioglass is a very important part of biomaterials as synthetic material. In 1967, it was developed the firstly by Professor Larry Hench and his colleagues. And then in 1969, they found the critical amounts of Ca and P ions in silicate-based glasses and glass-ceramics, and this hypothesis was not rejected by bone. Later that year, Hench made a small rectangle of 45S5 (44.5 weight % $SiO_{2)}$ glass, which was the first composition of bioglass. The long-time exposure of this glass in biological fields led to a transformation of the glass's surface from a silicate-rich composition to a phosphate-rich microstructure [8].

## 2.3 Composition and bonding in bioglass

As it was known, some compositions of glasses, ceramics and glass-ceramics have the ability to bond to bone, but only a few of them (specialised compositions of bioactive glasses) can both bond to soft tissues and bones [9-12]. During implantation, the

surface of the glass suffers some changes which dependent on the time and kinetic modifications, leading to a biologically-active hydroxyapatite carbonated layer, provides the bonding interface with tissues, form on the glass surface. This hydroxyapatite layer between the glass and tissues have certain strength thus may resist substantial mechanical forces. The bonding ability of the bioactive glass to bone was first reported to a compositional range of glasses that contained $SiO_2$, $Na_2O$, CaO, and $P_2O_5$ [13], and which have three key compositional features compare to the traditional soda-lime-silica glasses: (1) $SiO_2$ is less than 60 wt%; (2) a high $CaO/P_2O_5$ ratio; (3) high CaO and $Na_2O$ contents. For example, many bioactive silica glasses are based upon the formula called 45S5, signifying 45 wt% $SiO_2$ and a 5:1 molor ratio of CaO to $P_2O_5$, and glasses with lower ratios of CaO to $P_2O_5$ cannot bond to bone. However, adding a small amount of 3 wt% of $Al_2O_3$ into the 45S5 formula prevented bonding to bone [13].

Gross et al. [14] and Strunz [15] suggested that some alkali bioactive silica glass-ceramics (0–5 wt%) also have the ability to bond to bone, and they also reported that the addition of small amount of $Al_2O_3$, $Ta_2O_5$, $TiO_2$ or $ZrO_2$ can inhibit bone bonding.

Strunz et al. [16, 17] reported a composed of apatite $Ca_{10}(PO_4)_6(OHF_2)$ with two-phase silica-phosphate glass-ceramic and a residual silica glassy matrix, termed A-W glass-ceramic, also bonds with bone.

De Caluwé recently discussed that fluoride, which containing bioactive glass have advantages over the other bioactive glasses such as has a more stable fluorapatite thus can enhance bonding and remineralization of surrounding tissues [18].The research carried out by Arepalli et al. shows that the substitution of SrO with $SiO_2$ in ceramic has significant benefit such as enhanced HCA crystallinity on the glass surface and better compatibility to enhance the cell growth than substitution for CaO in the $Na_2O$-

$CaO\text{-}SrO\text{-}P_2O_5\text{-}SiO_2$ bioactive glass [19]. And Zhang et al. used a 3-D printing technique to fabricate three-dimensional strontium-containing mesoporous bioactive glass and showed that the bioactive glass have a very good apatite-forming ability and osteogenic capability which can stimulate new blood vessel formation [20].

The typically compositions of bone consists of 25 wt.% water, 15 wt.% organic materials and mineral phases such as carbonate, citrate, chloride, fluoride, hydroxyl, and magnesium ions etc.[7]. Therefore, calcium phosphates exist naturally in the body, but they also occur in nature or can be synthesised in the laboratory, see Table 2.1. Within the past two decades, the use of calcium phosphates as biomaterials attracts many attentions, but only few of them are useful for implantation application, as both their solubility and speed of hydrolysis increase with decreasing calcium-to-phosphorus ratios, e.g. a Ca:P ratio of less than 1:1 are not suitable for biological implantation [21].

**Table 2.1:** The Ca:P ratio of different calcium phosphates.

| **Ca:P** | **Mineral Name** | **Formula** | **Chemical Name** |
|---|---|---|---|
| 1.0 | Monetite | $CaHPO_4$ | Dicalcium phosphate |
| 1.0 | Brushite | $CaHPO_4 \cdot 2H_2O$ | Dicalcium phosphate Dihydrate |
| 1.33 | | $Ca_8(HPO_4)(PO_4)_4 \cdot 5H_2O$ | Octocalcium phosphate |
| 1.43 | Whitlockite | $Ca_{10}(HPO_4)(PO_4)_6$ | |
| 1.5 | | $Ca_3(PO_4)_2$ | Tricalcium phosphate (TCP) |
| 1.67 | Hydroxyapatite | $Ca_{10}(PO_4)_6(OH)_2$ | |
| 2.0 | | $Ca_4P_2O_9$ | Tetracalcium phosphate |

Due to the poor mechanical strength, toughness, and inferior mechanical properties, calcium phosphate ceramics are largely limited to use as the load bearing parts of the skeleton such as bone grafting in clinical applications. Therefore, interest has been

directed towards the use of calcium phosphate coatings on metallic implant substrates, partly for this reason [22-24].

However, the degradation or resorption of calcium phosphates can occur in vivo due to the phagocytosis of particles and the production of acids, enhance the match of calcium phosphates resorption rate and bone tissue regeneration rate is very important. For example, if the solubility of calcium phosphates is higher than the rate of tissue regeneration, they could not be used as defects filler of bones. As mentioned before, the dissolution rate of the calcium phosphate is closely related to the calcium-to-phosphorus ratio, and the decrease of calcium-to-phosphorus ratio could increase the life time of calcium phosphate, e.g. tricalcium phosphate [25], with a Ca:P ratio 1: 1.5 is more rapidly resorbed than hydroxyapatite.

## 2.4 The development of glass ionomer cements

Glass ionomer cements (GICs) or glass polyalkenoate cements (GPCs) have been extensively applied as cavity liners, restorative, and bases in dentistry since their development by Wilson and Kent in 1969, which form as a result of the reaction between a powder of a fluoro-aluminosilicate glass and an aqueous solution of polyacrylic acid (PAA) [26-29].

In 1975, the first commercial dental cements released to the market had considerably inferior properties compared to the materials used today [30, 31]. The glasses for incorporation into GICs are in general composed of 20–36 wt% $SiO_2$, 15–40% $Al_2O_3$, 0–35% CaO, 0–40% $CaF_2$, 0–10% $AlPO_4$, 0–6% $AlF_3$, and 0–5% $Na_3AlF_6$ which are commonly called “ionomer glasses” [32]. Cations are released into the aqueous phase and subsequently cross-link the PAA chains when the acid attacks the glass structure

in the setting reaction, resulting in the production of cement with a hydrated polysalt matrix in which the glass particles are embedded [33, 34]. The presence of a large quantity of fluoride is the most important characteristic in ionomer glasses, which leads to a lower refractive index of the glass, resulting in improved translucency of the cement. The compressive strength is enhanced and reaches values above 200 MPa due to the long-term fluoride release inhibits the formation of secondary caries [35, 36]. In order to control the slurry viscosities, instead of using PAA water solutions, a powdered type of PAA was developed, mixed with $H_2O$ and tartaric acid (TA) to form GIC materials [37-39].

In the past, there has been substantial development of ionomer glasses. For example, the new glass systems only lose very small amounts of fluorine during melting (in the form of $SiF_{4)}$ compared to earlier glass systems [40-44]. It has been reported that the compositions and structures of glasses have strong impacts on the subsequent cement properties, such as viscosity, fracture toughness, compressive strength and Young's modulus [45, 46]. In addition, glasses with appropriate compositions can be heat-treated to promote controlled crystallization, in which the main crystalline phase is apatite [47-50].

From 1979 to 1980, dental cements were also called water-mixed or water-hardened cements, which were distinguished from previous products by their improved shelf lives and mechanical properties.

The work carried out by Brook and Hatton [51] suggested that the osteoconductivity of GICs is dependent on the ion exchange ability with the biological environment. The binding of certain biological factors on GIC surface may recruit and regulate osteogenic cells and also assist the formation of a more stable bone-implant interface thus to improve the potential for clinical success [52-55].

The strength of GIC is around 7–14 MPa, which can only be used in low stress-bearing areas [56]. Some additions have been added into GIC materials to improve their mechanical properties; for example, Massler et al. [57] studied the influence of additional amalgam powder in zinc phosphate cement, and Mahler and Armen [58] proved that adding amalgam particles into zinc phosphate powder enhanced the transversal force, solvability, and dissolution of the new restorative cement. However, some difficulties were raised due to the inhomogeneous distribution of amalgam particles in GIC materials, resulting in accelerated erosion and degradation of wear properties.

## 2.5 The development of dental materials

The development of dental materials used to fill cavities goes back to the Chinese in the 7th century. In France, Taveau [59] developed a dental amalgam in 1816 by mixing silver coins and mercury, but with some severe problems such as expansion after replacement and mercury poisoning. In the 1890s, the amalgam composition of dental-filling materials was altered by dentists [60]. As an inexpensive dental material, amalgam has good durability and is easy to manipulate, but it also has some shortcomings such as mercury poisoning and short-term stress relaxation [61]; hence, the use of amalgam material in dental applications has been restricted.

Cement materials were first developed and used in dental application in the 19th century. [62] In 1855, Sorel presented the first dental restorative cement using zinc oxychloride [63]. Later, in 1879, Pierce [64] improved the previous zinc oxychloride by zinc oxide-phosphate cements, which exhibited low pulp irritation and good durability. The modern zinc phosphate cements were developed by the work of Armes

and Fleck around the 1900s [65, 66]. At the same time, Pierce and Flagg invented a zinc oxide eugenol cement, which became very popular due to the anodyne effect. Besides the zinc oxide eugenol cement, fluoride-added, silicate-based cements were developed by Fletcher and Shoenbeck [67, 68]. At the end of the 19th century, cements were already widely used as adhesives, temporary restoratives, and cavity base materials.

The next generation of cement materials were developed in 1988. Antonucci et al. [69] introduced the first light-cured, resin-modified glass ionomer cement (RM-GIC) in a laboratory, using 2-hydroxyethyl methacrylate and a polymeric solution. This cement combined the best properties of composite resins and glass ionomers. Meanwhile, it had low thermal expansion, hydrophilic and cariostatic properties, excellent fracture toughness (FT), and good wear resistance, and it was easy to polish. However, the RM-GIC materials have some shortcomings such as shrinkage and curing problems. The first commercial light-cured GIC, Vitrebond, was developed by Mitra in 1998 [70] and has a light-initiated polymerisation reaction and a glass ionomer acid-base reaction.

The further development of GIC materials focussed on improving their operability in practice. For example, in 1995, a highly viscous GIC was introduced for use in some countries where instruments and equipment were in short supply and fillings were mostly functional for atraumatic restorative treatment (ART) procedures [71]. By using this highly viscous GIC material, personnel with little dental experience are able to restore a tooth merely by excavating the caries using hand instruments and filling the resultant hole [72, 73]. A compomer material was announced by Dentspy that contains a fluoride-containing resin [74]. The compomer has many advantages, such as adhesion to teeth and releasing low levels of $F^-$ ions [75].

## 2.6 Glass compositions and designing rules

Many ionomer glass compositions have been studied as cement formers, which can be divided into three major categories:

(1) Zinc silicate glasses. The glasses are based on the general compositions of CaO-ZnO-$SiO_2$ or $Al_2O_3$-ZnO-$SiO_2$ [76-78]. In the CaO-ZnO-$SiO_2$ ternary system, Boyd et al. reported [76] that zinc acts as both a network modifier and an intermediate oxide-like alumina and the release of zinc directly activating the aminoacyl-tRNA synthetase in osteoblastic cells as well as stimulating cellular protein synthesis which enhances bone formation and mineralization. In addition, zinc has been recognised as an antibacterial agent which is important for the function of the immune system [77, 78]. There are also high percentages of zinc oxide and silica in both $Al_2O_3$-ZnO-$SiO_2$ and CaO-ZnO-$SiO_2$ glass compositions, with only a small amount of the third oxide. It shows great potential as cements formers and hard tissue-replacement materials. However, some studies have suggested that zinc glass-based cements have inferior mechanical properties compared to the corresponding aluminosilicate glasses for use in clinical dentistry [79].

(2) Aluminosilicate glasses. Aluminosilicate glasses are some of the oldest known glasses; they have good chemical durability, high temperature tolerance, and superior strength [80-82]. These glasses are based on the general composition of $SiO_2$-$Al_2O_3$-CaO or $SiO_2$-$Al_2O_3$-$CaF_2$, and have been studied mostly by Wilson and co-workers [83]. Some compounds such as NaF, $K_2O$ and $P_2O_5$ [84,85] were added into the glass in order to improve the properties of aluminosilicate glass. Nearly all the commercially available glass used for cement is aluminosilicate based, with some calcium and fluorine addition.

(3) Aluminoborate glasses. These glasses are based on the general composition of

$Al_2O_3$-$B_2O_3$, with the addition of $Na_2O$, BaO, ZnO, $Li_2O$ and $ZnF_2$ [86-90]. After heat treatment under certain conditions, aluminoborate glasses can be hydrolysed with a controlled reactivity of the glass ionomer cement; they also have higher electrical resistivity than silica [87,91]. However, the chemical durability and compressive strength of these aluminoborate glasses are poorer than aluminosilicate glass as a cement former [92,93]. Additionally, the increase of $B_2O_3$ addition can enhance the borosilicate glasses dissolution rate, therefore, the amount of $B_2O_3$ added should be carefully designed [94].

Both of the design and characterization of these glasses play very important roles in the development of new medical glasses. The properties of glasses and glass-ceramics are determined critically by their composition, the crystallisation process, and the microstructure, which will be discussed in this chapter.

Lots of models have been used to interpret glass structures; however, all models are based on Zachariasen's random network theory. In fact, the term "random network" was mainly written as an explanation for glass-formation tendencies, it's never appeared in Zachariasen's classic paper. And Zachariasen [95] indicated that the atomic forces and internal energy should be in the same order with very small differences in both the glasses and the related crystals. Meanwhile, an open and flexible structure is always required. Later, he defined a glass as "a substance that can form an extended three-dimensional network that is lacking periodicity with energy content comparable with that of the corresponding crystal network", and summarised several rules for a continuous 3-dimensional glass network to form as [96]:

(1) No more than two cations are required to link to each oxygen atom.

(2) For each oxygen polyhedron, at least three corners (not edges or faces) must be shared in order to form a 3D network.

(3) The oxygen coordination number of the network cation is small.

(4) The glass must contain a high percentage of network cations that are surrounded by oxygen tetrahedra.

(5) The oxygen tetrahedral only share corners with each other.

(6) Some oxygen atoms are only linked to two network cations and do not form further bonds with any other cation.

Zachariasen suggested that sharing corners is a crucial condition for obtaining a random structure. In this model, the individual $[SiO_4]^+$ tetrahedral are connected at the corners to form chains in the simplest glass network, and this structure will be changed when introduce aluminium, which can provide a negative charge to the glass structure. According to the Lowenstein's rule [97], aluminium in four-fold coordination can substitute for silicon in the tetrahedral $[AlO_4]^{5-}$ and break the electron balance by leaving a negative surplus charge in each tetrahedron. The ions like $Ca^{2+}$, $Na^+$, $Mg^{2+}$, or $Al^{3+}$, which have positive charge will compensate the negative charge and serves like the glass network modifiers. However, the ratio limit for Al/Si must not be excessed than 1 due to the aluminium is not able to adopt the tetrahedra which linked by one oxygen bridge; the centre of only one of them can be occupied by aluminium, whereas the others must be occupied by silicon or another small ion of 4 or more electrovalence such as phosphorus. The oxygen in the glass structure is bridging oxygen (BO), and the non-bridging oxygen (NBO) can be formed by including other species such as CaO and $Na_2O$ in the glass composition( the transformation of BO and NBO can take place [98]). A schematic diagram is shown in Figure 2.1, and in this structure, calcium is defined as a glass network modifier while aluminium is act as an independent cation with a coordination number of 5 or 6 towards oxygen.

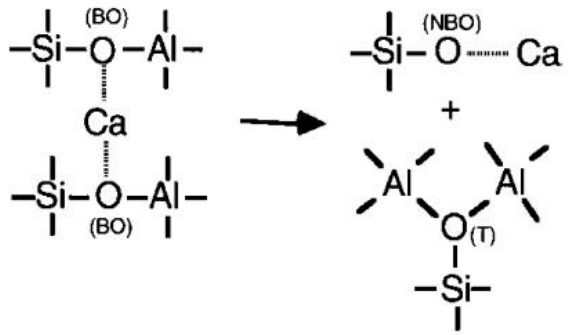


**Figure 2.1:** Schematic diagram of bridging oxygen (BO) to non-bridging oxygen (NBO) transformation according to Stebbins and Xu 1997 [98].

## 2.7 The glass structure

Many efforts were put forward to investigate the relationship between its structure and properties (thermodynamic and mechanical), which can be used to design of new materials [75,87]. Freeman and Hatton et al [4] reported that the calcium fluoro-aluminosilicate glasses are able to crystallize into apatite and mullite phases to form apatite-mullite glass-ceramics, which showed excellent osteointegration and osteo-conduction properties when implanted in the body. Besides, other aluminosilicate glasses systems with general composition of $SiO_2$-$Al_2O_3$-$P_2O_5$-CaO-$CaF_2$, was also extensively studied [100-104]. Factors such as the alkali content, the Al:Si ratio, and the fluorine and phosphorus contents have been shown to have an effect not only on the glass properties but also on the properties of the resulting glass-ionomer cements and glass ceramics [43,45].

Previous studies were indicated that the aluminium-to-silicon ratio (Al:Si )can be a dominant factor affecting the reactivity of glasses with simple compositions of CaO-$Al_2O_3$-$SiO_2$, as well as the properties of the corresponding glass ionomer cements [43, 83]. However, the research carried out by Griffin et al [41] suggested that the ratio of

Al:Si in some complicated glass compositions, containing phosphorus and fluorine, is less important to influence the properties of cement. Normally, the silicon and aluminium tetrahedra in glass are polymerized to form bridging oxygen (BO) sites Si-O-Si, Si-O-Al and Al-O-Al with small amounts of non-bridging oxygen (NBO) in charge-balanced aluminosilicate glasses [97, 98]. The phosphorus, occupies the neighbouring tetrahedral sites to $AlO_4$ tetrahedra with $P^{5+}$ ions, can balance the charge-deficient $Al^{3+}$ ions [105, 106]; therefore the numbers of Al-O-Si species available for acid hydrolysis are reduced. In addition, some alkali metal ions like sodium are also added to ionomer glasses to reduce the melting temperatures during glass production and help the release of fluoride ions by offering a soluble counter ion [31]. Recently, studies have been shown that the fluorine can influence the structure of the ionomer glass as [107, 108]: firstly, fluorine decreases the melting temperature and the viscosity of the glass; secondly, it disrupts the glass network facilitating the acid attack during cement formation [105]. As a network disruptor, the addition of calcium fluoride may lead to the formation of non-bridging fluorine as well as non-bridging oxygen, as illustrated in Figure 2.2 [44]. Meanwhile, the additional of calcium ions modifies the glass network, charge balancing NBOs and the charge-deficient $AlO_4$ tetrahedra [44]. In fluorine adopted glasses, the fluorine can replace BOs with non-bridging fluorine, which will lead to a decrease of glass transition temperatures, e.g. glasses based on the generic composition $4.5SiO_2$-$3.0Al_2O_3$-$1.5P_2O_5$-$(5.0-x)CaO$-$xCaF_2$ with x varying from 1 to 3.0 have been investigated by Griffin and Hill [41], and they found a decrease of 200° C in the glass transition temperatures.

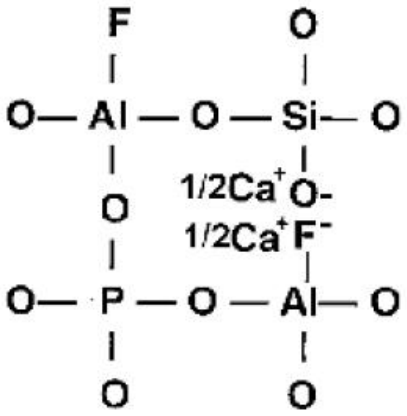


**Figure 2.2**: Schematic illustration showing the structural role of calcium and fluorine in ionomer glasses [44].

Recently, a number of MAS-NMR studies on the structure of aluminosilicate glasses have contributed profoundly to understanding the coordination environment of fluorine in the glass network. E.g. Hill and Wood [47] studied a series of glasses based on the composition of $2SiO_2$-$Al_2O_3$-$2(1-x)CaO$-$xCaF_2$ and reported that fluorine is bonded to aluminium atoms instead of silicon atoms. However, earlier studies by Wilson et al. [83, 109] on a series of glasses based on $xSiO_2$-$yAl_2O_3$-$zCaF_2$ suggested that the formation of Si-F and Al-F bonds in tetrahedral $SiO_3F$ and $AlO_3F$, respectively, indicating that fluorine could disrupt the glass network by substituting bridging oxygens with non-bridging fluorines. Zeng et al. [110] confirmed that considerable fractions of network Al-O bonds are replaced by weaker non-network Al-F bonds; they also suggested that the formation of non-network Si-F bonds are much more easily in aluminosilicate glasses, given that Si-F-Ca(n) species occur in the range of 123.4 to 134.5 ppm. Stebbins and Zeng [111] found evidences for the presence of Al-F-Ca(n) and F-Ca(n) species in the glass network (n represents the number of Ca next to the nearest neighbouring fluorine in a $2SiO_2$-$2Al_2O_3$-$0.5CaF_2$ glass).

The systematic MAS-NMR studies by Stamboulis and Hill [102, 103, and 112] on

fluorine-containing ionomer glasses provide extensive information about the fluorine environment within the aluminosilicate glass network. Stamboulis et al. reported that Si-F-Ca(n) species were clearly present and were identified by an increasingly stronger peak with fluorine content at −125 ppm in the high fluorine-containing glasses, with the general composition of $4.5SiO_2$-$3Al_2O_3$-$1.5P_2O_5$-(5-x)CaO-x$CaF_2$, where x = 0–3 (Figure 2.3) [113]. In addition, F-Ca(n) and Al-F–Ca(n) species were also identified to be present in all glasses at −90 ppm and −150 ppm, respectively. $^{27}Al$ MAS-NMR studies by Stebbins et al. [111] indicated that concentrations of 5 and 6 coordinated aluminium at fractions as small as 1% can be observed in aluminosilicate glasses using a high field (14.1–18.8 T) high-resolution MAS-NMR spectrometer. In addition, high-coordinated Al species are considered to be stabilised by the presence of one or more $F^-$ ions in the Al coordination shell. Stamboulis et al. and Hill et al. [102, 103 and 112] also applied $^{27}Al$ and $^{19}F$ MAS-NMR spectroscopy on a series of model fluorine-containing aluminosilicate glasses and commercial ionomer glasses. The peak position of four-fold coordinated Al(IV) for the phosphorus-containing glass was found to be lower by ca. 10 ppm, compared to phosphorus-free calcium aluminosilicate glass (60 ppm). This was probably caused by the formation of Al-O-P bonds because four-fold coordinated $Al^{3+}$ is short of one unit of positive charge, whilst $P^{5+}$ has an excess of one unit of positive charge. As a result, $Al^{3+}$ and $P^{5+}$ are located closely and locally charge balance each other. Therefore, the peak position of Al(IV) was shifted towards more negative values, as mentioned above, due to having more electro-negative phosphorus atoms compared to silicon atoms.

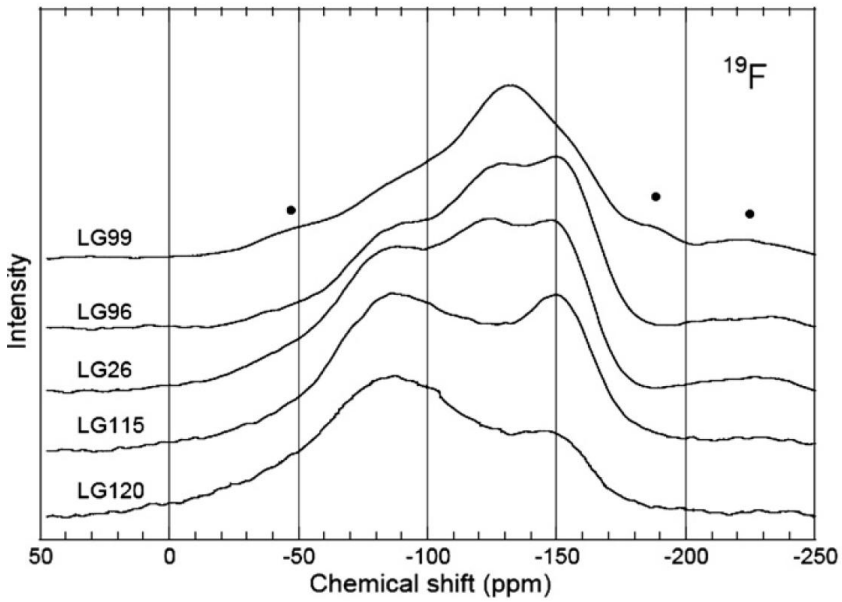


**Figure 2.3**: $^{19}F$ MAS-NMR spectra for a series of ionomer glasses. The spinning side bands are indicated by A. Stamboulis [113].

In Figure 2.4, two new peaks appeared at around 30 ppm and −5 ppm that were assigned to five-fold [Al(V)] and six-fold [Al(VI)] coordinated aluminium, respectively, implying that the introduction of fluorine in the glass network may favour the formation of high-coordinated aluminium. The $^{19}F$ MAS-NMR study here indicated that the concentration of Al-F-Ca(n) species increased with the fluoride content from 0.5 to 1.0 in phosphate-containing glasses, which could lead to the following assumption: the presence of Al-F bonds (incl. Al-F-Ca(n)) as well as the presence of F-Ca(n) species may result in lack of available cations for charge balancing, forcing aluminium to higher coordination states. However, there is no direct evidence showing that calcium is entirely coordinated by fluorine; on the contrary, evidence shows that calcium is indeed involved with NBOs and other oxygen species [102, 103].

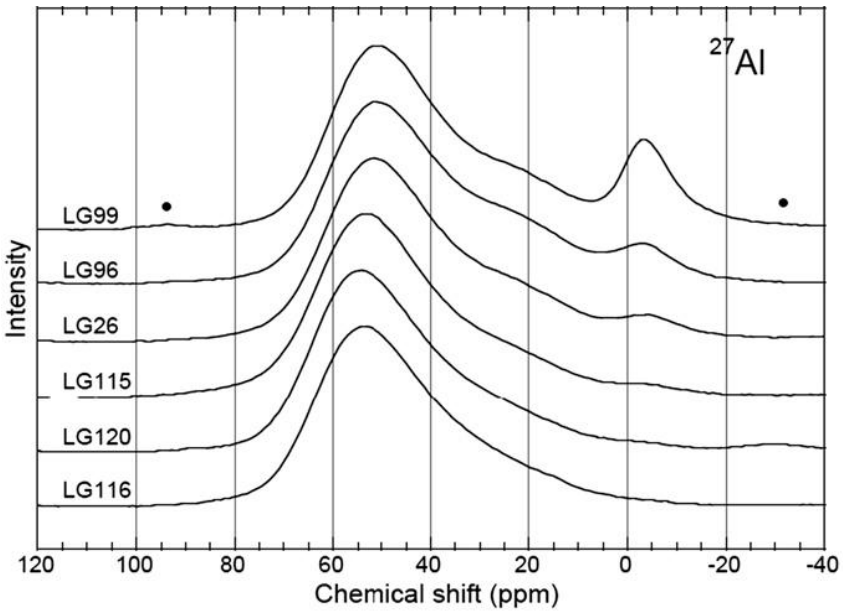


**Figure 2.4**: $^{27}$Al MAS-NMR spectra for a series of ionomer glasses. Spinning side bands are indicated by A. Stamboulis [113].

## 2.8 Crystallisation of glasses

Glass-ceramics belongs to a class of polycrystalline solids which can be prepared by the controlled crystallisation of glasses. The crystallisation of the glass could be achieved by subjecting suitable glasses to a designed heat-treatment schedule, which allows the crystal phase nucleation and growth within the glass. Comparing to the traditional ceramics, in which most of the crystalline material is introduced when the ceramic composition is prepared, the crystalline phases in glass-ceramics are entirely produced by crystal growth from a homogenous glass phase. However, some recrystallization may occur or new crystal types may arise due to solid-state reactions. Réaumur suggested that by using a suitable heat treatment, most glasses can be crystallised or devitrified [114].He showed that glass bottles packed into a mixture of sand and gypsum and subjected to red heat for several days will be converted into a

polycrystalline ceramic. However, he was unable to achieve control over the crystallisation process, which is necessary for the production of true glass-ceramics.

The photosensitive glasses are developed by S.D. Stookey at Corning Glass Works in the United States about 200 years after Réaumur's work, and later developments showed that photosensitive glasses could be opacified in irradiated regions by the precipitation of further crystals upon the original metallic crystals [115]. He found these materials had a much higher mechanical strength and a improved electrical insulation characteristic than the original glass, and the transformation from glass to a ceramic was accomplished without distortion of the articles and with only minor changes in dimensions.

This material represented the first true glass-ceramic. Evidently, the small metallic crystals acted as nucleation sites for the crystallisation of major phases from the glass. The large number of nuclei present and their uniform distribution throughout the glass ensured that crystal growth proceeded uniformly and that a skeleton of crystals was produced to maintain the glass article's rigidity as its temperature was increased [116].

The successful application of photosensitive metals as nucleation catalysts for the controlled crystallisation of glasses opened the way for other types of nucleation catalysts to develop that did not require the glasses to be irradiated. These later methods usually depend upon the precipitation of colloidal particles within the glass to act as nucleation sites [116]. S.D. Stookey developed a wide range of glass compositions containing titanium dioxide as the nucleating agent. The use of metallic phosphates to promote the controlled crystallisation of glasses was discovered by McMillan and co-workers in Great Britain [117]. Later studies by workers in a number of countries have led to the discovery of many different types of nucleating agents for glass-ceramics production [117].

As it was known, the ionomer glasses described above is that they can crystallise to form apatite-containing glass-ceramics, hence they are widely used in restoring and replacing hard tissues in the orthopaedic and dental fields, due to the apatite phase is similar to the biological apatite in teeth and bones [82, 118]. A large quantities of studies were carried out to develop the hydroxyapatite (HA)-based materials by using a sintering method. However, there are some problems that the materials may encounter: 1) the sintered HA can easily degrade at high temperatures; 2) compared low sintered strength and toughness; and 3) diamond-tipped tools are always used in subsequent machining, which is normally an expensive, difficult, and time-consuming process. Compared to sintering and machining, the properties of the apatite-based materials are closely associated with the annealing process. Over the past two decades, many glass-ceramics were developed and can be classified into three categories: (1) the apatite–wollastonite glass-ceramics, which based on a glass composition of $SiO_2$-$P_2O_5$-CaO-MgO [119]; (2) the mica-based materials, including the commercially available Dicor$^{TM}$ for producing dental crowns [120]; (3) the apatite–mullite glass-ceramics [47,101]. In addition, in apatite–wollastonite and apatite–mullite systems, apatite is the primary phase, which is particularly in accordance with fluorapatite in the apatite–mullite system.

Compared to hydroxyapatite mineral phase, the fluorapatite has high stability, which is due to the smaller size of fluoride ions thus leading to a more closely pack in the apatite crystal lattice. Besides, the releases of fluoride ion during service of the fluorapatite and its cariostatic effect make the apatite–mullite system more attractive to the growing application of tooth saving preparation methods, such as tunnel techniques. Hence, for this study, great emphasis will be placed on the crystallisation of castable apatite–mullite glass-ceramics based on the general composition of

$4.5SiO_2$-$3Al_2O_3$-$1.5P_2O_5$-(5-x) CaO-x$CaF_2$, where x is between 0 and 3.

Rafferty et al. [121] found high fluorine-containing glasses that could crystallise to fluorapatite (FAP, $Ca_5(PO_4)$) and mullite ($3Al_2O_32SiO_2$) during the heating process, accompanied by a decrease in crystallisation temperatures with increasing $CaF_2$ content. ß-$Ca_3(PO_4)_2$ (ß-tricalcium phosphate) and $CaAl_2Si_2O_8$ (anorthite) were the two crystalline phases formed in the fluorine-free glass-ceramics. So, it is suggested that fluorine may have a huge impact on the nucleation and crystallisation behaviour of glass-ceramics, which have high fracture toughness and high strength (260MPa) [47, 81] due to the FAP-mullite interlocking structure (Figure 2.5).

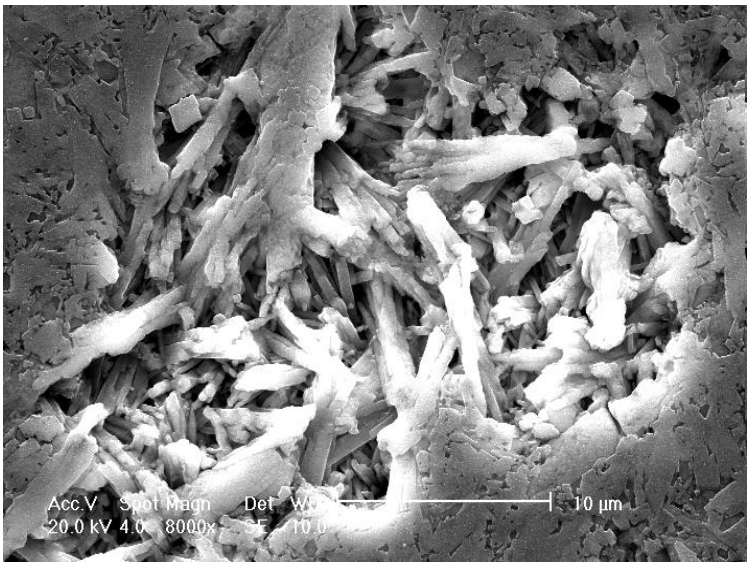


**Figure 2.5**: ESEM of an apatite–mullite glass-ceramic with a $4.5SiO_2$-$3Al_2O_3$-$1.5P_2O_5$-3CaO-$2CaF_2$ (FB0) composition, heat treated to the second crystallisation temperature exhibiting an interlocking microstructure [101].

As it was known, the thermodynamic driving force of the crystallisation of glasses is attributed to reduce the Gibbs' free energy; the amorphous phase separation (APS) or glass-in-glass phase form a nucleated phase earlier than they are would be formed in

the original glass. In reality, the microstructure of the glass is not as homogeneous as a perfect single crystal, which may due to: 1) a super cooled liquid mass always are required for crystallisation or devitrification; 2) some lattice distortion or definite chemical composition (based on phase diagram) are needed for the crystallisation of materials. The formation of the glass can be considered as a liquid undergoes a demixing process when it cools. If the phases in glass separated, it can be called liquid–liquid immiscibility. The immiscibility is defined as stable or metastable, which dependent on the temperatures for phase separation to occur (above or below the liquidus). If the phase separation below the liquidus temperature, there are two processes can cause the formation of discrete phases which are: the nucleation and growth mechanism [122-124], and the spinodal decomposition [123, 125].

Figure 2.6 [123] presents the microstructure of a) a soda lime silica glass heated at 740 $^{o}$C for 7.25 h showing nucleated droplet phase separation and b) a “Vycor” glass heated at 700 $^{o}$C for 5.5 hours showing spinodal decomposition. It can be seen that the morphologies of the separated phase due to the nucleation or spinodal decomposition is easy to be observed. During the spinodal decomposition, both phase compositions changed with times until reach to the equilibrium. Meanwhile, the second phase prefers to produce non-spherical particles with regularly position and size. That is to say, there is no change of composition of the second phase at a constant temperature during the nucleation and growth of the phases with a very sharpen interface.

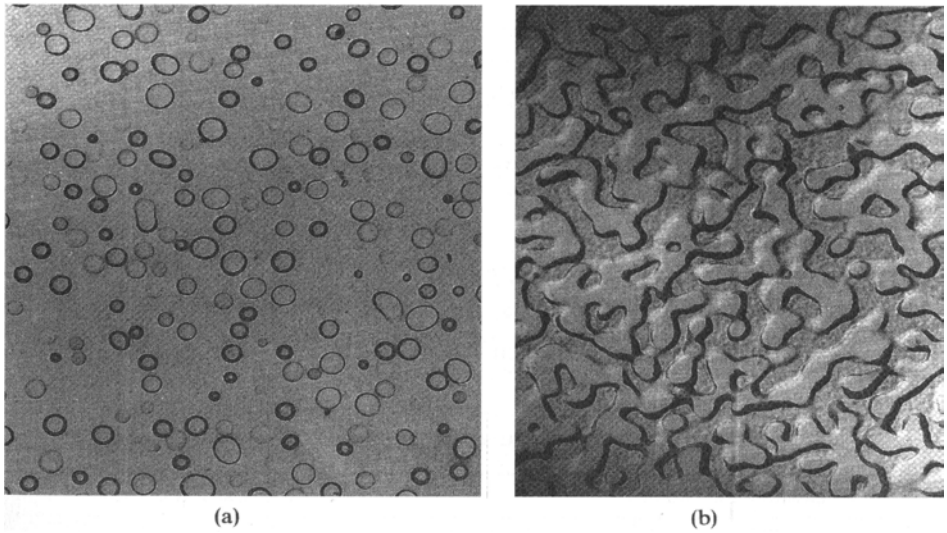


**Figure 2.6**: Microstructure of a) soda lime silica glass heated at 740 $^{o}$C for 7.25 h (14,000x) showing nucleated droplet phase separation and b) "Vycor" glass heated at 700 $^{o}$C for 5.5 h (24,000x) showing spinodal decomposition [123, 125].

TEM (Transmission electron microscopy) using a carbon platinum replica technique conducted by Clifford et al. [101] on the $4.5SiO_2$-$3Al_2O_3$-$YP_2O_5$-3CaO-$1.5CaF_2$ ($1.1 < Y < 2$) glasses showed evidence of amorphous phase separation yielding an interlocking structure after 1 h heat treatment at the first crystallisation peak temperature. Meanwhile, the study by Stanton et al. [32] on the strongly related glass compositions indicated that the presence of fluorine can aid amorphous phase separation and also have a dramatic effect on the following bulk nucleation process, as mentioned previously. It was suggested [47], that the high fluorine glasses in a $1.5(5-Z)SiO_2$-$(5-Z)Al_2O_3$-$1.5P_2O_5$-$(5-Z)$CaO-$ZCaF_2$ system where $Z > 1.0$ undergo phase separation into a calcium phosphate-rich glass phase and an aluminosilicate-rich glass phase, which then crystallise to FAP and mullite, respectively.

A multinuclear $^{27}$Al, $^{29}$Si, $^{31}$P, and $^{19}$F MAS-NMR was conducted by Stamboulis et al. [95] on glass with the composition $4.5SiO_2$-$3Al_2O_3$-$1.5P_2O_5$-$(5-x)$CaO-$xCaF_2$, in order

to better understand the crystallisation process of apatite–mullite glass-ceramics. The fluorine substitution for oxygen influenced the crystallisation process strongly by changing the crystalline phases from $Ca_3(PO_4)_2$ (whitlockite) and $CaAl_2Si_2O_8$ (anorthite), for fluorine-free glass-ceramics, to fluorapatite (FAP, $Ca_5(PO_4)$) and mullite ($3Al_2O_32SiO_2$), for high-fluorine glass-ceramics. This phase change can be explained by the removal of calcium and phosphate ions due to the crystallisation of FAP, which leads to insufficient charge-balancing cations available for maintaining Al in a four-fold coordination state; as a result, the mullite phase exhibiting both Al(IV) and Al(VI) is favoured instead of the anorthite [97]. The $^{27}Al$ MAS-NMR spectra showed that, although Al(V) and Al(VI) were present in the glasses, especially in the glass compositions with increased fluoride content, they were not present when glasses were heated from $T_{p1}$ to $(T_{p1} + T_{p2}) / 2$, although they appeared again when the glasses were heated to $T_{p2}$. At $T_{p2}$, Dollase et al. reported a small but distinct peak appeared at about −39 ppm assigned to $AlPO_4$ [126]. The phosphorus in the glass was initially present as Al-O-$PO_4^{3-}$ species, then FAP and a small amount of $AlPO_4$ were formed. A $^{19}F$ MAS-NMR analysis indicated that the two species F-Ca(n) and Al-F-Ca(n) observed in the NMR spectra decreased considerably with heat treatments, as shown in Figure 2.7 [104]. The F-Ca(n) species disappeared during heat treatment at Tp1, implying a contribution of F-Ca(n) to the formation of F-Ca(3) species, which correspond to crystalline FAP appearing at ca. −103 ppm. However, a proportion of a silica-rich glass phase still remains after crystallisation, as suggested by the $^{29}Si$ MAS-NMR spectra.

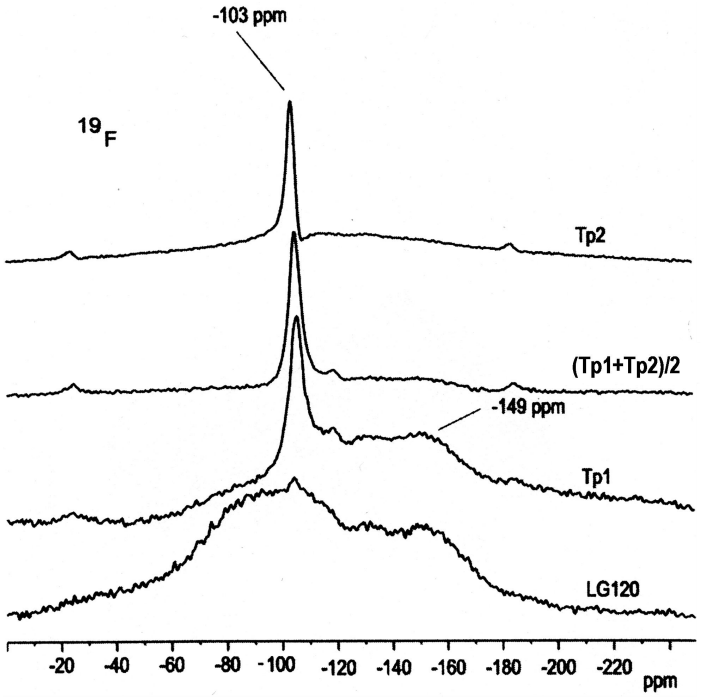


**Figure 2.7**: $^{19}F$ MAS-NMR spectra of glasses based on $4.5SiO_2$-$3Al_2O_3$-$1.5P_2O_5$-(5-x)CaO-x$CaF_2$ (LG120(x = 0.5)), heat treated to $T_{p1}$, ($T_{p1}$ + $T_{p2}$) / 2, and $T_{p2}$ [104].

Hill et al. [99] discovered evidence of an APS mechanism on a FAP-mullite glass-ceramic that involved both prior nucleation and spinodal decomposition using real-time small angle neutron scattering (SANS). The FAP glass-ceramic exhibited two characteristic scales of phase separation and underwent APS. The same phenomena were shown by the isothermal SANS studies at 740 and 750 $^oC$, but there was no further change in the scattering after 30 and 12 min, respectively, suggesting that further phase separation and crystal growth were restricted by the high glass transition temperature of the second glass phase. In other words, FAP crystals did not grow beyond the boundaries of the droplet phase until the higher glass transition temperature of the second phase was reached (Figure 2.8). Real-time neutron diffraction studies have shown [99] that the crystallisation of FAP in ionomer glasses occurred first, followed by the crystallisation of both FAP and mullite, then both

phases dissolving at higher temperatures, followed by re-crystallisation during the cooling process. The results showed that the volume fraction of FAP decreased during heat treatment at 1200 $^{o}$C and then FAP re-crystallised on cooling, suggesting that the mechanism of coarsening FAP involved the dissolution of the small crystals and the re-crystallisation of FAP on the remaining coarse crystallites. However, the mechanism should be controlled by the composition phase diagram and not the thermodynamic drive to reduce the surface energy.

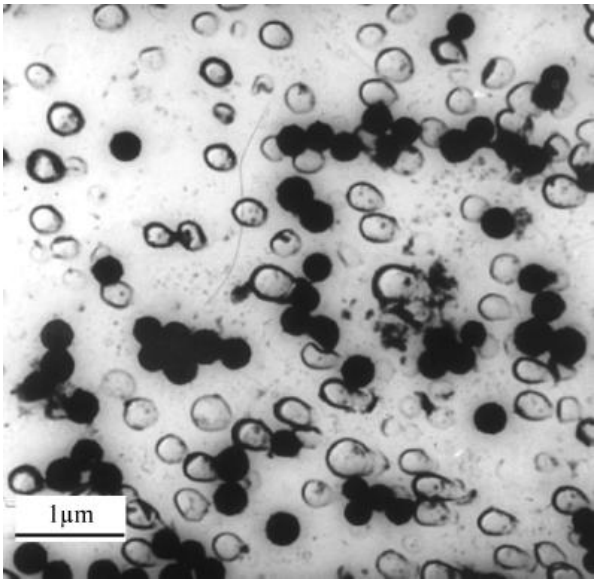


**Figure 2.8:** Carbon replica transmission electron micrograph of a calcium fluorapatite glass-ceramic showing evidence of amorphous phase separation giving rise to a droplet in the matrix microstructure [99].

### 2.9 The development of borosilicate glass

Borosilicate glass was first developed by German glassmaker Otto Schott in the late 19th century [127]. It has very low coefficients of thermal expansion (~3 × $10^{-6}$ / °C at 20 °C), which allows them to have higher resistant to thermal shock than any other common glass. Boron in the glass lowers the flow point and also lowers the energy

needed to produce the glass [127].

The $B_2O_3$–$Al_2O_3$–$SiO_2$ glass-ceramic is one of widely used borosilicate glasses in the fields of chemical engineering, electronics, mechanical and biomaterials due their high electrical resistivity, long chemical durability, low thermal expansion coefficient, and superior biocompatibility. In this composition, boron, as a glass former, is expected to substitute for aluminium and reduce the glass transition temperature and crystallisation temperature of the glass system. Liu and Wang [128] studied the relationship between the $SiO_2/B_2O_3$ mol ratio and the thermal expansion coefficient of $B_2O_3$–$Al_2O_3$–$SiO_2$ glasses, and they found the increase of $SiO_2/B_2O_3$ ratio could also increase the transformation temperature but decreased thermal expansion coefficient of these glasses. Similar to $SiO_2$ and $B_2O_3$, $P_2O_5$ is also one of the network-forming oxides, it is sometimes added into the $B_2O_3$–$Al_2O_3$–$SiO_2$ system. Since $Si^{4+}$ and $B^{3+}$ ions possess rather high field strength, there is a lack of non-bridging oxygen ions in the structure of a $SiO_2$-$Al_2O_3$-$P_2O_5$-$B_2O_3$ system, so calcium which has low field strength and plays a glass-modifier role is usually introduced.

$^{11}B$ and $^{19}F$ NMR have been used to investigate the structural details of a boron oxyfluoride glass, which was prepared by a cold synthesis to decompose with release of $BF_3$ gas above glass transition temperature. The $^{11}B$ spectrum results indicate that the most significant structural unit in the ceramic-glass is $BO_3$, which has trigonal $BO_2F$ units or trigonal $BOF_2$ units. NMR also shows the evidence for the presence of a small number of tetrahedral $BO_2F_2$ units [129].

Although the bonding microstructure of elements in borosilicate glasses are tested using MAS NMR [130-132], few researches are carried out to use $^{11}B$ NMR to identify $BO_3$ and $BO_4$ units in various amorphous systems [133, 134]. One reason for the lack of high-resolution applications is that the line-narrowing by MAS techniques

is incomplete and the resonances of planar and tetrahedrally coordinated boron overlap. In addition, the MAS NMR lineshapes of quadrupolar nuclei are thought to have little significance in glasses, since they are broadened by the distributions of both chemical shift and quadrupole-coupling parameters [133].

## Aims and objectives:

In the present study, the addition of boric trioxide to the ionomer glass compositions $4.5SiO_2$-$(3-x)Al_2O_3$-$1.5P_2O_5$-$5CaO$-$xB_2O_3$ and $4.5SiO_2$-$(3-x)Al_2O_3$-$1.5P_2O_5$-$3CaO$-$2CaF_2$-$xB_2O_3$ is expected to have an effect on the structure of the glass as well as the formed glass-ceramics. It is also expected that the produced glass-ceramics may have stimulatory effects on bone formation—but most importantly, if boron oxide can replace aluminium to a large extent or completely, then this will allow the design of new aluminium-reduced or aluminium-free glass compositions for biomedical applications.

The main objectives of this research are:

1. To produce and develop boron-substituted and aluminium-free or aluminium-reduced glass compositions.
2. To study the crystallization process and determine the crystalline phases of the glasses.
3. To study the structure of boron-substituted glasses and glass-ceramics and develop an understanding of the influence of glass network forming by using boron substitution for aluminium.

# CHAPTER 3 MATERIALS AND METHODS

## 3.1 Materials

### 3.1.1 Ca-aluminosilicate glass

A $4.5SiO_2$-$3Al_2O_3$-$1.5P_2O_5$-3CaO-$2CaF_2$ glass with an Ca : P : F = 5 : 3 : 1 was selected as the starting materials in this study. According to the Lowenstein's rule, whenever two tetrahedral are linked by one oxygen bridge, the aluminium atom can only occupy centre with the rest of centre occupy by some small ions with electrovalence of four or more, e.g. silicon and phosphorus [97]. According to Lowenstein's rule, the glass which has sufficient phosphorus and silicon can allow the aluminium to take up a four-fold coordination state in the glass network. Meanwhile, the selected glass compositions also in accordance with other glass criteria as: a) the glass must contain at least on NBO for each silicon atoms and b) in order to avoid the appearance of volatile $SiF_4$ during melting, the concentration of fluorine in the glass should not excess the concentration of aluminium [101]. The second criterion can be explained by the $Si^{4+}$ are more prone to involve with NBOs or $O^{2-}$ anions rather than a non-bridging fluorine or $F^-$ anion, which lead to the $Al^{3+}$ ions bond to $F^-$ anions, avoiding direct formation of Si-F bonds in the glass network. This explanations is similar to the trimethylsilylation analysis for the $2SiO_2$-$Al_2O_3$-CaO-$CaF_2$ glass with an absence of Si-F bonds in the glass structure [42].

### 3.1.2 Preparation of calcium-aluminosilicate and calcium fluoroaluminosilicate glasses with boron substitution

The molar composition of the fluorine-free and fluorine-containing aluminosilicate glasses are shown below in Table 3.1.

**Table 3.1**: Molar composition of boron-substituted aluminosilicate glasses.

| Glass code | $SiO_2$ | $Al_2O_3$ | $P_2O_5$ | CaO | $CaF_2$ | $B_2O_3$ |
|---|---|---|---|---|---|---|
| B0 | 4.5 | 3 | 1.5 | 5 | 0 | 0 |
| B2.5 | 4.5 | 2.925 | 1.5 | 5 | 0 | 0.075 |
| B5 | 4.5 | 2.85 | 1.5 | 5 | 0 | 0.15 |
| B7.5 | 4.5 | 2.775 | 1.5 | 5 | 0 | 0.225 |
| B10 | 4.5 | 2.7 | 1.5 | 5 | 0 | 0.3 |
| B12.5 | 4.5 | 2.625 | 1.5 | 5 | 0 | 0.375 |
| B15 | 4.5 | 2.55 | 1.5 | 5 | 0 | 0.45 |
| B25 | 4.5 | 2.25 | 1.5 | 5 | 0 | 0.75 |
| B50 | 4.5 | 1.5 | 1.5 | 5 | 0 | 1.5 |
| B75 | 4.5 | 0.75 | 1.5 | 5 | 0 | 2.25 |
| B100 | 4.5 | 0 | 1.5 | 5 | 0 | 3 |
| FB0 | 4.5 | 3 | 1.5 | 3 | 2 | 0 |
| FB2.5 | 4.5 | 2.925 | 1.5 | 3 | 2 | 0.075 |
| FB5 | 4.5 | 2.85 | 1.5 | 3 | 2 | 0.15 |
| FB7.5 | 4.5 | 2.775 | 1.5 | 3 | 2 | 0.225 |
| FB10 | 4.5 | 2.7 | 1.5 | 3 | 2 | 0.3 |
| FB12.5 | 4.5 | 2.625 | 1.5 | 3 | 2 | 0.375 |
| FB15 | 4.5 | 2.55 | 1.5 | 3 | 2 | 0.45 |
| FB25 | 4.5 | 2.25 | 1.5 | 3 | 2 | 0.75 |
| FB50 | 4.5 | 1.5 | 1.5 | 3 | 2 | 1.5 |
| FB75 | 4.5 | 0.75 | 1.5 | 3 | 2 | 2.25 |
| FB100 | 4.5 | 0 | 1.5 | 3 | 2 | 3 |

Stoichiometric amounts of the glass components silicon dioxide ($SiO_2$, Sigma-Aldrich, purum p.a. powder), aluminium oxide ($Al_2O_3$, Sigma-Aldrich, puriss powder), phosphorus pentoxide ($P_2O_5$, Sigma-Aldrich, puriss p.a powder), calcium fluoride ($CaF_2$, Sigma-Aldrich, natural powder), boron oxide ($B_2O_3$, Sigma-Aldrich, 99%(after heating)), and calcium carbonate ($CaCO_3$, Sigma-Aldrich, BioXtra)—which will calculated to provide 200 g calcium oxide (CaO) for each composition. The powders were firstly mixed by hand-shake for 30 min, and then transferred in a platinum rhodium (Pt, 5% Rh) crucible. The crucible was then placed into an electric furnace (EHF 17/3, Lenton, UK) under a temperature of 1450 °C for 1.5 hours. Then, molten glass will then water quenched prevent phase separation and crystallisation. All of the glasses were finally milled using a gyro mill to very fine particles (<45 μm) [229] for further analysis.

The compositions of B75, B100, FB75, and FB100 glass crystallised during glass making and therefore they will not be discussed further in the thesis. The compositions of B50 and FB50 glass became translucent (partly-crystallised) during glass making and they will be discussed further with all other glasses in the thesis.

## 3.2 Methods

### 3.2.1 Thermal analysis: Differential scanning calorimetry (DSC) and thermogravimetric analysis (TGA)

#### 3.2.1.1 Differential Scanning Calorimetry (DSC)

The thermal transitions in the glass were analysed using the differential scanning calorimetry (A Netzsch 404C DSC) along with pairs of matched platinum-rhodium

crucibles. Every sample powder were weighted to around 20 mg for each run, and the sample will firstly heated to 1200 $^{o}$C with the heating rate of 10 $^{o}$C/min and then air cooled. And the glass transition temperatures ($T_g$) and peak crystallisation temperature ($T_p$) were identified. It is reported that the $4.5SiO_2$-$3Al_2O_3$-$1.5P_2O_5$-3CaO-$2CaF_2$ glass has significant surface nucleation, so fine particle size (<45μm) will be used in this study [229].

#### 3.2.1.2 Thermogravimetric analysis (TGA)

Thermogravimetric analysis (TGA) is normally used to test the weight change of samples at different temperatures, which was usually used to measure the weight loss of sample during heat-treatment. In this experiment, a TGA (Netzsch 404C STA) was used with the pairs of matched platinum-rhodium crucibles, and all the test were carried out under the dry argon environment at a heating rate of 10 $^{o}$C/min.

### 3.2.2 Crystallisation of glasses

Before heat treatment, 2 g of the glass powder (<45 μm) were pressed into a die to make the test tablets for the heat treatment. Then the sample tablets were then placed to a platinum crucible and put into an electric furnace (EHF 17/3, Lenton, UK) During heat treatment, the furnace was firstly heat to 700°C with the heating rate of 10 °C/min, holding for 1 h for nucleation, and then heated to 900°C and 1100°C under the same rate, holding for 1 h for crystallisation to complete and finally furnace cooling to room temperature.

### 3.2.3 Helium pycnometer density measurements

The densities of all the samples were identified using the helium pycnometer method. The gas pycnometry uses a glass displacement method to test the sample volume, and the gas used in this experiment is helium. During the test, certain amount of inert gas was admitted into a sealed chamber with known volume and then expanded into another precision internal volume. Later, the pressure before and after the expansion is recorded to calculate the sample volume. Dividing this volume into the sample weight gives the gas displacement density.

In this experiment, an AccuPyc II 1340 Series Pycnometer was used with the sample mass of approximately 1 g and measured. For each sample, this instrument provides 10 consecutive measurements. In order to calculate the density of the glasses and glass-ceramics, we took the average of these 10 consecutive measurements. Then, the oxygen density (OD) in each glass was calculated by using the following equation:

$$OD = D \times \frac{no\ of\ moles\ of\ oxygens\ in\ the\ glass}{molecular\ weight\ of\ glass}, \quad \text{(Equation 3.1)}$$

where D is the density of the glass measured by the helium pycnometer.

### 3.2.4 Fourier transform infrared spectroscopy (FTIR) and Raman spectroscopy

#### 3.2.4.1 FTIR

The chemical structures of glasses are tested by Fourier transform infrared spectroscopy (FTIR, Spectrum2000, PerkinElmer, USA). During the test, the infrared radiation absorbed a specific wavenumber according to the functional groups in materials. Consequently, the wavenumbers and chemical structure are obviously related; thus, an unknown molecule can be identified by its FTIR spectrum [135, 136].

A 1:100 weight ratio between the sample and potassium bromide (KBr) was used to obtain the spectra. The background of the test trace was always taken by using a control sample of KBr prior to each measurement. A diffuse reflectance accessory was used to obtain a spectrum of 400–4000 nm with the resolution of 4 $cm^{-1}$ and number of scans of 100 per minute.

### 3.2.4.2 Raman Spectroscopy

Raman spectroscopy is commonly used to identify the types of molecules from the scattering of the monochromatic light. [137] During the test, laser light will interact with molecular vibrations, phonons or other excitations in the materials, causing the energy shifting thus give the information of the phonons in the detected system.

In this study, the Raman spectroscopy (WiTec Alpha 300R ) operates with a 785-nm diode laser (Toptica Photonics, Germany), 0.3 W, single–frequency and an Acton SP2300 triple-grating monochromator/spectrograph (Princeton Instruments, USA) over the wavenumber range 0–4,000 $cm^{-1}$ at a mean resolution of 3 $cm^{-1}$. The mean spectra were composed of a minimum of 500 accumulations, with individual spectra being acquired using an integration time of 0.5s.

### 3.2.5 X-ray powder diffraction (XRD)

X-ray diffraction is used to show the different crystal phases formed through boron substitution. All the glass samples were heated by increasing the temperature at 10$^{o}$C/min up to 700$^{o}$C, 900$^{o}$C and 1100$^{o}$C, holding for one hour and then furnace cooling to the room temperatures. The 2theta angle used in this experiment is from

10° to 90°, with a step size of 2θ = 0.0200°. A Philips analytical X-Pert XRD was used in Birmingham with Cu Ka, at 40 kV and 40 mA, and MAC Science Co.Ltd M21X XRD was used in Bei Jing with Cu Ka, at 40 kV and 130 mA.

### 3.2.6 Magic-angle spinning nuclear magnetic resonance

MAS-NMR analysis was conducted on $^{27}Al$, $^{29}Si$, $^{31}P$, $^{19}F$, and $^{11}B$ nuclei at resonance frequencies of 79.30, 104.01, 161.58, 375.54, and 128.07 MHz, respectively, using a Bruker ADVANCE 400 NMR spectrometer. The spinning rates of the samples at the magic angle were 5, 12, 12, 25, and 12 KHz for $^{29}Si$, $^{27}Al$, $^{31}P$, $^{19}F$, and $^{11}B$, respectively. The delay time was 1 s for $^{29}Si$, $^{27}Al$, $^{31}P$, and $^{11}B$ and 2 s for $^{19}F$. The reference materials used were tetramethylsilane (TMS) for $^{29}Si$, aluminium nitrate [$Al(NO_3)$] for $^{27}Al$, adenosine diphosphate (ADP) for $^{31}P$, $LiBF_4$ powder for $^{19}F$, and $BF_3 \cdot OEt_2$ for $^{11}B$.

### 3.2.7 Polishing of glasses and glass ceramics

#### 3.2.7.1 Cutting and hot mounting of glass

Before the test, sample blocks were cut into small pieces using a cutting machine (Struers Accutom-5) with a diamond cutting blade. Then, they were cold mounted using the epoxy allowing for SEM observation.

#### 3.2.7.2 Grinding and Polishing of glass-ceramic samples

Samples are ground and polished using a polishing machine (DAP-7 and Pedemin-S), and four discs—Piano, Largo, Chem, and Dac—were used to polish the samples.

During polishing (Piano disc's use), water was used as a lubricant with the loading force of around 5–15 N and lasted for approximately 10 min. Then, the Largo disc was used to polish sample with a liquid diamond suspension with a particle size of 9 μm, this process lasted almost 7min. Later, Dac disc was used with a liquid diamond suspension (a particle size of 3 μm) with a duration time of 7 min. Finally, the Chem disc was used to final polish the sample with a liquid diamond suspension of particle size of less than 1 μm. After polish, all the samples were coated with carbon or gold, allowing the surface of the sample electrical conductive for SEM observation, and silver paint was used so that the whole of the sample was conductive.

### 3.2.8 Environmental scanning electron microscope (ESEM) and EDX- energy dispersive X-ray analysis

An XL 30 ESEM&EDX FEG scanning electron microscope operated at 20 kV was used to investigate the morphology changes of the glasses under different heat treated temperatures. Then the Energy Dispersive Spectrometer (EDS) were analysed to study the composition of difference phases. The analysis took place under high-vacuum conditions. Prior to characterization all glass-ceramics were etched with HF (10%). All the glass-ceramic samples were coated with carbon using an SB250 coating machine.

# CHAPTER 4 RESULTS

## 4.1 Effect of boron substitution on the glass structure

### 4.1.1 Density and oxygen density of all substituted glasses

The measured density and oxygen density for boron-containing aluminosilicate glasses are shown in Table 4.1.1 and Figures 4.1.1 and 4.1.2. The density decreased proportionally with increasing boron substitution. The highest density was observed for B0 ($4.5SiO_2$-$3Al_2O_3$-$1.5P_2O_5$-5CaO; 2.791 g/cm$^3$) and the lowest density was observed for B50 ($4.5SiO_2$-$1.5Al_2O_3$-$1.5P_2O_5$-5CaO-$1.5B_2O_3$; 2.674g/cm$^3$). However, the calculated oxygen density based on the density values mentioned above increased slightly with boron substitution indicating a slightly more compact glass network.

**Table 4.1.1:** Density and oxygen density of boron-substituted fluorine-free glasses.

| **Glass** | **Boron substitution (mol %)** | **Density (g/cm$^3$)** | **Standard deviation (±g/cm$^3$)** | **Oxygen density (mol/cm$^3$)** |
|---|---|---|---|---|
| B0 | 0 | 2.791 | 0.0009 | 0.0796 |
| B5 | 5 | 2.760 | 0.0006 | 0.0791 |
| B10 | 10 | 2.752 | 0.0006 | 0.0792 |
| B15 | 15 | 2.742 | 0.0007 | 0.0793 |
| B25 | 25 | 2.740 | 0.0006 | 0.0800 |
| B50 | 50 | 2.674 | 0.0006 | 0.0799 |

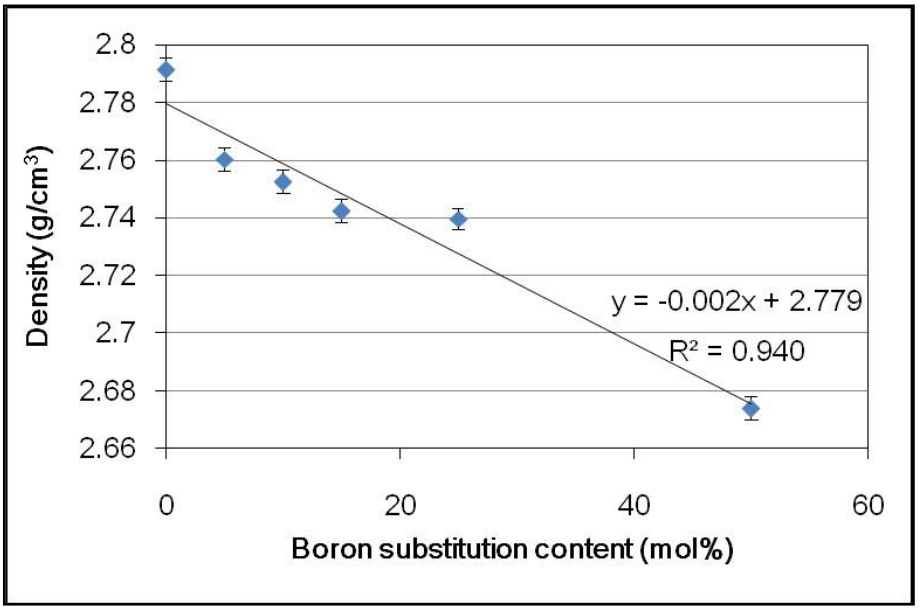


**Figure 4.1.1:** Density of boron substituted fluorine-free glasses.

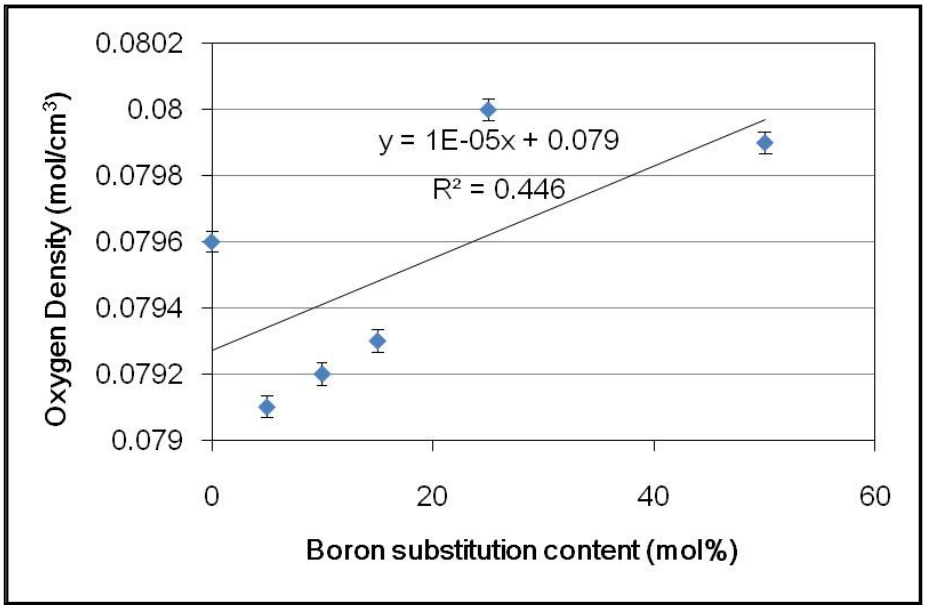


**Figure 4.1.2:** Oxygen density of boron-substituted fluorine-free glasses.

Table 4.1.2 and Figures 4.1.3 and 4.1.4 present the changes in density as well as the calculated oxygen density of boron substituted fluoroaluminosilicate glasses. With boron substitution, it is clear that the density decreased proportionally from FB0

(2.768 g/cm$^3$ of $4.5SiO_2$-$3Al_2O_3$-$1.5P_2O_5$-3CaO-$2CaF_2$) glass to FB50 (2.695 g/cm$^3$ of $4.5SiO_2$-$1.5Al_2O_3$ -$1.5P_2O_5$-3CaO-$2CaF_2$-$1.5B_2O_3$) glass, showing a linear relationship between the density and boron molar content in each glass. On the other hand, the boron introduction has a different effect on oxygen density, increasing the value gradually in the region of 0.0709 mol/cm$^3$ to 0.0721 mol/cm$^3$ and indicating a slightly more compact glass network.

**Table 4.1.2:** Density and oxygen density of boron-substituted fluorine-containing glasses.

| **Glass** | **Boron substitution (mol %)** | **Density (g/cm$^3$)** | **Standard deviation (± g/cm$^3$)** | **Oxygen density (mol/cm$^3$)** |
|---|---|---|---|---|
| FB0 | 0 | 2.768 | 0.0005 | 0.0709 |
| FB5 | 5 | 2.776 | 0.0007 | 0.0714 |
| FB10 | 10 | 2.760 | 0.0006 | 0.0713 |
| FB15 | 15 | 2.759 | 0.0008 | 0.0716 |
| FB25 | 25 | 2.739 | 0.0005 | 0.0717 |
| FB50 | 50 | 2.695 | 0.0006 | 0.0721 |

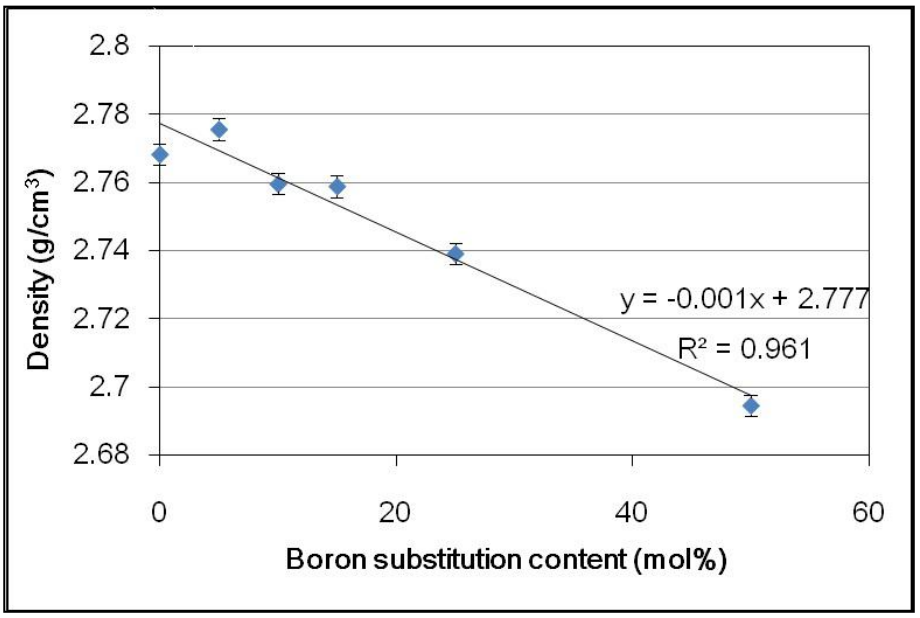


**Figure 4.1.3:** Density of boron-substituted fluorine-containing glasses.

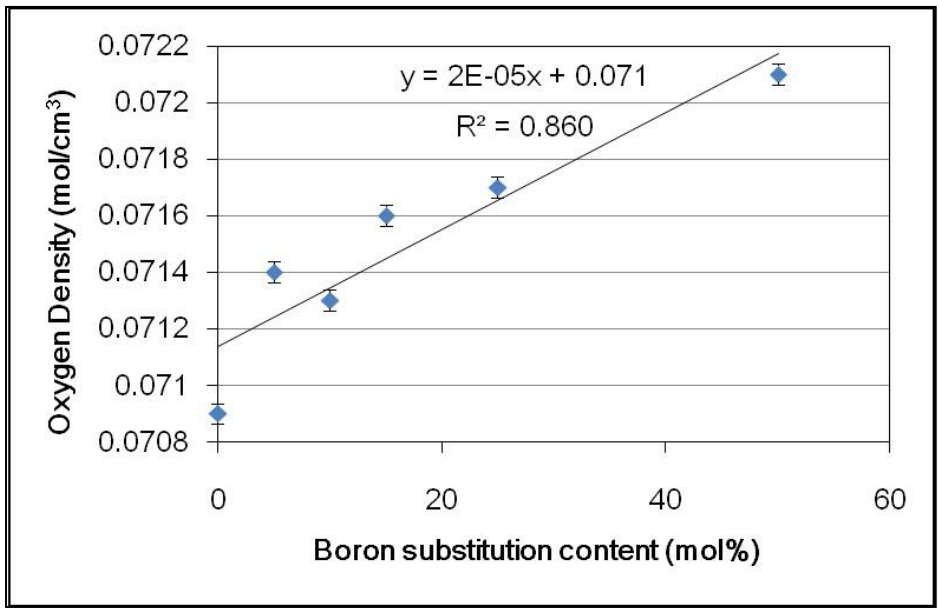


**Figure 4.1.4:** Oxygen density of boron-substituted fluorine-containing glasses.

### 4.1.2 FTIR and Raman study of all boron substituted glasses

Figure 4.1.5 shows the FTIR absorption spectra of all boron-containing fluorine-free glasses measured at room temperature. All glass spectra exhibit 4 broad absorption regions between 400–530 $cm^{-1}$, 530–620 $cm^{-1}$, 620–800 $cm^{-1}$ and 800-1200 $cm^{-1}$, which are assigned to bridging oxygen stretching and bending vibrations, respectively.

i) The band in the 400–530 $cm^{-1}$ region (centred at around 460 $cm^{-1}$), on the other hand, is related to bending vibrations of Si-O-Si;

ii) The bands between 530 and 620 $cm^{-1}$ (centred at 560 $cm^{-1}$) are connected with P-O bending vibrations and Si-O-Al linkages;

iii) And the absorption band in the 620-800 cm-1 (centred at 730 cm-1) region is due to stretching vibrations of Al-O bonds with Al in 4-fold coordination [138-143]. The band centred at 720 $cm^{-1}$ is also attributed to the oxygen bridging two trigonal $BO_3$ groups [144].

iv) the most intensive absorption bands lie in the 800–1200 $cm^{-1}$ region, which usually represent a superposition of some bands situated close together and assigned to the stretching vibration of $SiO_4$ tetrahedra with a different number of bridging oxygen atoms and P-O bonds. The region of 1000–1200 $cm^{-1}$ can arise from the overlapping contributions of silicate and borate groups [145, 146]. The broad band centred at 995 $cm^{-1}$ can be seen to consist of overlapping contributions of the Si-O-Si and B-O-B vibration modes i.e., it is attributed to Si-O-Si asymmetric bond stretching vibration [145] and B-O bonding vibration in $BO_4$ structural units [146]. It was not possible to separate the individual contributions in this region.

v) Furthermore, in all boron-substituted glasses, there is a new broad absorption in the absorption band in the 1200–1600 $cm^{-1}$ region (centred at 1400 $cm^{-1}$), which are attributed to the B-O stretching vibration of $BO_3$ units [147], and the shoulder located at 1278 $cm^{-1}$ is due to the stretching vibration of boroxol rings [148]. The band located at 1409 $cm^{-1}$ can arise from structural groups containing $BO_3$ units [149].

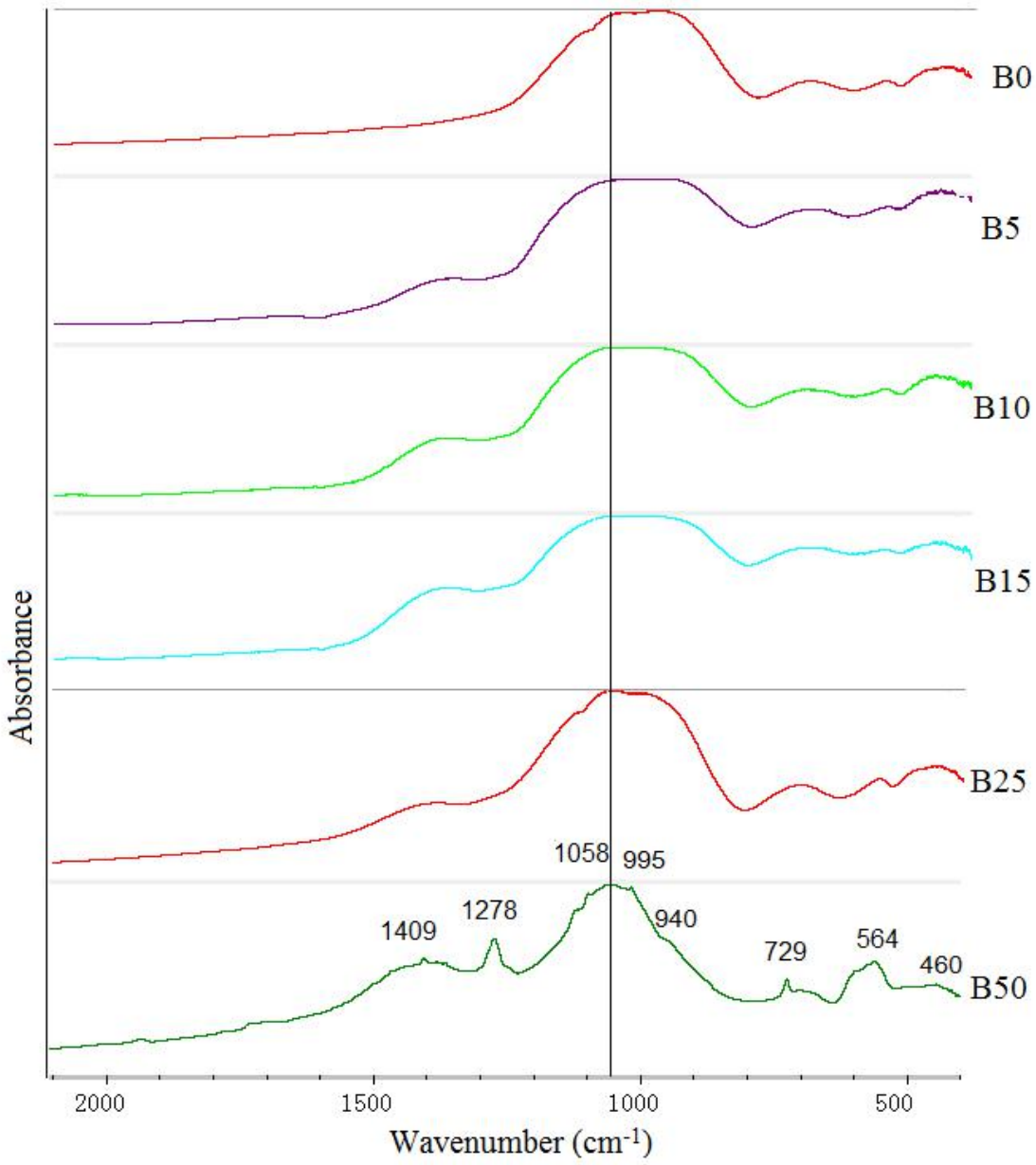


**Figure 4.1.5:** FTIR spectra of all boron-substituted fluorine-free glasses.

The FTIR spectra for boron-substituted fluorine-containing glasses are shown in Figure 4.1.6. Four broad absorption bands in the region of 4000 to 400 $cm^{-1}$ are identified:

i) The lowest band centred at around 460 $cm^{-1}$ in the region of 400–530 $cm^{-1}$ is associated with Si-O-Si bending vibrations.

ii) The band from 530–620 $cm^{-1}$ is associated with P-O bending and Si-O-Al linkages,

iii) The stretching vibrations of the Al-O bonds with aluminium ions in 4-fold coordination are present in the region of 620–800 $cm^{-1}$.

iv)The Si-O(s) stretching vibrations with a different number of bridging oxygen atoms and P-O bonds are observed in the 800–1200 $cm^{-1}$ region.

v) Additionally, in a manner very similar to boron-substituted fluorine-free glasses, the new bands located in the region between 1200 and 1600 $cm^{-1}$ are attributed to the B-O stretching vibration of $BO_3$ units [144-149].

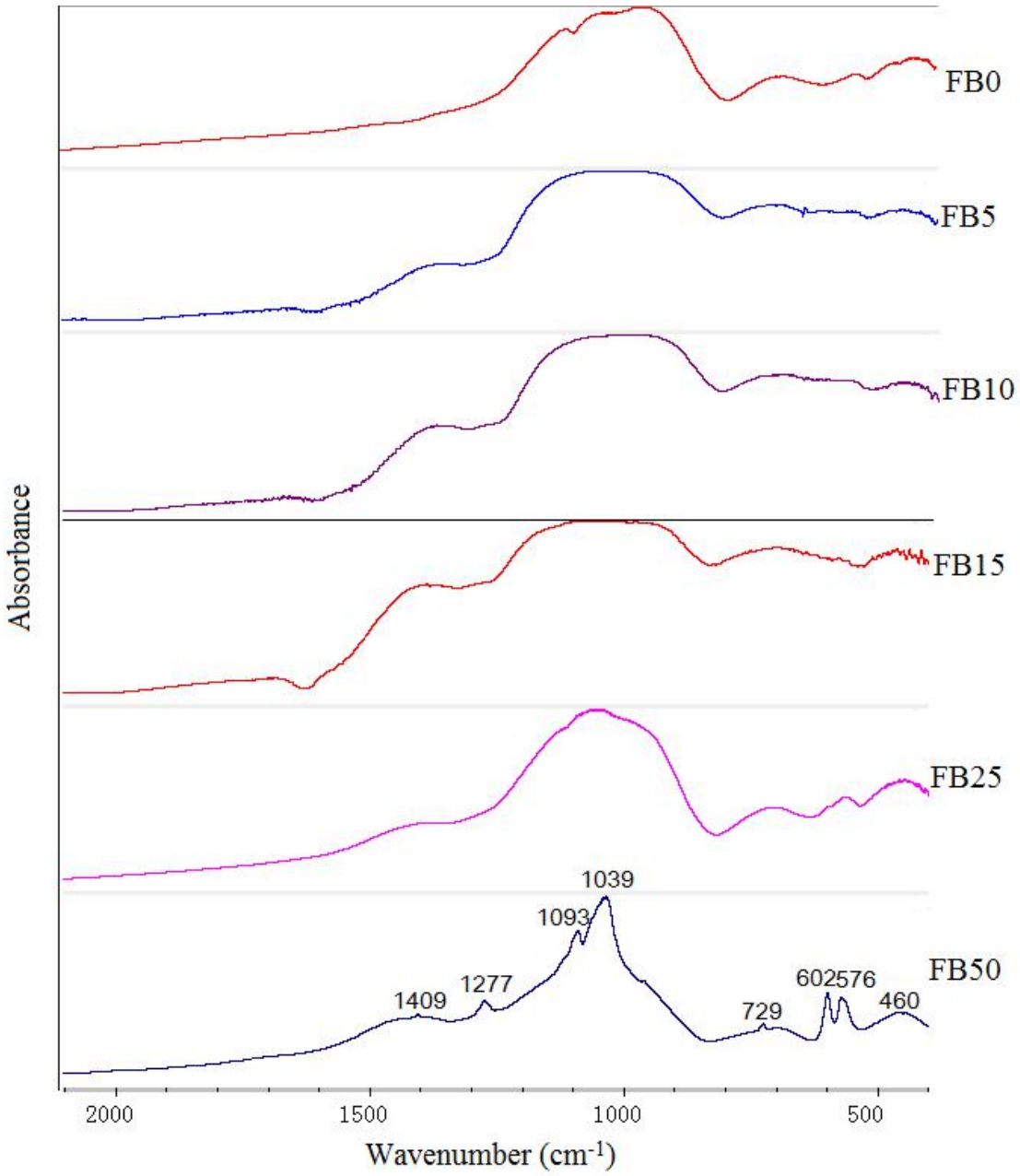


**Figure 4.1.6:** FTIR spectra of all boron-substituted fluorine-containing glasses.

The polarised Raman scattering were used to identify the types of bond in the boron-substituted glass by detecting the atomic motion through using the vibrational modes. And Table 4.2.1 illustrates the positions of spectral band for aluminosilicate glasses from literatures.

As can be seen, the increase of peaks intensity were observed both in boron-

substituted fluorine-containing and fluorine-free glass, which in the bands lower than 400 $cm^{-1}$ are attributed to the low-lying optic and high-lying acoustic modes in the glass network (≤100 $cm^{-1}$) [144-149], and also to the cation motion of the silicate network ($\nu_s$(Si-O-Si), 100–400 $cm^{-1}$) [152]. The peak around 540 $cm^{-1}$ is attributed to a symmetric aluminium tetrahedral network with 4 oxygen atoms in a bridging configuration. Peaks around 710 $cm^{-1}$ has been assigned to the appearance of octahedral in the glass [155], and the peaks around 767 $cm^{-1}$ is related to the $[AlO_4]^-$ tetrahedral.[153,154] In addition, the bands around 900–1200 $cm^{-1}$ relates to the high localised Si non-bridging oxygen stretching modes and normally used to identify the $SiO_4$ tetrahedra [156]. As can be seen from Figure 4.1.7 and 4.1.8, very broaden peaks were found in both boron-substituted fluorine-free and fluorine-containing glasses, which indicated the existence of Si-O-Si bond. And the intensity of these peaks increase with the increase of amount of boron. Besides, weak peaks were found at 980 $cm^{-1}$in FB50 and all boron-substituted fluorine-free glasses, which refers to the formation of Si-NBO in the structure. However, all the peaks detected by Raman are very weak, and need other methods to further identify different structures.

**Table 4.2.1:** Assignment of Raman peaks in alumino silicate glass networks from the literature.

| **Wavenumber ($cm^{-1}$)** | **Description** |
|---|---|
| 100-400 | Silicon atoms in the three-dimensional network structure (vs(Si-O-Si)) [152] |
| 500-800 | Symmetric $[AlO_4]^-$ tetrahedral network [153,154] |
| 900-1200 | Si-NBO stretching modes [156] |

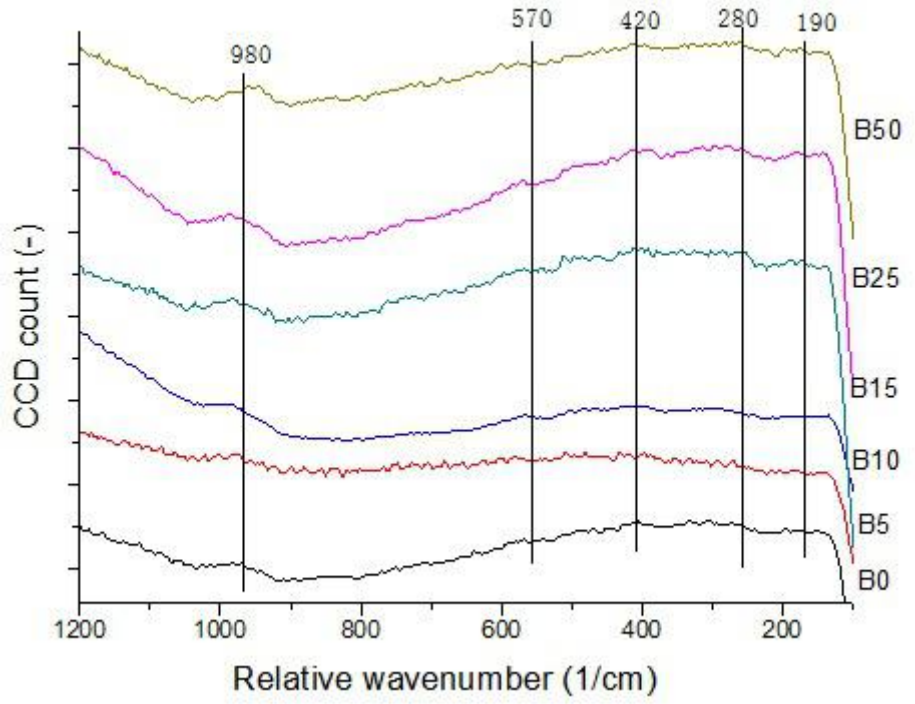


**Figure 4.1.7:** Raman spectra of all boron-substituted fluorine-free glasses.

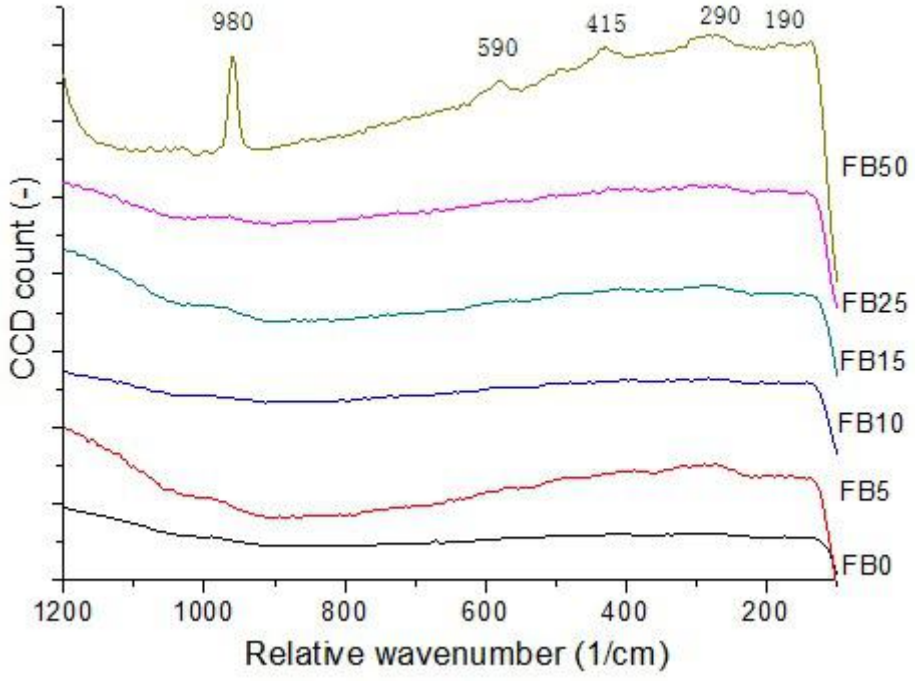


**Figure 4.1.8:** Raman spectra of all boron-substituted fluorine-containing glasses.

### 4.1.3 MAS-NMR study of all boron substituted glasses

#### 4.1.3.1 $^{29}$Si MAS-NMR spectroscopy

Table 4.1.3.1 and Figure 4.1.9 show the $^{29}$Si MAS-NMR spectra of boron-substituted glasses with 0, 5, 10, 15, 25, and 50% boron content. The chemical shift indicates the Si atom environment in the glass network. The $^{29}$Si spectrum of pure Ca glass consists of 4 overlapping peaks at around -87.8 ppm, -92.5 ppm, -103.4 ppm, and -108.2 ppm, which shift considerably when the boron content of the glasses is varied. In the case of an aluminosilicate glass, the above chemical shifts are in accordance with $Q^3$(4Al) , $Q^4$(3Al), $Q^4$(1Al), and $Q^4$(0Al) species [113, 157, 158].

**Table 4.1.3.1:** $^{29}$Si MAS-NMR spectroscopy on boron-substituted fluorine-free glasses.

| Glass | Boron substitution (mol %) | Chemical shift (ppm) |
|---|---|---|
| B0 | 0 | -83.3 |
| B5 | 5 | -86.6 |
| B10 | 10 | -84.5 |
| B15 | 15 | -86.9 |
| B25 | 25 | -88.9 |
| B50 | 50 | -103.5 |

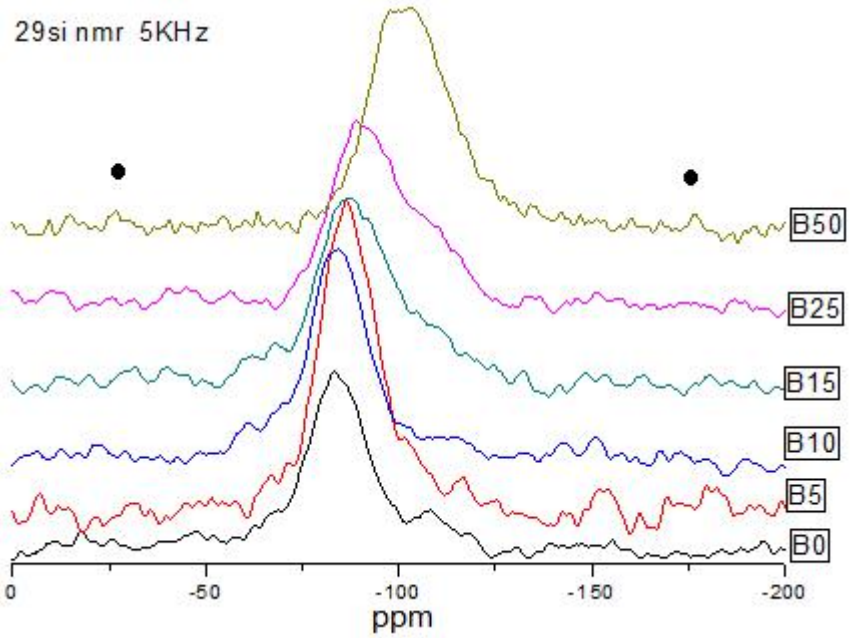


**Figure 4.1.9:** $^{29}$Si MAS-NMR spectra of different boron-substituted fluorine-free glasses. The spinning bands are marked with ●.

Table 4.1.3.2 and Figure 4.1.10 show the $^{29}$Si MAS-NMR spectra of boron-substituted fluorine-containing glasses. There are also 4 overlapping peaks observed. The respective chemical shifts, -87.8 ppm, -92.5 ppm, -97.6 ppm, and -108.2, are found for boron-substituted glass. The small change in the chemical shifts reflects a slight structural alteration around a Si atom in the glass network when Ca is replaced by boron. In this case, the above chemical shifts are in accordance with the $Q^3$(4Al), $Q^4$(3Al), $Q^4$(2Al), and $Q^4$(0Al) species reported elsewhere [113, 157, 158].

**Table 4.1.3.2:** $^{29}$Si MAS-NMR spectroscopy on boron-substituted fluorine-containing glasses.

| Glass | Boron substitution (mol %) | Chemical shift (ppm) |
|---|---|---|
| FB0 | 0 | -87.2 |
| FB5 | 5 | -86.9 |
| FB10 | 10 | -88.6 |
| FB15 | 15 | -91.3 |
| FB25 | 25 | -91.6 |
| FB50 | 50 | -99.4 |

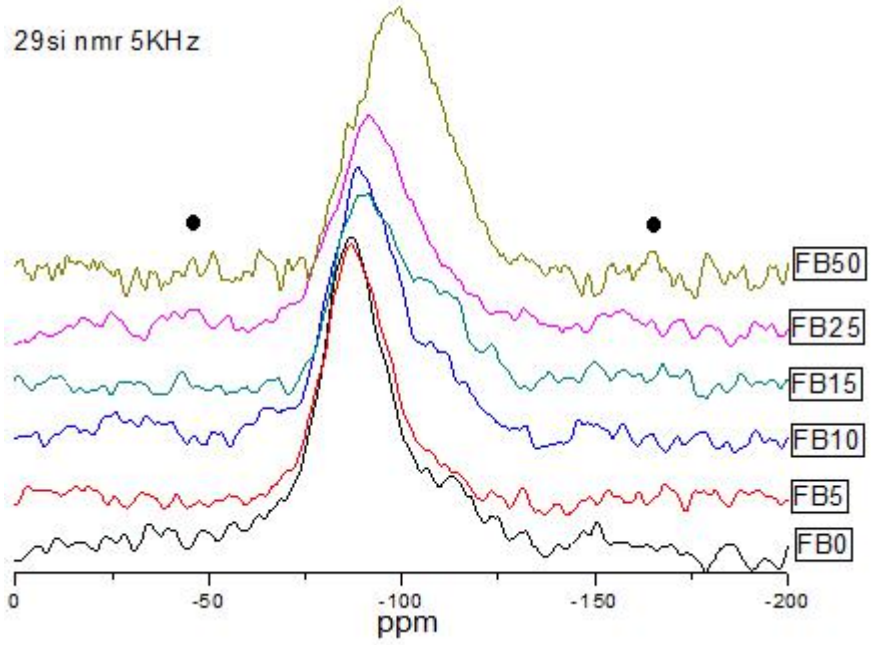


**Figure 4.1.10:** $^{29}$Si MAS-NMR spectra of different boron-substituted fluorine-containing glasses. The spinning bands are marked with ●.

### 4.1.3.2 $^{27}$Al MAS-NMR spectroscopy

Table 4.1.3.3 and Figure 4.1.11 shows the $^{27}$Al MAS-NMR spectra of different boron-substituted fluorine-free glasses. As expected, all spectra exhibit a broad peak at around 45 ppm assigned to 4-fold coordinated Al(IV), and a small overlap peak at

around 4 ppm assigned to six-fold coordinated Al(VI) [44, 102, 103, 158].

**Table 4.1.3.3:** $^{27}$Al MAS-NMR spectroscopy on boron-substituted fluorine-free glasses

| Glass | Boron substitution (mol %) | Chemical shift (ppm) |
|---|---|---|
| B0 | 0 | 49.1 |
| B5 | 5 | 49.0 |
| B10 | 10 | 47.6 |
| B15 | 15 | 47.5 |
| B25 | 25 | 45.9 |
| B50 | 50 | 45.6 |

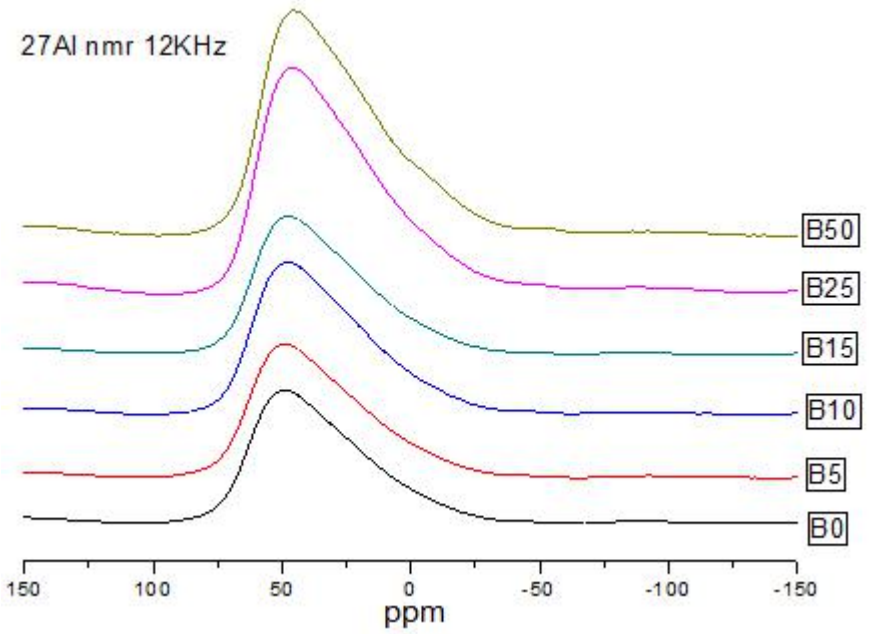


**Figure 4.1.11:** $^{27}$Al MAS-NMR spectra of different boron-substituted fluorine-free glasses.

Table 4.1.3.4 and Figure 4.1.12 show the $^{27}$Al MAS-NMR spectra of boron-substituted fluorine-containing glasses. The spectra show a large broad and

asymmetric peak around 45 ppm for all glasses due to 4-fold coordinated Al(IV). Both Al(V) and Al(VI) are likely to be present especially with increasing boron content. A clear small peak appears at around -4.0 ppm, which is attributed to six-fold coordinated Al(VI).

**Table 4.1.3.4:** $^{27}$Al MAS-NMR spectroscopy on boron-substituted fluorine-containing glasses.

| Glass | Boron substitution (mol %) | Chemical shift (ppm) |
|---|---|---|
| FB0 | 0 | 46.2 |
| FB5 | 5 | -4.3 ; 45.5 |
| FB10 | 10 | -4.3 ; 45.4 |
| FB15 | 15 | -4.3 ; 45.2 |
| FB25 | 25 | -4.3 ; 44.4 |
| FB50 | 50 | -4.3 ; 41.5 |

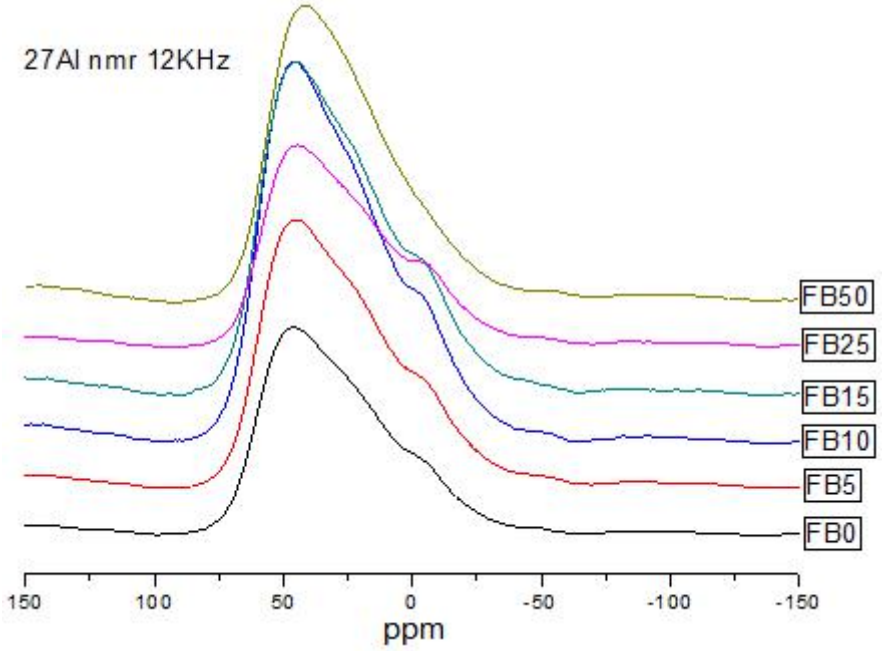


**Figure 4.1.12:** $^{27}$Al MAS-NMR spectra of boron-substituted fluorine-containing glasses.

### 4.1.3.3 $^{31}$P MAS-NMR spectroscopy

Table 4.1.3.5 and Figure 4.1.13 show the $^{31}$P MAS-NMR spectra of glasses with different boron content. A large broad symmetrical peak at around -5 ppm, which is assigned to $AlPO_4^{3-}$ ($Q^1$) species, is observed in the spectra of all glasses [112, 158].

**Table 4.1.3.5:** $^{31}$P MAS-NMR spectroscopy on boron-substituted fluorine-free glasses.

| Glass | Boron substitution (mol %) | Chemical shift (ppm) |
|---|---|---|
| B0 | 0 | -6.3 |
| B5 | 5 | -6.7 |
| B10 | 10 | -6.2 |
| B15 | 15 | -5.9 |
| B25 | 25 | -5.2 |
| B50 | 50 | 0.7 |

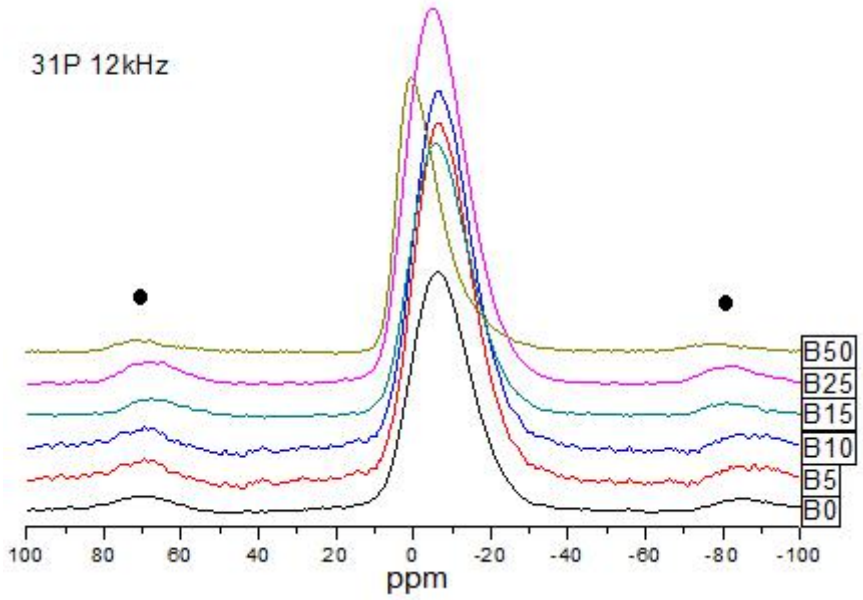


**Figure 4.1.13:** $^{31}$P MAS-NMR spectra of different boron-substituted fluorine-free glasses. The spinning bands are marked with ●.

Table 4.1.3.6 and Figure 4.1.14 show the $^{31}P$ MAS-NMR spectra of glasses with different boron content. A large broad symmetrical peak, also at around -5 ppm and assigned to $AlPO_4^{3-}$ ($Q^1$) species, is observed in the spectra of all glasses. The exception is FB50, which shows a very sharp peak at around 2.4 ppm, which is assigned to $Ca_3(PO_4)_2$ (tricalcium phosphate) [112, 158].

**Table 4.1.3.6:** $^{31}P$ MAS-NMR spectroscopy on boron-substituted fluorine-containing glasses.

| Glass | Boron substitution (mol %) | Chemical shift (ppm) |
|---|---|---|
| FB0 | 0 | -8.0 |
| FB5 | 5 | -8.1 |
| FB10 | 10 | -6.7 |
| FB15 | 15 | -6.5 |
| FB25 | 25 | -3.7 |
| FB50 | 50 | -18.3 ; 2.4 |

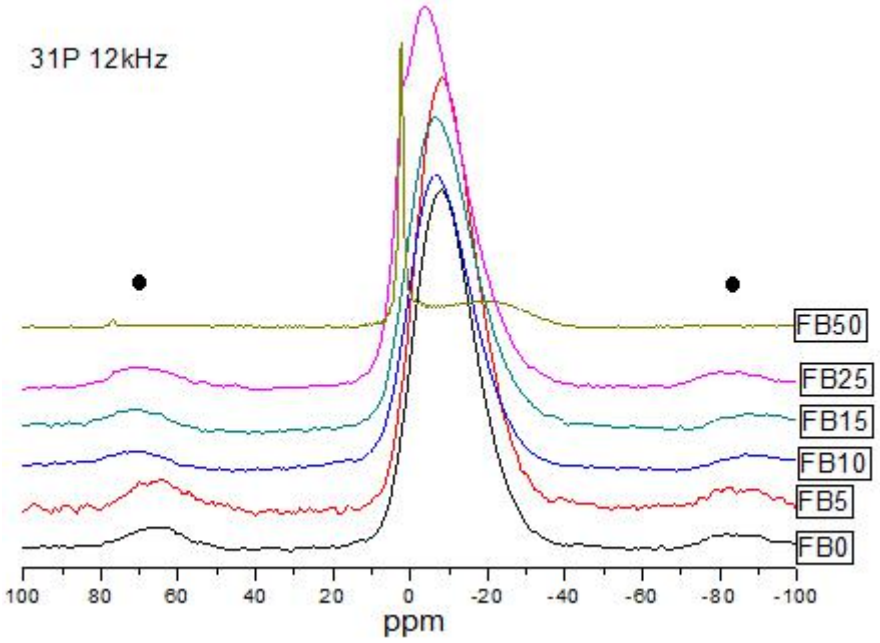


**Figure 4.1.14:** $^{31}P$ MAS-NMR spectroscopy on boron-substituted fluorine-containing glasses. The spinning bands are marked with ●.

### 4.1.3.4 $^{11}$B MAS-NMR spectroscopy

Table 4.1.3.7 and Figure 4.1.15 show the $^{11}$B MAS-NMR spectra of glasses with different boron content. Very similar and stable peaks are observed at around 1.0 ppm and 9.5ppm, which are assigned to $BO_4$ and $BO_3$ groups. Each $BO_3$ group is most probably connected to $SiO_4$ tetrahedra [159, 160].

**Table 4.1.3.7:** $^{11}$B MAS-NMR spectroscopy on boron-substituted fluorine-free glasses.

| Glass | Boron substitution (mol %) | Chemical shift (ppm) |
|---|---|---|
| B0 | 0 | ———— |
| B5 | 5 | 1.7 ; 9.3 |
| B10 | 10 | 1.7 ; 9.3 |
| B15 | 15 | 1.7 ; 9.3 |
| B25 | 25 | 1.7 ; 9.3 |
| B50 | 50 | 0.9 ; 9.2 |

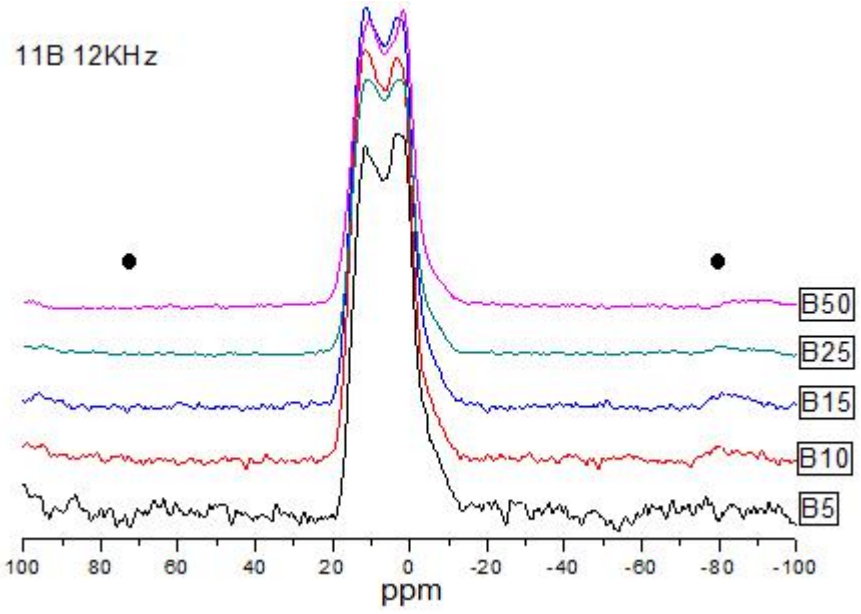


**Figure 4.1.15:** $^{11}$B MAS-NMR spectra of different boron-substituted fluorine-free glasses. The spinning bands are marked with ●.

Table 4.1.3.8 and Figure 4.1.16 show the $^{11}$B MAS-NMR spectra of glasses with

different boron content. Similar peaks are observed ranging from 0.8 to 0.2 and 9.0 to 9.5 ppm depending on the boron content in the glass. This peaks are assigned to $BO_4$ and $BO_3$ groups, respectively. Each $BO_3$ group is most probably connected to one $SiO_4$ tetrahedron [159, 160].

**Table 4.1.3.8:** $^{11}B$ MAS-NMR spectroscopy on boron-substituted fluorine-containing glasses

| Glass | Boron substitution (mol %) | Chemical shift (ppm) |
|---|---|---|
| FB0 | 0 | ———— |
| FB5 | 5 | 0.8 ; 9.0 |
| FB10 | 10 | 0.8 ; 9.5 |
| FB15 | 15 | 0.4 ; 9.5 |
| FB25 | 25 | 0.2 ; 9.4 |
| FB50 | 50 | 0.2 ; 9.3 |

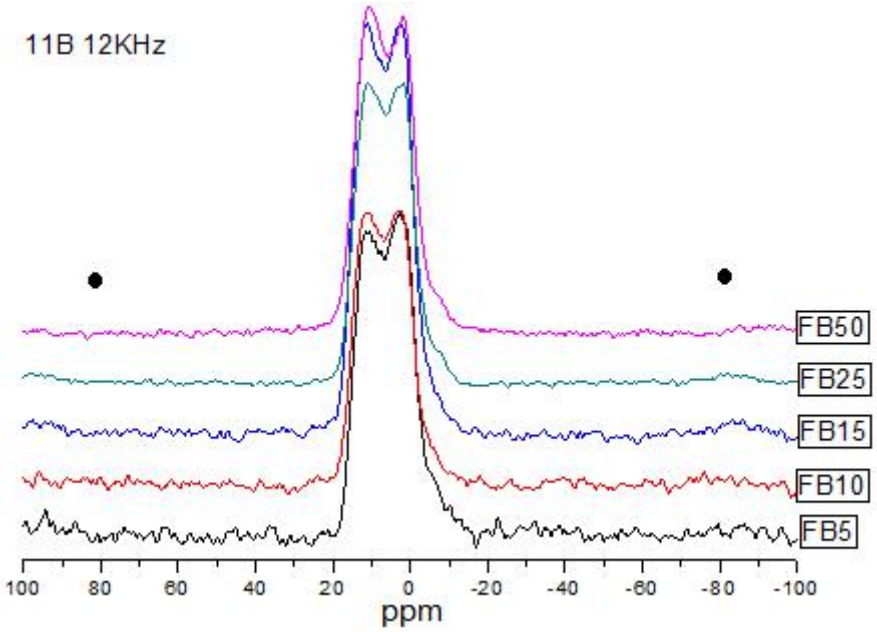


**Figure 4.1.16:** $^{11}B$ MAS-NMR spectra of different boron-substituted fluorine-containing glasses. The spinning bands are marked with ●.

### 4.1.3.5 $^{19}$F MAS-NMR Spectroscopy

Table 4.1.3.9 and Figure 4.1.17 show the $^{19}$F MAS-NMR spectra of boron-substituted fluorine-containing glasses. The two broad peaks observed in the spectrum of calcium-containing glass at -103 ppm and -110 ppm are assigned to the presence of F-Ca(n) and Al-F-Ca(n) species, respectively [103, 113]. In addition, only one peak is observed for boron-substituted glasses above FB15 associated with the presence of F-Ca(n) species. The lack of Al-F-Ca(n) species in higher boron content glasses is noticeable.

**Table 4.1.3.9:** $^{19}$F MAS-NMR spectroscopy on boron-substituted fluorine-containing glasses.

| Glass | Boron substitution (mol %) | Chemical shift (ppm) |
|---|---|---|
| FB0 | 0 | -109.9 ; -102.8 |
| FB5 | 5 | -110.1 ; -102.9 |
| FB10 | 10 | -110.1 ; -102.8 |
| FB15 | 15 | -102.7 |
| FB25 | 25 | -102.9 |
| FB50 | 50 | -103.1 |

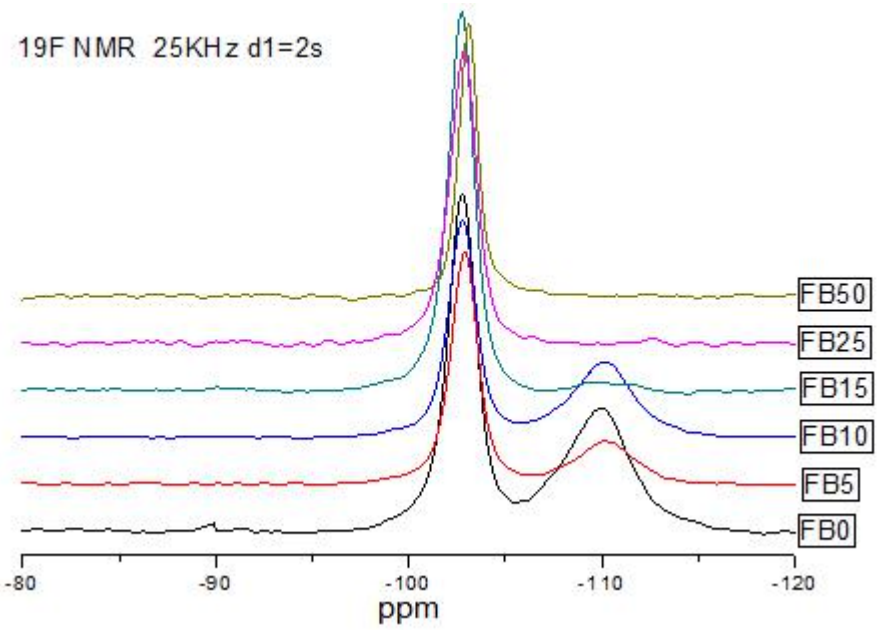


**Figure 4.1.17:** $^{19}F$ MAS-NMR spectra of different boron-substituted fluorine-containing glasses.

## 4.2 Effects of boron substitution on the crystallisation of glasses

### 4.2.1. Glass transition and crystallisation temperatures of substituted glasses

All the boron-substituted fluorine-free and fluorine-containing glasses were characterised by fine particle size (<45μm) using differential scanning calorimetry (DSC) at a heating rate of 10°C/min from room temperature to 1200°C. All the glass transition temperatures and crystallisation temperatures which are calculated by Proteus analysis software are shown in Tables 4.2.1, 4.2.2 and Figures 4.2.1 and 4.2.5 for boron-substituted fluorine-free and fluorine-containing glasses, respectively.

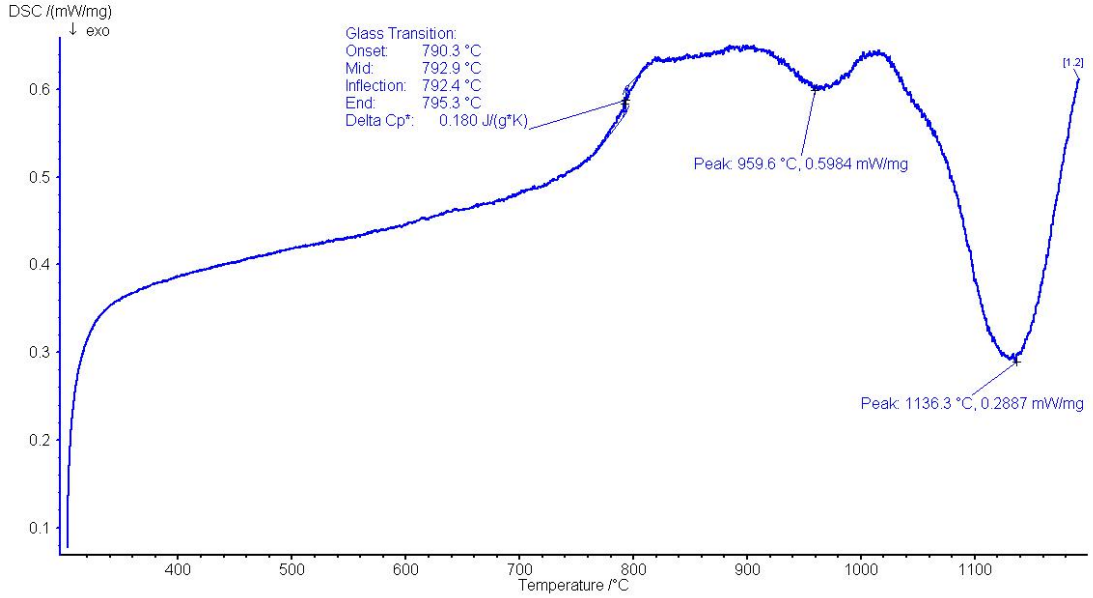


**Figure 4.2.1:** DSC trace of B0 glass with particle size <45µm measured at a heating rate of 10°C/min.

**Table 4.2.1:** DSC analysis data for all boron-containing fluorine-free glasses measured at a heating rate of 10°C/min.

| Glass | Boron substitution (molar %) | $T_g$(°C ) | $T_{p1}$(°C ) | $T_{p2}$(°C ) |
|---|---|---|---|---|
| B0 | 0 | 793 | 960 | 1136 |
| B2.5 | 2.5 | 803 | 963 | 1115 |
| B5 | 5 | 788 | 1082 | 1109 |
| B7.5 | 7.5 | 781 | 1062 | ---- |
| B10 | 10 | 781 | 991 | 1060 |
| B12.5 | 12.5 | 771 | 952 | 1038 |
| B15 | 15 | 764 | 928 | 1030 |
| B25 | 25 | 731 | 854 | 1012 |
| B50 | 50 | 693 | 746 | 956 |

In Figure 4.2.1, 4.2.2 and Table 4.2.1, the boron-substituted fluorine-free glasses show that the corresponding glass transition temperature ($T_g$) of the B0 sample increases slightly from 793°C to 803°C (B2.5), and then, when the content of boron substitution is increased, the $T_g$ of each sample decreases generally from 788°C (B5) to 693°C (B50).

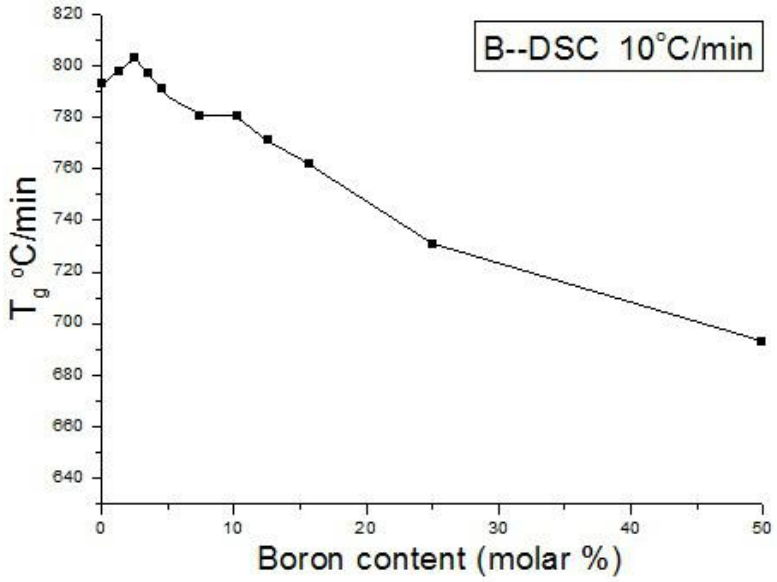


**Figure 4.2.2:** The variation in the glass transition temperature ($T_g$) with composition for boron-substituted fluorine-free glasses.

A slightly different changing tendency is found for the first crystallisation temperatures ($T_{p1}$) in boron-substituted fluorine-free glasses. The first crystallisation temperature, $T_{p1}$, increased initially but decreased following further boron substitution. In Table 4.2.1 and Figure 4.2.3, in the case of B5, the first crystallisation temperature increased from 960°C (B0) and 963°C (B2.5) to 1082°C. This was followed by a decrease to 1062°C in the case of B10 substitution, and, in the case of B50, a general decrease to 746°C.

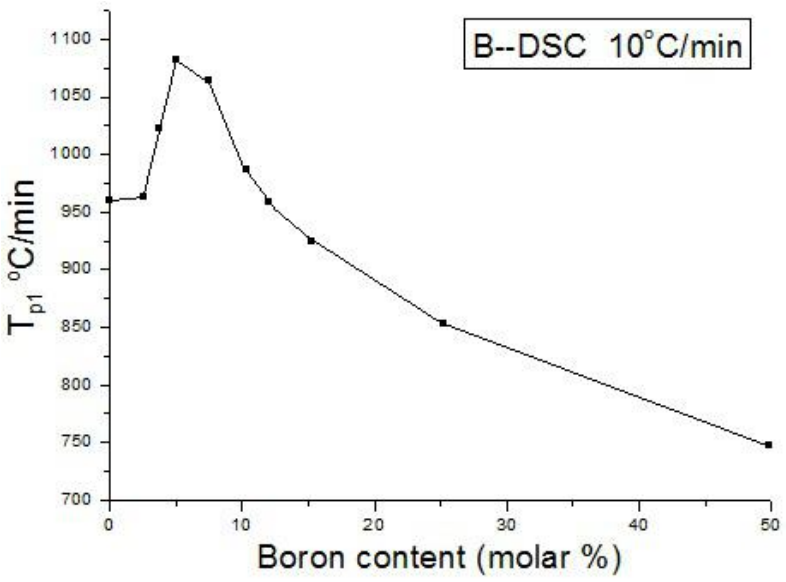


**Figure 4.2.3:** The variation in the first glass crystallisation temperature ($T_{p1}$) with composition for boron-substituted fluorine-free glasses.

For boron-substituted fluorine-free glasses, there is a consistent decreasing trend of the second crystallisation peak temperature ($T_{p2}$) with increasing substitution as shown in Figure 4.2.4. Table 4.2.1 also shows the second crystallisation peak temperature ($T_{p2}$) generally decreases from 1136°C (B0) to 956°C in the case of B50. As can be seen, the glass transition temperature and crystallisation temperature both decreased according to the increase in boron substitution for aluminium.

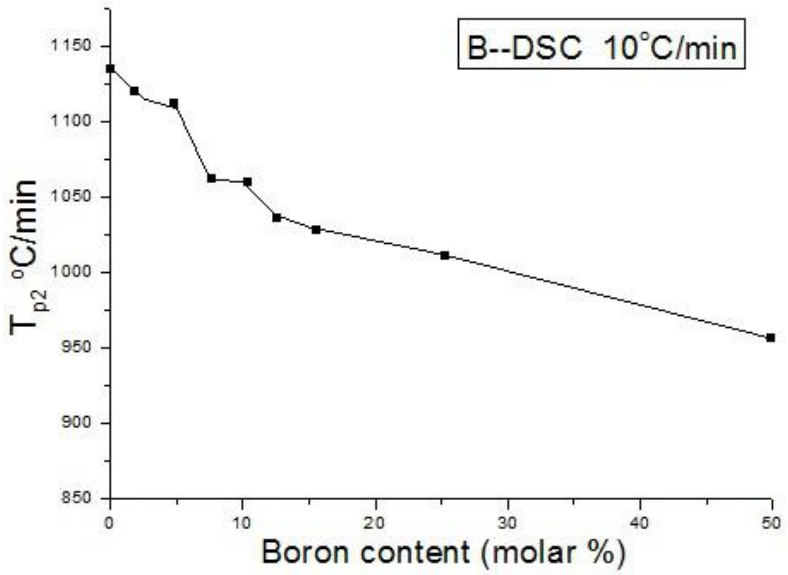


**Figure 4.2.4:** The variation in the second glass crystallisation temperature ($T_{p2}$) for boron-substituted fluorine-free glasses.

In Figure 4.2.5, 4.2.6 and Table 4.2.2, boron-substituted fluorine-containing glasses show that the corresponding glass transition temperatures ($T_g$) of the FB0 to the FB15 samples are very stable, from a region of 656°C to 647°C, and that the $T_g$ decreased to 605°C (FB25). In addition, the $T_g$ of FB50, in which the glass was part-crystallised during the glass-making process, is about 630°C.

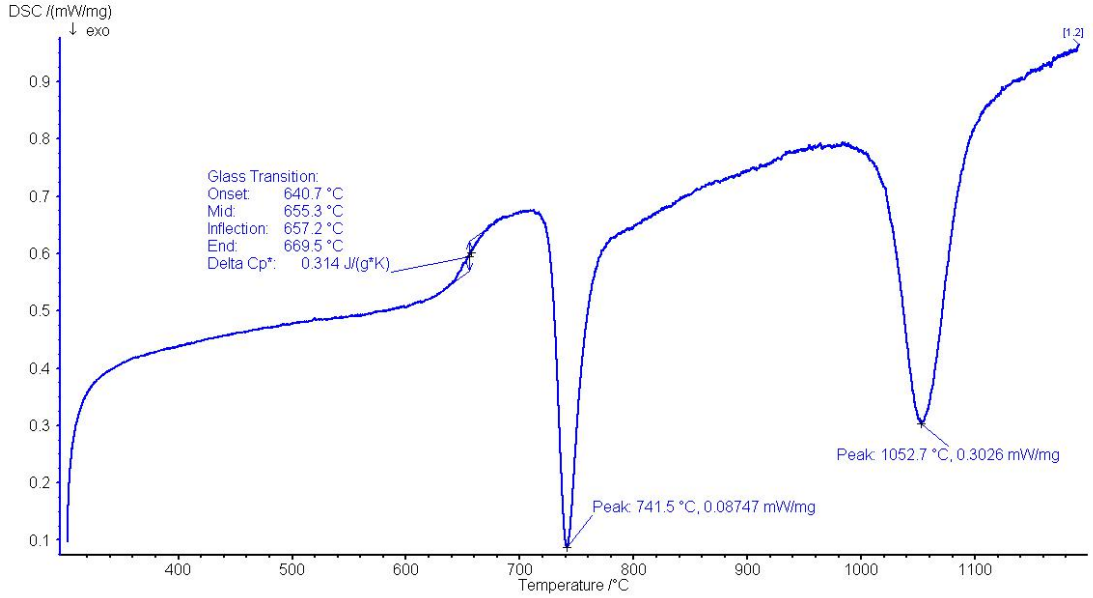


**Figure 4.2.5:** DSC trace of B0 glass with particle size <45µm measured at a heating rate of 10°C/min.

**Table 4.2.2:** DSC analysis data for all boron-substituted fluorine-containing glasses measured at a heating rate of 10°C/min.

| **Glass** | **Boron substitution (molar %)** | **$T_g$(°C )** | **$T_{p1}$(°C )** | **$T_{p2}$(°C )** | **$T_{p3}$(°C )** |
|---|---|---|---|---|---|
| FB0 | 0 | 653 | 741 | 1053 | ---- |
| FB2.5 | 2.5 | 655 | 748 | 1021 | ---- |
| FB5 | 5 | 647 | 728 | 977 | ---- |
| FB7.5 | 7.5 | 656 | 727 | 1014 | ---- |
| FB10 | 10 | 656 | 718 | 1014 | ---- |
| FB12.5 | 12.5 | 656 | 719 | 1116 | ---- |
| FB15 | 15 | 648 | 704 | 1089 | ---- |
| FB25 | 25 | 605 | 636 | 715 | 946 |
| FB50 | 50 | 630 | 643 | 763 | ---- |

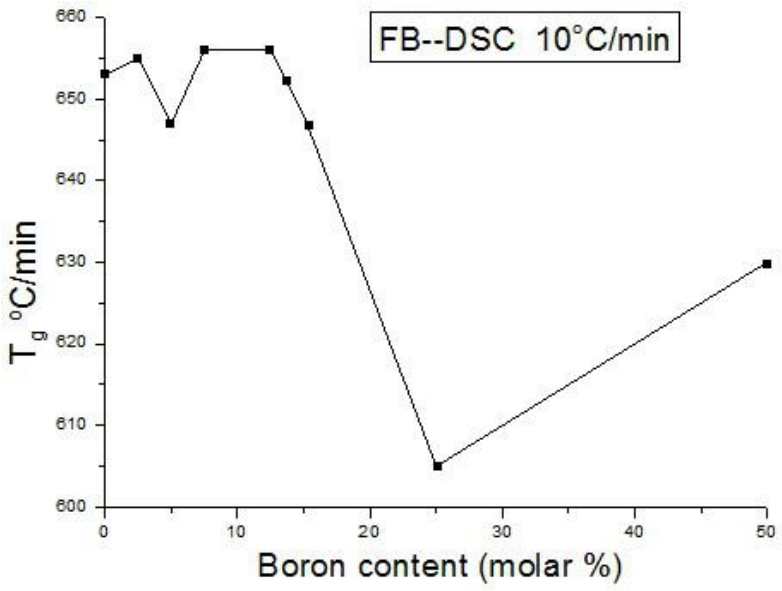


**Figure 4.2.6:** The variation in glass transition temperature ($T_g$) with composition for boron-substituted fluorine-containing glasses.

Figure 4.2.7 and Table 4.2.2 show that the first crystallisation temperatures of boron-substituted fluorine-containing glasses decreased, from 741°C, in the case of FB0, to 636°C, in the case of FB25. In the case of FB50, the first crystallisation temperature was slightly higher.

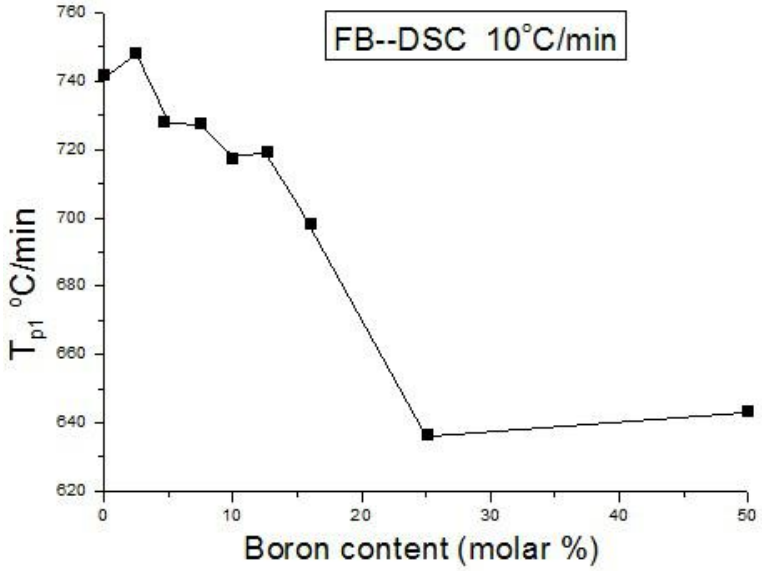


**Figure 4.2.7:** The variation in the first glass crystallisation temperature ($T_{p1}$) with composition for boron-substituted fluorine-containing glasses.

The values for $T_{p2}$ and $T_{p3}$ in boron-substituted fluorine-containing glasses are shown in Table 4.2.2 and Figure 4.2.8. As can be seen, the highest second crystallisation temperature, in the case of FB12.5, is 1116°C, while, in the case of FB25, three crystallisation temperatures are observed. It is interesting to mention that the FB25, which is not crystallised during glass making, shows the lowest $T_g$, $T_{p1}$, $T_{p2}$, and $T_{p3}$. It can be observed that there is a decreasing tendency in $T_{p1}$ and $T_{p2}$ (except FB12.5) by increasing the content of boron substitution on aluminium.

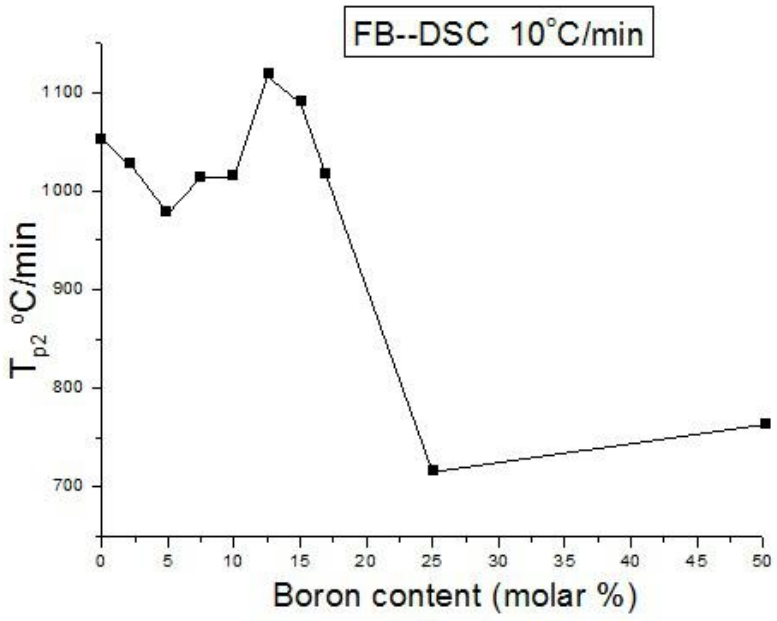


**Figure 4.2.8:** The variation in second glass crystallisation temperature ($T_{p2}$) with composition for boron-substituted fluorine-containing glasses.

All the glass transition temperatures and crystallisation temperatures are shown in Tables 4.2.3 and 4.2.4 for boron-substituted fluorine-free and fluorine-containing glasses with different heat rates of 10, 20, and 40°C/min, respectively.

**Table 4.2.3:** DSC analysis data by different heat rate for boron-substituted fluorine-free glasses.

| Glass | Boron substitution (molar %) | Heating rate (°C/min) | $T_g$(°C ) | $T_{p1}$(°C ) | $T_{p2}$(°C ) |
|---|---|---|---|---|---|
| B0 | 0 | 10 | 793 | 960 | 1136 |
| | | 20 | 800 | 982 | 1154 |
| | | 40 | 810 | 983 | 1159 |
| B5 | 5 | 10 | 788 | 1082 | 1109 |
| | | 20 | 795 | 1119 | ---- |
| | | 40 | 805 | 1173 | ---- |
| B10 | 10 | 10 | 781 | 991 | 1060 |
| | | 20 | 788 | 1023 | 1074 |
| | | 40 | 796 | 1066 | 1107 |
| B15 | 15 | 10 | 764 | 928 | 1030 |
| | | 20 | 772 | 960 | 1054 |
| | | 40 | 782 | 996 | 1091 |
| B25 | 25 | 10 | 731 | 854 | 1012 |
| | | 20 | 741 | 874 | 1015 |
| | | 40 | 753 | 895 | 1043 |
| B50 | 50 | 10 | 693 | 746 | 956 |
| | | 20 | 707 | 758 | 975 |
| | | 40 | 717 | 764 | 999 |

The glass transition temperatures and crystallisation temperatures are shown in Figure 4.2.9 for B0, B5, B10, B15, B25, and B50 boron-substituted fluorine-free glasses with different heating rates of 10, 20, and 40°C/min. The tendency of $T_g$, $T_{p1}$, and $T_{p2}$ for boron-substituted fluorine-free glasses increases when there are increases in the heating rate.

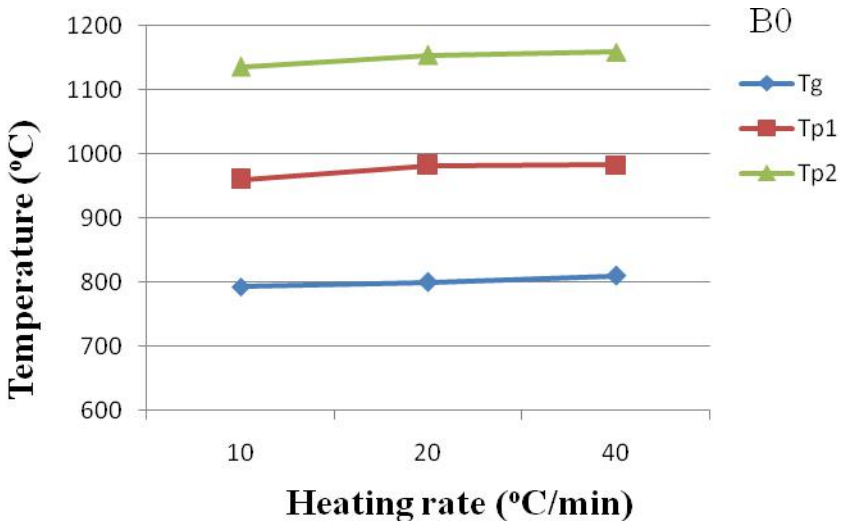
B0
Tg
Tp1
Tp2
Temperature (°C)
1200
1100
1000
900
800
700
600
10
20
40
Heating rate (°C/min)

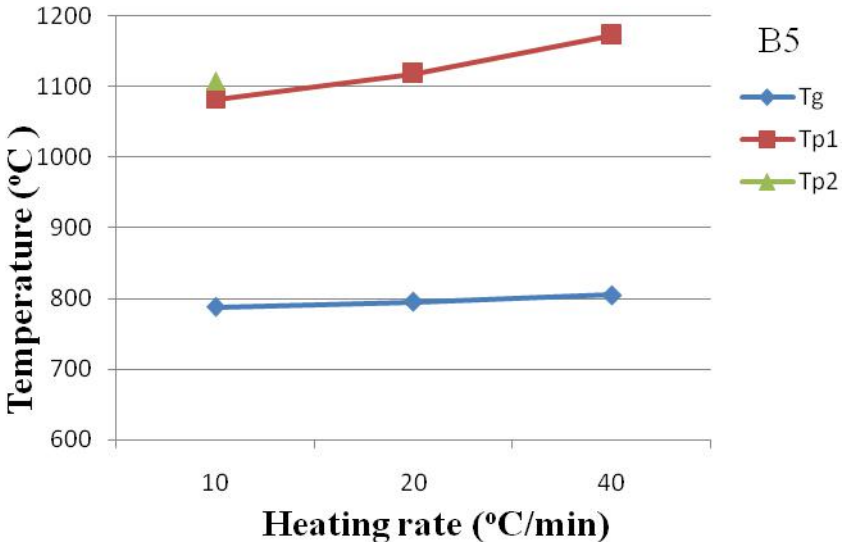
B5
Tg
Tp1
Tp2
Temperature (°C )
1200
1100
1000
900
800
700
600
10
20
40
Heating rate (°C/min)

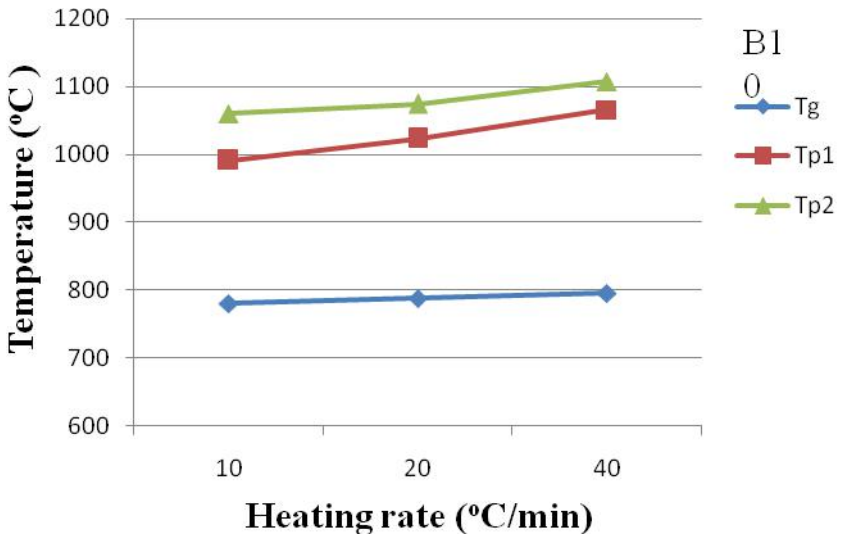
B10
Tg
Tp1
Tp2
Temperature (°C )
1200
1100
1000
900
800
700
600
10
20
40
Heating rate (°C/min)

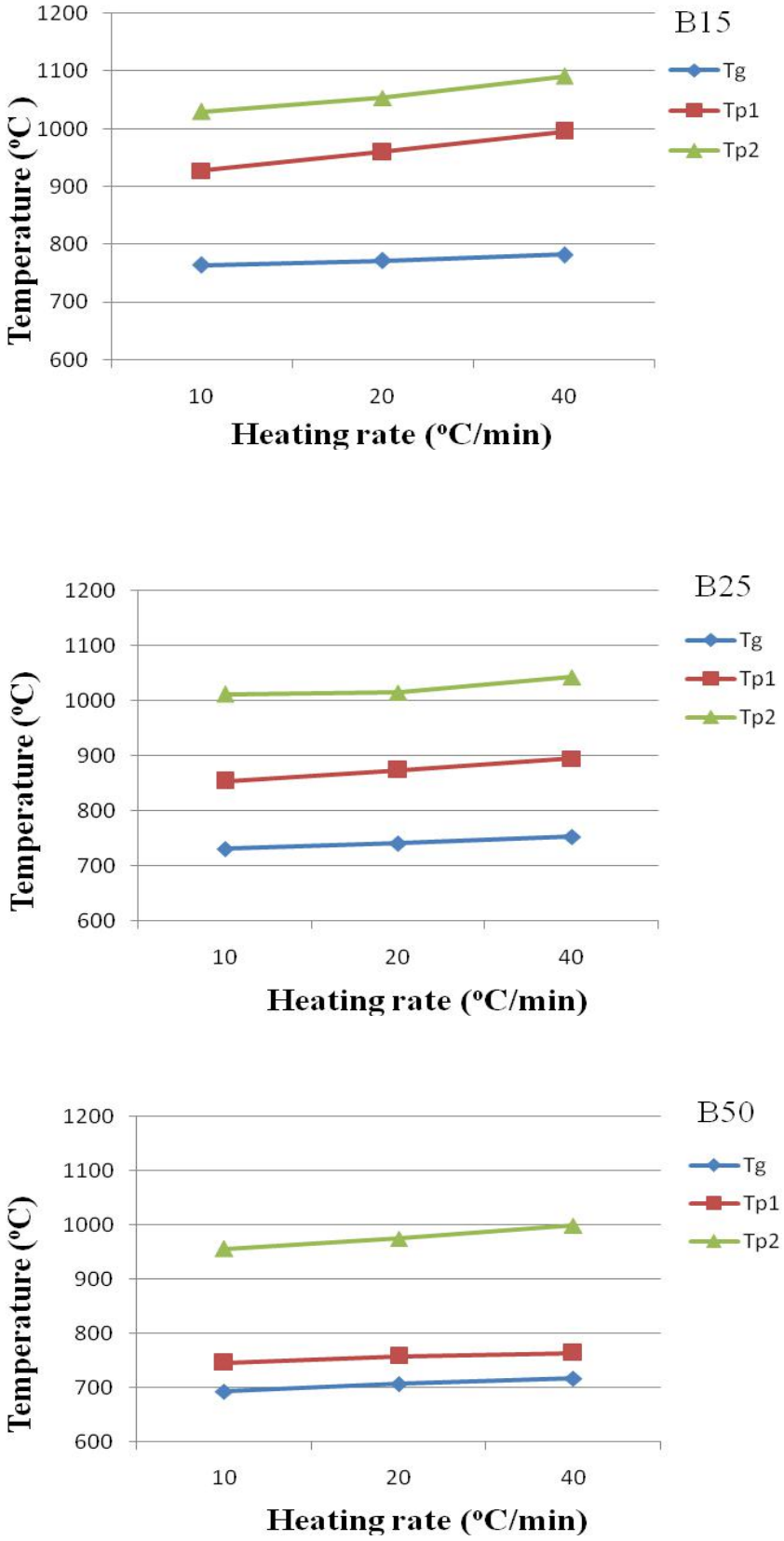


**Figure 4.2.9:** B0, B5, B10, B15, B25, and B50 boron-substituted fluorine-free glasses with different heating rates of 10, 20, and 40ºC/min.

**Table 4.2.4:** DSC analysis data by different heat rate for boron-substituted fluorine-containing glasses.

| Glass | Boron substitution (molar %) | Heating rate (°C/min) | $T_g$(°C ) | $T_{p1}$(°C ) | $T_{p2}$(°C ) | $T_{p3}$(°C ) |
|---|---|---|---|---|---|---|
| FB0 | 0 | 10 | 653 | 741 | 1053 | ---- |
| | | 20 | 664 | 764 | 1095 | ---- |
| | | 40 | 676 | 792 | 1136 | ---- |
| FB5 | 5 | 10 | 647 | 728 | 977 | ---- |
| | | 20 | 662 | 743 | 1025 | ---- |
| | | 40 | 667 | 764 | 1139 | ---- |
| FB10 | 10 | 10 | 656 | 718 | 1014 | ---- |
| | | 20 | 653 | 731 | 1063 | ---- |
| | | 40 | 669 | 747 | 1114 | ---- |
| FB15 | 15 | 10 | 648 | 704 | 1089 | ---- |
| | | 20 | 651 | 716 | 1121 | ---- |
| | | 40 | 666 | 733 | 1134 | ---- |
| FB25 | 25 | 10 | 605 | 636 | 715 | 946 |
| | | 20 | 611 | 645 | 733 | 967 |
| | | 40 | 624 | 657 | 749 | 1018 |
| FB50 | 50 | 10 | 630 | 642 | 763 | ---- |
| | | 20 | 637 | 653 | 810 | ---- |
| | | 40 | 649 | 657 | 819 | ---- |

The glass transition temperatures and crystallisation temperatures are shown in Figure 4.2.10 for FB0, FB5, FB10, FB15, FB25, and FB50 boron-substituted fluorine-containing glasses with different heating rates of 10, 20, and 40°C/min. This is a very similar tendency to that of fluorine-free glasses in that the $T_g$ and $T_p$ for boron-substituted fluorine-containing glasses show increases when there are increases in the heating rate.

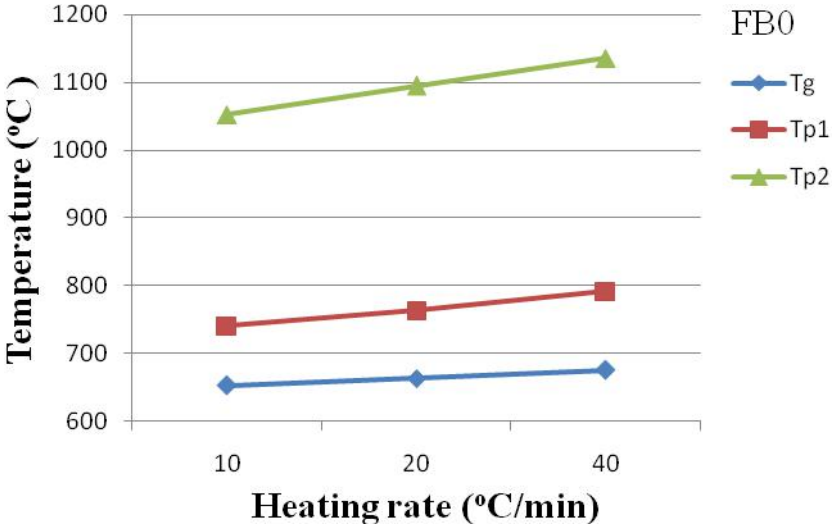
FB0
Tg
Tp1
Tp2
Temperature (ºC )
1200
1100
1000
900
800
700
600
10
20
40
Heating rate (ºC/min)

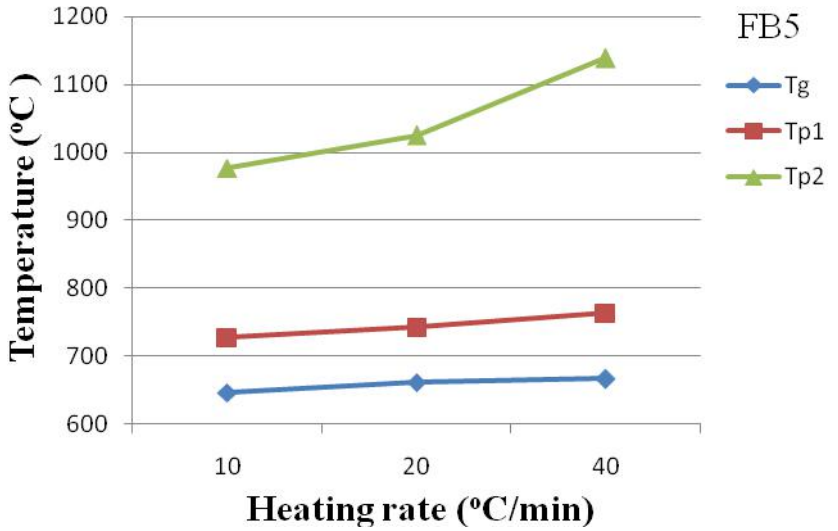
FB5
Tg
Tp1
Tp2
Temperature (ºC )
1200
1100
1000
900
800
700
600
10
20
40
Heating rate (ºC/min)

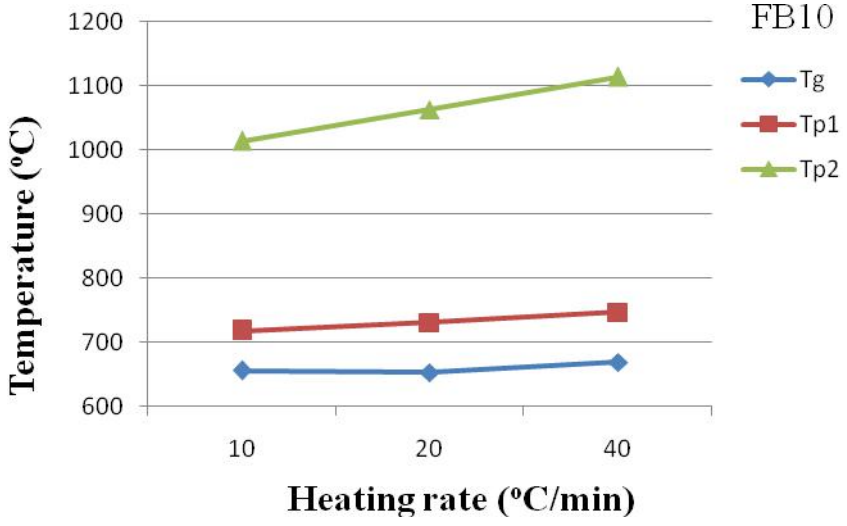
FB10
Tg
Tp1
Tp2
Temperature (ºC)
1200
1100
1000
900
800
700
600
10
20
40
Heating rate (ºC/min)

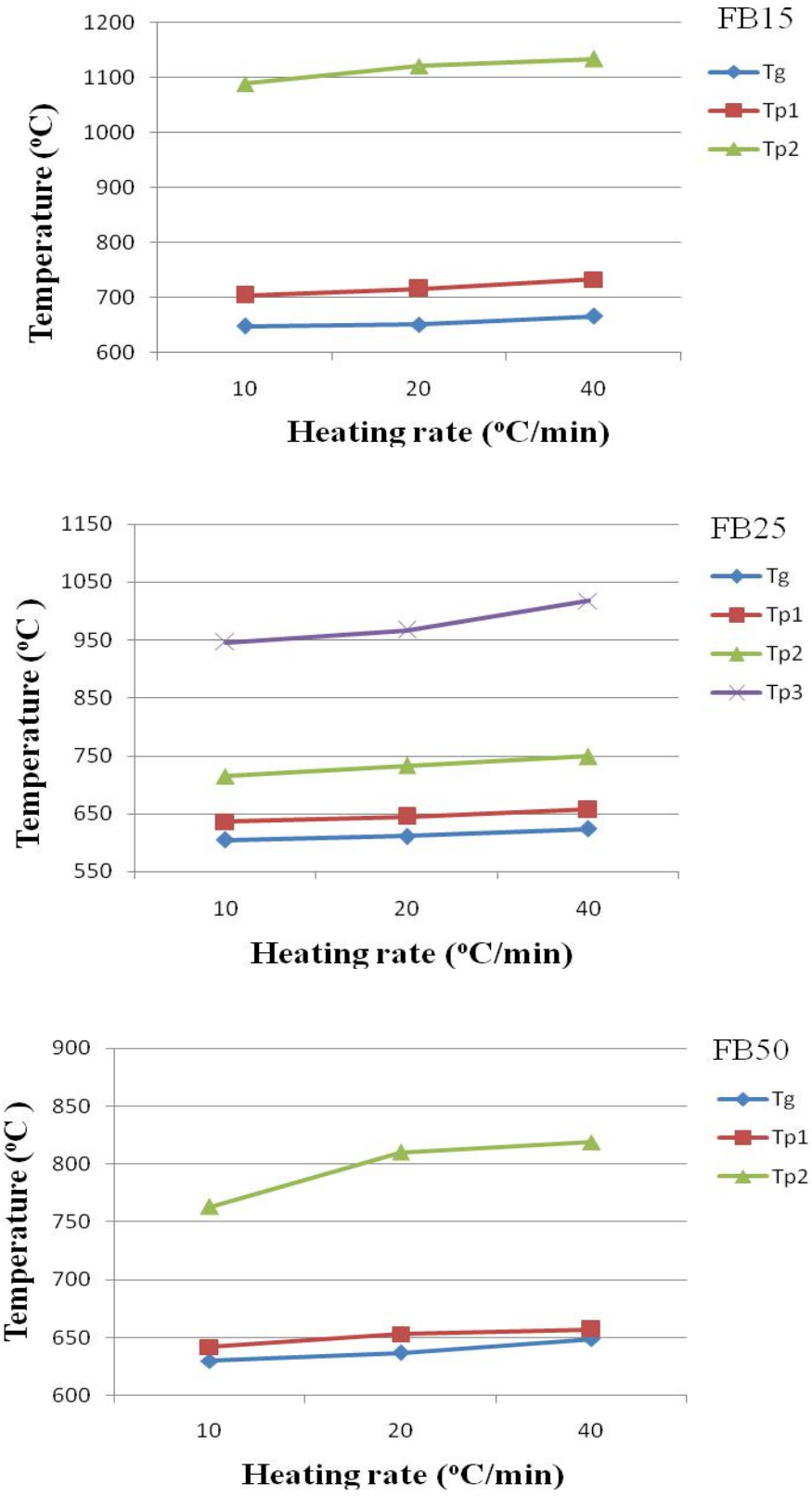


**Figure 4.2.10:** FB0, FB5, FB10, FB15, FB25, and FB50 boron-substituted fluorine-containing glasses with different heating rates of 10, 20, and 40°C/min.

### 4.2.2 TGA thermal analysis

In Table 4.2.5 it is clear that the total weight loss in boron-substituted fluorine-free and fluorine-containing glasses is around 2.9 and 2.2%, respectively. The tendency for weight loss in each glass is very similar (the green curve), though only two examples are shown here in Figure 4.2.11.

**Table 4.2.5:** Thermogravimetric analysis of all boron-substituted glasses.

| Glass | Weight loss (%) | Glass | Weight loss (%) |
|---|---|---|---|
| B0 | 2.8 | FB0 | 2.1 |
| B2.5 | 2.8 | FB2.5 | 2.1 |
| B5 | 2.9 | FB5 | 2.2 |
| B7.5 | 2.9 | FB7.5 | 2.2 |
| B10 | 2.9 | FB10 | 2.2 |
| B12.5 | 2.9 | FB12.5 | 2.2 |
| B15 | 2.9 | FB15 | 2.2 |
| B25 | 2.9 | FB25 | 2.2 |
| B50 | 2.9 | FB50 | 2.2 |

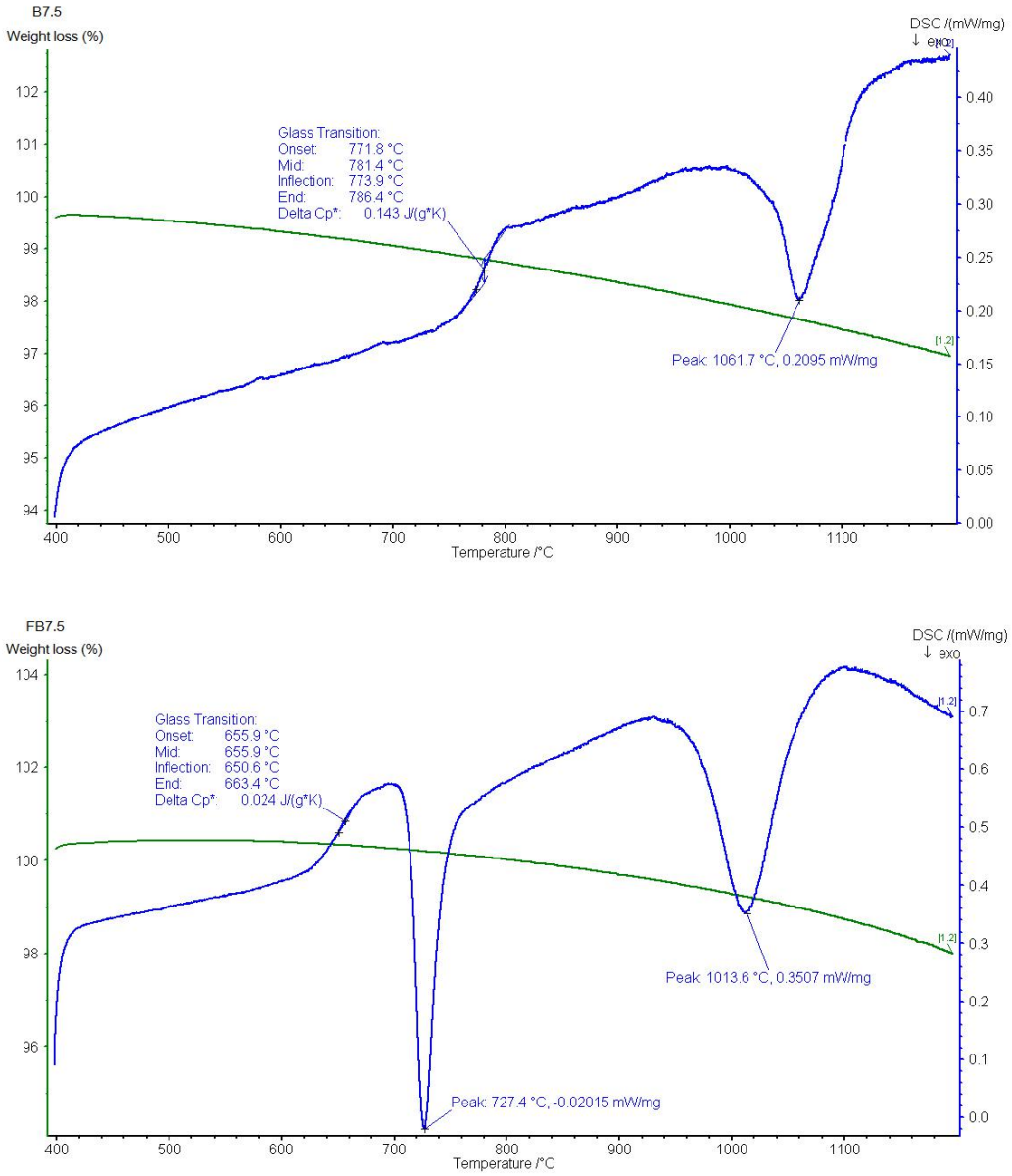


**Figure 4.2.11:** TGA and DSC analysis of B7.5 and FB7.5 glasses.

### 4.2.3 XRD study of substituted glass ceramics

Tables 4.2.6 to 4.2.9 show the main phases using X-ray powder diffraction analysis of all boron-substituted glasses and glass ceramics at a heating rate of 10°C/min from room temperature to sintering temperatures of 700°C, 900°C, and 1100°C, holding for

one hour, then furnace cooling to room temperature, respectively.

It is shown in Table 4.2.6 and Figure 4.2.12 that, B0 to B25 boron-substituted glasses are amorphous except for B50 glass, which exhibits a minor amount tetracalcium phosphate crystal phase [$Ca_4P_2O_9$, Ref.Code (00-011-0232)], and FB50 glass, which shows clearly a peak in the diffraction pattern related to fluorapatite [$Ca_5(PO_4)_3F$, Ref.Code (00-003-0736)].

**Table 4.2.6:** Main crystal phases in boron-substituted glasses.

| Glass | Crystal phases | Glass | Crystal phases |
|---|---|---|---|
| B0-B25 | Amorphous | FB0-FB25 | Amorphous |
| B50 | $Ca_4P_2O_9$ | FB50 | $Ca_5(PO_4)_3F$ |

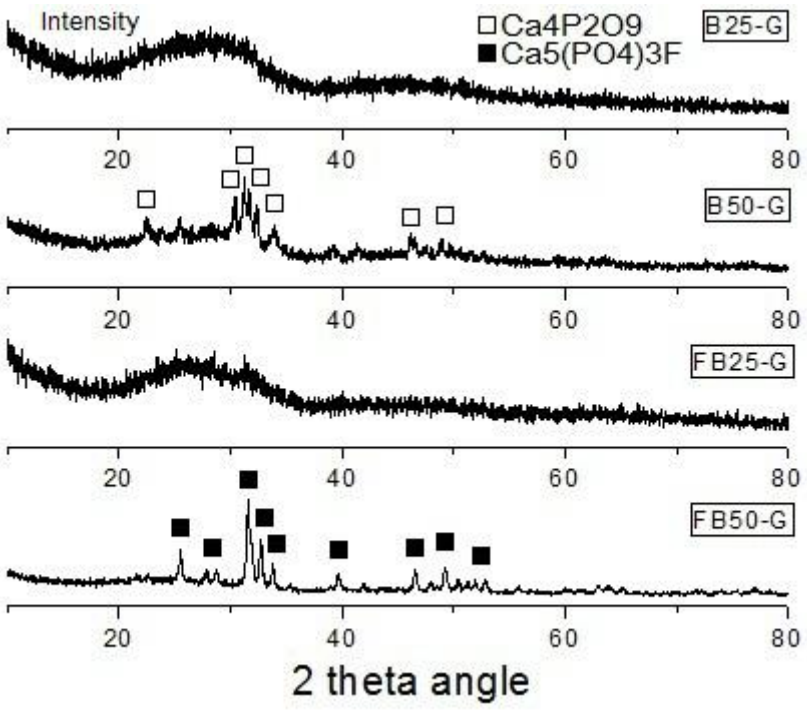


**Figure 4.2.12:** XRD results of B25, B50, FB25, and FB50 boron-substituted glasses.

Table 4.2.7 presents the crystal phases formed after the crystallisation of glasses heat treated at 700°C with a 1-hour hold.

**Table 4.2.7:** Main crystal phases in boron-substituted glass ceramics (hold temperature at 700°C)

| Glass | Crystal phases | Glass | Crystal phases |
|---|---|---|---|
| B0-B25 | Amorphous | FB0 | Amorphous |
| B50 | $Ca_4P_2O_9$ | FB2.5-FB50 | $Ca_5(PO_4)_3F$ |

Figure 4.2.13 shows the X-ray diffractogramm of boron-substituted glass. It is shown that, all glasses from 0% to 25% boron substitution are amorphous. B50 on the other hand was partly crystallised to calcium phosphate (most likely tetracalcium phosphate). On the other hand, only FB0 remained amorphous after sintering at 700°C, while FB2.5 to FB50 glasses crystallised to fluorapatite. The intensity of fluorapatites peaks in the X-ray diffractogram increased with increasing boron substitution.

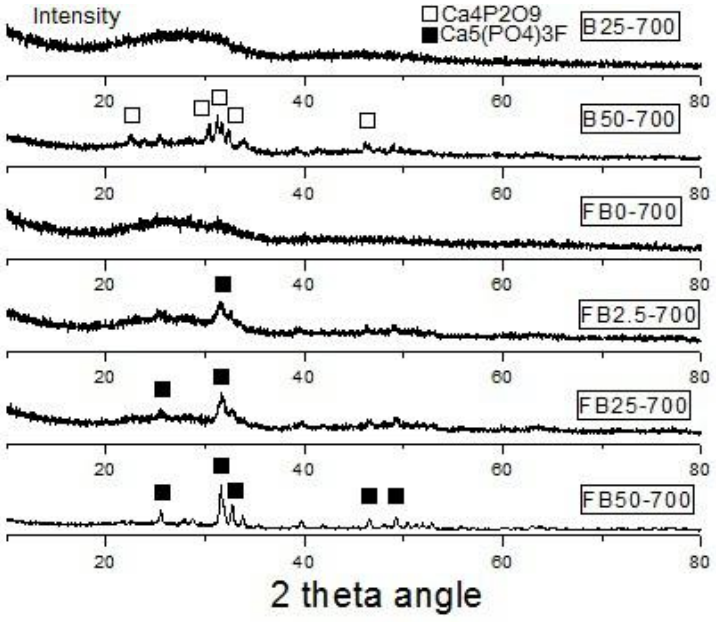


**Figure 4.2.13:** XRD results of 25, B50 and FB0, FB2.5, FB25, FB50 boron substituted glasses hold temperature at 700°C.

Table 4.2.8 presents the crystal phases formed after the crystallisation of glasses heat treated at 900°C with a 1-hour hold.

**Table 4.2.8:** Main crystal phases in boron-substituted glass ceramics (hold temperature at 900°C).

| Glass | Crystal phases | Glass | Crystal phases |
|---|---|---|---|
| B0 | $Ca_4P_2O_9$ | FB0 | $Ca_5(PO_4)_3F$ |
| B2.5 | $Ca_4P_2O_9$ | FB2.5 | $Ca_5(PO_4)_3F$ |
| B5 | $Ca_4P_2O_9$ | FB5 | $Ca_5(PO_4)_3F$ |
| B7.5 | $Ca_4P_2O_9$ | FB7.5 | $Ca_5(PO_4)_3F$ |
| B10 | $Ca_4P_2O_9$ | FB10 | $Ca_5(PO_4)_3F$ |
| B12.5 | $Ca_4P_2O_9$ | FB12.5 | $Ca_5(PO_4)_3F$ |
| B15 | $Ca_4P_2O_9$ | FB15 | $Ca_5(PO_4)_3F$ |
| B25 | $Ca_4P_2O_9$ | FB25 | $Ca_5(PO_4)_3F$ |
| B50 | $Ca_4P_2O_9$ | FB50 | $Ca_5(PO_4)_3F$ |

It is observed in Figure 4.2.14 that all boron-substituted fluorine-free glasses exhibited one crystal phase; tetracalcium phosphate [$Ca_4P_2O_9$, Ref.Code (00-011-0232)], while the intensity of the observed XRD peaks increased with increasing boron substitution.

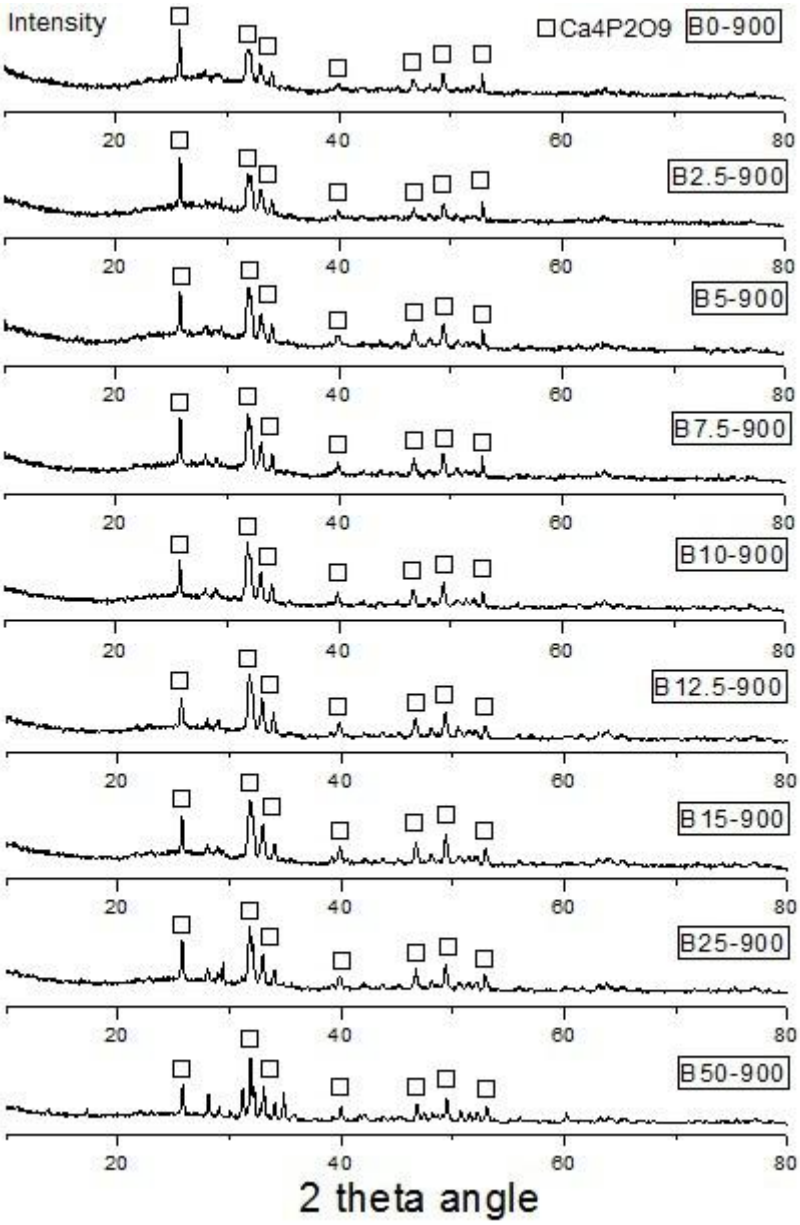


**Figure 4.2.14:** XRD results of boron substituted fluorine-free glasses hold temperature at 900ºC.

Figure 4.2.15 shows the X-ray diffractogramm of boron-substituted fluorine-containing glasses sintered at 900ºC with a 1-hour hold. All glasses are crystallised, mainly to a fluorapatite [$Ca_5(PO_4)_3F$, Ref.Code (00-003-0736)] phase.

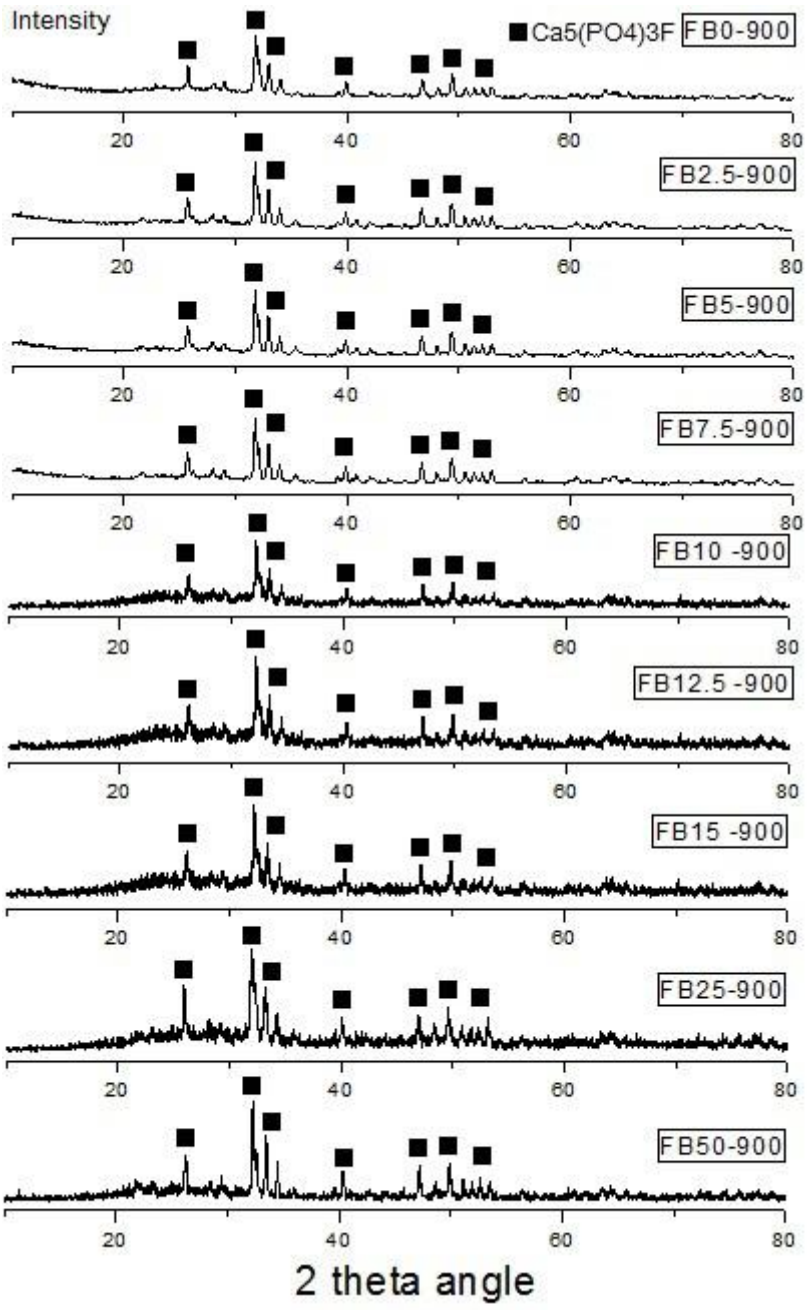


**Figure 4.2.15:** XRD results of boron substituted fluorine containing glasses hold temperature at 900ºC

Table 4.2.9 presents the crystal phases formed after the crystallisation of glasses heat treated at 1100ºC with a 1-hour hold.

**Table 4.2.9:** Main crystal phases in boron-substituted glass ceramics (hold temperature at 1100°C).

| Glass | Crystal phases | | |
|---|---|---|---|
| B0 | $Ca_3(PO_4)_2$ | $CaAl_2Si_2O_8$ | $AlPO_4$ |
| B2.5 | $Ca_3(PO_4)_2$ | $CaAl_2Si_2O_8$ | $AlPO_4$ |
| B5 | $Ca_3(PO_4)_2$ | $CaAl_2Si_2O_8$ | $AlPO_4$ |
| B7.5 | $Ca_3(PO_4)_2$ | $CaAl_2Si_2O_8$ | $AlPO_4$ |
| B10 | $Ca_3(PO_4)_2$ | $CaAl_2Si_2O_8$ | $AlPO_4$ |
| B12.5 | $Ca_3(PO_4)_2$ | $CaAl_2Si_2O_8$ | $AlPO_4$ |
| B15 | $Ca_3(PO_4)_2$ | $CaAl_2Si_2O_8$ | $AlPO_4$ |
| B25 | $Ca_3(PO_4)_2$ | $CaAl_2Si_2O_8$ | $AlPO_4$ |
| B50 | $Ca_3(PO_4)_2$ | $CaAl_2Si_2O_8$ | X |
| FB0 | $Ca_5(PO_4)_3F$ | $Al_6Si_2O_{13}$ | $AlPO_4$ |
| FB2.5 | $Ca_5(PO_4)_3F$ | $Al_6Si_2O_{13}$ | $AlPO_4$ |
| FB5 | $Ca_5(PO_4)_3F$ | $Al_6Si_2O_{13}$ | $AlPO_4$ |
| FB7.5 | $Ca_5(PO_4)_3F$ | $Al_6Si_2O_{13}$ | $AlPO_4$ |
| FB10 | $Ca_5(PO_4)_3F$ | $Al_6Si_2O_{13}$ | $AlPO_4$ |
| FB12.5 | $Ca_5(PO_4)_3F$ | $Al_6Si_2O_{13}$ | $AlPO_4$ |
| FB15 | $Ca_5(PO_4)_3F$ | $Al_6Si_2O_{13}$ | $AlPO_4$ |
| FB25 | $Ca_5(PO_4)_3F$ | $Al_6Si_2O_{13}$ | $AlPO_4$ |
| FB50 | $Ca_5(PO_4)_3F$ | $Al_6Si_2O_{13}$ | $AlPO_4$ |

The crystal phases occur after the crystallisation of the glasses. Figures 4.2.16 and 4.2.17 show the X-ray diffraction of boron-substituted fluorine-free glass ceramics. The B0 glass crystallises mainly to tricalciumphopshate [$Ca_3(PO_4)_2$, (Ref.Code 00-003-0681)] and anorthite (ordered) [$CaAl_2Si_2O_8$, (Ref.Code 00-020-0020)], a minor phase was the aluminium phosphate [$AlPO_4$ (Ref.Code 00-011-0500)] phase. It is observed that with increasing boron substitution for aluminium, the XRD peaks of the anorthite and calcium phosphate phases show a greater intensity from B0 to B15. However, for B25 and B50 glass ceramics, the content of the anorthite and aluminium phosphate phase decreases because of the lack of aluminium.

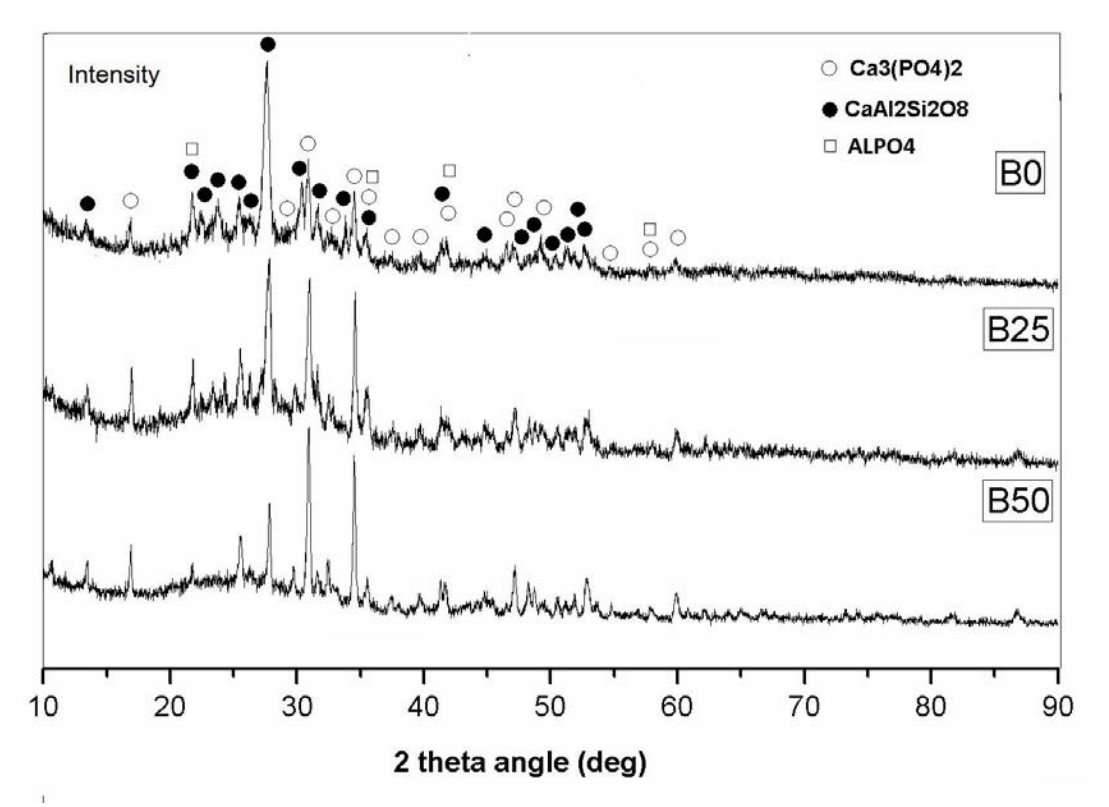


**Figure 4.2.16:** X-ray powder diffraction spectra of heat-treated (1100°C), boron-substituted fluorine-free glass ceramics. The heat-treated B0 glass spectrum is presented as reference material. ○ = calcium phosphate, ● = anorthite, □ = aluminium phosphate.

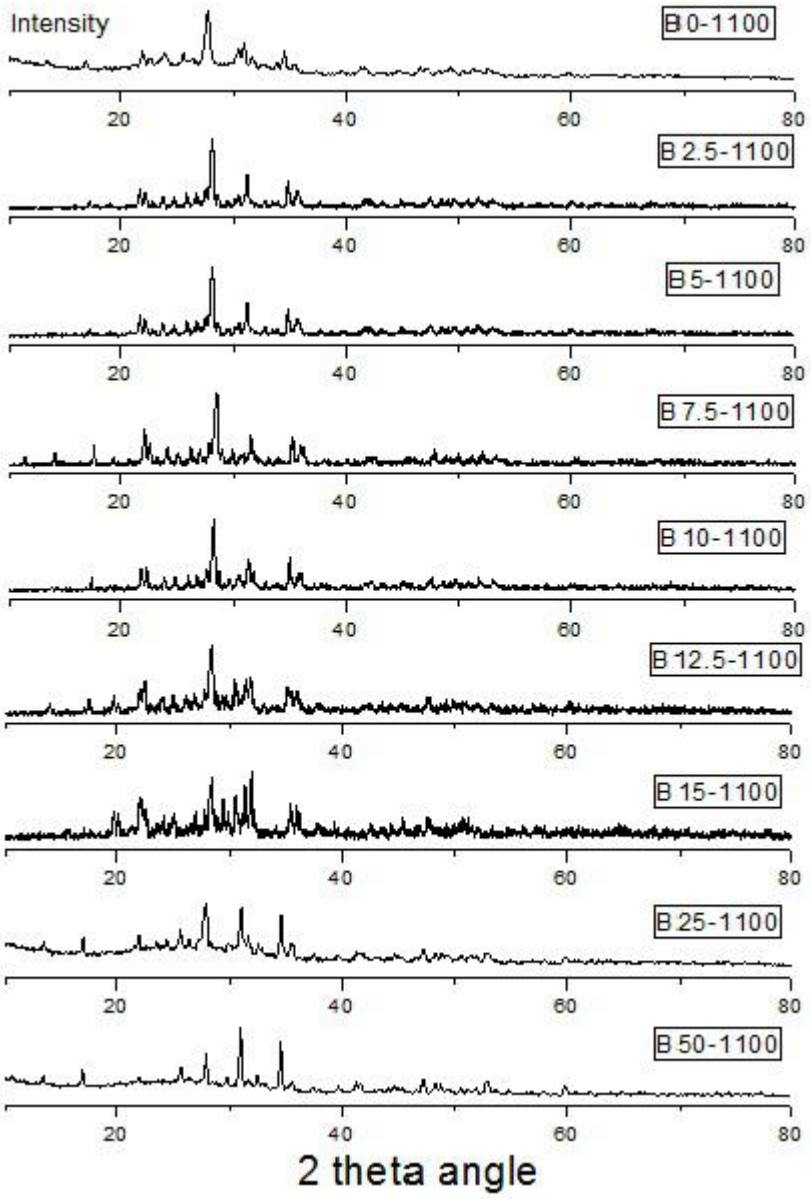


**Figure 4.2.17:** XRD results of boron substituted fluorine-free glasses sintered temperature at 1100$^{o}$C.

Figures 4.2.18 and 4.2.19 represent the diffraction patterns of boron-substituted fluorine-containing crystallised glasses. For the FB0 glass ceramics, fluorapatite [$Ca_5(PO_4)_3F$ (Ref.Code 00-015-0876)] and mullite [$Al_6Si_2O_{13}$ (Ref.Code 00-015-0776)] were the main phases, while a minor phase was the aluminium phosphate [$AlPO_4$ (Ref.Code 00-011-0500)] phase; with the boron substitution increasing, the

intensity of the XRD peaks for the fluorapatite and mullite phases increases in the FB2.5 to FB15 glass ceramics, whereas for FB25 and FB50 glass ceramics, the intensity of the XRD peaks of the mullite and aluminium phosphate phases decreases with increasing boron substitution. In the case of FB50 mullite and aluminium phosphate are only minor crystal phases.

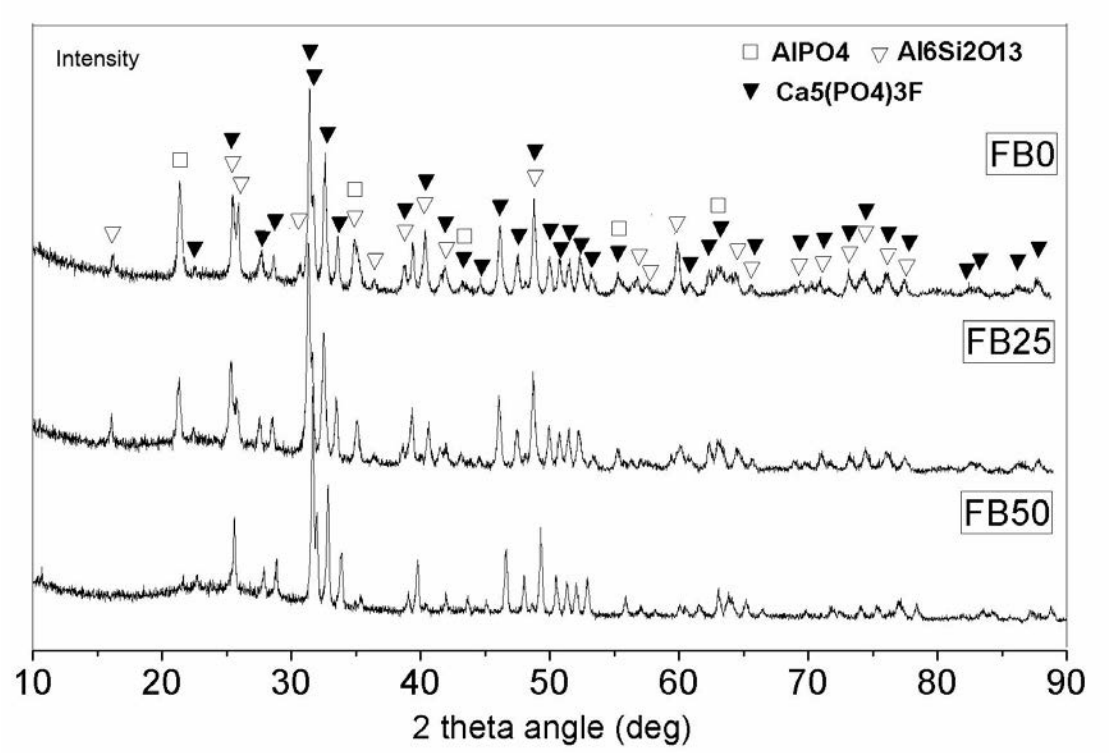


**Figure 4.2.18:** X-ray powder diffraction spectra of heat-treated (1100°C), boron-substituted fluorine-containing glass ceramics. The heat-treated FB0 glass spectrum is presented as reference material. □ = aluminium phosphate, ▼= fluorapatite, ▽ = mullite.

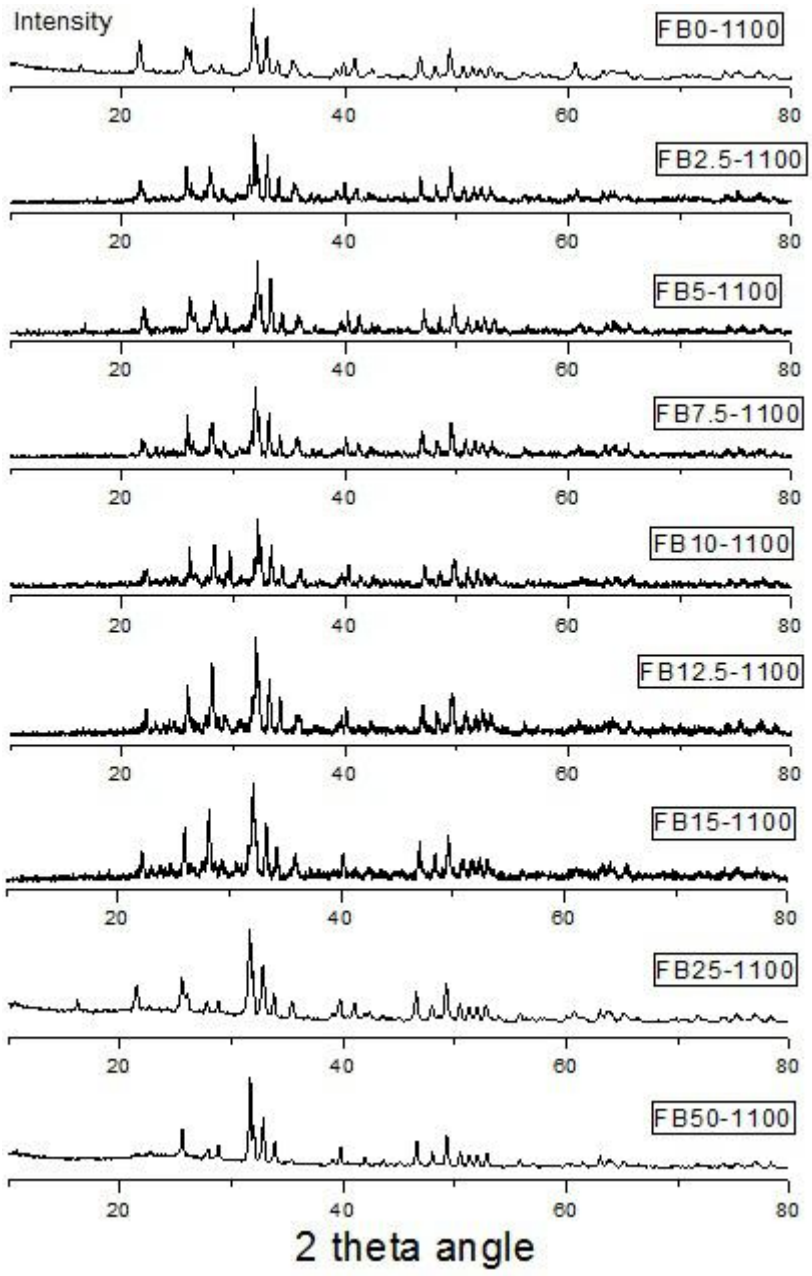


**Figure 4.2.19:** XRD results of boron substituted fluorine containing glasses sintered temperature at 1100ºC.

## 4.3 Effect of boron substitution on the properties and structure of glass ceramics

### 4.3.1 Density of all substituted glass ceramics

In the case of glass ceramics (heat treated temperature at 1100$^{o}$C), the density decreased with increasing boron substitution, from 2.808 g/cm$^3$ for B0 to 2.636 g/cm$^3$ for B50, as shown in Table 4.3.1. In Figure 4.3.1, it is observed that there is a linear relationship between density and boron molar content.

**Table 4.3.1:** Density of boron-substituted fluorine-free glass ceramics (heat treated temperature at 1100$^{o}$C).

| Glass ceramic | Boron substitution (mol %) | Density (g/cm$^3$) | Standard deviation (±g/cm$^3$) |
|---|---|---|---|
| B0-GC | 0 | 2.808 | 0.0003 |
| B5-GC | 5 | 2.770 | 0.0007 |
| B10-GC | 10 | 2.780 | 0.0005 |
| B15-GC | 15 | 2.732 | 0.0006 |
| B25-GC | 25 | 2.691 | 0.0002 |
| B50-GC | 50 | 2.636 | 0.0003 |

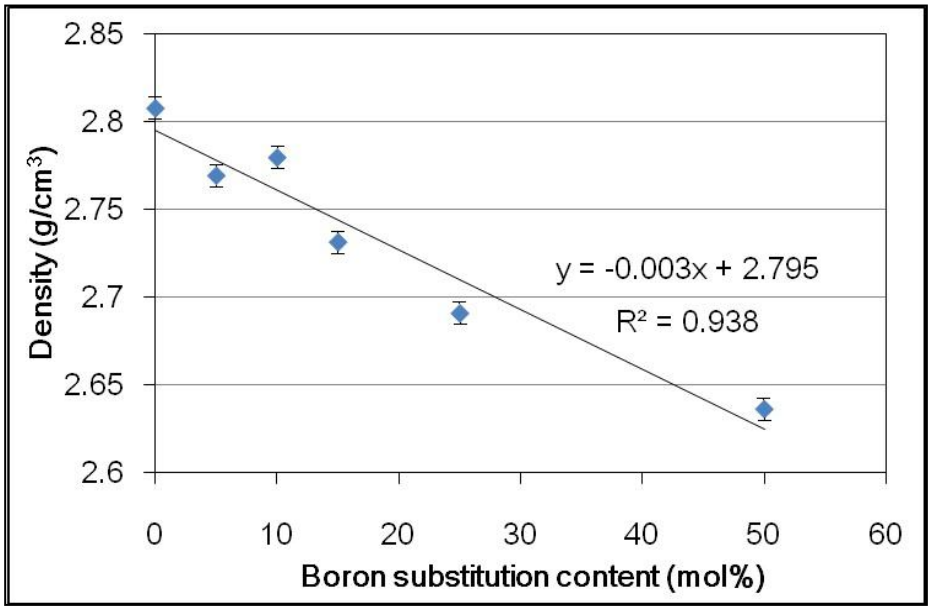


**Figure 4.3.1:** Density of boron-substituted fluorine-free glass ceramics (heat treated temperature at 1100°C).

In Table 4.3.2, it can be seen that the density also decreases with increasing boron substitution, from 2.932 g/cm$^3$ for FB0 to 2.665 g/cm$^3$ for FB50. In Figure 4.3.2, it is shown that the density does not change a lot with a little boron substitution, such as FB5, which is nearly 2.925 g/cm$^3$; on the other hand, for FB10 the density decreases significantly to 2.786 g/cm$^3$. Above 10% of boron substitution there is a linear relationship between the density and boron molar content.

**Table 4.3.2:** Density of boron-substituted fluorine-containing glass ceramics (heat treated temperature at 1100°C).

| Glass ceramic | Boron substitution (mol %) | Density ($g/cm^3$) | Standard deviation ($\pm g/cm^3$) |
|---|---|---|---|
| FB0-GC | 0 | 2.932 | 0.0007 |
| FB5-GC | 5 | 2.925 | 0.0007 |
| FB10-GC | 10 | 2.786 | 0.0016 |
| FB15-GC | 15 | 2.77 | 0.0007 |
| FB25-GC | 25 | 2.744 | 0.0006 |
| FB50-GC | 50 | 2.665 | 0.0004 |

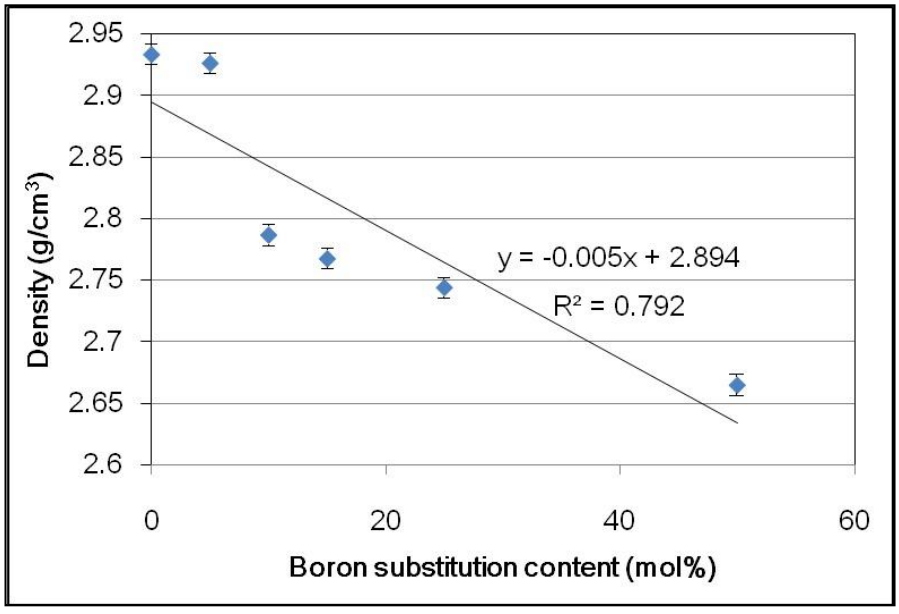


**Figure 4.3.2:** Density of boron-substituted fluorine-containing glass ceramics (heat treated temperature at 1100°C).

### 4.3.2 FTIR and Raman study of substituted glass ceramics

In order to investigate the structural changes after the crystallisation, all boron-substituted glasses were heated to 900$^{o}$C and 1100$^{o}$C and held at that temperature for 1 hour before then being furnace cooled to room temperature and finally characterised by FTIR in the wavenumber range of 4000–400 $cm^{-1}$.

All boron-substituted glasses were heated up to 900$^{o}$C and held at this temperature for 1 hour, then the furnace was left to cool down to room temperature. The FTIR absorbance spectra of the crystallised glass samples are shown in Figure 4.3.3 and Figure 4.3.4. The original broad peaks in the glass spectra in the 800–1200 $cm^{-1}$ region and around 560 $cm^{-1}$ and 730 $cm^{-1}$ shown in Figure 4.1.5 and Figure 4.1.6 were decomposed into several narrow peaks, and new peaks appeared at 595 $cm^{-1}$ and 566 $cm^{-1}$, which might be caused by the formation of the new crystal phases. The absorption band centred at 1085 $cm^{-1}$ is attributed to the P-O asymmetric stretching vibrations ($v_3$) of phosphate tetrahedra with 4 NBOs ($PO_4^{-3}$), while the peak at 942 $cm^{-1}$ is assigned to the symmetric stretching of phosphate groups ($v_1$) [161,162]. Al-O bonds with 4 coordination numbers were found be present around 707 $cm^{-1}$ and 560 $cm^{-1}$, while the band at 688 $cm^{-1}$ was related to the vibration of Al-O(VI) [163,164]. The region between 1200 $cm^{-1}$ and 1600 $cm^{-1}$ is attributed to the B-O stretching vibration of $BO_3$ units. When the boron substitution for aluminium increased, new peaks appeared at around 1396 $cm^{-1}$, 1003 $cm^{-1}$, and 896 $cm^{-1}$, suggesting that the boron introduction might have resulted in a phase separation during the crystallisation process. However, a lot of broad peaks are still seen in the boron-substituted glass-

ceramic spectra.

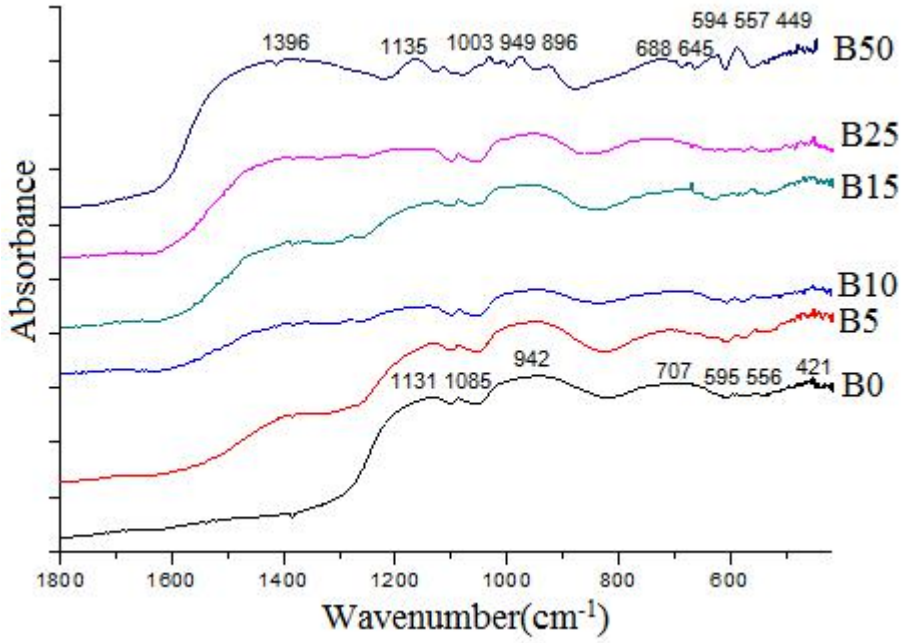


**Figure 4.3.3:** FTIR spectra of all boron-substituted fluorine-free glass ceramics (hold at 900°C).

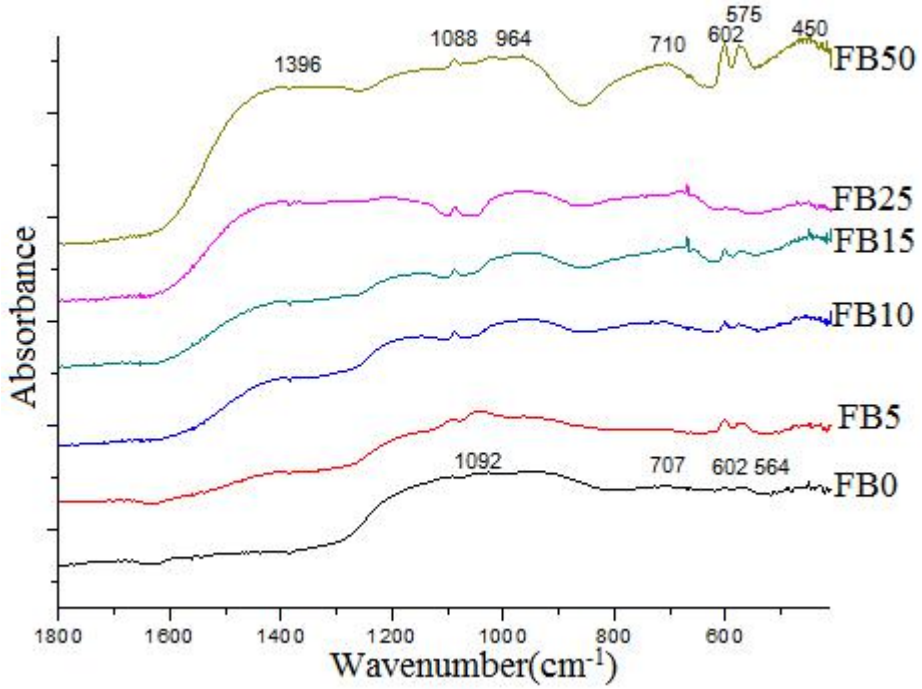


**Figure 4.3.4:** FTIR spectra of all boron-substituted fluorine-containing glass ceramics (hold at 900°C).

The FTIR absorption spectra of boron-substituted glass ceramics are shown in Figure 4.3.5 and Figure 4.3.6. All the glasses were crystallised by heating the glass samples to above 1100°C for 1 hour, followed by furnace cooling to room temperature. In Figure 4.3.5, the absorption bands centred at 1083 $cm^{-1}$ are attributed to the asymmetric stretching vibrations (P-O, $\nu_3$) of phosphate tetrahedral, and the symmetric stretching of phosphate ($\nu_1$) is located at 977 $cm^{-1}$, 963 $cm^{-1}$, and 950 $cm^{-1}$ [161,165]. Two bands at 557 $cm^{-1}$ and 615 $cm^{-1}$ are attributed to the O-P-O bending of phosphate ($\nu_4$), whereas the band centred at 451 $cm^{-1}$ is caused by the phosphate bending ($\nu_2$) vibration [162]. Compared to the glass spectra and glass-ceramic spectra, which were sintered at 900ºC, two significant changes were observed: (1) the original broad peaks in the region at 800–1200 $cm^{-1}$ and at 560 $cm^{-1}$ and 707 $cm^{-1}$ were decomposed into several narrow peaks assigned mainly to P-O stretching and bending vibrations, and (2) new peaks appeared at 668 $cm^{-1}$, 615 $cm^{-1}$ and 557 $cm^{-1}$ due to the formation of new crystal phases. The band centred at 668 $cm^{-1}$ is related to the Al-O bond in $AlO_6$, while the two peaks at 557 $cm^{-1}$ and 615 $cm^{-1}$ are connected with $\nu_4$ O-P-O bending vibrations of phosphate [161,162]. In addition, band in the region between 1200 $cm^{-1}$ and 1600 $cm^{-1}$, which is centred at 1396 $cm^{-1}$, are attributed to the B-O stretching vibration of $BO_3$ and $BO_4$ units, the intensity of which are increased with increasing boron substitution.

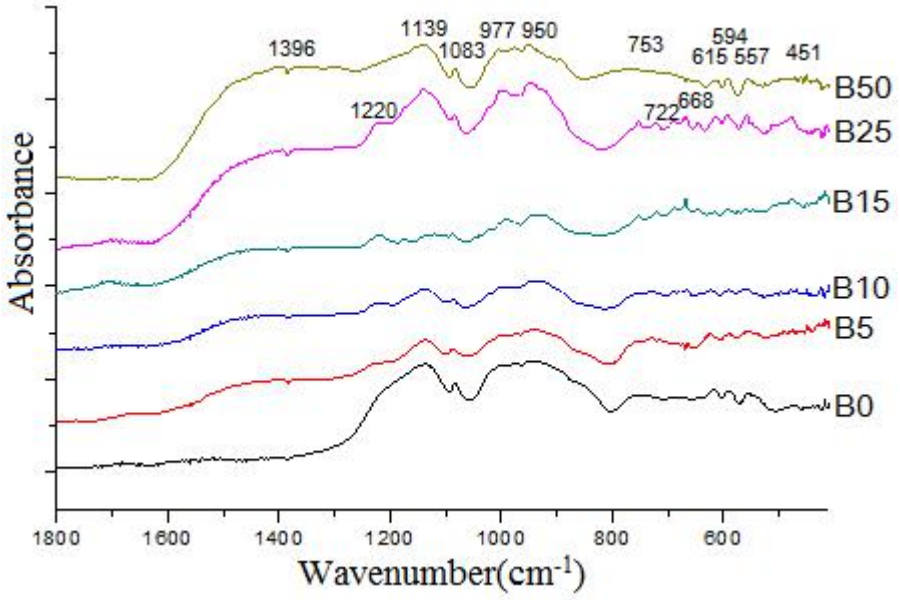


**Figure 4.3.5:** FTIR spectra of all boron-substituted fluorine-free glass ceramics (hold at 1100°C).

Figure 4.3.6 shows that the most intense absorption bands centred at 1098 $cm^{-1}$ and 1042 $cm^{-1}$ are attributed to the asymmetric stretching vibrations (P-O, $\nu_3$) of phosphate tetrahedral, while the symmetric stretching of phosphate ($\nu_1$) is located at 980 $cm^{-1}$ [161,165]. Two bands at 566 $cm^{-1}$ and 603 $cm^{-1}$ are attributed to the O-P-O bending of phosphate ($\nu_4$), whereas the band centred at 472 $cm^{-1}$ is caused by the phosphate bending ($\nu_2$) vibration [162]. It is clear that the incorporation of boron decreased significantly the absorption intensity of the peaks at 1098 $cm^{-1}$ and 735 $cm^{-1}$, implying that some of the phases might disappear due to the composition change. In addition, Al-O($AlO_4$) bonds were found to be present around 735 $cm^{-1}$ [141]. The peak at 1098$cm^{-1}$ also assigned for Si-O-Si stretching ($Q^3$) and 980$cm^{-1}$ for Si-O-[NBO] bands, the intensity of the band associated with Si-O-[NBO] generally decreased. The declination of the intensity of Si-O-[NBO] suggests that there was

more Si-O-Si as well as bridging-oxygens formed in the glass network.

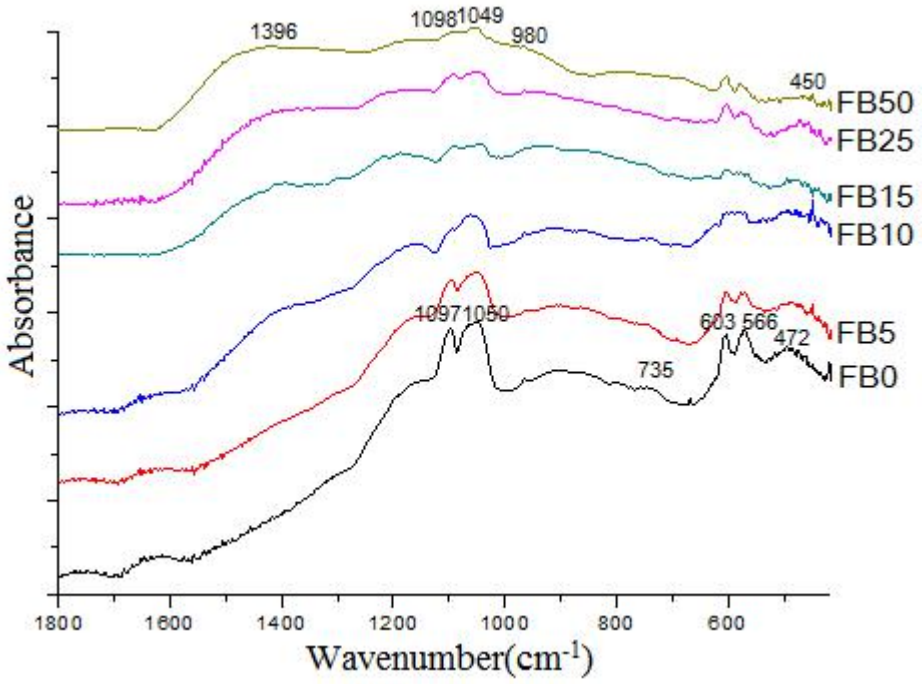


**Figure 4.3.6:** FTIR spectra of all boron-substituted fluorine-containing glass ceramics (hold at 1100°C).

The Raman spectra of boron-substituted glass ceramics are shown in Figure 4.3.7 and Figure 4.3.8. All the glasses were crystallised by heating the glass samples to above 1100°C for 1 hour followed by furnace cooling to room temperature.

There are a number of reviews of Raman scattering in solids, though the author referred to these works [166, 167]. A concise summary of the theory is presented below. An isolated $[PO_4]^{3-}$ has $T_d$ symmetry and 4 normal modes of vibration: $A_1$ ($\nu_1$) = 955 $cm^{-1}$, E ($\nu_2$) = 425 $cm^{-1}$, $T_2$ ($\nu_3$) = 1043 $cm^{-1}$, and $T_2$ ($\nu_4$) = 578 $cm^{-1}$, where the species-E vibrations are doubly degenerate and the $T_2$ vibrations are triply degenerate [168, 169]. The effects of the crystal field of the fluorapatite lattice on the internal vibrational modes may be understood by considering the phosphate site symmetry in

Table 4.3.1. The $T_d$ symmetry of a free tetrahedral $[PO_4]^{3-}$ ion is reduced to Cs in the crystal lattice. This symmetry change removes some of the degeneracies of the vibrational wave functions which would have characterised the free $[PO_4]^{3-}$ ion. The peak at 1120 $cm^{-1}$ is probably due to P-O stretching in units that may resemble the 3-dimensionally interconnected structure of $AlPO_4$ [170]. Generally, all glass ceramics exhibit similar Raman peaks, and one of the main differences is the difference in the intensity of the peaks.

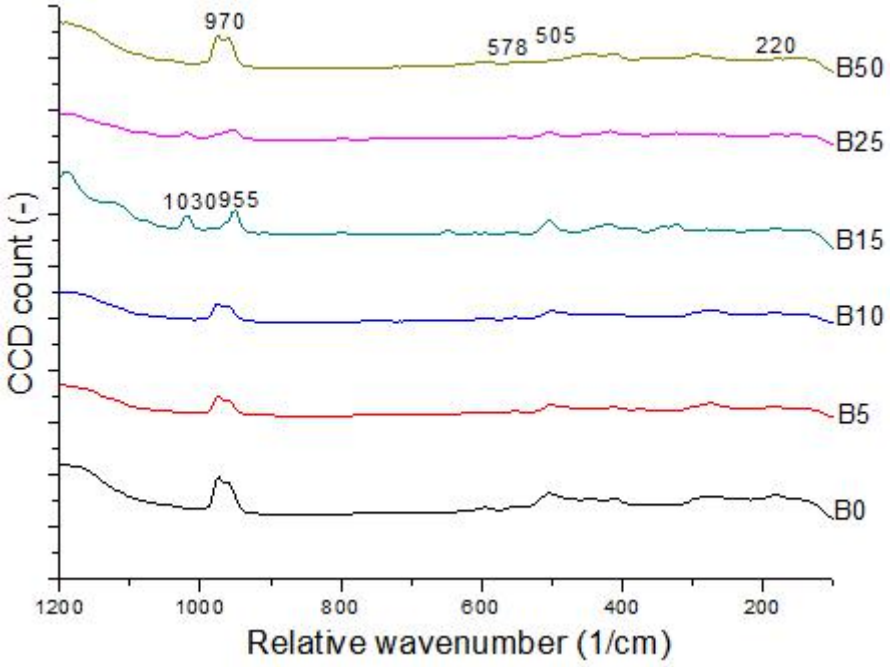


**Figure 4.3.7:** Raman spectra of boron-substituted fluorine-free glass ceramics (hold at 1100°C).

**Table 4.3.1:** Assignment of Raman peaks in fluorapatite from the literature.

| **Wavenumber ($cm^{-1}$)** | **Description** |
|---|---|
| 425 | $v_2$ ($PO_4$) bending vibration |
| 588 | $v_4$ （$PO_4$） bending vibration |
| 955 | $v_1$ ($PO_4$) symmetric stretching vibration |
| 1043 | $v_3$ ($PO_4$) anti-symmetric stretching vibration [166-169] |

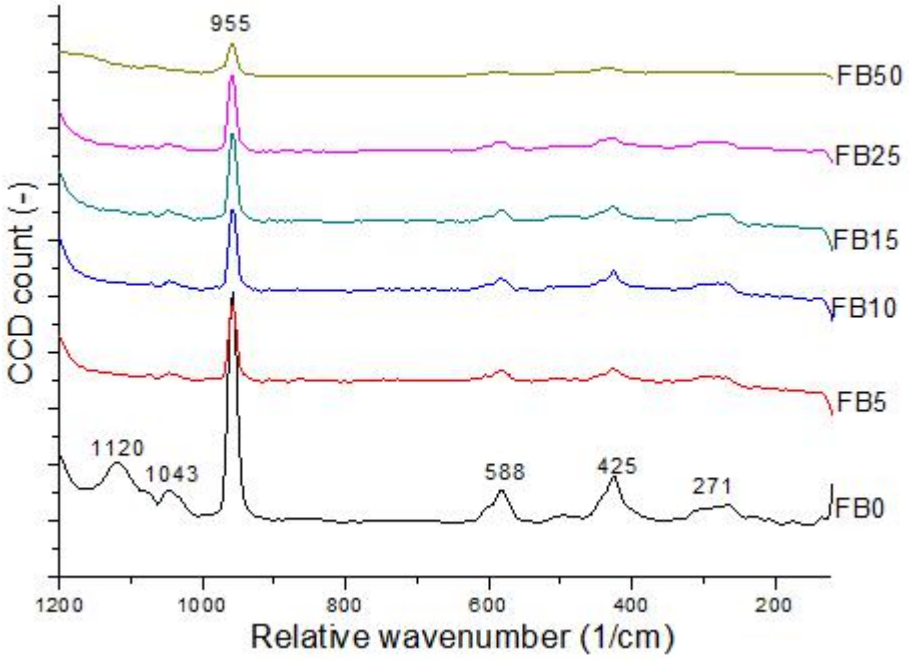


**Figure 4.3.8:** Raman spectra of boron-substituted fluorine-containing glass ceramics (hold at 1100°C).

### 4.3.3 MAS-NMR study of boron-substituted glass ceramics

#### 4.3.3.1 Spectroscopy of $^{29}$Si MAS-NMR

Table 4.3.3.1 and Figure 4.3.3.1 show the $^{29}$Si MAS-NMR spectra of boron-substituted fluorine-free glasses heat treated at 1100°C. The spectrum of boron-substituted glass ceramics exhibits several peaks at –87.8, -92.5, -97.6, -103.4, and -108.2 ppm, assigned by Klinowski et al [171, 172] to $Q^4$(4Al), $Q^4$(3Al), $Q^4$(2Al), $Q^4$(1Al), and $Q^4$(0Al) species, respectively.

**Table 4.3.3.1:** $^{29}Si$ MAS-NMR spectroscopy of boron-substituted fluorine-free glass ceramics heat treated at 1100°C.

| Glass | Boron substitution (mol %) | Chemical shift (ppm) |
|---|---|---|
| B0-GC | 0 | -105.9 ; -84.5 |
| B5-GC | 5 | -107.6 ; -84.2 |
| B10-GC | 10 | -106.1 ; -86.6 |
| B15-GC | 15 | -105.5 ; -87.6 |
| B25-GC | 25 | -101.8 ; -89.6 |
| B50-GC | 50 | -99.9 |

The peaks at around -87.8 ppm observed in the spectrum of boron-substituted fluorine-free glass ceramics are due to the $Q^4(4Al)$ species observed in the $^{29}Si$ and $^{27}Al$ MAS-NMR spectra of $CaAl_2Si_2O_8$. With the boron substitution for aluminium, the intensity of the peaks at around -103.4 ppm and -108.2 ppm increased, which is due to the $Q^4(1Al)$ and $Q^4(0Al)$ species, while the intensity of the peak at around -87.8 ppm decreased.

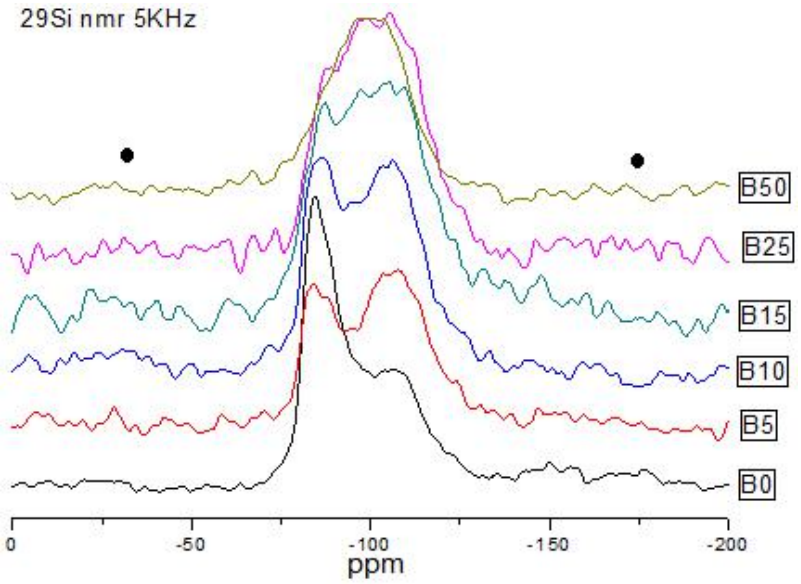


**Figure 4.3.3.1:** $^{29}Si$ MAS-NMR spectra of boron-substituted fluorine-free glass ceramics heat treated at 1100°C. The spinning bands are marked with ●.

Table 4.3.3.2 and Figure 4.3.3.2 show the $^{29}Si$ MAS-NMR spectra of boron-substituted fluorine-containing glasses heated at 1100°C. They are very similar to fluorine-free glass ceramics, where a dominant peak is present at around -87.8 ppm, associated with $Q^4(4Al)$ in the mullite phase ($Al_6Si_2O_{13}$). The peaks at around -103.4 ppm and -108.2 ppm mentioned above are also attributed to $Q^4(1Al)$ and $Q^4(0Al)$ species, the intensities of which are also increased by increasing boron substitution. It seems that significant overlapping occurs in the case of FB50 as it can be observed only one broad peak.

**Table 4.3.3.2:** $^{29}Si$ MAS-NMR spectroscopy of boron-substituted fluorine-containing glass ceramics heat treated at 1100°C.

| **Glass** | **Boron substitution (mol %)** | **Chemical shift (ppm)** |
|---|---|---|
| FB0-GC | 0 | -108.8 ; -86.0 |
| FB5-GC | 5 | -107.3 ; -86.6 |
| FB10-GC | 10 | -104.3 ; -88.3 |
| FB15-GC | 15 | -106.1 ; -89.6 |
| FB25-GC | 25 | -104.0 ; -89.6 |
| FB50-GC | 50 | -101.4 ; -89.6 |

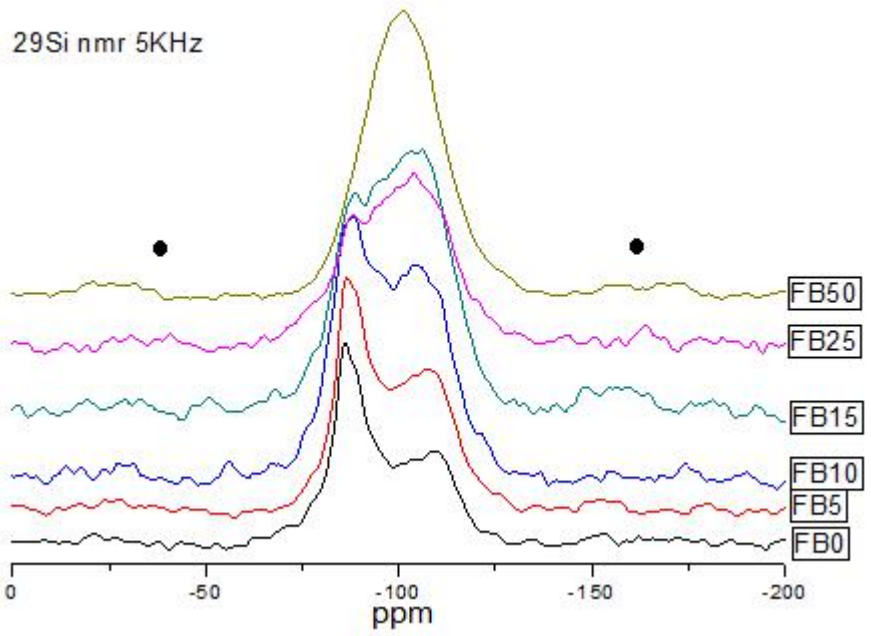


**Figure 4.3.3.2:** $^{29}$Si MAS-NMR spectra of boron-substituted fluorine-containing glass ceramics heat treated at 1100$^{o}$C. The spinning bands are marked with ●.

### 4.3.3.3 Spectroscopy of $^{27}$Al MAS-NMR

Tables 4.3.3.3 to 4.3.3.4 and Figures 4.3.3.3 to 4.3.3.4 show the $^{27}$Al MAS-NMR spectra of boron-substituted glasses heated at 1100$^{o}$C. All the spectra of the heat-treated samples exhibit an overlapping peak region between 57 ppm and 63 ppm, assigned to Al(IV). The peak around 50 ppm for all glass ceramics, due to 4-fold coordinated Al(V), and Al(VI) respectively, might also be present but difficult to conclude, as there is no apparent peak in the spectra. In boron-substituted fluorine-free glass ceramics (Figure 4.3.3.3), Al(VI) is present at about -10 ppm, related possibly to anorthite ($CaAl_2Si_2O_8$). The peak just before 50 ppm is most likely due to the presence of $AlPO_4$ in the glass ceramic. This seems to be more intense for B0,B5

and B10. Then in the case of B15 and above, a broader peak is observed (also this means that for some reason the degree of crystallinity is lower) where it can still be observed a shoulder or perhaps the same peak only broader. Generally, the peak becomes very broad in the case of B50 with a very sharp aluminium VI associated with anorthite formation. In boron-substituted fluorine-containing glass ceramics (Figure 4.3.3.4), it is shown very asymmetric peaks which are similar with fluorine-free samples, Al(VI), in which the $AlO_6$ are cross-linked by $SiO_4$ and $AlO_4$ tetrahedral, is found at around 0 ppm, which is associated with the formation of mullite. $AlPO_4$ is observed at around 39 ppm in all FB samples which seems to be more intense for FB0,FB5 and FB10.

**Table 4.3.3.3:** $^{27}Al$ MAS-NMR spectroscopy of boron-substituted fluorine-free glass ceramics heat treated at 1100$^{o}$C.

| **Glass** | **Boron substitution (mol %)** | **Chemical shift (ppm)** |
|---|---|---|
| B0-GC | 0 | -9.9 ; 39.9 ; 53.3 |
| B5-GC | 5 | -9.7 ; 40.4 ; 53.7 |
| B10-GC | 10 | -9.7 ; 41.0 ; 53.1 |
| B15-GC | 15 | -9.6 ; 51.0 |
| B25-GC | 25 | -9.6 ; 50.0 |
| B50-GC | 50 | -9.6 ; 45.5 |

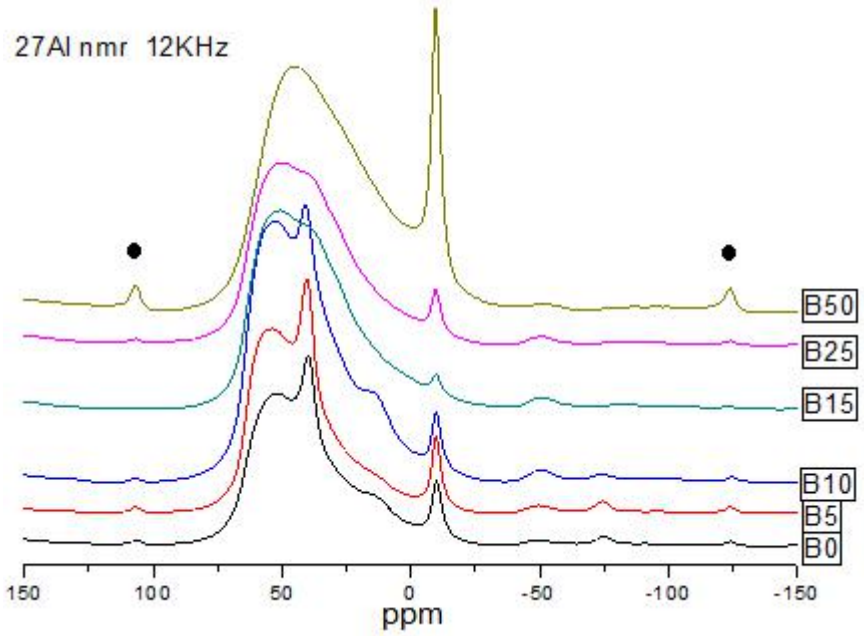


**Figure 4.3.3.3:** $^{27}$Al MAS-NMR spectroscopy of boron-substituted fluorine-free glass ceramics heat treated at 1100$^{o}$C. The spinning bands are marked with ●.

**Table 4.3.3.4:** $^{27}$Al MAS-NMR spectroscopy of boron-substituted fluorine-containing glass ceramics heat treated at 1100$^{o}$C.

| **Glass** | **Boron substitution (mol %)** | **Chemical shift (ppm)** |
|---|---|---|
| FB0-GC | 0 | -0.8 ; 39.9; 55 |
| FB5-GC | 5 | -0.4 ;39.7; 55 |
| FB10-GC | 10 | -0.4 ; 39.8; 55 |
| FB15-GC | 15 | -0.4 ; 43 |
| FB25-GC | 25 | 2.4 ; 48 |
| FB50-GC | 50 | 50 |

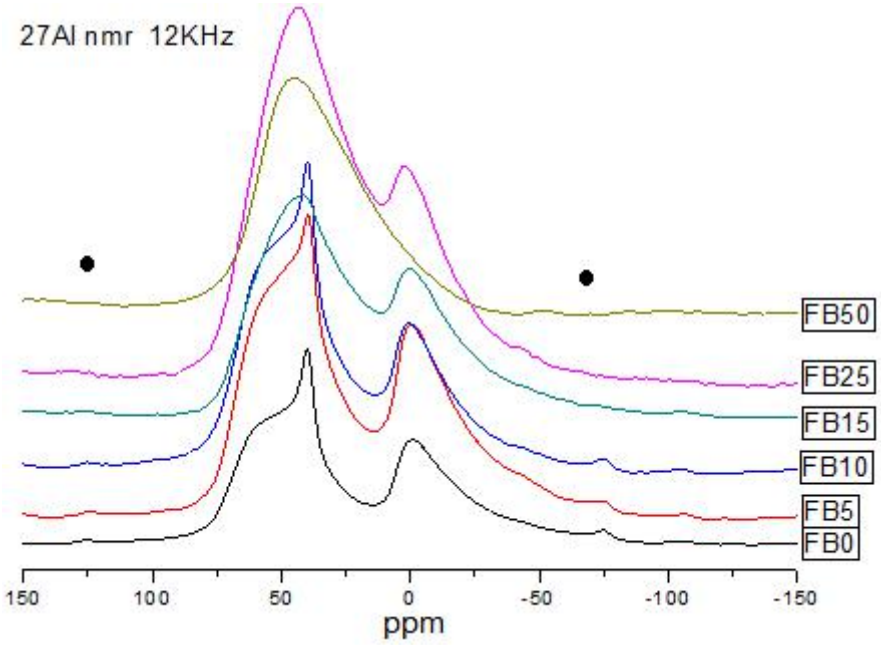


**Figure4.3.3.4:**$^{27}$Al MAS-NMR spectroscopy of boron-substituted fluorine-containing glass ceramics heat treated at 1100$^{o}$C. The spinning bands are marked with ●.

### 4.3.3.4 Spectroscopy of $^{31}$P MAS-NMR

Tables 4.3.3.5 to 4.3.3.6 and Figures 4.3.3.5 to 4.3.3.6 show the $^{31}$P MAS-NMR spectra of boron-substituted glasses after heat treatment at 1100$^{o}$C. The spectrum of boron-substituted crystallised glasses exhibits 3 peaks at about 2.4, -3, and -28 ppm, as seen in Figures 4.3.3.5 and 4.3.3.6, which are assigned to orthophosphate, metaphosphate, or polyphosphate glass residue, which are crystallised tricalcium phosphate (-3ppm) in boron-substituted fluorine-free glass ceramics and fluorapatite (2.4 ppm) in boron-substitited fluorine-containing glass ceramics and a minor phase of $AlPO_4$ (-28 ppm) , respectively [163]. It seems that $AlPO_4$ is present in B0-B15. A little bit in B25 but none at all in B50. This is interesting to notice that in FB50 the rest of the peaks correspond to orthophosphates in fluorapatite. It is agree with the

data in XRD data that FB50 lacks most of mullite.

**Table 4.3.3.5:** $^{31}$P MAS-NMR spectroscopy of boron-substituted fluorine-free glass ceramics heat treated at 1100$^{o}$C.

| Glass | Boron substitution (mol %) | Chemical shift (ppm) |
|---|---|---|
| B0-GC | 0 | -25.6 ; -2.7 |
| B5-GC | 5 | -27.7 ; -3.0 |
| B10-GC | 10 | -27.6 ; -3.1 |
| B15-GC | 15 | -21.4 ; -2.8 |
| B25-GC | 25 | -23.5 ; -3.1 |
| B50-GC | 50 | -3.0 |

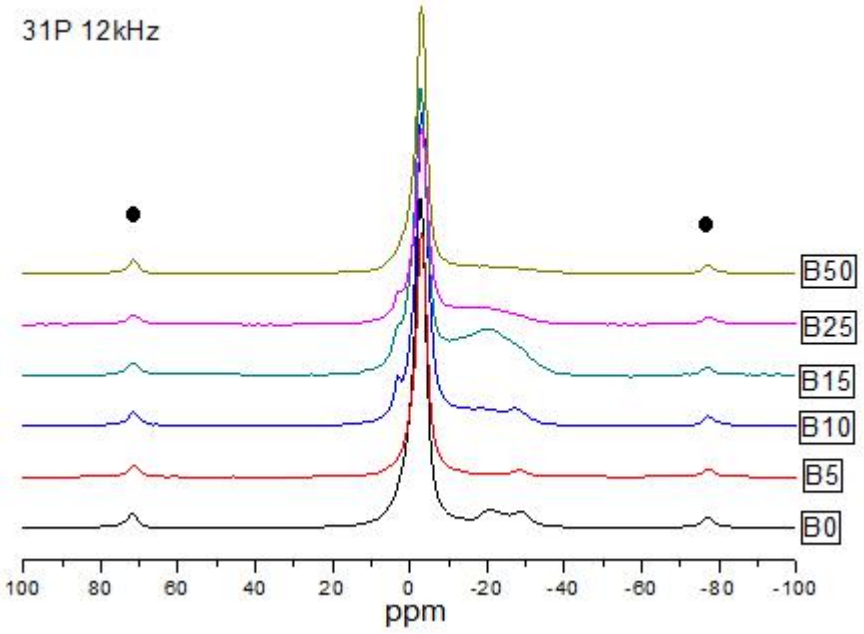


**Figure 4.3.3.5:** $^{31}$P MAS-NMR spectroscopy of boron-substituted fluorine-free glass ceramics heat treated at 1100$^{o}$C. The spinning bands are marked with ●.

**Table 4.3.3.6:** $^{31}P$ MAS-NMR spectroscopy of boron-substituted fluorine-containing glass ceramics heat treated at 1100°C.

| Glass | Boron substitution (mol %) | Chemical shift (ppm) |
|---|---|---|
| FB0-GC | 0 | -29.6 ; 2.3 |
| FB5-GC | 5 | -26.6 ; 2.3 |
| FB10-GC | 10 | -26.6 ; 2.3 |
| FB15-GC | 15 | -23.1 ; 2.4 |
| FB25-GC | 25 | -24.2 ; 2.4 |
| FB50-GC | 50 | -20.7 ; 2.4 |

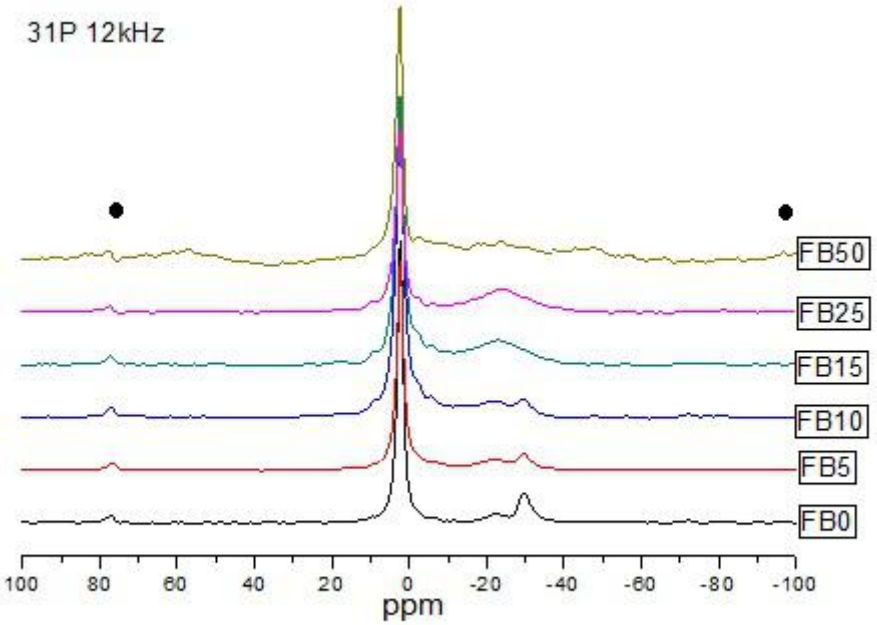


**Figure 4.3.3.6:** $^{31}P$ MAS-NMR spectroscopy of boron-substituted fluorine-containing glass ceramics heat treated at 1100°C. The spinning bands are marked with ●.

### 4.3.3.5 Spectroscopy of $^{11}B$ MAS-NMR

Tables 4.3.3.7 to 4.3.3.8 and Figures 4.3.3.7 to 4.3.3.8 show the $^{11}B$ MAS-NMR spectra of boron-substituted glasses after heat treatment at 1100°C. The spectrum of

boron-substituted fluorine-free and fluorine-containing crystallised glasses exhibits 2 similar peaks at around 0.5 and 9.5 ppm in Figures 4.3.3.7 and 4.3.3.8, which are assigned to the $BO_4$ group and $BO_3$ group, respectively.

**Table 4.3.3.7:** $^{11}B$ MAS-NMR spectroscopy of boron-substituted fluorine-free glass ceramics heat treated at 1100°C.

| Glass | Boron substitution (mol %) | Chemical shift (ppm) |
|---|---|---|
| B0-GC | 0 | ———— |
| B5-GC | 5 | 0.8 ; 9.8 |
| B10-GC | 10 | 0.5 ; 9.2 |
| B15-GC | 15 | 0.8 ; 9.6 |
| B25-GC | 25 | 0.4 ; 8.9 |
| B50-GC | 50 | 0 ; 7.3 |

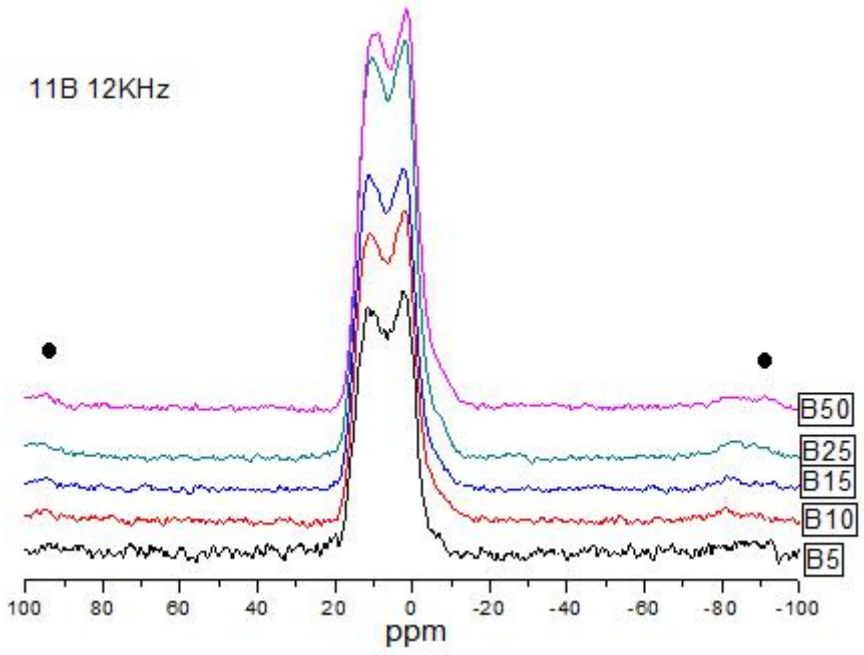


**Figure 4.3.3.7:** $^{11}B$ MAS-NMR spectroscopy of boron-substituted fluorine-free glass ceramics heat treated at 1100°C. The spinning bands are marked with ●.

**Table 4.3.3.8:** $^{11}B$ MAS-NMR spectroscopy of boron-substituted fluorine-containing glass ceramics heat treated at 1100°C.

| Glass | Boron substitution (mol %) | Chemical shift (ppm) |
|---|---|---|
| FB0-GC | 0 | ———— |
| FB5-GC | 5 | 2.0 ; 7.4 |
| FB10-GC | 10 | 1.3 ; 7.2 |
| FB15-GC | 15 | 1.5 ; 6.7 |
| FB25-GC | 25 | 1.6 ; 7.0 |
| FB50-GC | 50 | -0.3 ; 7.9 |

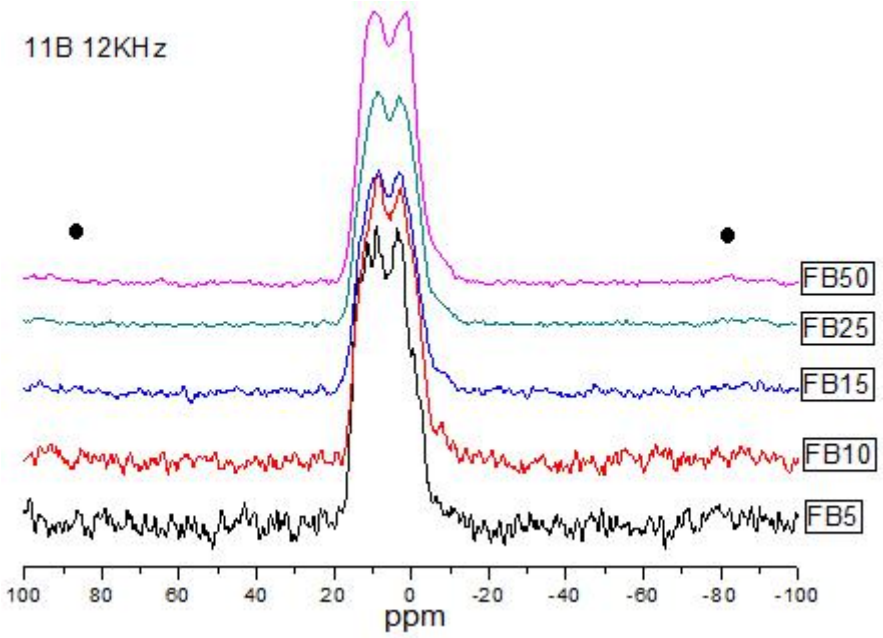


**Figure 4.3.3.8:** $^{11}B$ MAS-NMR spectroscopy of boron-substituted fluorine-containing glass ceramics heat treated at 1100°C. The spinning bands are marked with ●.

### 4.3.3.6 Spectroscopy of $^{19}F$ MAS-NMR

Table 4.3.3.9 and Figure 4.3.3.9 show the $^{19}F$ MAS-NMR spectra of boron-substituted fluorine-containing glasses heat treated at 1100°C. A sharp peak at about -103 ppm,

assigned to F-Ca(3) in crystalline FAP, is observed in all spectra of boron-substituted glass ceramics. With increasing boron substitution, another peak at -110 ppm decreased in FB0 to FB10 glass ceramics, which is thought to be related to an Al-F-Ca(3) phase, and the peak at -110 ppm is not present from FB15 and above and it suggested the peak at -110 ppm corresponds to Al-F-Ca species in residual glass.

**Table 4.3.3.9:** $^{19}F$ MAS-NMR spectroscopy of boron-substituted fluorine-containing glass ceramics heat treated at 1100$^{o}$C.

| Glass | Boron substitution (mol %) | Chemical shift (ppm) |
|---|---|---|
| FB0-GC | 0 | -109.9 ; -102.8 |
| FB5-GC | 5 | -110.3 ; -102.9 |
| FB10-GC | 10 | -110.1 ; -102.7 |
| FB15-GC | 15 | -102.7 |
| FB25-GC | 25 | -102.8 |
| FB50-GC | 50 | -103.0 |

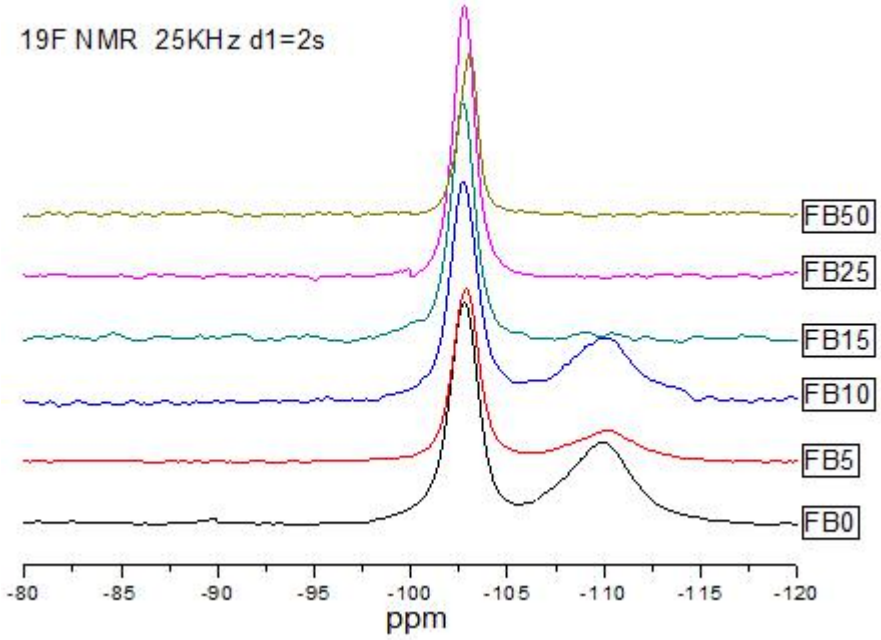


**Figure 4.3.3.9:** $^{19}F$ MAS-NMR spectroscopy of boron-substituted fluorine-containing glass ceramics heat treated at 1100$^{o}$C.

### 4.3.4 ESEM and EDX studies of boron-substituted glass ceramics

Figures 4.3.4.1 to 4.3.4.7 show the SEM micrograph and EDX analysis of all boron-substituted glasses heat treated at 1100$^{o}$C with a 1-hour hold. The SEM micrograph shows the morphology of each glass ceramic. EDX analysis was conducted on the glass ceramics given the real composition of the glass ceramics after synthesis.

Figure 4.3.4.1 shows an SEM micrograph and EDX analysis for the B0 glass ceramic. The surface in the micrograph exhibits needle like phase morphology (calcium phosphate) and the atomic fraction of O, Al, Si, P, and Ca for point A, which is suggested by the calcium phosphate phase in the ranges of 43–44at %, 5–6at %, 2–3at %, 13–14at %, and 35–36at %, respectively. Point B indicates a matrix phase, the atomic fraction of O, Al, Si, P, and Ca is in the ranges of 56–57at %, 10–11at %, 18–19at %, 6–7at %, and 9–10at %, respectively.

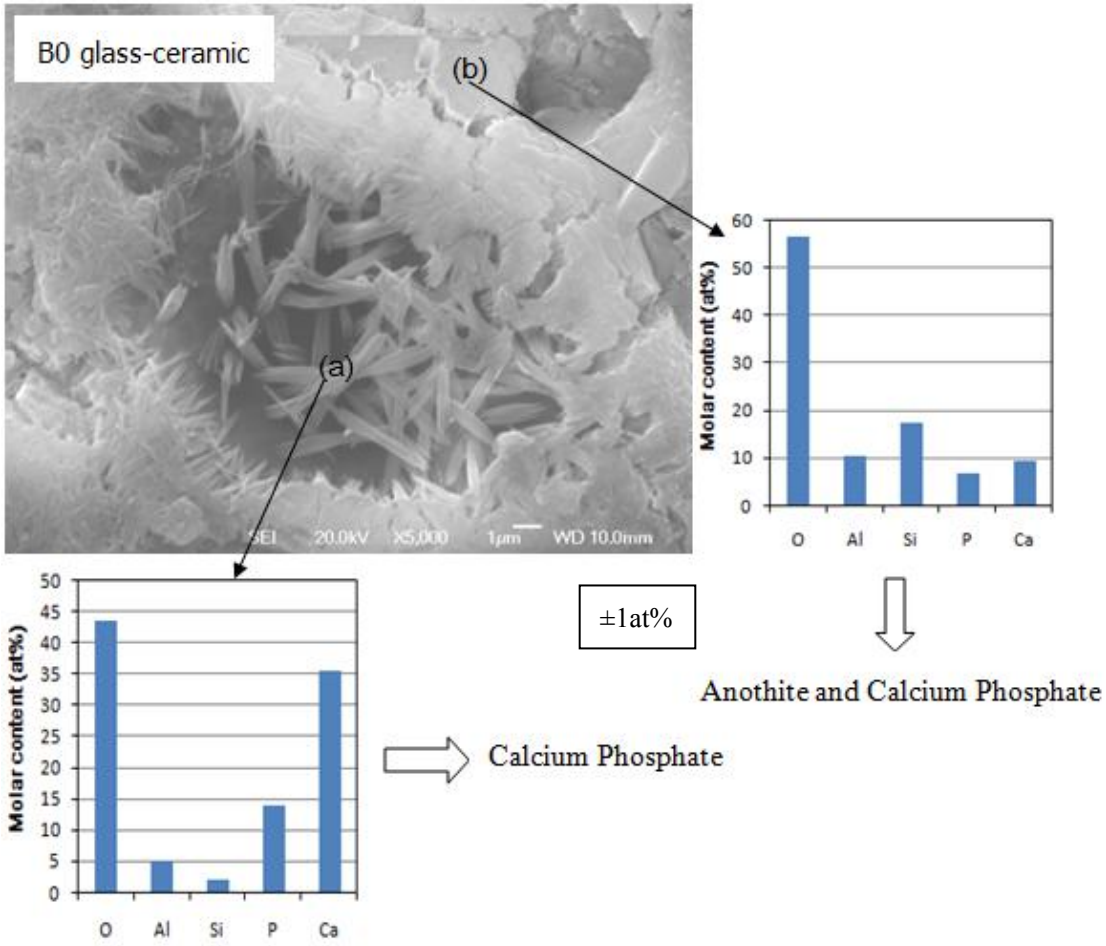


**Figure 4.3.4.1**: SEM and EDX analysis of B0 glass ceramic heat treated at 1100°C.

Figure 4.3.4.2 shows the SEM micrograph and EDX analysis for the B2.5 and B5 glass ceramics. The surface in the micrograph shows very similar phase morphology to B0: needle-like (calcium phosphate). The atomic fraction of O, Al, Si, P, and Ca for point A is 57–58at %, 2–3at %, 2–3at %, 13–14at %, and 24–25at %, respectively. Region B, which is suggested as a calcium phosphate and anothite mixed phase, is in the ranges of 58–59at %, 9–11at %, 9–10at %, 8–9at %, and 13–14at %, respectively. In region A, the needle-like morphology is non-oriented.

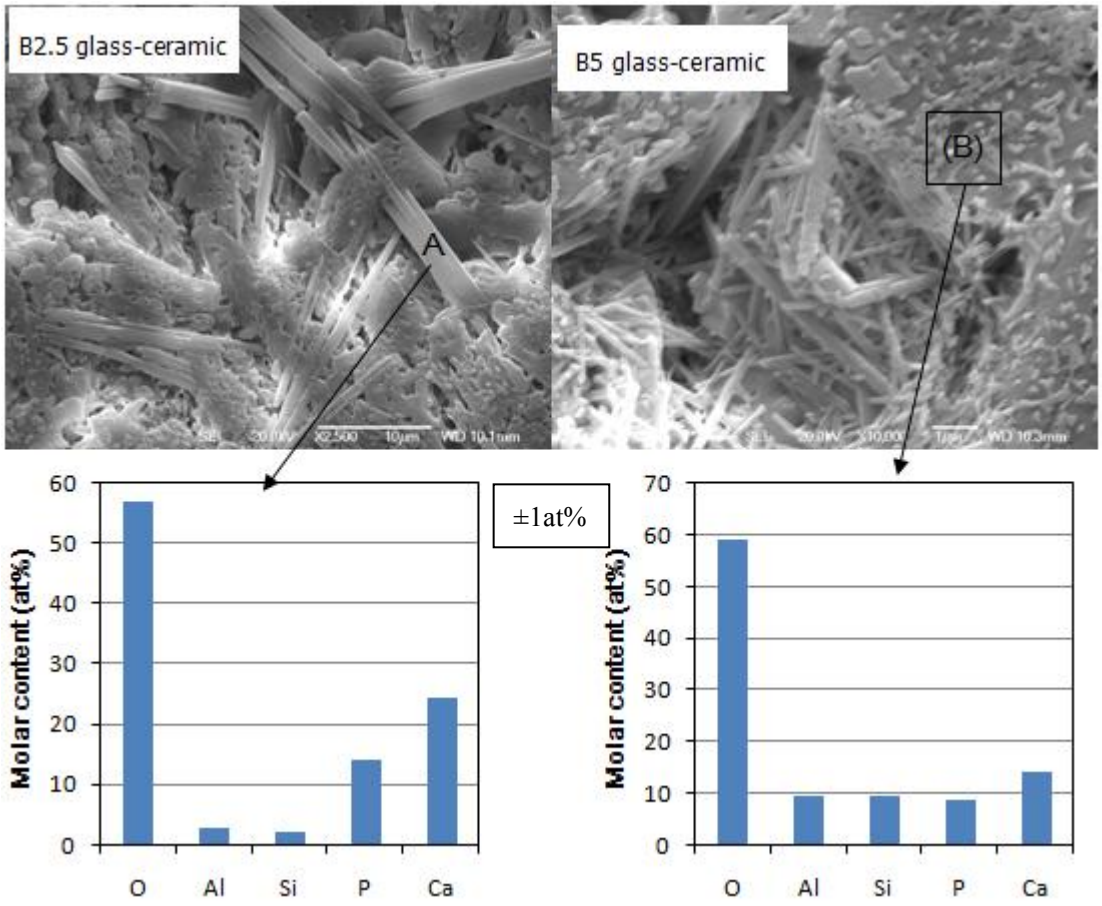


**Figure 4.3.4.2:** SEM and EDX analysis of B2.5 and B5 glass ceramic heat treated at 1100$^{o}$C.

Figure 4.3.4.3 shows the SEM micrograph and EDX analysis of B7.5 to B15 glass ceramics. It is shown that the single needle-like phase is combined together, which is interlocked and non-oriented, and the atomic fraction of O, Al, Si, P, and Ca for regions A and B, which are suggested as the calcium phosphate main phase, are in the ranges of 46–47at %, 7–8at %, 7–8at %, 9–10at %, and 27–28at % to 42–43at %, 14–15at %, 12–13at %, 9–10at %, and 22–23at %, respectively.

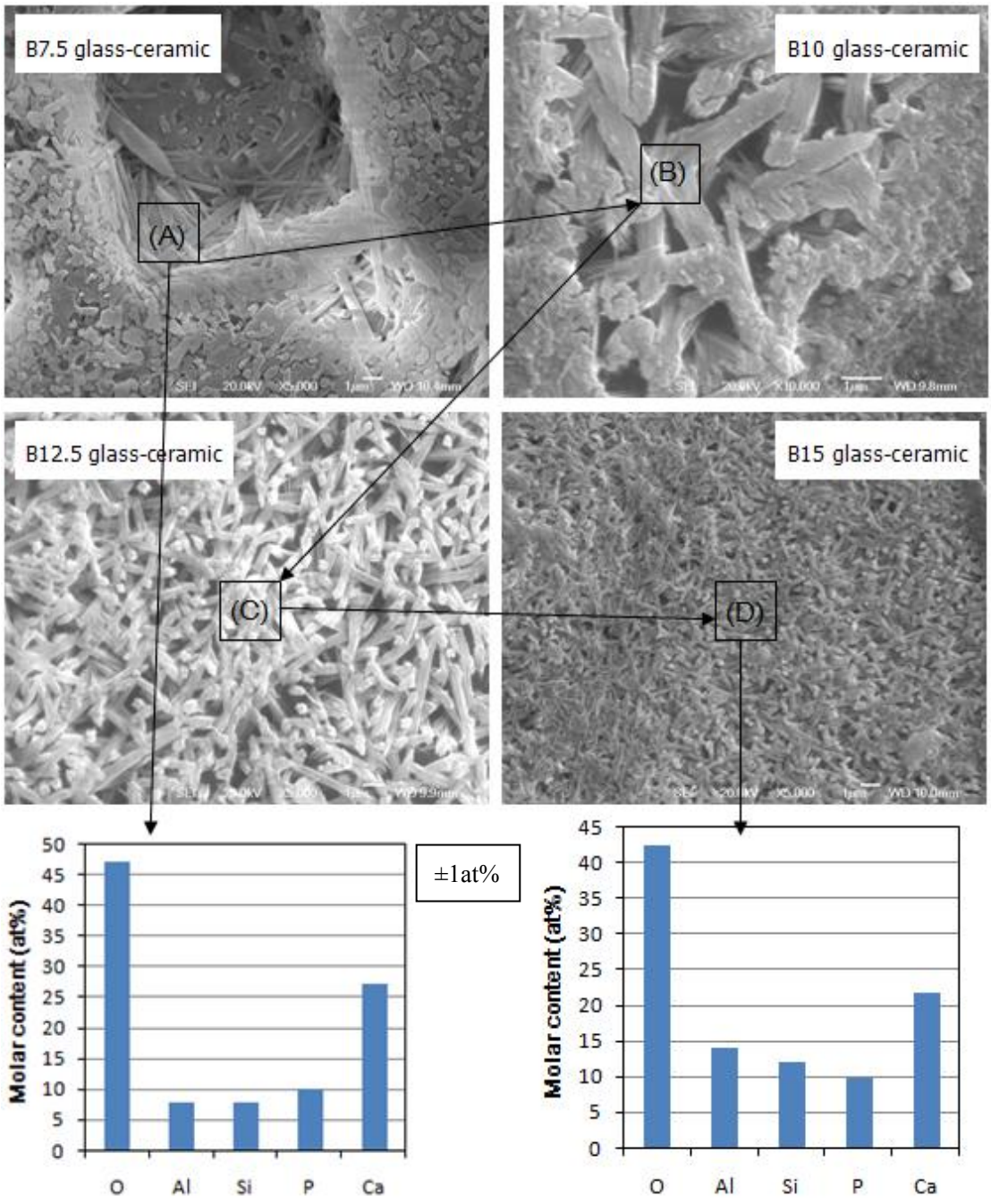


**Figure 4.3.4.3:** SEM and EDX analysis of B7.5-B15 glass-ceramics heat treated at 1100°C.

Figure 4.3.4.4 shows the SEM micrograph and EDX analysis for B25 and B50 glass ceramics. In these, a similar needle-like phase is combined together. Regions A and B show a calcium phosphate main phase and a silicate aluminium main phase,

respectively. In addition, 2–3% and 6–7% boron can be detected in B25 and B50 glass ceramics, respectively.

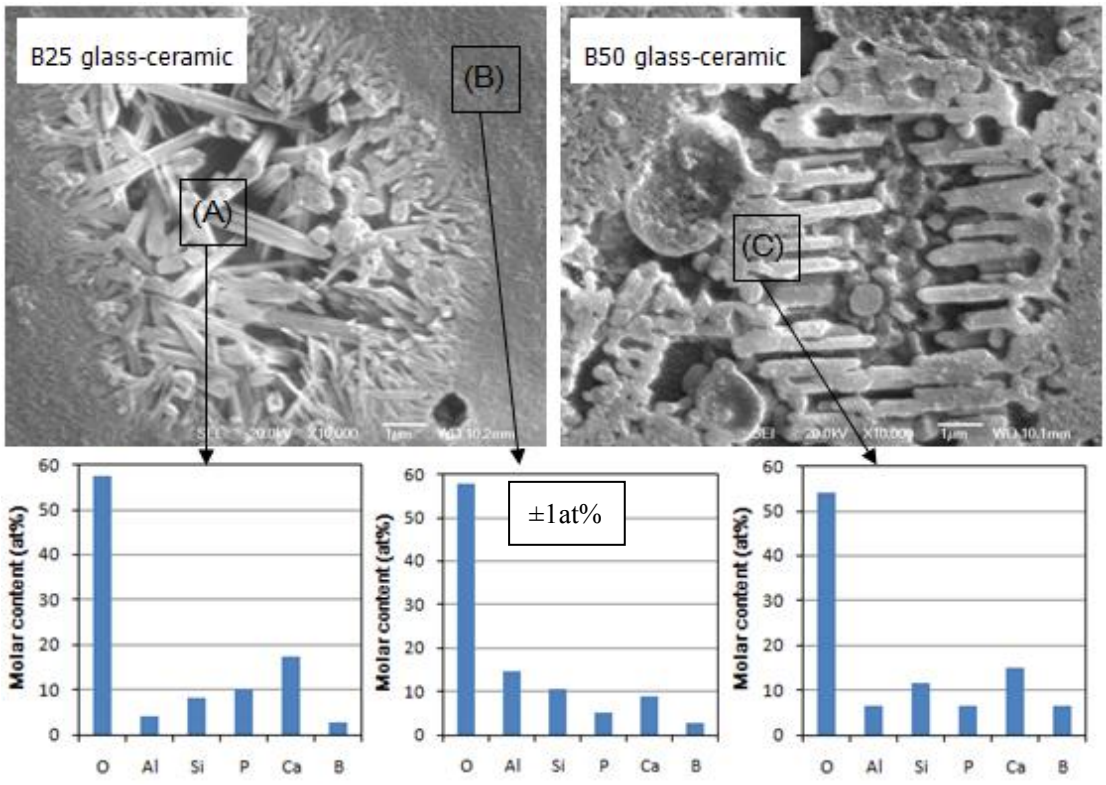


**Figure 4.3.4.4:** SEM and EDX analysis of B25 and B50 glass-ceramics heat treated at 1100$^{o}$C.

Figure 4.3.4.5 shows an SEM micrograph and EDX analysis for FB0 glass ceramic. The surface in the micrograph above exhibits a calcium rich phase and an aluminium rich phase respectively, and the morphology of calcium rich phase is needle-like (fluorapatite). The atomic fraction of O, Al, Si, F, P, and Ca for region A, which is suggested of a mullite and fluorapatite mixed phase, is in the range of 36–37at %, 11–12at %, 8–9at %, 19–20at %, 7–8at %, and 16–17at %, respectively.

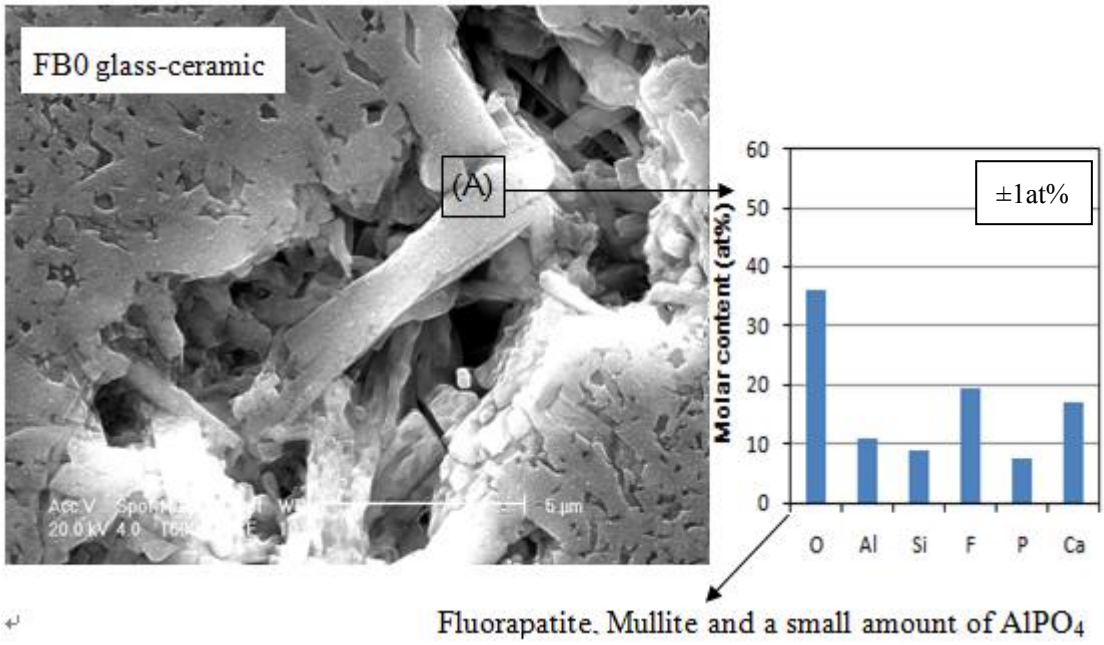


**Figure 4.3.4.5:** SEM and EDX analysis of FB0 glass-ceramic heat treated at 1100°C.

Figure 4.3.4.6 shows an SEM micrograph and EDX analysis of FB2.5 to FB10 glass ceramics. An interlocked micrograph is shown, as opposed to the needle-like (fluorapatite) phase. The atomic fraction of O, Al, Si, F, P, and Ca for region A is in the ranges of 48–49at %, 12–13at %, 11–12at %, 4–5at %, 8–9at %, and 13–14at %, respectively. The atomic fraction of O, Al, Si, F, P, and Ca for region B is in the ranges of 36–37at %, 10–11at %, 8–9at %, 19–20at %, 7–8at %, and 16–17at %, respectively. The atomic fraction of O, Al, Si, F, P, and Ca for region C, which suggests an aluminium and silicate main phase, is in the ranges of 50–51at %, 20–21at %, 16–17at %, 2–3at %, 3–4at %, and 6–7at %, respectively. The atomic fraction of O, Al, Si, F, P, and Ca for region D, which is related to the fluorapate phase, is in the ranges of 54–55at %, 1–2at %, 1–2at %, 7–8at %, 13–14at %, and 21–22at %, respectively.

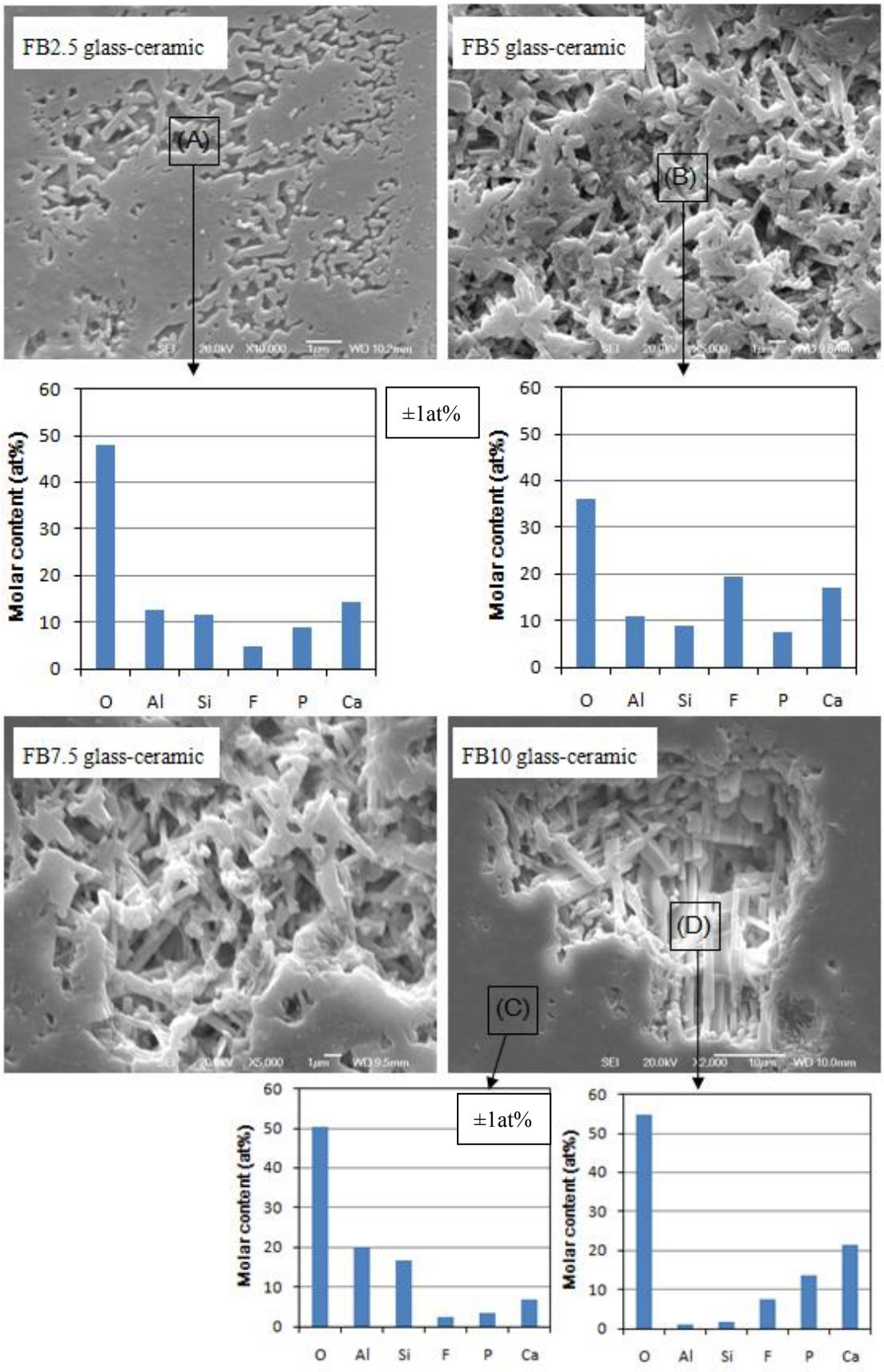


**Figure 4.3.4.6:** SEM and EDX analysis of FB2.5-Fb10 glass-ceramics heat treated at 1100$^{o}$C.

It is observed in Figure 4.3.4.7 by SEM mapping and EDX analysis that the light areas are related to a calcium, phosphorus, and fluorine main phase; on the other hand, the dark areas are related to an aluminium and silicate main phase.

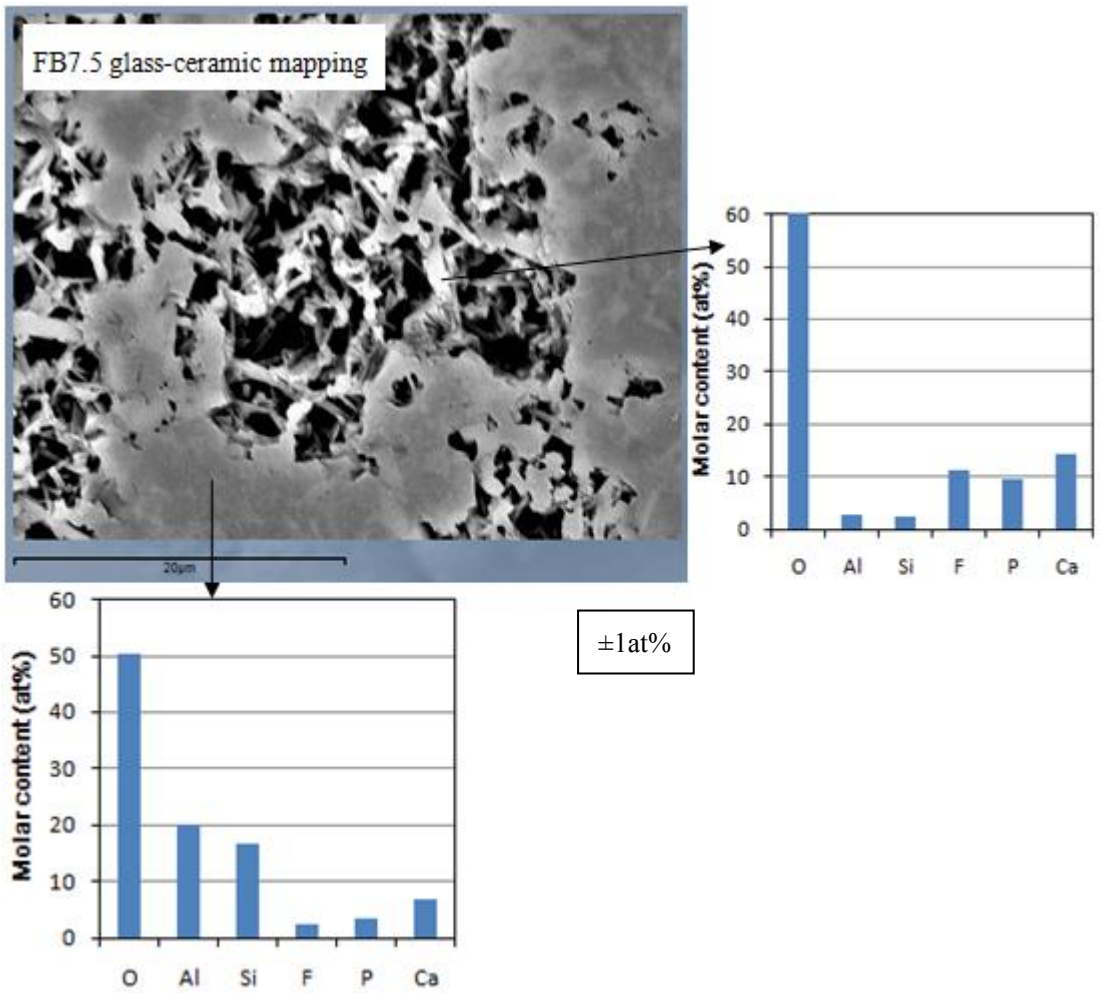


**Figure 4.3.4.7:** SEM mapping and EDX analysis of FB7.5 glass-ceramic heat treated at 1100°C.

Figure 4.3.4.8 shows the SEM micrograph and EDX analysis of FB12.5 to FB50 glass ceramics. In regions A, B, C, and E, a similar needle-like phase, which is a calcium, phosphorous, and fluorine main phase, is observed. Region D shows an aluminium silicate main phase. In addition, 2–3% and 6–7% boron can be detected in F25 and

FB50 glass ceramics, respectively.

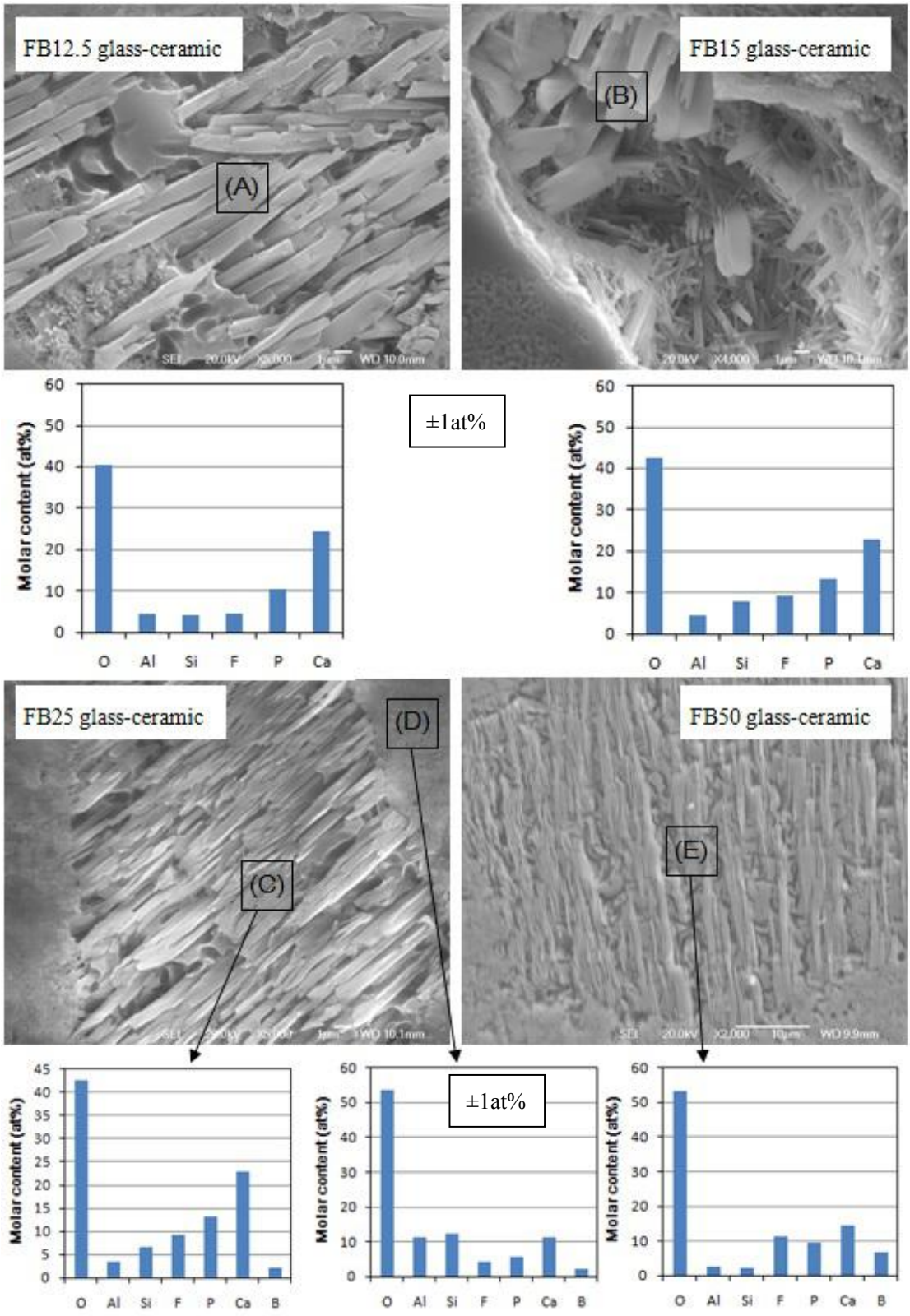


**Figure 4.3.4.8:** SEM mapping and EDX analysis of FB12.5 to FB50 glass-ceramics heat treated at 1100°C.

# CHAPTER 5 DISCUSSION

## 5.1 Effects of boron substitution on glasses

### 5.1.1 Density and Oxygen Density

The measured density values decreased with increasing the molar content of boron from 2.791 g/cm$^3$ of B0 glass to 2.674 g/cm$^3$ of B50 glass, as shown in Figure 4.1.1. The substitution of boron for aluminium decreases the density of glass because boron has a lighter atomic weight (AW = 10.81) than that of aluminium (AW = 26.98), and the shorter ionic radius for B(III) 4-coordinate, tetrahedral is 25 pm and B(III) 6-coordinate (octahedral) is 41 pm compared to the ionic radius of Al(III) 4-coordinate (tetrahedral), which is 53 pm, and Al(III) 6-coordinate (octahedral), which is 67.5 pm. Since the atomic weight of boron and aluminium are significantly different, the linear decrease in density indicates that the atomic weight change has a more significant effect on the density values than the ionic radius. In the glass network, the oxygen density reflects the degree of packing of the atoms. There is a slight floating of the calculated oxygen density in boron-substituted, fluorine-free glasses, suggesting that boron substitution for aluminium results in a very similar glass network. On the other hand, with boron-substituted, fluorine-containing glasses, it is interesting to mention that similar effects on density are expected due to the lighter atomic weight and smaller ionic radius of boron, which can been observed in Figure 4.1.3. The substitution of boron for aluminium results in a linear decrease of density from 2.768

g/cm$^3$ of FB0 glass to 2.695 g/cm$^3$ of FB50 glass. However, the oxygen density slightly increases from 0.0709 mol/cm3 of FB0 to 0.0721 mol/cm3 of FB50 glass. It is possible that with or without fluorine in the glass, the atomic weight variation has a stronger influence than the difference in the ionic radius on the density of the glass. Whereas there is a slightly linear increase in oxygen density values with boron-substituted, fluorine-containing glasses, indicating a closer-packed glass network, it has been reported [174] that in a similar glass composition with 25, 50, 75 and 100% magnesium substitution for calcium ($4.5SiO_2$- $3Al_2O_3$-$1.5P_2O_5$-3MgO- $2MgF_2$) the density of the glasses shows a linear decrease, as Mg has a smaller atomic weight (AW = 24.3) and ionic radius (0.086 nm) than that of Ca, and the oxygen density of the glasses shows a slight linear increase, suggesting a closer-packed glass network [42]. In addition, the magnesium plays a role as a glass modifier and boron as a glass former in the glass. It is therefore suggested that smaller atoms lead to a more densely packed glass network.

### 5.1.2 FTIR and Raman Spectroscopy

Figures 4.1.6 to 4.1.7 show the FTIR spectra of boron-substituted, fluorine-free and fluorine-containing glasses. All spectra exhibit four absorption regions. The first region, between 800 and 1400 cm$^{-1}$, is assigned to the Si-O(s) stretching vibrations with a different number of bridging oxygen atoms and P-O bonds; the second region, between 620 and 800 cm$^{-1}$, is due to the stretching Al-O vibration bonds, with

aluminium in fourfold coordination; the third region, between 530 and 620 $cm^{-1}$, is associated with P-O bending and Si-O-Al linkages; and the fourth region of 400–530 $cm^{-1}$ corresponds to Si-O-Si bending vibrations [138-143]. In addition, in all boron-substituted glasses, there is a new broad absorption in the absorption band that can be seen in the 1200–1600 $cm^{-1}$ region that consists of overlapping contributions of the Si-O-Si and B-O-B vibration modes.

$B_2O_3$ is a glass former that could exist in the glass network with oxygen to form the triangular boron–oxygen units (boroxol rings). With the presence of other glass formers and modifiers, a part of boron can transform into tetrahedral coordination [175]. $SiO_2$ is also a glass former in the glass network with tetrahedral $[SiO_{4/2}]^0$ units, but the addition of CaO modifiers can break the linkages of Si–O. The lack of sharp features in the FTIR spectra indicates a disorder in the silicate network with a wide distribution of $Q^n$ units in the glasses. The results of depolymerisation in the formation of orthosilicates, pyrosilicates and metasilicates in the order $[SiO_4]^{4-}$, $[SiO_{1/2}O_3]^{3-}$, $[SiO_{2/2}O_2]^{2-}$, $[SiO_{3/2}O]^-$ and $[SiO_4/2]^0$, are designated as $Q^0$, $Q^1$, $Q^2$, $Q^3$ and $Q^4$ with the region of 850, 900, 950, 1100, and 1200 $cm^{-1}$, respectively [176]. When Si is substituted by an Al atom, the values are shifted to lower wave numbers as a consequence of the weaker Al-O bond [141]. As a strong glass former, $P_2O_5$ exists in the glass network as the $PO_4$ structural units. By bridging with oxygens, the $PO_4$ tetrahedrals are linked together with covalent bonding in chains or rings [177]. CaO acts as a modifier; generally, $Ca^{2+}$ ions occupy the interstitial positions while the oxygens of these oxides break the local symmetry and introduce coordinate defects in

the glass [178]. Early studies[179,180] showed that the aluminium ions occupy both tetrahedral sites with $AlO_4$ (viz., substitutional or network-forming positions) and octahedral sites with $AlO_6$ (viz., interstitial or network modifiers) structural unit in mechanisms:

$2Al_2O_3 \rightarrow [Al^{3+}]O + 3\ [AlO_{4/2}]$

The $AlO_4$ tetrahedrons may enter the glass network and alternate with $PO_4/BO_4$ tetrahedrons, as indicated below:

$Al_2O_3 + P_2O_5 \rightarrow 2\ [AlO_{4/2}]^- + 2\ [PO_{4/2}]^+$

$Al_2O_3 + B_2O_3 \rightarrow 2[AlO_{4/2}]^- + 2\ [BO_{4/2}]^-$

When $Al_2O_3$ concentrations is high, the dominate structure of aluminium ions is $AlO_4$ structural units whereas for low $Al_2O_3$ concentrations, the dominates structure change to $AlO_6$ [181, 182], e.g. a possible structural of $Al^{3+}$ in the $SiO_2$–$Al_2O_3$-$P_2O_5$–CaO-$B_2O_3$-based glass network is illustrated in Figure 5.1.1.

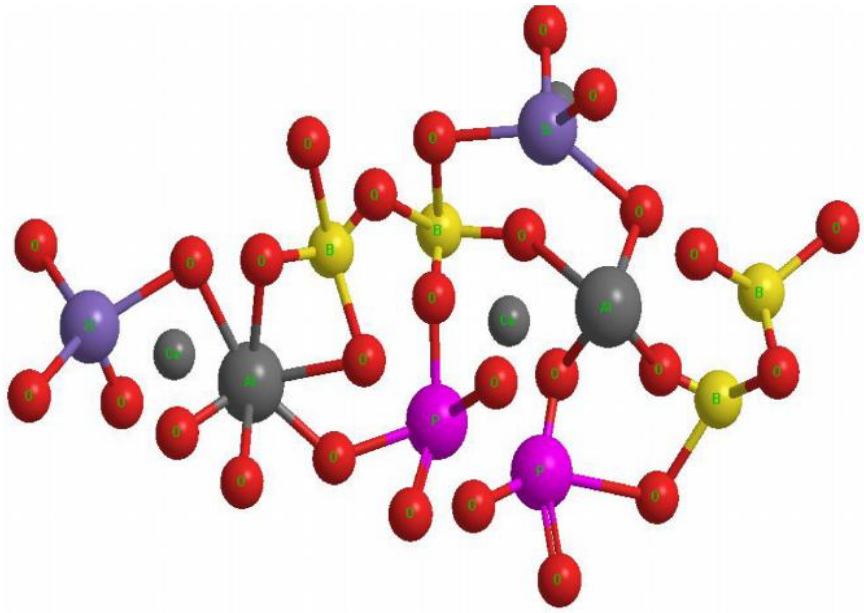

**Figure 5.1.1:** A possible structural fragment of $SiO_2$–$Al_2O_3$-$P_2O_5$–CaO-$B_2O_3$ glass.

Creating more NBOs in the glass structure weakens/disturbs the general stability of the glass network, this having been observed previously when introducing calcium fluoride ($CaF_2$) (a strong network modifier) into an aluminosilicate glass network. The introduction of $CaF_2$ ions destabilises the glass network by reducing the cross link density of the glass. All $F^-$ ions form a complex with the [$SiO_3F$] and [$AlO_3F$] tetrahedral, which can result in the formation of NBF, thereby increasing the reactivity of the glass towards acid attack [36, 45].

Figures 4.1.5 and Figure 4.1.6 show that from B0 to B25 and FB0 to FB25 boron-substituted glasses the main broad absorption did not changed significantly. However, it is indicated that B50 and FB50 glasses were partially crystallised, with the most intense absorption bands at 1058 $cm^{-1}$ (B50) and 1039 $cm^{-1}$ (FB50) due to the asymmetric stretching vibration (P-O, $v_3$) of the phosphate tetrahedral with 4 NBOs ($PO_4$), while the absorption peak at 940 $cm^{-1}$ is due to the symmetric stretching of the phosphate group ($v_1$). It is obvious that the P-O peak in the FB50 glass ceramic is the result of two bonds (602 and 576 $cm^{-1}$) that correspond to the O-P-O bending of phosphate groups ($v_4$) and are characteristic of an apatite crystalline phase. (4) Al-O ($AlO_4$) bonds are found to be present at 729 $cm^{-1}$ [161, 162].

The Raman spectra of glassy silicate materials are characterised by a number of broad features, reflecting the multiple coordinations of Si–O bonds. It is described by Colomban [183] that this complex picture invoking several types of chain, sheet and three-dimensional structures labelled $Q^4$–$Q^0$, which can be assigned as follows: $Q^4$, representing $SiO_2$ and tectosilicates with a band in the range of 1250–1150 $cm^{-1}$; $Q^3$,

representing silicate sheets with a band near 1100cm$^{-1}$; $Q^2$, representing silicate chains with bands in the region of 1100–1050 cm$^{-1}$; $Q^1$, representing $Si_2O_7$ groups, with a band near 950 cm$^{-1}$; and $Q^0$, representing monomer $SiO_4$ units, with bands in the region 850–800 cm$^{-1}$ [184]. It is worth noticing that the current spectra are very broad and often the peaks seemed to be overlapping.

### 5.1.3 MAS–NMR Spectroscopy

#### 5.1.3.1 $^{29}$Si MAS–NMR Spectroscopy

The chemical shift observed for Si in a fourfold-coordinated state is between -60 and -100 ppm, depending on the chemical environment around the silicon atoms. Engelhardt et al. [157] reported that the chemical shift of Si in aluminosilicate glasses was determined by both the number of bridging oxygens (m) per $SiO_4$ unit and the number of aluminium atoms (n) linked to the $SiO_4$ unit by oxygen. In an aluminosilicate glass expressed as $Si(OSi)_{m-n}(OAl^-)_n(O^-)_{4-m}$,$(Q^m(nAl)$, $0 \leq n \leq m \leq 4$), the chemical shift increases with decreasing m or increasing n. It can be interpreted that the chemical shift depends on the number of both NBOs and BOs connected with the Si atom, as well as on the number of next nearest neighbours of aluminium. Increasing the number of NBOs results in the peak shifting to a positive position, while the peak shifts to a more negative position by increasing the number of next nearest neighbour aluminium. In general, the substitution of Al for each of the four silicon atoms surrounding the central Si of a Q unit results in a change in the $^{29}$Si

chemical shift of about 5 ppm towards less negative values. Thus, the $^{29}Si$ chemical shift range of a $Q^4$ unit with no bounded Al atoms (denoted $Q^4$ (0Al)) is about -102 to -116 ppm; this becomes about -97 to -107 ppm for $Q^4$(1Al), -92 to -100 ppm for $Q^4$(2Al), -85 to -94 ppm for $Q^4$(3Al) and -82 to -92 ppm for $Q^4$(4Al). It is indicated from the range of these values, although the shifts overlap, that these valus can also be used as a guide to the degree of Al-for-Si substitution, which can provide information about the disordering of an aluminosilicate framework.

In Figure 4.1.9 and Table 4.1.3.1, the $^{29}Si$ MAS–NMR spectrum of B0 glass shows an overlapping peak at around -83.3 ppm, assigned to $Q^3$(3Al) and $Q^4$(4Al) species, respectively [113, 157, 158]. With the boron-substituted aluminium increasing, the B5 and B10 glasses shown exhibit a similar overlapping peak at around -86.6 and -84.5 ppm, associated mainly with $Q^3$(3Al) and $Q^4$(4Al) species, respectively. With the substitution up to B15, B25 and B50, a broad overlapping peak was shown at around -86.9, -88.9 and -103.5 ppm, with a weak shoulder at -109.9, -111.9 and -112.5 ppm, which are shifted to more negative values compared to the corresponding MAS–NMR spectrum of B0 glass, implying that the glass network in these glasses must be different. In addition, the negative shift in boron-substituted, fluorine-free glasses indicates a structural change around the Si atom due to B substitution for Al, which may be related to the presence of small amounts of $Q^4$(3Al), $Q^4$(2Al) and $Q^4$(1Al) species in the glass network. Therefore, it is suggested that $Q^4$(3Al), $Q^4$(2Al) and $Q^4$(1Al) are present in the B15, B25 and B50 glasses in addition to $Q^4$(4Al) and

$Q^3$(3Al).

When trying to understand the structure of boron-substituted glasses, the situation becomes more complicated if one asks whether Si-O-P linkages could be present in the glass network. It has been proposed [105, 106, 185] that Si-O-P species appear between -113 and -117 ppm in the $^{29}$Si MAS–NMR spectra of $Na_2O$-$2SiO_2$-$pP_2O_5$ glass (p = 0.26–4.0). In addition, Dupree et al. reported that a peak at around -33 ppm in the $^{31}$P MAS–NMR spectra of $Na_2O$-$2SiO_2$-$pP_2O_5$ glass ( $p \geq 2$) corresponds to the presence of Si-O-P linkages [186]. Therefore, it is hard to identify Si-O-P species in the $^{29}$Si and $^{31}$P MAS–NMR spectra (Figure 4.1.9 and Figure 4.1.13, respectively) of the B25 and B50 glasses due to peak overlap. The previous work by Dupree et al. [176] also indicated that Si in Si-O-P linkages is present as Si(VI), which makes the possibility of Si-O-P being present in the current boron-substituted glasses very small, as Si is present in four-fold coordination. In addition, Si-O-P is highly unstable because it is prone to hydrolysis [186]. It is possible that any Si-O-P present in the glass is hydrolysed during quenching in water. It is clear, however, that the amount of Si-O-P, if present, must be very small.

The $^{29}$Si NMR spectra of a series of sodium borosilicate glasses show that, in compositions containing 30–40% mol $B_2O_3$, the predominant structural unit is $Q^4$ (-110 ppm), but at lower $B_2O_3$ contents the $^{29}$Si shift becomes less negative, reflecting an increase in the number of $Q^4$(1B) (-105 ppm) and $Q^3$(0B) units (-90 ppm). The latter component could also arise from the presence of $Q^4$(3B) units, but this possibility is ruled out by the glass stoichiometry [187]. It is indicated that in $^{29}$Si

NMR spectra may have overlapping peaks by increasing boron substitution, like $Q^4$(1Al) and $Q^4$(1B).

The chemical shift of $^{29}$Si for calcium aluminosilicate glasses was determined by Maeda et al. [188] by adjusting the composition to only one structural unit present $Q^m$(nAl), indicated as follows: $Q^4$(1Al) at -104.0 ppm, $Q^4$(2Al) at -97.2 ppm, $Q^4$(3Al) at -89.6 ppm, $Q^4$(4Al) at -87.1 ppm and $Q^3$(1Al) at -81.6 ppm. The boron-substituted, fluorine-containing glasses also lead to overlapping peaks in the $^{29}$Si MAS–NMR spectra in Figure 4.1.10 and Table 4.1.3.2, which appear at around -87.2 ppm and -86.9 ppm for FB0 and FB5 glasses and at -88.6 ppm, -91.3 and -91.6 ppm for FB10, FB15 and FB25 glasses, assigned to $Q^3$(3Al), $Q^4$(4Al) and $Q^4$(3Al) species, respectively. On the other hand, there is one broad peak at -99.4 ppm in FB50 glass. The shift towards more negative values of the chemical shift compared to FB0 glass suggests that an increasing amount of $Q^4$ species is present in the glass network, which is in good agreement with the FTIR study on boron-substituted glasses wherein an increase in the number of bridging oxygens is observed. Initially, due to the smaller cation size of B, it was thought that B may act as network former, taking up fourfold coordination and forming $BO_4$ structural units.

### 5.1.3.2 $^{27}$Al MAS–NMR Spectroscopy

The resolution and sensitivity of quadrupolar nuclei such as $^{27}$Al (I = 5/2) MAS–NMR spectroscopy is usually inadequate due to the inherent distribution of the quadrupolar

coupling interactions in disordered materials. Magic-angle spinning (MAS) can be used to effectively eliminate the most anisotropic interactions by which the non-quadrupolar nucleus is dominated. But it is difficult for MAS alone to narrow the peaks of half-integer quadrupolar nuclei. A peak is broadened by the second-order quadrupolar coupling to lower frequencies corresponding to the isotropic chemical shift. The application of a high magnetic field can increase the Larmour frequency, leading to better frequency dispersion and less second-order quadrupolar effect on the nucleus. Stebbins et al. [111] studied the effect of different magnetic fields in order to eliminate the quadrupolar coupling in fluorine-containing aluminosilicate glasses, indicating that high-coordinated Al species as small as a fraction of 1% can be observed by a high magnetic field MAS–NMR. Therefore, $^{27}$Al MAS–NMR is preferred to be conducted at a high magnetic field strength. However, due to the limited availability of a high magnetic field strength, the samples were analysed by a Bruker ADVANCE 400 NMR spectrometer. The spectra in Figures 4.1.11 and 4.1.12 show a large, broad and asymmetric peak around 45 ppm for all glasses, and the curves show nearly no change, due to fourfold-coordinated Al(IV). Al(V) and Al(VI) might also be present but difficult to conclude, as there is no apparent peak in the spectra.

Generally, the chemical shift of Al(IV) in phosphorus-free aluminosilicate glasses should be around 50 ppm [157]. Stamboulis et al. [102] studied the structure of fluorine-containing calcium aluminosilicate glasses based on the composition $2SiO_2$-$Al_2O_3$-(2-x) CaO-x$CaF_2$ by using $^{27}$Al MAS–NMR and reported a chemical shift at

around 50 ppm assigned to the Al(IV) state. However, all the chemical shifts observed for the glasses under study are at lower values, between 49.1 ppm for B0 glass and 41.5 ppm for FB50 glass, as shown in Figures 4.1.11 and 4.1.12. This decrease in the chemical shift is probably caused by the formation of Al-O-$PO_3^{3-}$ bonds due to the presence of $P_2O_5$. Al-O-$PO_3^{3-}$ species are favoured because fourfold-coordinated $Al^{3+}$ is short of one unit of positive charge, while $P^{5+}$ in –O-$PO_3^{3-}$ has an excess of one unit of positive charge; therefore, $P^{5+}$ ions can locally charge balance the charge-deficient $Al^{3+}$ ion, resulting in the formation of Al-O-$PO_3^{3-}$. As phosphorus atoms are more electronegative than silicon atoms, the formation of Al-O-$PO_3^{3-}$ bonds leads to a negative shift of the peak observed in the $^{27}Al$ MAS–NMR spectra. With more boron substitution for Al, a small but obvious peak with increasing intensity appears at -4.3 ppm, attributed to sixfold-coordinated Al(VI), which is present in FB5 to FB50 glasses (Figure 4.1.12). The glasses are designed to be in accordance with Lowenstein's rules for maintaining Al in a four-fold coordination state. The presence of Al(VI) is therefore not expected, even in a small amount. However, recent studies by Hill et al. [99] showed that a similar FB0 glass undergoes amorphous phase separation into a Ca and P–rich region and an aluminosilicate-rich region. Stamboulis et al. reported that a mullite phase always exhibits aluminium in four- and six-fold coordination [104]. This would explain the presence of Al(VI) in amorphous-separated glasses. It is supported that in aluminosilicate glass melts aluminium is present in sixfold coordination. Annealing would allow the glass network structure to relax, resulting in aluminium taking up fourfold coordination, and consequently, the

peak associated with sixfold coordinated aluminium would disappear. Therefore, if Al(VI) is present in such glass compositions, it is most likely that this is due to the above-mentioned reason. However, this is not always the case, as glasses of different compositions do not show the Al(VI) peak consistently. As a result of the lack of available cations for charge balancing, aluminium is forced to move to the higher coordination state Al(VI). Zeng and Stebbins [110] reported that fluoride was attached mostly to Al(V) or Al(VI) in a fluoride-containing anorthite glass in Al-F-Ca(n) species. On the other hand, Matsuya and Stamboulis [113] suggested that Al(IV) could also be present in Al-F bonds in calcium aluminosilicate glasses. Therefore, it can be suggested that Al in all glasses can be present predominantly as Al(IV) network former or Al(VI) in $[AlOxFy]^{n-}$, where x = 3-6, y = (6-x) and n = charge of the total complex and Al(IV) in a small amount of $[AlO_3F]^-$, depending on the fluorine content.

### 5.1.3.3 $^{31}$P MAS–NMR Spectroscopy

There is a slight shift in the $^{31}$P MAS–NMR spectra with the increasing content of boron substitutions for aluminium in fluorine-free glasses. It is shown in Figures 4.1.13 and 4.1.14 that a broad, symmetrical peak at around -5 ppm is observed for B0 to B25 and FB0 to FB25 glasses, which are assigned to $AlPO_4^{3-}$ ($Q^1$) species. On the other hand, B50 and FB50 glasses show a positive peak at around 0.7 and 2.4 ppm, respectively. Oliveira et al. [189] reported that an orthophosphate ion situated at

around 2 ppm was observed in a calcium silicon phosphate glass. Dollase et al. [126] conducted $^{31}P$ MAS–NMR studies on $Na_{3-3x}Al_xPO_4$ (x = 0-0.5) and reported that the varied chemical shifts of $^{31}P$ depend on the number of Al atoms surrounding the $PO_4^{3-}$ tetrahedron, listed as the following: P (0Al) at 13.4–13.8 ppm, P (1Al) at 5.3–6.1 ppm, P (2Al) at -4.9–-3.8 ppm, P (3Al) at -15 ppm and P (4Al) at -26.3 ppm.

Cody et al. [187] investigated the structure of sodium aluminosilicate glasses [$(x)Na_2O$, $(1-x)A_2O_3$, $0.9SiO_2$] containing a constant amount of phosphorus at various Na/Al ratios using multinuclear MAS–NMR and suggested that the two peaks at 4.3 and 3.5 ppm observed were attributed to $Na_2PO_4(AlR_3)^{-1}$ and $Na_2PO_4(SiR_3)$, respectively, where R represents the cluster connected with the glass network. In addition, Gan et al. [190] proposed that pyrophosphate species appeared at -1.1 ppm in different $SiO_2$-$Al_2O_3$-$K_2O$ systems. Grussaute et al. [191] reported that the replacing sodium with calcium moved the chemical shift to a more negative position. Therefore, the peak at around -5 ppm in the B0 to B25 and FB0 to FB25 glasses is assigned to a pyrophosphate environment. As $^{27}Al$ MAS–NMR spectra show the presence of Al-O-P species, it can be suggested that $AlPO_4^{3-}(Q^1)$ species are present in the glass network.

According to Kirkpatrick et al. [105], when phosphorus is added to silicate glasses, phosphorus does not copolymerize with the silicate portion of the glass; rather, it forms phosphate-rich regions with low polymerizations. In addition, phosphorus has the ability to scavenge charge-balancing network modifiers from the silicate portion of the glass, increasing its polymerization according to the following reaction:

P-O-P + Si-O-M ⟶ P-O-M + Si-O-Si (Eq. 5.1)

where M = network modifier (which in our composition is Ca)

As a result, more silicon $Q^4$ species are formed at the expense of $Q^3$. In the absence of aluminium, Si-O-P linkages form, evidenced by increased shielding on both $^{29}Si$ and $^{31}P$ MAS–NMR spectra. If the ratio of P/Si is lower than 1, then silicone linked to phosphorus takes on sixfold coordination. If the P/Si ratio is higher than 1, then the addition of aluminium leads to substitution of aluminium for phosphorus, reducing the amount of sixfold-coordinated silicon by forming more stable Al-O-P linkages. In high-silicon containing glasses, on the other hand, the structural role of phosphorus depends strongly on the M/Al ratio. If there is an excess of network modifiers to charge balance all the aluminium as Al(IV), then NBOs are formed on the silicon tetrahedra. An addition of $P_2O_5$ leads to the removal of NBOs from the silicon tetrahedra and the formation of depolymerised M phosphate domains according to the reaction Eq. 5.1 above. For compositions where insufficient M is present for charge balancing aluminium in fourfold coordination, some aluminium must occur in other higher energy sites, and the addition of $P_2O_5$ leads to the formation of more stable Al-O-P linkages. Kirkpatrick et al. suggested that aluminium in this case is present predominantly as Al(VI) [188]. When sufficient M is available for charge balancing aluminium, adding phosphorus must compete for M with the low-energy Al(IV) sites that are charge balanced by M. In this case, both Al-O-P linkages and polymerised $Q^2$

M phosphate species are formed, for which the M here is Ca.

For the compositions under study, it is clear that changes occur with the substitution of boron. It is shown in Figures 4.1.13 and 4.1.14 that B50 and FB50 glasses are part crystallised to calcium phosphate species, and these are discussed above in the FTIR section.

#### 5.1.3.4 $^{11}$B MAS–NMR Spectroscopy

Borosilicate glasses are the most widely useful family of glass compositions for applications ranging from laboratory ware to optical glasses and nuclear waste encapsulation. In the low-Na composition range, all boron is in either symmetric trigonal or tetrahedral sites, with the concentration of tetrahedral B directly proportional to the Na content. When the Na content becomes greater than that required forming diborate, the excess Na enters the silicate network to form $NaBSi_4O_{10}$ units containing tetrahedral B with four Si next-nearest neighbours. $^{11}$B MAS–NMR has been used to study these changes in boron coordination with composition in a series of sodium borosilicate glasses [189]. The spectra of the boron-rich compositions indicate phase separation into sodium borate and silicate-rich phases. The spectra of the sodium-rich compositions indicate a homogeneous borosilicate network structure containing tetrahedral boron with non-bridging oxygens, providing a charge compensation mechanism [189].

A series of sodium boroaluminosilicate glasses with compositions between $NaBSi_3O_8$ and $NaAlSi_3O_8$ have been studied by $^{11}B$ NMR [187]. The spectra indicate that the $BO_3/BO_4$ ratio increases as the ratio of Al/B increases; for low-boron glasses, most of the boron is present as $BO_3$, located in borate-rich regions, coexisting with separate boroaluminosilicate regions containing $BO_4$ [187]. $^{11}B$ MAS–NMR has been used to determine the fraction of tetrahedral boron in a series of alkaline earth (Mg, Ca, Sr) boroaluminate glasses as a function of composition. The results confirm that the proportion of $BO_4$ decreases with increasing $Al_2O_3$ content, this trend being essentially independent of the alkaline earth cation [190].

$^{11}B$ MAS–NMR has been used in conjunction with $^{29}Si$ and $^{31}P$ NMR to determine the nature of borate and other species in a series of sodium borosilicophosphate glass [191]. In glasses with molar boron fractions less than about 0.5, the borate species is solely $BO_4$, but at about this composition, the peak broadens, suggesting the presence of two types of tetrahedral boron, corresponding to the appearance of two different sodium phosphate units. At higher B contents the proportion of $BO_4$ decreases with the formation of $BO_3$, and the peak position progressively moves to a higher frequency, indicating that the $^{11}B$ is becoming less shielded. These results are consistent with calculations made on the basis that $P_2O_5$ reacts with both $Na_2O$ and $B_2O_3$ [192].

It is shown in Figures 4.1.15 and 4.1.16 that there is no change in any of the boron-substituted glasses. The $^{11}B$ MAS–NMR spectra are observed around 1.0 ppm and 9.5 ppm, which are assigned to the $BO_4$ and $BO_3$ groups, respectively. There is also no effect on the boron bond with increasing boron substituted for aluminium, suggesting

boron atoms are very stable to form $BO_4$ and $BO_3$ groups in $4.5SiO_2$-$3Al_2O_3$-$1.5P_2O_5$-5CaO and $4.5SiO_2$-$3Al_2O_3$-$1.5P_2O_5$3CaO-$2CaF_2$ systems.

### 5.1.3.5 $^{19}$F MAS–NMR Spectroscopy

Zeng and Stebbins studied a glass based on a composition of $2SiO_2$-$Al_2O_3$-0.5CaO-$0.5CaF_2$ and suggested that fluorine is present as F-Ca(n), with a chemical shift at -103 ppm, and Al-F-Ca(n), with a chemical shift at around -110 ppm [110, 193]. The $^{19}$F MAS–NMR spectra of boron-substituted, fluorine-containing glass in Figure 4.1.17 show two overlapped peaks at around -103 ppm and -110 ppm, implying that fluorine is preferentially present as F-Ca(n) species and Al-F-Ca(n) species, respectively, where n corresponds to the number of calcium atoms surrounding an atom of fluorine [102, 110]. Progressively substituting boron for aluminium (above FB15) leads to one peak that disappears at -110 ppm, which is assigned to Al-F-Ca(n). Stebbins and Kroeker et al. [111] suggested that fluorine is mostly connected with Al(V) or Al(VI) in a fluorine-containing anorthite glass, as $AlF_5$ in an Al(V) site and as $AlF_6$ in an Al(VI) site. In the current glass compositions, Al ions remain in the glass network mainly as Al(IV), with decreasingly small amounts of Al(V) and Al(VI) with boron substitution. Al(V) and Al(VI) are not present in high-boron-substitution glasses. The presence of high-coordinated Al may result from the insufficient availability of charge-balancing cations. As discussed before, Al is suggested to be present as $[AlOxFy]^{n-}$, where x = 3-6, y = (6-x) and n = the charge of the total

complex with Al(IV), Al(V) and Al(VI) present. It should be mentioned that Al is present in the glass network, most likely as $[AlO_3F]^-$, as there is only a small quantity of high-coordinated aluminium present.

### 5.1.4 Summary

The series of $4.5SiO_2$-$3Al_2O_3$-$1.5P_2O_5$-$5CaO$ and $4.5SiO_2$-$3Al_2O_3$-$1.5P_2O_5$-$3CaO$ - $2CaF_2$ glass compositions corresponding to different boron substitutions for aluminium have been studied. All the samples are consistent with the designed compositions except for fluorine content, which is measured to be slightly smaller than the initial composition. This is most likely due to the formation and escape of a very small amount of $SiF_4$ from the glass surface.

The smaller cation substitution of boron for aluminium results in a decrease of the glass density and a slight increase of the oxygen density. It is proposed that a smaller cation forms a more packed glass network.

The FTIR spectra of all boron-substituted glasses exhibit five absorption regions, which are related to the following bonds:

1. Si-O-Si ($Q^4$) and Si-O-Si ($Q^3$) stretching vibrations, as well as Si-O-[NBO],
2. Al-O vibrations with Al in a fourfold coordination state,
3. P-O bending vibrations and Si-O-Al linkages,
4. Si-O-Si bending vibrations and
5. B-O-B bending vibration.

Except the FTIR spectra of B50 and FB50, glasses show some crystallised peaks.

The $^{29}Si$ MAS–NMR study indicates the presence of $Q^4(4Al)$ and $Q^3(3Al)$ species in all glass samples. In the case of boron substitution for aluminium above 15 molar percentage glasses, the species present also include $Q^4(3Al)$, $Q^4(2Al)$ and $Q^4(1Al)$, and there is an increase in $Q^4(2Al)$ and $Q^4(1Al)$ species with increasing boron substitution, which is also due to the decreasing of aluminium.

$^{27}Al$ MAS–NMR shows the presence of Al(IV) in all glasses and a small amount of Al(V) and Al(VI) in the case of boron-substituted glasses.

Phosphorus is present in the pyrophosphate environment $AlPO_4^{3-}(Q^1)$, as suggested by the $^{31}P$ MAS–NMR spectra. The presence of Si-O-P species in boron-substituted samples is most unlikely for two reasons: 1. If Si-O-P species were present, most likely Si would be in sixfold coordination instead of fourfold coordination, as observed in $^{29}Si$ MAS–NMR spectra, and 2. Si-O-P species are unstable and susceptible to hydrolysis.

The $^{19}F$ MAS–NMR spectra for boron-substituted glasses show the presence of fluorine species F-Ca(n) and Al-F-Ca(n), and there is a decrease in Al-F-Ca(n) species with increasing boron substitution for aluminium.

## 5.2 Effect of boron substitution on the crystallisation of Glasses

### 5.2.1 DSC and TGA thermal analysis

Tables 4.2.1 presents the glass transition temperature and the crystallisation

temperatures of all boron-substituted, fluorine-free glasses with fine particle sizes (<45μm). It is clear in Figure 4.2.1 and 4.2.2 that the glass transition temperature mainly decreased with boron substitution. The first crystallisation temperature first increased to 1082°C (B5) and then decreased to 746°C with boron substitution in Figure 4.2.3. It is shown in Table 4.2.1 and Figure 4.2.4 that the second crystallisation temperature decreased generally from 1136°C (B0) to 956°C (B50). It is interesting to note that B7.5 glass shows only one broad peak, which indicates the first and second crystallisation peaks overlapped together. This finding agrees with R. Hill, who reported that when z is 0 in $4.5SiO_2$-$3Al_2O_3$-$1.5P_2O_5$-(5-z)CaO-$zCaF_2$ composition, the glass transition temperature is around 800°C, and the phases according to the crystallisation temperatures are β-tricalcium phosphate ($Ca_3(PO_4)_2$) and anorthite ($CaAl_2Si_2O_8$) [184]. It also agrees with the XRD results above. It is observed that with more boron substitution for aluminium the transition temperature and second crystallisation temperature decreased. On the other hand, the first crystallisation temperature increased at first, but when the boron substitution was above 5 molar percentage points, the temperature decreased again with more boron substitution, suggesting that the decreasing of aluminium had a larger effect on this composition and that boron atoms go to the amorphous phase and promote phase separation. Different models [194-196] have been used to interpret the mixed cation effect, assuming either a large structural modification induced by mixing mobile species of different sizes or a specific interaction between dissimilar mobile species. Pevzner et al. [197] studied the $RO(R_2O) \cdot 2B_2O_3$ glasses (where R2O = Na2O, RO = BaO, MgO)

upon replacement of $Na_2O$ with BaO or MgO and BaO with MgO and proposed that the mixed cation effect was associated with the difference in energy of cation-oxygen bonds and a different effect of cations on the coordination state of boron. Ingram et al. [194] suggested a 'leader follower' mechanism that involved dynamic coupling between the majority (faster) and minority (slower) cations, which required the opening up of additional sites for the slower follower (minority) cations due to the mismatch effects, resulting in a disturbed glass network. It is most likely that the lower Tg in our case is due to the above-described mixed cation effect.

Tables 4.2.2 presents the glass transition temperature and the crystallisation temperatures of all boron-substituted, fluorine-containing glasses with fine particle sizes (<45μm). It is clear in Figure 4.2.5 and 4.2.6 that the glass transition temperature shows to be very stable, around 650$^o$C, from FB0 to FB15 glasses. On the other hand, FB25 shows the lowest glass transition temperature at 605$^o$C. According to the XRD results, it is indicated that there is a crystallised phase in FB50 glasses. It is shown in Figures 4.2.7 and 4.2.8 that the first crystallisation temperature decreased from 741$^o$C (FB0) to 643$^o$C (FB50), while the second crystallisation temperature seems to be more complicated. It is shown in Table 4.2.2 that the highest $T_{p2}$ is FB15 glass, and the lowest $T_{p2}$ is FB25, which is also observed in the third crystallisation peak at 946$^o$C. It is interesting to observe that there are mainly two crystallisation temperatures in boron-substituted, fluorine-free glasses. As reported previously for the 100% Ca glass [174], the first crystallisation temperature (around 620$^o$C) is due to fluorapatite formation, whereas the second crystallisation temperature is due to

mullite formation. Similarly, the first crystallisation temperature in the FB0 to FB50 glasses corresponds to the fluorapatite phase, whereas the second crystallisation temperature corresponds to mullite formation.

It is indicated in Table 4.2.3 and Figure 4.2.9 that glass transition temperature and crystallisation temperature increased with increasing the heating rate to 20 and 40$^{o}$C/min, respectively. The activation energies for crystallisation can be calculated by employing either the method proposed by Marotta et al. or the modified Kissinger method proposed by Matusita et al. [198-203]. The method developed by Marotta et al. is based on the Eq. 5.2:

$$Ln\,{}^{1}\!/_{r} = E_C / RT_P + cons\tan t \quad \text{(Eq. 5.2)}$$

where $r$ is the heating rate, $E_C$ is the activation energy of the process, $T_P$ is the temperature corresponding to the maximum of the crystallisation peak and R is the universal gas constant.

The basis of the modified Kissinger method suggested by Matusita and Sakka is shown in equation 5.3:

$$Ln\left(T_P^2 / r^n\right) = -mE_C / RT_P + cons\tan t \quad \text{(Eq. 5.3)}$$

where $T_P$ is the crystallisation peak temperature, $r$ is the heating rate, R is the universal gas constant and n and m are the numerical constants that depend on the crystallisation mechanism. In the case of surface nucleation n = m = 1. However, it is not necessary to calculate the activation energies for crystallisation in boron-substituted glasses. It is observed that, according to the XRD results, the calcium phosphorus main phase appeared at a lower temperature while the aluminium silicate

main phase appeared at a higher temperature, but a new-expected boron phase is not shown with boron substitution for aluminium in all fluorine-free/fluorine-containing glasses. Similarly, it is shown in Table 4.2.4 and Figure 4.2.10 that the glass transition temperature and crystallisation temperature increased with increasing the heating rate to 20 and 40$^{o}$C/min. According to the XRD results above, Ca-FAP is the first phase to be formed in the boron-substituted, fluorine-containing glasses, and mullite is crystallised subsequently as a second phase, but a boron-containing phase is not shown. It is interesting to notice that the glass transition temperature generally decreased with boron substitution increasing in fluorine-free and fluorine-containing glasses; the crystallisation temperature slightly increased in a small amount of boron substitution compositions due to the boron playing a role as a glass former and the smaller atoms leading to a more packed glass network. With more boron substitution for aluminium, the phase separation was made more obvious due to less effect from the aluminium. This is a good way for us to find a medium composition with less aluminium and a more packed glass network, lower glass transition and crystallisation temperature, and more expected phases in glass ceramics.

A small weight loss was observed in the TGA analysis, as shown in Table 4.2.5 and Figure 4.2.11. It is worth noting that all the thermogravimetric analyses were conducted on fine particle sizes (<45μm) glass samples, and it was expected that if there was a weight loss it would be due to the larger surface area. It is shown that the weight loss is very similar in all boron-substituted glasses, indicating the glass structure is very stable with boron substitution for aluminium. It is suggested that in

boron-substituted, fluorine-containing glasses there is a small fluorine loss from the surface of the glasses due to possible $SiF_4$ formation during heating. The loss of $SiF_4$ could cause an increase in the cross-link density of the glass and, thereby, hinders crystallisation, but it has not been proven experimentally; however, it is expected that some very small loss occurs during glass making as well as during heat treatments. It is suggested that boron takes part in the glass network formation, which may result in phase separation. Unfortunately, the Raman spectra of glasses were not very helpful, as the peaks were very broad and the interpretation of the data was based on rather a few assumptions.

### 5.2.2 X-Ray Diffraction Analysis

It is indicated in Table 4.2.6 and Figure 4.2.12 that most of the boron-substituted glasses show an amorphous phase after glass making. Nevertheless, a high amount of boron-substituted glasses (B50 glass and FB50) show crystal phase peaks that are assigned to calcium phosphate ($Ca_4P_2O_9$) and fluorapatite ($Ca_5(PO_4)_3F$). Tetracalcium phosphate (TTCP, $Ca_4(PO_4)_2O$) is the only calcium phosphate phase with a Ca/P ratio greater than stoichiometric hydroxyapatite (HA), and it is formed in the $CaO–P_2O_5$ system at temperatures >1300 °C. In contrast to other calcium orthophosphates such as hydroxyapatite (HA, $Ca_5(PO_4)_3OH$) or monetite (DCPA, $CaHPO_4$), which are widely used as food ingredients, in toothpastes, in pharmaceutical applications or in chromatography [204], phase-pure TTCP has found application only as a ceramic biomaterial. It is the most basic of the calcium phosphates and has a Ca/P ratio of 2,

making it the most phosphorus-poor phosphate. Fluorapatite crystallises in a hexagonal crystal system. It is often combined as a solid solution with hydroxylapatite ($Ca_5(PO_4)_3OH$ or $Ca_{10}(PO_4)_6(OH)_2$) in biological matrices. Compare to oxygen and hydroxyl, the fluoride ion pack more tightly into the apatite lattice, and it promote the nucleation and crystallisation of FAP. After studying the magic-angle spinning NMR, Jana and Braun [205, 206] also found the formation FAP from apatite phase related to the alkali metals, and the fluorine was one of the critical elements to help apatite formation. The FTIR and NMR results both agree with the XRD that the B50 and FB50 glasses were crystallised during the glass making.

It can be seen in Table 4.2.7 and Figure 4.2.13 that only B50 glass shows a crystallised phase in boron-substituted fluorine-free glasses during sintering at 700$^{o}$C. On the other hand, it is interesting to notice that only boron-free glass shows an amorphous phase in boron-substituted fluorine-containing glasses during sintering at 700$^{o}$C. With boron substitution increasing in fluorine-containing glasses, the crystallised peak can be seen more in Figure 4.2.13, which suggests that the boron substitution promotes the phase separation and decreases the crystallisation temperature of the fluorapatite phase. Furthermore, it can also be seen in the DSC result that the first crystallisation temperature is around 700$^{o}$C in boron-substituted fluorine-containing glasses, which agrees with the XRD results that the first crystallised phase is fluorapatite.

It can be seen in Table 4.2.8 and Figure 4.2.14, 4.2.15 that all the boron-substituted fluorine-free glasses are assigned a calcium phosphate phase and that boron-

substituted fluorine-containing glasses are assigned a fluorapatite phase by a sintering temperature of 900$^{o}$C, respectively.

When the sintering temperature increases to 1100$^{o}$C, it can be seen in Table 4.2.9 that the boron-substituted fluorine-free glasses show β- tricalcium phosphate (β-TCP, $Ca_3(PO_4)_2$), anorthite ($CaAl_2Si_2O_8$), and a very small amount of aluminium phosphate ($AlPO_4$) phases and that boron-substituted fluorine-containing glasses show fluorapatite ($Ca_5(PO_4)_3F$), mullite ($Al_6Si_2O_{13}$) and aluminium phosphate ($AlPO_4$) phases [121].

The fluorine-free glasses, with sintering at 1100 $^{o}$C, crystallised to β-TCP and anorthite and a small amount of $AlPO_4$ phases. The failure to crystallise to an apatite phase in fluorine-free glasses indicated that the fluorine is a key element for apatite formation. E.g. glasses with compositions similar to bone china can crystallise to anorthite ($CaAl_2Si_2O_8$) and β-TCP ($Ca_3(PO_4)_2$) rather than to an apatite phase [121], and the β-TCP in the glass has the similar Ca:P ratio of 1.5 compare to the apatite at 1.67. However, some researches [207-212] show that due to surface nucleation, for certain types of apatite-wollastonite-containing glass-ceramics (A-W glass-ceramics), the apatite phase can still form without fluorine. The study carried out by Galliano and Lopez [213] showed that ability of a glass to crystallise to apatite mostly related to the glass compositions rather than fluorine element, and the separation of some amorphous phase also help the glass to crystallisation.

For the fluorine-containing glass, besides of forming fluorapatite, mullite is also a

important phase in this glass. It occurs as the principal crystalline phase after apatite crystallisation for two reasons: First, the formation of crystalline fluorapatite removes all the $PO_4$ tetrahedra from the glass network, according to Lowenstein's rules that request high coordination states of aluminium atoms, which are favourable for mullite formation since it contain both four and six coordination states[159]. Second, due to the formation of fluorapatite, both calcium and phosphorus are lost from the glass network, which lead to the aluminium to occupy higher coordination states and similarly favours the formation of mullite.

A change can be seen in the XRD pattern with the substitution of boron for aluminium in fluorine-free glass ceramics in Figure 4.2.16 and 4.2.17, with the peak of the anorthite phase decreasing and the peak of the β-TCP phase increasing as boron substitution increases, suggesting that the increase in boron promotes the crystallisation of the calcium phosphate-rich phase and a decrease in the silicate aluminium-rich phase. In addition, with the increase in boron, new phases do not appear, suggesting that the boron enters an amorphous phase.

On the other hand, it can be seen that in fluorine-containing glass ceramics in Figure 4.2.18 and 4.2.19 that the peak of the aluminium phosphate and mullite phases decreases as boron substitution increases. In particular, the aluminium phosphate phase nearly disappears with 50% boron-substitution glass-ceramic. Furthermore, the peak of the fluorapatite phase doesn't change much in all the boron-substituted fluorine-containing glass ceramics, suggesting that the boron enters an amorphous phase again without new phases appearing.

### 5.2.3 Summary

With increasing substitution of boron for aluminium, the glass transition temperature $T_g$ reduces generally in fluorine-free glasses, and the Tg remains almost stable in fluorine-containing glasses. It can be observed that the first crystallisation peak temperature $T_{p1}$ increases at first due to a more packed glass network and then decreases with further boron substitution in fluorine-free glasses. It can also be observed that the second crystallisation temperature decreases with boron substitution. On the other hand, the first crystallisation temperature generally decreases with boron substitution in fluorine-containing glasses. Also, FB25 glass shows the lowest $T_g$ and $T_p$ in fluorine-containing glass.

Calcium phosphate ($Ca_4P_2O_9$) enters a crystallised phase in B50 glass and a fluorapatite ($Ca_5(PO_4)_3F$) phase is shown in FB50 glass. With different sintering temperatures of 700$^o$C, 900$^o$C and 1100$^o$C, it can be seen that in the fluorine-free glass-ceramics, calcium phosphate ($Ca_4P_2O_9$) is the first phase to be formed below the sintering temperature of 900$^o$C and that when the sintering temperature rises to 1100$^o$C, the calcium phosphate ($Ca_4P_2O_9$) phase converts to a tricalcium phosphate [$Ca_3(PO_4)_2$] phase and that anorthite is crystallised subsequently as a second phase and aluminium phosphate phase is a minor phase. With increasing boron substitution, the anorthite and aluminium phosphate phases decrease and there is no boron-containing phase, which suggests that the boron remains in the amorphous glass. The

fluorapatite phase is the first phase to be formed in fluorine-containing glass-ceramics, and with the sintering temperature rising to 1100°C, mullite and aluminium phosphate phases are crystallised in the glass structure, which decrease as boron substitution increases [214].

It can be suggested that the glass shows a more packed structure and a slightly higher glass crystallisation temperature with a small amount of boron substitution. With a high amount of boron substitution for aluminium, the $T_g$ and $T_p$ decreased obviously, which promoted the Ca-P main phase and crystallised at a lower temperature [215].

## 5.3 Effect of boron substitution on the properties and structure of glass ceramics

### 5.3.1 Density of Boron-Substituted Glass-Ceramics

Table 4.3.1 and Figure 4.3.1 show the measured density of boron substituted fluorine-free glass ceramics when the sintering temperature is at 1100°C. It is clear that the density of glass ceramics decreases with boron substitution from 2.808 g/cm$^3$ for B0 ($4.5SiO_2$-$3Al_2O_3$-$1.5P_2O_5$-5CaO) to 2.636 g/cm$^3$ for B50 ($4.5SiO_2$-$1.5Al_2O_3$-$1.5P_2O_5$-5CaO-$1.5B_2O_3$). It can be observed that a linear relationship exists between the density and the boron-molar content. In addition, in this case, the density depends on the amount of phases formed in glass-ceramics. As discussed in the XRD section, as the boron substitution increases, thereby promoting the calcium phosphate crystallisation (when the density of β-TCP is around 3.14 g/cm$^3$), the silicate

aluminium phase decreases (when the density of anorthite is 2.76 g/cm$^3$, and aluminium phosphate ($AlPO_4$ is 2.57 g/cm$^3$), and no new phase appears. It is interesting to note that the density of B10-GC is a little bit higher than B5-GC, which suggests that the increase in the β-TCP phase in glass-ceramics has more of an effect than the decrease of the anorthite phase in the 10% molar boron substitution for aluminium glass-ceramics.

The measured density values for fluorine-containing glass ceramics decrease with an increase in the molar content of boron from 2.932 g/cm$^3$ for FB0 glass ceramic to 2.665 g/cm$^3$ for FB50 glass ceramic, as shown in Table 4.3.2 and Figure 4.3.2. This happens because the density depends on the type of phases as well as the amount of each phase formed in the glass ceramics. For instance, it can be seen from the XRD reference that the density of crystal phases such as fluorapatite ($Ca_5(PO_4)_3F$) with reference code (00-015-0876), mullite ($Al_6Si_2O_{13}$) with reference code (00-015-0776) and aluminium phosphate ($AlPO_4$) with reference code (00-011-0500) are 3.15 g/cm$^3$, 3.00 g/cm$^3$ and 2.57 g/cm$^3$ respectively [216]. Consequently, an increase in boron substitution for aluminium promotes the crystallisation of the fluorapatite phase and decreases the amount of the mullite and aluminium phosphate phases. This should be also consistent with the decrease in the formation of Al-F-Ca species. From Table 4.3.2, it can be seen that the density of FB10-GC decreases more dramatically than FB5-GC, which suggests that the decrease in aluminium has more of an effect than the increase of boron in more than 10% molar boron-substitution fluorine-containing glass-ceramics.

### 5.3.2 Fourier Transform Infrared Spectroscopy Analysis

The spectra shown in Figure 4.3.3 and 4.3.6 all exhibit phosphate stretching and bending vibrations. The absorption bands at 1088, 1085 and 1083 $cm^{-1}$ are due to the asymmetric stretching vibrations (P-O, $\nu_3$) of phosphate tetrahedra with 4 NBOs ($PO_4$), while the absorption peak at around 950 $cm^{-1}$ is due to the symmetric stretching of phosphate groups ($\nu_1$) [161]. The peak situated at 450 $cm^{-1}$ is due to $\nu_2$ phosphate bending vibrations [162]. In addition, it is obvious that the P-O peak at 564 $cm^{-1}$ in the original FB0 glass is split into two bands (575 and 602 $cm^{-1}$) that correspond to the O-P-O bending of phosphate groups ($\nu_4$) and are characteristic of an apatite crystalline phase [142]. The XRD results also confirm the formation of fluorapatite (FAP) in the crystallised FB0-containing glasses. When the boron content increases, an increment in the absorbance intensity of both peaks (602 and 564 $cm^{-1}$) can be detected in the FTIR spectra of boron-substituted glass ceramics when the sintering temperature is 900$^{o}$C, implying an increasing preference of calcium phosphate and fluorapatite formation, as proved by the XRD study. More peaks can be seen in boron-substituted glass-ceramics with a sintering temperature of 1100$^{o}$C. The stretching vibrations of the Al-O bonds with aluminium ions in a fourfold coordination occur at around 735 $cm^{-1}$. In the region of 620-810 $cm^{-1}$, the peak is assigned to Al-O ($AlO_6$), which stretches the vibration of the rings and forms mica-like sheets in the structure of the anorthite $CaAl_2Si_2O_8$ [164]. The peak at around 980$cm^{-1}$ for Si-O-[NBO] bands, and

the intensity of the band associated with Si-O-[NBO] generally decreased which suggests that there was more Si-O-Si as well as bridging-oxygens formed in the glass network. Besides, the intensity of the increase in a new broad peak emerges at around 1396 $cm^{-1}$ with increasing boron content attributed to B-O stretching vibration in Figure 4.3.3 to 4.3.6.

In Table 4.3.1, it can be seen that an isolated $[PO_4]^{3-}$ has $T_d$ symmetry and 4 normal modes of vibration: $A_1$ ($v_1$) = 955 $cm^{-1}$, E ($v_2$) = 425 $cm^{-1}$, $T_2$ ($v_3$) = 1043 $cm^{-1}$ and $T_2$ ($v_4$) = 578 $cm^{-1}$, where the species-E vibrations are doubly degenerate and the $T_2$ vibrations are triply degenerate [168]. All glass ceramics with boron substitution exhibit very similar Raman peaks, which does not contribute much to the discussion.

### 5.3.3 MAS–NMR Spectroscopy of glass ceramics

#### 5.3.3.1 $^{29}$Si MAS–NMR Spectroscopy

The $^{29}$Si MAS–NMR spectrum of boron-substituted glass ceramics in Table 4.3.3.1 and 4.3.3.2 show a peak at around -86 ppm with a shoulder at around -106 ppm (Figure 4.3.3.1 and 4.3.3.2). The spectrum of boron-substituted glass ceramics exhibits several peaks at –87.8, -92.5, -97.6, -103.4 and -108.2 ppm, which are related to $Q^4$(4Al), $Q^4$(3Al), $Q^4$(2Al) and $Q^4$(0Al) species, demonstrating the adjacent environment of the $SiO_4$ tetrahedron, respectively [171, 172]. As previously identified by the XRD, anorthite and mullite are produced during the crystallisation process of boron-substituted glass. Phillips et al. [217] suggested that the anorthite spectra are

between -80 and -90 ppm in the $^{29}Si$ MAS–NMR spectra. Phillips et al. [217] also studied a series of synthetic samples based on the composition $Sr_xCa_{1-x}Al_2Si_2O_8$ ($0 \leqq x \leqq 1$) and reported that the two different $Q^4(4Al)$ species in $SrAl_2Si_2O_8$ were present at -83.8 and -85.4 ppm. Jaymes et al. [218] reported several sites in the $^{29}Si$ MAS–NMR spectra of a series of mullite solid solutions. It is interesting to note that in all cases the main site produced a broad line centred at -88.5 ppm with a small shoulder at -80 ppm representing 50-76% of the total $SiO_4$ tetrahedra and alumina-rich mullite, respectively. The latter peak was observed by Ban and Okada [219] only in the case of aluminium-rich mullite. In addition, the peak observed in -86 ppm was attributed to a sillimanite ($Al_2SiO_5$) type site $SiO_4$ in which all Si tetrahedra were surrounded by Al tetrahedra in the double chains. The sites at -90 and -94 ppm were attributed to rearrangements of the sillimanite type Si tetrahedra sites by replacing one or two Al tetrahedra by $SiO_4$ around the silicon atoms, respectively [218]. In addition, Jaymes et al. also noticed a peak at -109 ppm in the case of the stoichiometric mullite composition (60% $Al_2O_3$), which corresponded clearly to free silica [218, 220]. Dove et al. [221] studied Si sites in cordierite by $^{29}Si$ MAS–NMR and reported that cordierite exhibits two groups of peaks that corresponded to two different Al and Si environments depending on the crystalline order of the system. Specifically, he reported that in the most ordered state of cordierite, the spectra were dominated by one peak at -80 ppm associated with $SiO_4$ tetrahedra linked to four $AlO_4$ tetrahedra and another peak at -100 ppm associated with $SiO_4$ tetrahedra linked with three $AlO_4$ and one $SiO_4$ tetrahedra. It is therefore likely that the dominant aluminosilicate phase

is anorthite in fluorine-free glass ceramics and mullite in the fluorine-containing glass ceramics. There is a visible change in the $^{29}Si$ NMR spectra of all boron-substituted glass ceramics; as the boron substitution increases, the intensity at around -86 ppm peak decreases and the intensity at around -105 ppm increases and then these two peaks move to the medium broad overlapped peak at around -100 ppm. This suggests that the $Q^4$(4Al) species decreases with boron substitution for aluminium and moves to $Q^4$(3Al), $Q^4$(2Al) and $Q^4$(0Al) species. Furthermore, the $^{29}Si$ MAS–NMR study is in agreement with the XRD analysis in which the anorthite and mullite are identified with one of the crystalline phases that also decreases as boron substitution increases. In B50 and FB50 glass-ceramics, there is a board peak at around -100 ppm, which might be related to silicate left in the residual glass.

#### 5.3.3.2 $^{27}Al$ MAS–NMR Spectroscopy

In Table 4.3.3.3, the $^{27}Al$ MAS–NMR spectra boron-substituted fluorine-free glass ceramics exhibit three peaks at around 50, 40 and -10 ppm. The peak at around 50 ppm is due to four-fold coordinated Al(IV) and five-fold coordinated Al(V); Al(VI) is present at around -10 ppm, and these three resonances are related to anorthite ($CaAl_2Si_2O_8$). With boron substitution for aluminium increasing, all the peaks decreased, except B50 glass-ceramic, which showed a very board region and a sharp peak due to the fact that the B50 glass is crystallised during the glass making. It can be seen in Table 4.3.3.4 that the $^{27}Al$ MAS–NMR spectra boron-substituted fluorine-

containing glass ceramics exhibit three peaks at around 55, 40 and 0 ppm, which are related to the presence of mullite ($Al_6Si_2O_{13}$) and aluminium phosphate ($AlPO_4$). Bodart et al. [222] reported that mullite synthesized by a sol-gel method exhibits three partially resolved resonances at -3, 43 and 56 ppm. He et al. [223] also reported the chemical shifts of mullite synthesized from different kaolinites as follows: Si-rich mullite exhibited peaks at -6, 45 and 64 ppm assigned to Al(VI) and two different Al(IV) environments, respectively. However, only two peaks at 0 ppm (Al(VI)) and 55 ppm (Al(IV)) were indicated in Si-deficient mullite spectra. The peak at around 40 ppm, which is observed in the spectrum of fluorine-containing glass-ceramic, is assigned to crystalline $AlPO_4$ [126]. In the present work, the peaks at around 40 ppm decreased as boron substitution increased. Furthermore, as discussed above in the XRD and the $^{29}Si$ MAS–NMR study, anorthite and mullite are formed after crystallisation in boron-substituted fluorine-free and fluorine-containing glass ceramics, respectively.

#### 5.3.3.3 $^{31}P$ MAS–NMR Spectroscopy

The $^{31}P$ MAS–NMR spectrum of boron-substituted fluorine-free glass heated at 1100$^oC$ shows a strong sharp peak at -3 ppm, which is assigned to the metaphosphate in tricalcium phosphate ($Ca_3(PO_4)_2$) [173], in Figure 4.3.3.5. This peak does not change as boron substitution increases. A small peak can be seen at around -28 ppm, which may be assigned to the polyphosphate in aluminium phosphate ($AlPO_4$) and

may indicate that there is a small amount of $AlPO_4$ phase crystallised in the boron-substituted fluorine-free glass-ceramics. However, no clear evidence was found in the XRD analysis, which implies that this phase must exist only in a very small amount. Stamboulis et al. [104] reported a $^{31}P$ NMR spectrum pattern of β-$Ca_3(PO_4)_2$ with two overlapped peaks at 0 and -2 ppm, whereas Aramendia et al. [224] pointed out that crystalline $Mg_3(PO_4)_2$ is present at -0.5 ppm in the $^{31}P$ MAS–NMR spectra of magnesium oxide-magnesium orthophosphate systems.

In Table and Figure 4.3.3.6, for boron-substituted fluorine-containing glass ceramics, the strong peak at around 2.4 ppm must be attributed to the orthophosphate groups in fluorapatite [$Ca_5(PO_4)_3F$], evidenced by the presence of a peak at -103 ppm in the $^{19}F$ MAS–NMR spectrum discussed below. On the other hand, for the fluorine-containing glass ceramics, a small peak at around -28 ppm in the $^{31}P$ NMR spectrum was assigned to $PO_4^{3-}$ in crystalline $AlPO_4$ by several authors [101, 126]. Dollase et al. [126], for example, suggested that the $^{31}P$ MAS–NMR chemical shift could be affected by the number of Al atoms around a $PO_4^{3-}$ tetrahedron. Furthermore, the peak assigned to $AlPO_4$ decreased gradually with increasing boron content. Aissa et al. [225] conducted $^{31}P$ MAS–NMR analysis on a series of barium/strontium fluorapatite solid solutions $Ba_{(10-x)}Sr_x(PO_4)_6F_2$ ($0 \leqq x \leqq 10$) and reported a chemical shift of 3.06 ppm for the Sr fluorapatite phase. Moran et al. [226] also obtained the $^{31}P$ MAS–NMR spectrum of a model compound $Sr_5(PO_4)_3F$, suggesting a chemical shift of 3.3 ppm for the above phase. Walter et al. [227] conducted a $^{31}P$ MAS–NMR study on the invert glass system $CaO\text{-}Na_2O\text{-}MgO\text{-}P_2O_5$ and claimed that polyphosphate glasses with a

metaphosphate composition were present in a chemical shift range from -15 to -21 ppm. In another published work, Scrimgeour et al. [173] also reported that phosphorus in metaphosphate was present between -15 and -25 ppm. A very broad peak at around -22 ppm in FB50 glass-ceramic was found, related possibly to metaphosphate or more likely to polyphosphates, which were most probably derived from residual glass. The XRD analysis indicates that both fluorapatite ($Ca_5(PO_4)_3F$) and aluminium phosphate ($AlPO_4$) phases are formed in fluorine-containing glass ceramics.

#### 5.3.3.4 $^{11}B$ MAS–NMR Spectroscopy

It is interesting to note, in Table 4.3.3.7 and 4.3.3.8, that the spectrum of boron-substituted fluorine-free and fluorine-containing crystallised glasses exhibits two similar peaks at around 0.5 and 9.5 ppm, which are assigned to the $BO_4$ group and $BO_3$ group, respectively. These are the same for all boron-substituted glasses, which suggests that the boron atom in glass ceramics was also very stable to form the $BO_4$ and $BO_3$ group and that no boron-containing crystallised phase was formed. And it is reported by Boussard-Plédel 33 ppm for $^{19}F$ (0 ppm for $C_6F_6$) and 12 ppm for $^{11}B$ (0 ppm for $Et_2OBF_3$) correspond to the resonance position of the respective nuclei in the $BF_3$ molecule, and the presence of the $BF_3$ in material is above $T_g$ (320K) [129]. However, it is not shown in our $^{11}B$ the NMR results, which suggest it is possible has a small amount $BF_3$ vaporized in boron substituted fluorine-containing glasses during

glass making.

### 5.3.3.5 $^{19}$F MAS–NMR Spectroscopy

Figure 4.3.3.9 shows the $^{19}$F MAS–NMR spectra of boron-substituted fluorine-containing glasses heat treated at 1100$^{o}$C. The peak associated with F-Ca(3) species in fluorapatite is present at -103 ppm in all fluorine-containing glass ceramics [95, 99]. The chemical shift of Ca-FAP does not change with the gradual boron substitution, and no boron phase is detected by either the XRD or the $^{19}$F MAS–NMR study on the above glass ceramics, which can be explained by the insufficient presence of B-F-Ca(n) species in the corresponding amorphous glasses. Stamboulis and Hill [104] suggested that F-Ca(n) species instead of Al-F-Ca(n) is preferentially used to form FAP. In addition, it can be seen that a small peak is present at about -110 ppm in FB0, FB5 and FB10 glass ceramics, the intensity of which decreases as the boron content increases and finally disappears in the case of FB15, FB25 and FB50 glass ceramics. Kiczenski and Stebbins [228] have assigned a series of peaks at -110 ppm to the Al-F-Ca(3) species. It is very difficult to conclude about the type of species present, as there is no other evidence to support the presence of Al-F-Ca crystalline phases in the glass ceramics. Therefore, it can only be suggested that the peak at around -110 ppm is most likely for the Al-F-Ca(3) species in $CaAlF_5$. Since only one peak has been observed in the current study and the main crystalline phase that contains fluorine has been identified as fluorapatite by XRD, it is logical to conclude that the peak at -103 ppm should correspond to F-Ca(3) species in fluorapatite.

### 5.3.4 ESEM and EDX analysis of boron-substituted glass ceramics

All the glass ceramics were etched by hydrofluoric acid, and the morphology and content of the crystal phase were shown in ESEM micrograph and EDX analysis.

Figure 4.3.4.1 shows an ESEM micrograph and EDX analysis for the fluorine-free glass ceramic (B0). The surface in the micrograph in Fig. 4.3.4.1exhibits 2-phase morphology: needle-like (tricalcium phosphate) and bulk-like (anorthite).

Figures 4.3.4.2 to 4.3.4.4 show (B2.5-B50) that calcium phosphorus's main phase, which is indicated by EDX, exhibits needle-like microstructure and morphology and aluminosilicate's main phase, which is indicated by EDX, exhibits bulk-like morphology. With an increase of boron-substituted aluminium, the needle-like morphology increased and clustered together. On the other hand, the bulk-like morphology got smaller and interlocked with non-oriented needle-like morphology. It seems that the crystal phases can be seen in a matrix of amorphous glass that was suggested by the XRD and the FTIR spectroscopy data. It is suggested that because of the lack of boron containing crystal phases in the glass ceramics, boron should be present in the remaining amorphous glass.

Figures 4.3.4.5 to 4.3.4.8 show the microstructure and morphology of different boron-substituted fluorine-containing glass ceramics. Figure 4.3.4.5 represents the ESEM and EDX analysis for FB0 glass ceramic. The etched surface of the glass ceramic seems to be very similar to the etched surfaces observed in previous work where

needle-like fluorapatite was present [229]. EDX analysis also showed that the needle-like morphology is due to the presence of fluorapatite and mullite. It is worth noticing in Fig. 4.3.4.7 that the light areas show needle-like morphology is related to a phase containing calcium phosphorus and fluorine, which was assigned to the fluorapatite phase, and the dark areas show a silicate aluminium main phase, which was assigned to the mullite phase, is interlocked with light areas. Figures 4.3.4.5 to 4.3.4.8 indicate that the needle-like crystals show the interlocked non-oriented morphology first and then show oriented morphology with a higher amount of boron substitution. The EDX measurements show clearly the presence of boron in the high amount of boron substitution glass ceramics although no boron-containing crystal phase was identified in the glass ceramics. This leads to the conclusion that boron must have remained in the amorphous glass. As explained in the XRD analysis section, with the lack of an increase of aluminium, the silicate aluminium main phase decreased, resulting in silicate being available within the amorphous glass network. Another possibility could be that fluorine forms Si-F linkages, resulting in the formation of $SiF_4$ and therefore some loss of weight at high temperatures, as observed in the TGA results. And with boron substitution, the morphology of the needle-like phase got bigger, which, due to the high amount of boron substitution for aluminium, decreased the $T_g$ and $T_p$, thus promoting the crystallisation of tricalcium phosphate and fluorapatite, respectively.

### 5.3.5 Summary

The smaller cation substitution of boron for aluminium also resulted in a decrease of the glass ceramic density due to the decrease of the aluminosilicate phase with boron substitution for aluminium, and no boron-containing phase appeared.

The FTIR spectra showed the O-P-O bending of phosphate groups ($\nu_4$) and were characteristic of a calcium phosphorus crystallised phase. When the sintering temperature was raised to 1100 $^{o}$C, there were more narrow peaks, which were assigned Al-O ($AlO_6$) stretching vibration and the Si-O-Si stretching ($Q^3$) and Si-O-[NBO] bands. The intensity of the band associated with Si-O-[NBO] generally decreased, which suggested that there was more Si-O-Si as well as bridging oxygens formed in the glass network.

The $^{29}$Si MAS-NMR spectra of the glasses heat-treated at above $T_{p2}$ (1100 $^{o}$C) showed the presence of $Q^4$(4Al) species in the anorthite phase in fluorine-free samples, one $Q^4$(4Al) species in the mullite phase in relevant fluorine-containing samples, and other $Q^4$(nAl) species (n = 0,1,2,3) in the glass residue. The $^{27}$Al MAS-NMR spectra indicated that Al(IV) and Al(VI) were present in all boron substitution heat-treated samples mainly due to the anorthite or mullite phase, while both $CaAl_2Si_2O_8$ and $Al_6Si_2O_{13}$ present in boron-substituted glass ceramics exhibited two different $Q^4$(4Si) species. Besides, crystalline $AlPO_4$ was found at a chemical shift of -39 ppm for all fluorine-containing crystallised samples. The presence of an orthophosphate environment ($PO_4^{3-}$, $Q^0$) due to different crystalline phases [e.g., $Ca_3(PO_4)_2$, $Ca_5(PO_4)_3F$] and phosphorus in a $Q^4$ environment ($AlPO_4$, $Q^4$) were identified by the

$^{31}P$ MAS-NMR spectra of corresponding crystallised samples with some phosphorous left in residual glass. It was suggested in $^{11}B$ MAS-NMR spectra that all the boron substitution glass ceramics in this study showed the same $BO_3$ and $BO_4$ groups, and it will not change by different boron content substitution, which suggests the boron atoms all go into the glass amorphous structure. $^{19}F$ MAS-NMR spectra suggested that F-Ca(3) species are associated with $Ca_3(PO_4)_2$ and $Ca_5(PO_4)_3F$. It is therefore reasonable to conclude that the presence of fluorine-containing species has a strong effect on the crystallisation of the glasses. There is clearly a connection between these species with the crystalline phases observed.

It is clear to see the microstructure and morphology of all boron-substituted glass ceramics, in which the needle-like phase is assigned to calcium phosphorus main phases and the bulk-like phase is assigned to silicate aluminium main phases. The needle-like morphology is non-oriented in fluorine-free glass ceramics. Nevertheless, the needle-like morphology is oriented in the case of a high amount of boron substitution for aluminium-fluorine-containing glass ceramics.

# CHAPTER 6 CONCLUSION

The effect of boron substitution for aluminium on the structure of both fluorine-free ($4.5SiO_2$-$3Al_2O_3$-$1.5P_2O_5$-5CaO) and fluorine-containing ($4.5SiO_2$-$3Al_2O_3$-$1.5P_2O_5$-3CaO-$2CaF_2$) glasses and the resultant glass ceramics has been studied by using a combination of analytical tools like helium pycnometer, FTIR, Raman, XRD, multinuclear MAS-NMR spectroscopy and thermal analysis by DSC and TGA. The morphology of the crystal phases was observed by ESEM, and the identification of the crystals observed was achieved by EDX.

High amount of boron-substituted aluminium glass (75 and 100 molar%) couldn't be processed due to phase separation and glass crystallisation. Boron couldn't substitute for a larger amount of aluminium in the glass structure. It is very hard to make aluminium-free glass, but we can reduce the content of aluminium (less than 50mol%) in the glass composition which is expected in the objectives.

The density of both boron-substituted aluminium glasses and glass ceramics decreased with increasing boron content. The oxygen density of both glasses slightly increased, which suggested a more compact glass network. Boron atoms in the glass acted as glass formers also indicated by FTIR spectroscopy that suggested an increase of bridging oxygens with boron substitution. The glasses and glass ceramics with lower density and more compact network structure will be expected have better mechanical property.

The glass transition temperature decreased generally with an increase of boron

substitution in fluorine-free glasses, and the $T_g$ remained almost stable in fluorine-containing glasses. It is suggested that the glass shows a more packed structure and a little bit higher glass crystallisation temperature with a small amount of boron substitution. With a high amount of boron substitution for aluminium, the $T_g$ and $T_p$ decreased obviously, which promoted the Ca-P main phase crystallising at a lower temperature. The $T_g$ and $T_p$ increased with increasing the heating rate to 20 $^oC$/min and 40 $^oC$/min, respectively. It is likely that the mixed cation effect is also present for the crystallisation peak temperature $T_p$ in all samples. It is worth noticing that all the thermogravimetric analyses were conducted on fine powder glass samples and it was expected that if there was a weight loss this should be due to the larger surface area. It is suggested that there was a small fluorine loss from the surface of the fluorine-containing glasses due to possible $SiF_4$ formation during heating.

The FTIR and Raman spectra were not very conclusive. There were 5 absorption regions in the FTIR spectra of all boron-substituted glasses, associated with the following bonds: (1) Si-O-Si ($Q^4$) and Si-O-Si ($Q^3$) stretching vibrations as well as Si-O-[NBO], (2) Al-O vibrations with Al in a fourfold coordination state, (3) P-O bending vibrations and Si-O-Al linkages, (4) Si-O-Si bending vibrations, and (5) B-O-B bending vibrations, respectively. With an increase of the boron substitution for aluminium, the peaks related to Si-O-NBOs decreased in intensity, suggesting that there was a decrease in the number of NBOs. When the sintering temperature was raised to 1100 $^oC$, 2 bands at 566 $cm^{-1}$ and 603 $cm^{-1}$ were attributed to the O-P-O bending of phosphate ($\nu_4$), whereas the band centred at 472 $cm^{-1}$ was caused by the

phosphate bending ($\nu_2$) vibration. Al-O($AlO_4$) bonds were found to be present around 735 $cm^{-1}$, and the band centred at 668 $cm^{-1}$ was related to the Al-O bond in $AlO_6$. This was observed in the FTIR spectra of all boron-substituted glass ceramics, implying an increasing preference of Ca-P formation proved by the XRD study as well.

With different sintering temperatures of 700 $^oC$, 900 $^oC$, and 1100 $^oC$, it was indicated in the fluorine-free glass ceramics that calcium phosphate ($Ca_4P_2O_9$) was the first phase to be formed below the sintering temperature at 900 $^oC$. When the sintering temperature was raised to 1100 $^oC$, the calcium phosphate ($Ca_4P_2O_9$) phase transferred to the tricalcium phosphate [$Ca_3(PO_4)_2$] phase, and anorthite was crystallised subsequently as a second phase. With increasing boron substitution, the anorthite phase was decreased and there was no boron-containing phase, which suggested the boron goes into an amorphous phase. The fluorapatite phase was the first phase to be formed in the fluorine-containing glass ceramics, and with the sintering temperature raised to 1100 $^oC$, the mullite and aluminium phosphorus phases were crystallised in the glass structure and were decreased with the increase of boron substitution. Tricalcium phosphate and fluorapatite phases are expected to afford good bioability in glasses and glass ceramics, Moreover, anorthite and mullite phases are expected to improve mechanical properties.

The Si atoms were present as both $Q^4(4Al)$ and $Q^3(3Al)$ species in the lower amount ( < 15%) of boron-substituted glass samples within the current work, but more different Si species, including $Q^4(4Al)$, $Q^4(3Al)$, $Q^4(2Al)$, and $Q^4(1Al)$, were present in the case of a high amount ($\geqq$15%) of boron-substituted glasses, indicated by the

$^{29}Si$ MAS-NMR study. The $^{29}Si$ MAS-NMR spectra of the glasses heat-treated at above $T_{p2}$ (1100 $^{o}C$) showed the presence of $Q^4(4Al)$ species in the anorthite phase in fluorine-free samples and one $Q^4(4Al)$ species in the mullite phase in relevant fluorine-containing samples.

The $^{27}Al$ MAS-NMR spectra indicated that Al(IV) was present in all boron-substituted glasses. However, in the case of boron-substituted fluorine-containing glasses, a small but clear peak with increasing intensity appeared at -4.0 ppm attributed to sixfold coordinated Al(VI). The $^{27}Al$ MAS-NMR spectra indicated that Al(IV) and Al(VI) were present in all boron substitution heat-treated samples mainly due to the anorthite or mullite phase, and the crystalline $AlPO_4$ was found at a chemical shift of -39 ppm for all fluorine-containing crystallised samples.

The $^{31}P$ MAS-NMR spectrum of boron-substituted glass ceramics showed the presence of orthophosphate ($PO_4^{3-}$, $Q^0$), associated with calcium phosphate ($Ca_3(PO_4)_2$) in fluorine-free glass ceramic samples and fluorapatite ($Ca_5(PO_4)_3F$) in fluorine-containing glass ceramic samples. In addition, phosphorus in a $Q^4$ environment ($AlPO_4$) was identified by the $^{31}P$ MAS-NMR spectra in fluorine-containing crystallised samples.

The $^{11}B$ MAS-NMR spectra of all the boron substitution glasses and glass ceramics in this study showed the same $BO_3$ and $BO_4$ groups, and this was not changed by different boron content substitutions, which suggested the boron atoms remain the amorphous glass structure.

Fluorine was present as F-Ca(n) species and Al-F-Ca(n) species in boron-substituted

glasses. On the other hand, there were mixed fluorine species F-Ca(n) and Al-F-Ca(n) present in the case of boron-substituted glasses. And there was a decrease in Al-F-Ca(n) species with increasing boron substitution for aluminium. In all boron-substituted glass ceramics $^{19}F$ MAS-NMR spectra suggested that fluorine atoms were present as F-Ca(3) species in $Ca_3(PO_4)_2$ and $Ca_5(PO_4)_3F$. The MAS-NMR research shows strong evidence to characterize the details of bonds and phases.

From ESEM and EDX analysis, the microstructure and morphology of all boron-substituted glass ceramics indicated a needle-like phase was assigned to calcium phosphate main phases and the bulk-like phase was assigned to crystalline aluminosilicate main phases. The needle-like morphology was non-oriented in fluorine-free glass ceramics ( < 15mol%). However, the needle-like morphology was oriented in cases of a high amount (≧15mol%) of boron substitution for aluminium-fluorine-containing glass ceramics.

**Summary:**

In this work, in order to reduce the aluminum contents in biological ceramic-glass, boron was used in this glass to substitution aluminum. The phases of tricalcium phosphate, anorthite and fluorapatite, mullite crystallized separately in boron substituted aluminium fluorine-free and fluorine-containing glass ceramics.

In the low amount of boron substitution ( < 15mol%), the glasses and glass-ceramics show more stable and interlocking phases in glass microstructure which will potentially improve mechanical and biological properties. In high amount of boron

substitution (≧15mol%), the glasses and glass-ceramics indicate more uncontrolled phase separation and crystallization, which increase the solubility of boron-containing glasses thus increase the overall dissolution of alminium.

# CHAPTER 7 FUTURE WORK

Due to the split-location PhD programme, I also did a study on the effect of boron-substituted aluminium in secondary nickel slag glass ceramics ($SiO_2$-$Al_2O_3$-CaO-$Na_2O$-$K_2O$-BaO-ZnO-$CaF_2$) in China. This material is a decorate-building glass ceramic, and the boron-substituted aluminium showed some similar influences: 1) it decreased the $T_g$ and $T_p$, 2) it promoted the phase separation, and 3) it increased the mechanical property of glass ceramics when the boron substitution was less than 15 mol%. We also built a factory in China in 2012 to produce this nickel slag glass ceramic, which is used in a composition for 10 mol% boron-substituted aluminium based on a $SiO_2$-$Al_2O_3$-CaO- $Na_2O$-$K_2O$-BaO-ZnO-$CaF_2$ system. This product is now exported to the Middle East and Japan as a decorative material. In the future, further work should be carried out in order to develop a complete understanding of the crystallisation mechanism for boron-substituted glasses as well as the structures of both glasses and glass ceramics and to improve the glass composition:

1. The multinuclear MAS-NMR study has been used to study the atomic environment of $^{29}Si$, $^{27}Al$, $^{31}P$, $^{11}B$, and $^{19}F$ in both glasses and glass ceramics, but $^{17}O$ MAS-NMR would give more insight into the structure and confirm some of our suggestions made in the current study so far.
2. An X-ray fluorescence (XRF) and attenuated total reflection (ATR) study should be conducted on all boron-substituted glasses and glass ceramics in order to establish the content of fluorine in the fluorine-containing glasses and glass

ceramics and the exact boron bonds in the amorphous phase in all the glasses and glass ceramics.

3. Biocompatibility tests should be conducted on all crystallised samples in order to assess their possibility as bone replacements for medical and dental applications.
4. Mechanical tests should also be conducted on all crystallised samples due to the more packed glass structure by using a small amount of boron to substitute for aluminium.
5. Finally, the glass composition should be improved by adding in a new element (like Ge, germanium) to substitute for the aluminium in order to develop aluminium-free bioglasses and bioglass ceramics.

# REFERENCES

[1] A. Clifford, R. Hill, "The influence of calcium to phosphate ratio on the nucleation and crystallization of apatite glass-ceramics", *Journal of Materials Science: Materials in Medicine*, vol. 12, pp. 461-469, 2001.

[2] W. Höland, P. Wange, "Control of phase formation processes in glass-ceramics for medicine and technology", *Journal of Non-Crystalline Solids*, vol. 129, pp. 152-162, 1991.

[3] T. Kokubo, J. M. Sautier, "Bioactive glass-ceramic containing crystalline apatite and wollastonite initiates biomineralization in bone cell cultures." *Calcified Tissue International*, vol. 55(6), pp. 458-466, 1994.

[4] C. O. Freeman, I. M. Brook, A. Johnson, P. V. Hatton, K. T. Stanton, R. G. Hill, "Crystallization modified osteoconductivity in an apatite-mullite glass-ceramic". *Journal of Materials Science: Materials in Medicine*, vol. 14, pp. 985-990, 2003.

[5] R. A. Martin, Z. Jaffer, A. Stamboulis, "An X-ray micro-fluorescence study to investigate the distribution of Al, Si, P and Ca ions in the surrounding soft tissue after implantation of a calcium phosphate-mullite ceramic composite in a rabbit animal model." *Journal of Materials Science: Materials in Medicine*, vol. 22, pp. 2537-2543, 2011.

[6] M. Bengisu, R. K. Brow, *Journal of Non-Crystalline Solids*, vol. 352, pp. 3668-3676, 2006.

[7] F. J. Schoen, "Chapter II.2.1 - Introduction: Biological Responses to Biomaterials". *Biomaterials Science (Third Edition)*, B. D. R. S. H. J. S. E. Lemons, Academic Press: 499-503, 2013.

[8] L. L. Hench, D. R. Ulrich, "Composite Structures", *Science of Ceramic Chemical Processing*, vol. 7, pp. 227, 1987.

[9] M. N. Rahaman, "Bioactive ceramics and glasses for tissue engineering", *Tissue Engineering Using Ceramics and Polymers (Second Edition)*, pp. 67-114, 2014.

[10] E. Verné, M. Bruno, "Bioactive ceramics and glasses for tissue engineering",

*Materials Science and Engineering*, vol. 53, pp. 95-103, 2015.

[11] S. Xu, X. Yang, "Effect of borosilicate glass on the mechanical and biodegradation properties of 45S5-derived bioactive glass-ceramics", *Journal of Non-Crystalline Solids*, vol. 405, pp. 91-99, 2014.

[12] M. C. Crovace, M. T. Souza, "Biosilicate® — A multipurpose, highly bioactive glass-ceramic. In vitro, in vivo and clinical trials", *Journal of Non-Crystalline Solids*, vol. 432, pp. 90-110, 2016.

[13] O. Peitl, E.D. Zanotto, G.P. La Torre, L.L. Hench, "Bioactive ceramics and method of preparing bioactive ceramics", Patent WO/1997/041079, 1997.

[14] M. Vogel, C. Voigt, U. M. Gross, "In vivo comparison of bioactive glass particles in rabbits", *Biomaterials*, vol. 22, pp. 357-362, 2001

[15] M. Bunte, V. Strunz, "Ceramic augmentation of the lower jaw", *Journal of Maxillofacial Surgery*, vol. 5, pp. 303-309, 1977.

[16] V. Strunz, U. Gross, "Transfixation of teeth with titanium plasma-coated pins in animal experiments fixation", *International Journal of Oral and Maxillofacial Surgery*, vol.17, pp. 149, 1988.

[17] D. Schumacher, V. Strunz, "Does piezoceramic influence avian bone formation in the early postoperative phase?", *Biomaterials*, vol. 4, pp. 215-217, 1983.

[18] T. De Caluwé, C. W. J. Vercruysse, "Bioactivity and biocompatibility of two fluoride containing bioactive glasses for dental applications." *Dental Materials* vol. 32, pp. 1414-1428, 2016.

[19] S. K. Arepalli, H. Tripathi, "Enhanced bioactivity, biocompatibility and mechanical behavior of strontium substituted bioactive glasses." *Materials Science and Engineering: C*, vol. 69, pp. 108-116, 2016.

[20] S. Zhao, J. Zhang, "Three-dimensional printed strontium-containing mesoporous bioactive glass scaffolds for repairing rat critical-sized calvarial defects." *Acta Biomaterialia* vol. 12, pp. 270-280, 2015.

[21] F. C. M. Driessens, M. G. Boltong, "The Ca/P range of nanoapatitic calcium phosphate cements", *Biomaterials*, vol. 23, pp. 4011-4017, 2002.

[22] F. BarrÈre, P. Layrolle, K. de Groot, "Biomimetic calcium phosphate coatings on Ti6Al4V: a crystal growth study of octacalcium phosphate and inhibition by $Mg^{2+}$and $HCO^{3-}$", *Bone*, vol. 25, pp. 107S-111S, 1999.

[23] S. Yamada, D. Heymann, "Osteoclastic resorption of calcium phosphate ceramics with different hydroxyapatite/β-tricalcium phosphate ratios", *Biomaterials*, vol. 18, pp. 1037-1041, 1997.

[24] M. Benahmed, J. M. Bouler, "Biodegradation of synthetic biphasic calcium phosphate by human monocytes *in vitro*: a morphological study", *Biomaterials*, vol. 17, pp. 2173-2178, 1996.

[25] L. Xie, H. Yu, "Preparation, characterization and in vitro dissolution behavior of porous biphasic α/β-tricalcium phosphate bioceramics", *Materials Science and Engineering*, vol. 59, pp. 1007-1015, 2016.

[26] M. D. Snyder, B. R. Lang, and M. E. Razzoog, "The efficacy of luting all-ceramics crowns with resin-modified glass ionomer cement", *American Dental Association*, vol. 134, pp. 609-612, 2003.

[27] A. D. Wilson and B. E. Kent, "Dental Cements: Decomposition of the Powder", *Journal of Dental Research*, pp. 7-13, 1970.

[28] A. D. Wilson and B. E. Kent, "A new translucent cement for dentistry", *British Dental Journal*, vol. 132, pp. 133-135, 1972.

[29] J. E. Shelby, "Introduction to Glass Science and Technology (RSC paperbacks)", *The Royal Society of Chemistry*, 1997.

[30] J. W. Nicholson, "Chemistry of glass-ionomer cements: a review", *Biomaterials*, vol. 19, pp. 485-494, 1998.

[31] A. D. Wilson, D. M. Groffman & A. T. Kuhn, *Biomaterials*, vol. 6, pp. 431-433, 1985.

[32] K. Stanton, R. Hill, "The role of fluorine in the devitrification of $SiO_2 \cdot Al_2O_3 \cdot P_2O_5 \cdot CaO \cdot CaF_2$ glasses", *Journal of Materials Science*, vol. 35, pp. 1911–1916, 2000.

[33] C.M. Crowley, J. Doyle, M. R. Towler, R. G. Hill, and S. Hampshire, "The influence of capsule geometry and cement formulation on the apparent viscosity of

dental cement", *Journal of Dentistry*, vol. 34, pp. 566-573, 2006.

[34] M. R. Towler, C. M. Crowley, and R. G. Hill, "Investigation into the ultrasonic setting of glass ionomer cements: Part I. Postulated modalities", *Journal of Materials Science Letters*, vol. 22, pp. 539-541, 2003.

[35] A. Guida, R. G. Hill, M. R. Towler, S. Eramo, "Fluoride release of model glass ionomer cements", *Journal of Materials Science: Materials in Medicine*, vol. 13, pp. 645-649, 2002.

[36] S. G. Griffin and R. G. Hill, "Influence of glass composition on the properties of glass polyalkenoate cements. Part IV: influence of fluorine content", *Biomaterials*, vol. 2, pp. 693–698, 2000.

[37] D. J. Fleck, "The chemistry of oxyphosphates", *Dent Items Interest*, vol. 24, pp. 906, 1902.

[38] N. Garg, A. Garg, Textbook of Operative Dentistry, 2nd Edition. Jaypee Brothers Medical Publishers (P) Ltd., New Dehli., pp. 428, 2013.

[39] B. M. Culbertson, "Glass-ionomer dental restoratives", *Progress in Polymer Science*, vol. 26, pp. 577-604, 2001.

[40] C. J. Whitters, R. Strang, "Dental materials: 1997 literature review", *Journal of Dentistry*, vol. 27, pp. 401-435, 1999.

[41] S. G. Griffin and R. G. Hill, "Influence of glass composition on the properties of glass polyalkenoate cements. Part I: influence of aluminium to silicon ratio", *Biomaterials*, vol. 20, pp. 1579–1586, 1999.

[42] R. Hill, D. Wood, and M. Thomas, "Trimethylsilylation analysis of the silicate structure of fluoro-alumino-silicate glasses and the structural role of fluorine", *Journal of Materials Science*, vol. 34, pp. 1767-1774, 1999.

[43] S. G. Griffin and R. G. Hill, "Influence of glass composition on the properties of glass polyalkenoate cements. Part II: influence of phosphate content", *Biomaterials*, vol. 21, pp. 399–403, 2000.

[44] R. G. Hill, A. Stamboulis, and R. V. Law, "Characterisation of fluorine containing glasses by F-19, Al-27, Si-29 and P-31 MAS-NMR spectroscopy", *Journal of Dentistry*, vol. 34, pp. 525–532, 2006.

[45] E. De Barra, R. G. Hill, "Influence of glass composition on the properties of glass polyalkenoate cements. Part III: influence of fluorite content", *Biomaterials*, vol. 21, pp. 563–569, 2000.

[46] S. G. Griffin, R. G. Hill, "Glass composition influence on glass polyalkenoate cement mechanical properties", *Journal of Non-Crystalline Solids*, vol. 196, pp. 255-259, 1996.

[47] R. Hill, D. Wood, "Apatite-mullite glass ceramics", *Journal of Materials Science*, vol. 6, pp. 311–318, 1995.

[48] C. M. Gorman, R. G. Hill, "Heat-pressed ionomer glass-ceramics. Part I: an investigation of flow microstructure", *Dental Materials*, vol.19, pp. 320-326, 2003.

[49] C. Moisescu, C. Jana, S. Habelitz, G. Carl, and C. Russel, "Oriented fluoroapatite glass-ceramics", *Journal of Non-Crystalline Solids*, vol. 248, pp. 176-182, 1999.

[50] J. C. C. Chan, R. Ohnsorge, K. Meise-Gresch, H. Eckert, W. Holand, and V. Rheinberger, "Apatite crystallization in an aluminosilicate glass matrix: Mechanistic studies by X-ray powder diffraction, thermal analysis, and multinuclear solid-state NMR spectroscopy", Chemistry of Materials, vol. 13, pp. 4198-4206, 2001.

[51] I. M. Brook, P. V. Hatton, "Glass-ionomers: bioactive implant materials", *Biomaterials*, vol. 19, pp. 565-571, 1998.

[52] I. M. Brook, G. T. Craig, D. J. Lamb, "In vitro interaction between primary bone organ cultures, glass ionomer cements and hydroxyapatite/tricalcium phosphate ceramics". *Biomaterials*, vol. 12, pp. 179-186, 1991.

[53] P. V. Hatton, I. M. Brook, "Characterisation of the ultrastructure of glass ionomer (poly-alkenoate) cement. *British Dental Journal*, vol. 173, pp. 275-277, 1992.

[54] P. V. Hatton, I. M. Brook, "X-ray microanalysis of bone and implanted bone substitutes". *Micron and Microscopica Acta*, vol. 23, pp. 363-364, 1992.

[55] P. V. Hatton, K. Hurrell-Gillingham, I. M. Brook, "Biocompatibility of glass ionomer bone cements". *Journal of Dentistry*, vol. 34, pp. 598-601, 2006.

[56] D. Xie, W. A. Brantley, B. M. Culbertson, and G. Wang, "Mechanical properties and microstructures of glass-ionomer cements", *Dental Materials*, vol. 16, pp. 129-138, 2000.

[57] M. Massler, D. S. Berman,and V. E. James, "Pulp capping and pulp amputation", *Dental Clinics of North America*, pp. 797, 1957.

[58] D. B. Mahler, G. K. Armen, "Addition of amalgam alloy to zinc phosphate cement", *Journal of Prosthetic Dentistry*, vol. 12(1), pp. 157-164, 1962.

[59] D. K. Bremner, "The story of dentistry", *Revised. 3rd ed. Brooklyn: Dental Items of Interest Publishing Co Inc.*, 1954.

[60] J. Forrai, "Culture history of dentistry", *Budapest: Dental Press*; pp. 84-113, 2005.

[61] R. B. McCoy, "Dental amalgam: the state of the art and science", *3rd ed. Philadelphia: Saunder*s, 1993.

[62] U. Lohbauer, "Dental glass ionomer cements as permanent filling materials? - properties, limitations and future trends", *Materials*, vol. 3(1), pp. 76-96, 2010.

[63] H. F. Albers. "Tooth-colored restoratives: principles and techniques", *9th Edition. BC Beckers Inc.*, pp. 44, 2002.

[64] C. H. Pierce. "Discussion, Pennsylvania Association of Dental Surgery", vol. 21, pp. 696-697, 1870.

[65] W. V. B. Ames, "A new oxyphosphate for crown setting", *Dental Cosmos*, vol. 34, pp. 392-394, 1892.

[66] D. J. Fleck, "The chemistry of oxyphosphates", *Dent Items Interest*, vol. 24, pp. 906, 1902.

[67] P. Steenbock, "Improvements in and relating to the manufacture of a material designed for the production of cement", *UK Patents Nos. 15176*, *15181*, 1954.

[68] F. Schoenbeck, "Process for the production of tooth material", *US Patent No. 897160*, 1908.

[69] J. M. Antonucci, J. E. McKinney, and J. W. Stansbury, "Resin- modified glass-ionomer cement", *US Patent Application, 160:856*, 1988.

[70] S. B. Mitra, "Photocurable ionomer cement systems", *European Patent Application No. 0 323 120 A2.*, 1989.

[71] R. J. Smales, H. Yip, "The atraumatic restorative treatment (ART) approach for primary teeth: review of literature", *American Academy of Pediatric Dentistry*, vol.22, pp. 294-298, 2000.

[72] T. S. Carvalho, T. R. Ribeiro, M. Boenecker, E.C. Pinheiro, and V. Colares, "The Atraumatic Restorative Treatment approach: an “atraumatic” alternative", *Medicina Oral, Patología Oraly Cirugía Buca*l, vol. 14, pp. 668-673, 2009.

[73] A. U. Yap, Y. S. Pek, and P. Cheang, "Physico-mechanical properties of a fast-set highly viscous GIC restorative", *Journal of Oral Rehabilitation*, vol. 30, pp. 1-8, 2003.

[74] K. M. Y. Hse, S. K. Leung, and S. H. Y. Wei, "Resin-ionomer restorative materials for children: A review", *Australian Dental Journal*, vol. 44, pp. 1-11, 1999.

[75] USAF Dental Evaluation & Consultation Service.

[76] D. Boyd, M. R. Towler, R. V. Law, and R. G. Hill, "An investigation into the structure and reactivity of calcium-zinc-silicate ionomer glasses using MAS-NMR spectroscopy", *Journal of Materials Science: Materials in Medicine*, vol. 17, 2006.

[77] B.E. Yekta, P. Alizadeh, and L. Rezazadeh, "Synthesis of glass-ceramic glazes in the $ZnO$-$Al_2O_3$-$SiO_2$-$ZrO_2$ system", *Journal of the European Ceramic Society*, vol. 27, pp. 2311-2315, 2007.

[78] G. Lusvardi, G. Malavasi, L. Menabue, and M. C. Menziani, "Synthesis, characterization, and molecular dynamics simulation of $Na_2O$-$CaO$-$SiO_2$-$ZnO$ glasses", *Journal of Physical Chemistry B*, vol. 106, pp. 9753-9760, 2002.

[79] Y.-H. Cho, S.-J. Lee, J. Y. Lee, S. W. Kim, C. B. Lee, W. Y. Lee, and M. S. Yoon, "Antibacterial effect of intraprostatic zinc injection in a rat model of chronic bacterial prostatitis", *International Journal of Antimicrobial Agents*, vol. 19, pp. 576-582, 2002.

[80] C. M. Gorman and R. G. Hill, "Heat-pressed ionomer glass-ceramics. Part II. Mechanical property evaluation", *Dental Materials*, vol. 20, pp. 252-261, 2004.

[81] A. Calver, R. G. Hill and A. Stamboulis, "Influence of fluorine content on the crystallization behavior of apatite-wollastonite glass-ceramics", *Journal of Non-*

*Crystalline Solids*, vol. 248, pp. 169-175, 1999.

[82] A. Clifford and R. Hill, "Apatite-mullite glass-ceramics", *Journal of Materials Science*, vol. 39, pp. 2601-2603, 2004.

[83] A. D. Wilson, S. Crisp, H. J. Prosser, B. G. Lewis, and S. A. Merson, "Aluminosilicate glasses For Poly-Electrolyte Cements", *Industrial & Engineering Chemistry Product Research And Development*, vol. 19, pp. 263-270, 1980.

[84] K. Greene, M. J. Pomeroy, S. Hampshire, and R. Hill, "Effect of composition on the properties of glasses in the K2O-BaO-MgO-$SiO_2$-$Al_2O_3$-$B_2O_3$-$MgF_2$ system", *Journal of Non-Crystalline Solids*, vol. 325, pp. 193-205, 2003.

[85] C. Moisescu, C. Jana, and C. Russel, "Crystallisation of rod-shaped fluoroapatite from glass melts in the system $SiO_2$-$Al_2O_3$-CaO-$P_2O_5$-$Na_2O$-$K_2O$-F", *Journal of Non-Crystalline Solids*, vol. 248, pp. 169-175, 1999.

[86] L. vanWullen, L. Zuchner, W. MullerWarmuth, and H. Eckert, "B-11{Al-27} and Al-27{B-11} double resonance experiments on a glassy sodium aluminoborate", *Solid State Nuclear Magnetic Resonance*, vol. 6, pp. 203-212, 1996.

[87] M. Bengisu, R. K. Brow, E. Yimaz, A. Mogus-Milankovic, and S. T. Reis, "Aluminoborate and aluminoboro silicate glasses with high chemical durability and the effect of $P_2O_5$ additions on the properties", *Journal of Non-Crystalline Solids*, vol. 352, pp. 3668-3676, 2006.

[88] H. Doweidar, Y. M. Moustafa, S. Abd El-Maksoud, and H. Silim, "Properties of $Na_2O$-$Al_2O_3$-$B_2O_3$ glasses", *Materials Science And Engineering A-Structural Materials Properties Microstructure And Processing*, vol. 3001, pp. 207-212, 2001.

[89] G. El-Damrawi and H. Doweidar, "Dependence of properties on structural units in $Li_2O$-$Al_2O_3$-$SiO_2$ glasses", *Physics And Chemistry of Glasses*, vol. 42, pp. 116-120, 2001.

[90] P. Pernice, S. Esposito, A. Aronne, and V. N. Sigaev, "Structure and crystallization behavior of glasses in the BaO-$B_2O_3$-$Al_2O_3$ system", *Journal of Non-Crystalline Solids*, vol. 258, pp. 1-10, 1999.

[91] A. D. Neve, V. Piddock, and E. C. Combe, "Development of novel dental cements. I. Formulation of aluminoborate glasses", *Clinical Materials*, vol. 9, pp. 7-

12, 1992.

[92] A. D. Neve, V. Piddock, and E. C. Combe, "The effect of glass heat treatment on the properties of a novel polyalkenoate cement", *Clinical Materials*, vol. 12, pp. 113-115, 1993.

[93] A. D. Neve, V. Piddock, and E. C. Combe, "Development of novel dental cements. II. Cement properties", *Clinical Materials*, vol. 9, pp. 13-20, 1992.

[94] I. W. Donald, B. L. Metcalfe, D. J. Bradley, M. J. C. Hill, L, McGrath, and A. D. Bye, "The preparation And Properties Of Some Lithium Borate Based Glasses", *Journal Of Materials Science*, vol. 29, pp. 6379-6396, 1994.

[95] W. H. Zachariasen, "The atomic arrangements in glass", *Journal of the American Chemical Society*, vol. 54, pp. 3841-3851, 1932.

[96] J. E. Shelby, "Introduction to Glass Science and Technology (RSC paperbacks)", The Royal Society of Chemistry, 1997.

[97] W. Lowenstein, "The distribution of aluminium in the tetrahedral of silicates and aluminates", *American Mineralogist*, vol. 39, pp. 92-96, 1954.

[98] J. F. Stebbins and Z. Xu, " NMR evidence for excess non-bridging oxygen in an aluminosilicate glass", *Nature*, vol. 390, pp. 60-62, 1997.

[99] R. Hill, A. Calver, A. Stamboulis, and N. Bubb, "Real time nucleation and crystallization studies of a fluorapatite glass-ceramics using small angle neutron scattering and neutron diffraction", *Journal of the American Ceramic Society*, vol. 90, pp. 763-768, 2007.

[100] R.Hill, A. Calver, S. Skinner, A. Stamboulis, and R. Law, "A MAS-NMR and combined Rietveldt study of mixed calcium/strontium fluorapatite glass-ceramics", in *Bioceramics 18, Pts 1 And 2, vol. 309-311, Key Engineering Materials*, pp. 305-308, 2006.

[101] A. Clifford, A. Rafferty, R. Hill, P. Mooney, D. Wood, B. Samuneva, and S. Matsuya, "The influence of calcium to phosphate ratio on the nucleation and crystallization of apatite glass-ceramics", *Journal of Materials Science: Materials in Medicine*, vol. 12, pp. 461-469, 2001.

[102] A. Stamboulis, R. G. Hill, and R. V. Law, "Characterization of the structure of

calcium alumino-silicate and calcium fluoro-alumino-silicate glasses by magic angle spinning nuclear magnetic resonance (MAS-NMR)", *Journal of Non-Crystalline Solids*, vol.333, pp. 101–107, 2004.

[103] A. Stamboulis, R. G. Hill, and R. V. Law, "Structural characterization of fluorine containing glasses by F-19 Al-27 Si-29 and P-31 MAS-NMR spectroscopy", *Journal of Non-Crystalline Solids*, vol. 351, pp. 3289-3295, 2005.

[104] A. Stamboulis, R. G. Hill, R. V. Law, and S. Matsuya, "MAS-NMR study on the crystallization process of apatite-mullite glass ceramics", *Physics and Chemistry of Glasses*, vol. 45, pp. 127-133, 2004.

[105] R. J. Kirkpatrick and R. K. Brow, "Nuclear-Magnetic-Resonance investigation of the structures of phosphate and phosphate-containing glasses- a review", *Solid State Nuclear magnetic Resonance*, vol. 5, pp. 9-21, 1995.

[106] R. Dupree, D. Holland, M. G. Mortuza, J. A. Collins, and M. W. G. Lockyer, "Magic angle spinning NMR of alkali phosphor-aluminosilicate glasses", *Journal of Non-Crystalline Solids*, vol. 112, pp. 111-119, 1989.

[107] B. E. Kent, B. G. Lewis, and A. D. Wilson, "Glass ionomer cement formulations. 1. Preparation of novel fluoroaluminosilicate glasses high in fluorine", *Journal of Dental Research*, vol. 58, pp. 1607-1619, 1979.

[108] T. J. Kiczenski, L.-S. Du, and J. F. Stebbins, "F-19 NMR study of the ordering of high field strength cations at fluoride sites in silicate and aluminosilicate glasses", *Journal of Non-Crystalline Solids*, vol. 337, pp. 142-149, 2004.

[109] R. G. Hill and A. D. Wilson, "Some structural aspects of glasses used in ionomer cements", *Glass Technology*, vol. 29, pp. 150-157, 1988.

[110] Q. Zeng and J. F. Stebbins, "Fluoride sites in aluminosilicate glasses: High-resolution F-19 NMR results", *American Mineralogist*, vol. 85, pp. 863-867, 2000.

[111] J. F. Stebbins, S. Kroeker, S. K. Lee, and T. J. Kiczenski, "Quantification of five- and six-coordinated aluminum ions in aluminosilicate and fluoride-containing glasses by high-field, high-resolution Al-27 NMR", *Journal of Non-Crystalline Solids*, vol. 275, pp. 1-6, 2000.

[112] A. Stamboulis, R. V. Law, and R. G. Hill, "Characterisation of commercial

ionomer glasses using magic angle nuclear magnetic resonance(MAS-NMR)," *Biomaterials*, vol. 25, pp. 3907-3913, 2004.

[113] S. Matsuya, A. Stamboulis, R. G. Hill, and R. V. Law, "Structural characterisation of ionomer glasses by multinuclear solid state MAS-NMR spectroscopy," *Journal of Non-Crystalline Solids*, vol. 353, pp. 237-243, 2007.

[114] F. M. Ernsberger, D.R. Uhlmann, and N.J. Kreidle, "In Glass: Science and Technology", *Eds; Acad. New York*, vol. 5, 1980.

[115] L. Kathy, "Profiles in Ceramics: S. Donald Stookey". *American Ceramic Society Bulletin:*, pp. 34–39. 2000.

[116] W. Höland, G. Beall, "Glass-Ceramic Technology", *The American Ceramic Society*, 2002.

[117] P.W. McMillan, "Glass-Ceramics", *Academic Press, New York*, 1979.

[118] S. Jalota, S. B. Bhaduri, and A. C. Tas, "A new rhenanite (beta-NaCaPO4) and hydroxyapatite biophasic biomaterial for skeletal repair," *Journal Of Biomedical Materials Research Part B-Applied Biomaterials*, vol. 80B, pp. 304-316, 2007.

[119] T. Nakamura, T. Yamamuro, S. Higashi, T. Kokubo, and S. Itoo, "A New Glass-Ceramic For Bone-Replacement - Evaluation Of Its Bonding To Bone Tissue," *Journal Of Biomedical Materials Research*, vol. 19, pp. 685-698, 1985.

[120] P. J. Adair, D. G. Grossman, "The castable ceramic crown," *Int J Periodontics Restorative Dent*, vol. 4, pp. 32-46, 1984.

[121] A. Rafferty, A. Clifford, R. Hill, D. Wood, B. Samuneva, and M. Dimitrova-Lukacs, "Influence of fluorine content in apatite-mullite glass ceramics," *Journal of the American Ceramic Society*, vol. 83, pp. 2833-2838, 2000.

[122] L. L. Burgner, M. C. Weinberg, "Crystal growth mechanisms in inorganic glasses," *Physics and Chemistry of Glasses*, vol. 42, pp. 184-190, 2001.

[123] A. K. Varshneya, "Fundamentals of inorganic glasses", *Society of Glass Technology*, 2006.

[124] W. Hoeland, V. Rheinberger, and M. Frank, "Mechanisms of nucleation and controlled crystallisation of needle-like apatite in glass-ceramics of the $SiO_2$-$Al_2O_3$-$K_2O$-CaO-$P_2O_5$ crystallisation of needle-like apatite in glass-ceramics of the $SiO_2$-

$Al_2O_3$-$K_2O$-CaO-$P_2O_5$crystallisation of needle-like apatite in glass-ceramics of the $SiO_2$-$Al_2O_3$-$K_2O$-CaO-$P_2O_5$ system," *Journal of Non-Crystalline Solids*, vol. 253, pp. 170-177, 1999.

[125] J. W. Cahn and R. J. Charles, "Initial Stages Of Phase Separation In Glasses," *Physics And Chemistry Of Glasses*, vol. 6, pp. 181-191, 1965.

[126] W. A. Dollase, L. H. Merwin, and A. Sebald, "Structure of $Na_{3-3x}Al_xPO_4$ x=0-0.5," *Journal of Solid State Chemistry*, vol. 83, pp. 140-149, 1989.

[127] Schott, Otto Phd thesis. "Contributions to the Theory and Practice of Glass Fabrication", 1973.

[128] H. N. Xiao, T. Sun, H. B. Liu, and Y. Cheng, "Crystallization Behavior and Microstructure of $B_2O_3$-$Al_2O_3$-$SiO_2$ Glass-Ceramics", *Advanced Materials Research*, vol. 51, pp. 149-154, 2008.

[129] C. Boussard-Plédel, M. Le Floch, "The structure of a boron oxyfluoride glass, an inorganic cross-linked chain polymer", *Journal of Non-Crystalline Solids*, vol. 209, pp. 247-256, 1997.

[130] G. L. Turner, K. A. Smith, R. J. Kirkpatrick, and E. Oldfield, "Boron-11 Nuclear Magnetic Resonance Spectroscopic Study of Borate and Borosilicate Minerals and a Borosilicate Glass," *J. Magn. Reson*. vol. 67, pp. 544-550, 1986.

[131] K.L. Geisinger, R. Oestrike, A. Navrotsky, G.L. Turner and R.J. Kirkpatrick, "Structural environment of Al dissolved in $2PbO{\cdot}B_2O_3$ glasses used for solution calorimetry: an $^{27}Al$ NMR study", *Dept. of Geological & Geophysical Sciences*, vol. 72, pp. 788-791, 1987.

[132] B.C. Bunker, D.R. Tallant, R.J. Kirkpatrick and G.L.Turner, "Multinuclear nuclear magnetic resonance and Raman investigation of sodium borosilicate glass structures", *Phys. Chem. Glasses*, vol. 31, pp. 30-41, 1990.

[133] H. Eckert, "Structural characterization of noncrystalline solids and glasses using solid state NMR", vol. 24, pp. 159-293, 1992.

[134] W. Müller-.Warmuth, H. Eckert, "Nuclear Magnetic Resonance and Mössbauer Spectroscopy of Glasses", *Phys. Rep.*, vol. 5, pp. 91-149, 1982.

[135] P. Griffiths, de J. A. Hasseth, "Fourier Transform Infrared Spectrometry (2nd ed.)", *Wiley-Blackwell. ISBN 0471194042*, 2007.

[136] C. N. Banwell, E. M. McCash, "Fundamentals of Molecular Spectroscopy (4th ed.)", *McGraw-Hill. ISBN 0-07-707976-0*, 1994.

[137] D. J. Gardiner, "Practical Raman spectroscopy", *Springer-Verlag. ISBN 978-0387502540*, 1989.

[138] C. Huang and E. C. Behrman, "Structure And Properties Of Calcium Aluminosilicate Glasses," *Journal Of Non-Crystalline Solids*, vol. 128, pp. 310-321, 1991.

[139] L. Stoch and M. Sroda, "Infrared spectroscopy in the investigation of oxide glasses structure," *Journal of Molecular Structure*, vol. 512, pp. 77-84, 1999.

[140] L. G. Hwa, S. L. Hwang, and L. C. Liu, "Infrared and Raman spectra of calcium alumino-silicate glasses," *Journal Of Non-Crystalline Solids*, vol. 238, pp. 193-197, 1998.

[141] N. J. Clayden, S. Esposito, A. Aronne, and P. Pernice, "Solid state Al-27 NMR and FTIR study of lanthanum aluminosilicate glasses," *Journal Of Non-Crystalline Solids*, vol. 258, pp. 11-19, 1999.

[142] O. Peitl, E. D. Zanotto, and L. L. Hench, "Highly bioactive $P_2O_5$-$Na_2O$-CaO-$SiO_2$ glass-ceramics," *Journal Of Non-Crystalline Solids*, vol. 292, pp. 115-126, 2001.

[143] S. A. MacDonald, C. R. Schardt, D. J. Masiello, and J. H. Simmons, "Dispersion analysis of FTIR reflection measurements in silicate glasses," *Journal Of Non-Crystalline Solids*, vol. 275, pp. 72-82, 2000.

[144] R. Iordanova, V. Dimitrov, Y. Dimitriev, and D. Klissurski, "Glass formation and structure of glasses in the $V_2O_5$ -$MoO_3$ -$Bi_2O_3$ system", *J. Non-Cryst. Solids*, vol. 180, pp. 58-65, 1994.

[145] Y. D. Yiannopoulos, and G. D. Chryssikos, "Structure and properties of alkaline earth borate glasses", *Physics and Chemistry of Glasses*, vol. 42, pp. 164-172, 2001.

[146] A. Kumar, S.B. Rai, and D.K. Rai, "Effect of thermal neutron irradiation on Gd3+ ions doped in oxyfluoroborate glass: an infra-red study", *Materials Research Bulletin*, vol. 38, pp. 333-339, 2003.

[147] P. Pascuta, L. Pop, S. Rada, M. Bosca, and E. Culea, "The local structure of bismuth borate glasses doped with europium ions evidenced by FT-IR spectroscopy", *Journal of Materials Science: Materials in Electronics*, vol. 19, pp. 424-428, 2008.

[148] E.I. Kamitsos, M.A. Karakassides, and G.D. Chyssikos, "Vibrational spectra of magnesium-sodium-borate glasses. 2. Raman and mid-infrared investigation of the network structure", *The Journal of physical chemistry*, vol. 91 (5), pp. 1073-1079, 1987.

[149] J. Krogh-Moe, "The structure of vitreous and liquid boron oxide", *Journal of Non-Crystalline Solids*, vol. 1, pp.269-284, 1969.

[150] R. Shuker and R. W. Gammon, *Physics. Rev. Lett*. vol. 25, pp. 222, 1970.

[151] R. Shuker and R.W. Gammon, *Journal of Physics And Chemistry of Solids*, vol. 25, pp. 222, 1970.

[152] J. Etchepare, in Amorphous Materials, eds. R. W. Douglas and B. Ellis, pp. 337,1970.

[153] P.L. Higby, R.J. Ginther, I.D. Aggarwal, E.J. Friebele, *Journal of Non-Crystalline Solids*, vol. 126, pp. 209, 1990.

[154] MacMillan, B. Piriou, *Journal of Non-Crystalline Solids*, vol. 55, pp. 221, 1983.

[155] C. Huang, E.C. Behrman, *Journal of Non-Crystalline Solids*, vol. 128, pp. 310, 1991.

[156] C.I. Merzbacher, W.B. White, *Journal of Non-Crystalline Solids*, vol. 130, pp. 18, 1991.

[157] G. Engelhardt, M. Nofz, K. Forkel, F. G. Wihsmann, M. Magi, A. Samoson, and E. Lippmaa, "Structural Studies Of Calcium Aluminosilicate Glasses By High-Resolution Solid-State Si-29 And Al-27 Magic Angle Spinning Nuclear Magnetic-Resonance," *Physics And Chemistry Of Glasses*, vol. 26, pp. 157-165, 1985.

[158] R. Hill, A. Stamboulis, R. V. Law, A. Clifford, M. R. Towler, and C. Crowley, "The influence of strontium substitution in fluorapatite glasses and glass ceramics," *Journal of Non-Crystalline Solids*, vol. 336, pp. 223-229, 2004.

[159] B.C. Bunker, R. J. Kirkpatrick, R. K. Brow, G. L. Turner and C. Nelson, "Local Structure of Alkaline-Earth Boroaluminate Crystals and Glasses: II, 11B and 27Al

MAS NMR Spectroscopy of Alkaline-Earth Boroaluminate Glasses", *Journal of the American Ceramic Society*, vol. 74, pp. 1430, 1991.

[160] K. L. Geisinger, R. Oestrike, A. Navrostky, G. L. Turner and R. J. Kirkpatrick, "Thermochemistry and structure of glasses along the join $NaAlSi_3O_8$-$NaBSi_3O_8$", *Geochimica et Cosmochimica Acta*, , vol. 52, pp. 2405-2414, 1988.

[161] R. N. Panda, M. F. Hsieh, R. J. Chung, and T. S. Chin, "FTIR, XRD, SEM and solid state NMR investigations of carbonate-containing hydroxyapatite nano-particles synthesized by hydroxide-gel technique," *Journal Of Physics And Chemistry Of Solids*, vol. 64, pp. 193-199, 2003.

[162] S. Haque, I. Rehman, and J. A. Darr, "Synthesis and characterization of grafted nanohydroxyapatites using functionalized surface agents," *Langmuir*, vol. 23, pp. 6671-6676, 2007.

[163] M. Chatterjee and M. K. Naskar, "Sol-gel synthesis of lithium aluminum silicate powders: The effect of silica source," *Ceramics International*, vol. 32, pp. 623-632, 2006.

[164] A. Aronne, S. Esposito, C. Ferone, M. Pansini, and P. Pernice, "FTIR study of the thermal transformation of barium-exchanged zeolite A to celsian," *Journal Of Materials Chemistry*, vol. 12, pp. 3039-3045, 2002.

[165] B. Sreedhar, M. Sairam, D. K. Chattopadhyay, and K. Kojima, "Preparation and characterization of lithium fluorophosphate glasses doped with $MoO_3$," *Materials Chemistry And Physics*, vol. 92, pp. 492-498, 2005.

[166] L. Kravitz, J.Kingsley, and E. Elkin, *Journal of Chemical Physics.* vol. 49, pp. 4600, 1968.

[167] A. Schulte, S. Buchler, and B. Chai, Proc. Soc. Photo-Opt. Instrument. Engeering, vol. 34, pp. 2380, 1995.

[168] W. Griffith, *Nature* (Landon), vol. 224, pp. 264, 1969.

[169] M. Sha, Z. Li, R. Bradt, *Journal of Applied Physics,* vol. 75, pp. 7784, 1994.

[170] G. Herzberg, Infrared and Raman Spectra, Van Nostrand, New York, 1945.

[171] R. J. Kirkpatrick, R. A. Kinsey, K. A. Smith, D. M. Henderson, and E. Oldfield, "High-Resolution Solid-State Na-23, Al-27, And Si-29 Nuclear Magnetic-Resonance

Spectroscopic Reconnaissance Of Alkali And Plagioclase Feldspars," *American Mineralogist*, vol. 70, pp. 106-123, 1985.

[172] K. J. D. MacKenzie, R. H. Meinhold, J. E. Patterson, H. Schneider, M. Schmücker, and D. Voll, "Structural evolution in gel-derived mullite precursors," *Journal of the European Ceramic Society*, vol. 16, pp. 1299, 1996.

[173] S. N. Scrimgeour, J. A. Chudek, and C. H. Lloyd, "The determination of phosphorus containing compounds in dental casting investment products by 31P solid-state MAS-NMR spectroscopy," *Dental Materials*, vol. 23, pp. 415, 2007.

[174] Fei Wang, Cation substitution in ionomer glasses: effect on glass structure and crystallization, PhD thesis (2009), University of Birmingham.

[175] M.A. Azooz, T.H.M. Abou Aiad, F.H.E lbatal, G. ElTabii, "Characterization of bioactivity in transition metal doped-borosilicate glasses by infrared reflectionand dielectric studies", *Indian Journal of Pure and Applied Physics*, vol. 46, pp. 880–888, 2008.

[176] K.J. Rao, "Structural Chemistry of Glasses", Elsevier, Amsterdam, 2002.

[177] G. Little Flower, M. Srinivasa Reddy, M.V. Ramana Reddy, and N. Veeraiah, "Influence of chromium ions on the dielectric properties of the $PbO–Ga_2O_3–P_2O_5$ glass system", *Zeitschrift fuer Naturforschung, A: Physical Sciences*, vol. 62, pp. 315–323, 2007.

[178] M. Srinivasa Reddy, G. Naga Raju, G. Nagarjuna, and N. Veeraiah, "Structural influence of aluminium, gallium and indium metal oxides by means of dielectric andspectroscopic properties of $CaO–Sb_2O_3–B_2O_3$ glass system", *Journal of Alloysand Compounds*, vol. 438, pp. 41–51, 2007.

[179] D. Muller, G. Berger, I. Grunze, G. Ladwig, E. Hallas, U. Haubenreisser, "Influence of aluminum ions on fluorescent spectra and upconversion in codoped $CaF_2–Al_2O_3–P_2O_5–SiO_2$: $Ho^{3+}$ and $Er^{3+}$ glass system", *Physics and Chemistry of Glasses*, vol. 24, pp. 37–45, 1983.

[180] R.K. Brow, D.R. Tallant, "Structural design of sealing glasses", *Journal of Non-Crystalline Solids*, vol. 222, pp. 396–406, 1997.

[181] Ch. Srinivasa Rao, V. Ravi Kumar, T. Srikumar, Y. Gandhi, and N. Veeraiah,

"The role of coordination and valence states of tungsten ions on some physical properties of $Li_2O–Al_2O_3–ZrO_2–SiO_2$ glass system", *Journal of Non-Crystalline Solids*, vol. 357, pp. 3094–3102, 2011.

[182] A. Belkebir, J. Rocha, A.P. Esculcas, P. Berthet, and B.Z. Gilbert, "Structural characterisation of glassy phases in the system $Na_2O–Al_2O_3–P_2O_5$ by MAS and solution NMR, EXAFS and vibrational spectroscopy", *Spectrochimica Acta*, vol. 55, pp. 1323–1336, 1999.

[183] P. Colomban, H. G. M. Edwards, and J. M. Chalmers, "Recognition of ancient technology from the Raman spectra", pp. 192–206, 2000.

[184] A. Jayaraman, D. L. Wood, and R. G. Maines, "High pressure Raman study of the vibrational modes in $AlPO_4$ and $SiO_2$ (α-quartz)", *Physics*., vol. 35, pp. 8316–8321, 1987.

[185] R. Dupree, D. Holland, M. G. Mortuza, J. A. Collins, and M. W. G. Lockyer, "An Mas Nmr-Study Of Network - Cation Coordination In Phosphosilicate Glasses," *Journal Of Non-Crystalline Solids*, vol. 106, pp. 403-407, 1988.

[186] R. Dupree, D. Holland, and M. G. Mortuza, "6-Coordinated Silicon In Glasses," *Nature*, vol. 328, pp. 416-417, 1987.

[187] G. Cody, B. Mysen, G. Saghi-Szabo, and J. A. Tossel, "Silicate phosphate interactions in silicate glasses and melts: Part I. A multinuclear ($^{27}Al$, $^{29}Si$, $^{31}P$) MAS-NMR and ab initio chemical shift shielding $^{31}P$ study of phosphorus speciation in silicate glasses," *Geochimica et Cosmochimica Acta*, vol. 65, pp. 2395-2411, 2001.

[188] T. Maeda, S. Matsuya, and M. Ohta, "29Si, 27A1 NMR and ESCA study on $SiO_2$ -$Al_2O_3$-CaO glasses," *Journal of Japanese Society for Dental Materials and Devices*, vol. 12, pp. 765, 1993.

[189] J. M. Oliveira, R. N. Correira, M. H. Fernandes, and J. Rocha, "Influence of the Cao/MgO ratio on the structure of phase separated glasses: a solid sate $^{29}Si$ and $^{31}P$ MAS-NMR study," *Journal of Non-Crystalline Solids*, vol. 265, pp. 221-229, 2000.

[190] H. Gan and P. C. Hess, "Phosphate Speciation In Potassium Aluminosilicate Glasses," *American Mineralogist*, vol. 77, pp. 495-506, 1992.

[191] H. Miyoshi, D. Chen, "Effect of calcium additive on structural changes under

heat treatment in sodium borosilicate glasses", *Journal of Non-Crystalline Solids*, vol. 345–346, pp. 99-103, 2004.

[192] F. Fayon, D. Massiot, K. Suzuya, and D. L. Price, "P-31 NMR study of magnesium phosphate glasses," *Journal Of Non-Crystalline Solids*, vol. 283, pp. 88-94, 2001.

[193] J. F. Stebbins and Q. Zeng, "Cation ordering at fluoride sites in silicate glasses: a high-resolution F-19 NMR study," *Journal of Non-Crystalline Solids*, vol. 262, pp. 1-5, 2000.

[194] M. D. Ingram, C. T. Imrie, and I. Konidakis, "Activation volumes and site relaxation in mixed alkali glasses," *Journal of Non-Crystalline Solids*, vol. 352, pp. 3200, 2006.

[195] A. Pradel and M. Ribes, "Ion transport in superionic conducting glasses," *Journal of Non-Crystalline Solids*, vol. 172-174, pp. 1315, 1994.

[196] D. E. Day, "Mixed alkali glasses -- Their properties and uses," *Journal of Non-Crystalline Solids*, vol. 21, pp. 343, 1976.

[197] B. Z. Pevzner and V. P. Klyuev, "Manifestation of the mixed-cation effect in dilatometric properties of RO ($R_2O$) center dot $2B_2O_3$ borate glasses upon replacement of Na2O by BaO, $Na_2O$ by MgO, and BaO by MgO," *Glass Physics And Chemistry*, vol. 30, pp. 506-514, 2004.

[198] P. Islam, R. Hill, and A. Stamboulis, "Activation energy for crystal growth in stoichiometric $CaAl_2Si_2O_8$ and $Ca_2Al_2Si_2O_9$ glasses," *Journal of Materials Science Letters*, vol. 22, pp. 1287-1289, 2003.

[199] W. Sha, "Communication: Determination of Activation Energy of Phase Transformation and Recrystallization Using a Modified Kissinger Method," *Metallurgical and Materials Transactions A*, vol. 32, pp. 2903-2904, 2001.

[200] E. A. Marseglia, "Kinetic-theory of crystallization of amorphous materials," *Journal of Non-Crystalline Solids*, vol. 41, pp. 31-36, 1980.

[201] H. E. Kissinger, "Reaction Kinetics in Differential Thermal Analysis," *Analytical Chemistry*, vol. 29(11), pp. 1702-1706, 1957.

[202] K. Matusita and S. Sakka, "Kinetic study of crystallization of glass by

differential thermal analysis—criterion on application of Kissinger plot," *Journal of Non-Crystalline Solids*, vol. 40, pp. 149-158, 1980.

[203] A. Marotta, S. Saiello, and A. Buri, "Remarks on determination of the avrami exponent by non-isothermal analysis," *Journal of Non-Crystalline Solids*, vol. 57, pp. 473, 1983.

[204] L. Medvecky, M. Giretova, and T. Sopcak, "Preparation and properties of tetracalcium phosphate-monetite biocement", *Materials Letters*, vol. 100, pp. 137–140, 2013.

[205] C. Jana, M. Braun, "$^{19}$F NMR spectroscopy of glass ceramics containing fluorapatites", *Biomaterials*, vol. 17(21), pp. 2065, 1996

[206] M. Braun, C. Jana, "$^{19}$F NMR spectroscopy of fluoridated apatites", *Chemical Physics Letters*, vol. 245, pp.19-22, 1995.

[207] T. Kokubo, "Bioactive glass ceramics: properties and applications", *Biomaterials*, vol. 12, pp. 155-163,1991.

[208] T. Kokubo, M. Shigematsu, Y. Nagashima, M. Tashiro, T. Nakamura, and T. Yamamuro, S. Higashi, "Apatite- and wollastonite-containing glass-ceramics for prosthetic application", *Bull. Inst. Chem. Res. Kyoto Univ.*, vol. 60, pp. 260–268, 1982.

[209] T. Kokubo, S. Ito, S. Sakka, and T. Yamamuro, "Formation of a high-strength bioactive glass-ceramic in the system MgO-CaO-$SiO_2$-$P_2O_5$", *J. Mater. Sci.*, vol. 21, pp. 536–540, 1986.

[210] T. Kokubo, H. Kushitani, C. Ohtsuki, S. Sakka, and T. Yamamuro, "Surface reaction of bioactive glass ceramic A-W in a simulated body environment", *Materials in Medicine* (Submitted).

[211] T. Kokubo, S. Ito, M. Shigematsu, S. Sakka, and T. Yamamuro, "Mechanical properties of a new type of apatite-containing glass ceramic for prosthetic application", *J. Mater. Sci.*, vol. 20, pp. 2001–2004, 1985.

[212] T. Kokubo, S. Ito, M. Shigematsu, S. Sakka, and T. Yamamuro, "Fatigue and life time of bioactive glass ceramic A-W containing apatite and wollastonite", *J. Mater. Sci.*, vol. 22, pp. 4067–4070, 1987.

[213] J. Gallardo, P. G. Galliano, J. M. P. Lopez, *Biomaterials*, vol. 23, pp. 4277, 2002.

[214] A. Clifford, "Apatite–Mullite Glass-Ceramics", Ph.D. Thesis. University of Limerick, Limerick, Ireland, 1997.

[215] R. G. Hill, C. Goat, and D. Wood, "Thermal Analysis of a $SiO_2$–$Al_2O_3$–CaO – $CaF_2$ Glass", *J. Am. Ceram. Soc.*, vol. 75, pp. 778–85, 1992.

[216] S. W. Kieffer, Rev. Geophys. *Space Phyics*. vol. 17, pp. 20, 1979.

[217] R. Dupree, D. Holland, P. W. McMillan, and R. F. Pettifer, "The structure of soda-silica glasses: A MAS-NMR study," *Journal of Non-Crystalline Solids*, vol. 68, pp. 399, 1984.

[218] I. Jaymes, A. Douy, D. Massiot, and J. P. Coutures, "Evolution of the Si environment in mullite solid solution by Si-29 MAS-NMR spectroscopy," *Journal Of Non-Crystalline Solids*, vol. 204, pp. 125-134, 1996.

[219] T. Ban and K. Okada, "Analysis Of Local Cation Arrangement In Mullite Using Si-29 Magic-Angle-Spinning Nuclear-Magnetic-Resonance Spectra," *Journal Of The American Ceramic Society*, vol. 76, pp. 2491-2496, 1993.

[220] S. Gomes and M. Francois, "Characterization of mullite in silicoaluminous fly ash by XRD, TEM, and $^{29}$Si MAS NMR," *Cement and Concrete Research*, vol. 30, pp. 175, 2000.

[221] M. T. Dove, "The use of Si-29 MAS-NMR and Monte Carlo methods in the study of Al/Si ordering in silicates," *Geoderma*, vol. 80, pp. 353-368, 1997.

[222] P. R. Bodart, J. Parmentier, R. K. Harris, and D. P. Thompson, "Aluminium environments in mullite and an amorphous sol-gel precursor examined by 27Al triple-quantum MAS NMR," *Journal of Physics and Chemistry of Solids*, vol. 60, pp. 223, 1999.

[223] H. He, J. Guo, J. Zhu, P. Yuan, and C. Hu, "29Si and 27Al MAS NMR spectra of mullites from different kaolinites," *Spectrochimica Acta Part A: Molecular and Biomolecular Spectroscopy*, vol. 60, pp. 1061, 2004.

[224] M. A. Aramendia, V. Borau, C. Jimenez, J. M. Marinas, F. J. Romero, and J. R. Ruiz, "XRD and solid-state NMR study of magnesium oxide magnesium orthophosphate systems," *Journal Of Solid State Chemistry*, vol. 135, pp. 96-102, 1998.

[225] A. Aissa, B. Badraoui, R. Thouvenot, and M. Debbabi, "Synthesis, X-ray structural analysis and spectroscopic investigations (IR and P-31 MAS NMR) of mixed barium/strontium fluoroapatites," *European Journal Of Inorganic Chemistry*, pp. 3828-3836, 2004.

[226] L. B. Moran, J. K. Berkowitz, and J. P. Yesinowski, "F-19 and P-31 magic-angle spinning nuclear magnetic resonance of antimony(III)-doped fluorapatite phosphors: Dopant sites and spin diffusion," *Physical Review B*, vol. 45, pp. 5347, 1992.

[227] G. Walter, J. Vogel, U. Hoppe, and P. Hartmann, "The structure of CaO-Na2O-MgO-$P_2O_5$ invert glass," *Journal of Non-Crystalline Solids*, vol. 296, pp. 212, 2001.

[228] T. J. Kiczenski, J. F. Stebbins, "Fluorine sites in calcium and barium oxyfluorides: F-19 NMR on crystalline model compounds and glasses", *Journal of Non-Crystalline Solids*, vol. 306, pp. 160-168, 2002.

[229] Siqi Zhang, A. Stamboulis, "Effect of zinc substitution for calcium on the crystallisation of calcium fluoro-alumino-silicate glasses." *Journal of Non-Crystalline Solids*, vol. 432, Part B: pp. 300-306, 2016.